UNIVERSITY OF BATH

PHD

Analytical Studies of Uranium Oxides and Minerals

Driscoll, Richard

Award date:
2016

Awarding institution:
University of Bath

[Link to publication](#)

ANALYTICAL STUDIES OF URANIUM OXIDES AND MINERALS

Richard J. P. Driscoll

A thesis submitted for the degree of Doctor of Philosophy

University of Bath

Department of Chemistry

August 2016

Abstract

The aim of this thesis is to investigate the vibrational properties of a range of uranium based materials and to demonstrate the benefit of using vibrational data to identify and distinguish these materials in a forensic scenario. The ability to rapidly detect and identify radioactive samples is of particular importance to countries interested in controlling the distribution of nuclear material, as well as environmental scientists investigating the remediation of nuclear sites. The materials of interest to this study are U_3O_8 and UO_3, which are the two primary oxidation products of UO_2, and a range of minerals containing the uranyl UO_2^{2+} cation that readily form from UO_2 in the environment. Raman spectroscopy is a promising technique, with experimental data indicating that it may be used to distinguish between uranyl minerals, hence it is a particular focus of this thesis. Earlier work used group theory to interpret the spectra, whereas in this study the vibrational properties have been compared with density functional theory (DFT) simulations. This strategy has provided both an interpretation of vibrational modes and insight into how the vibrational properties change in response to structural or compositional changes.

Chapter 1 provides background information on binary uranium oxides, uranyl minerals and strategies that may be used to study them. Furthermore, the aims of this thesis are discussed. A summary of the theory of Raman and IR spectroscopy is described in Chapter 2 and the computational methods used are detailed in Chapter 3. Chapters 4 and 5 are focused on the simulation of vibrational spectra for the various polymorphs of U_3O_8 and UO_3, with comparisons made to experimental Raman and IR spectra. In Chapter 6 experimental Raman spectra for a range of uranyl minerals from Cornwall, UK are presented, with an emphasis on identifying differences that may be used to discriminate between samples. In Chapter 7 DFT is used to simulate the vibrational spectra for a set of uranyl phosphate and arsenate minerals, known as autunite minerals, with systematic variations in composition. Finally, the conclusions from all chapters are collated and discussed in Chapter 8, alongside possible areas of continued research.

Acknowledgements

Publications and Presentations

A Raman Spectroscopic Study of Uranyl Minerals from Cornwall, R. J. P. Driscoll, D. Wolverson, J. M. Mitchels, J. M. Skelton, S. C. Parker, M. Molinari, I. Khan, D. Geeson and G. C. Allen, **RSC Advances** (2014), 4:103, 59137

Vibrational Properties of U_3O_8 Polymorphs: Effect of Layer Stacking, R. J. P. Driscoll, N. A. Brincat, M. Molinari, S. C. Parker, G. C. Allen, D. Wolverson, I. Khan and D. Geeson, **Paper in preparation**

Vibrational Properties of UO_3 Polymorphs: A Combined Computational and Experimental Study, R. J. P. Driscoll, G. C. Allen, N. A. Brincat, M. Molinari, S. C. Parker, D. Wolverson, I. Khan and D. Geeson, **Paper in preparation**

A Forensic Investigation into the Vibrational Properties of Uranyl Minerals, **Poster**, Plutonium Futures, Las Vegas, Nevada, USA, September 2014

A Forensic Investigation into the Vibrational Properties of Uranyl Minerals, **Poster**, Dalton Discussions 14: Advancing the chemistry of the f-elements, Edinburgh, UK, July 2014

An Investigation into the Vibrational Properties of Uranium Minerals, **Talk**, HPC Symposium, University of Bath, June 2014

A Forensic Investigation of Uranium Minerals, **Talk**, IOM[3] Young Persons' Lecturing Competition, Bath, Swansea and London, February–April 2014

An Analytical Study of Uranium Minerals from Cornwall, England, **Talk**, Ussher Conference, Weston-Super-Mare, January 2014

An Atomistic and Experimental Investigation to Index Uranium Minerals, **Poster**, CCP5 Annual Meeting: Advances in Modern Day Computer Simulations, Kent, UK, September 2013

An Analytical Study of Uranium Minerals from Cornwall, England, **Talk**, Minerals for Life: Overcoming Resource Constraints, Edinburgh, UK, June 2013

Contents

Chapter 1

Introduction

All countries that utilise nuclear technology are required to control the distribution of radioactive materials and prevent it from being illegally obtained by nations or organisations that are not recognised as 'nuclear states' by the Nuclear Non-Proliferation Treaty [1]. The field of nuclear forensics has emerged to track, detect and identify suspect radioactive material, using a variety of analytical techniques [2]. The knowledge and methods used for forensics can also be applied to follow the contamination and remediation of nuclear sites and to investigate the processes affecting waste storage [3–6]. In this thesis, the value of using vibrational spectroscopy to identify and distinguish between uranium based minerals and materials is explored. Raman spectroscopy has been shown as capable of rapidly collecting data for samples *in situ* without damaging or changing the material. Maintaining an extensive database of spectra for known materials would be a powerful tool when analysing unknown samples [7]. This chapter provides context for the project, with background information on nuclear power generation, uranium oxides and minerals and the application of Raman and infrared (IR) spectroscopies. A more detailed review is given in each chapter, which includes previously published structural and vibrational information. The major aims of this thesis are given in Section 1.4.

1.1 Nuclear Fission and Power Generation

The generation of electricity in nuclear reactors is centred around the process of nuclear fission (Figure 1.1). This can occur spontaneously in some heavy element isotopes, but these atoms decay more readily through α or β emission. In nuclear reactors, fission is induced by bombarding the heavy atoms with neutrons, resulting in the former separating into two smaller nuclei, known as fission products, and the emission of neutrons and γ radiation. The heat generated by this reaction is then absorbed by the reactor coolant, usually water, which produces steam that drives a set of turbines to produce electricity.

Some of the neutrons released by fission reactions have sufficient energy to induce further fission reactions, which may be sustained as a nuclear chain reaction, providing a constant supply of electricity. The most common design of reactors in use today, thermal reactors [8], utilise control rods to maintain the chain reaction, but avoid overheating the
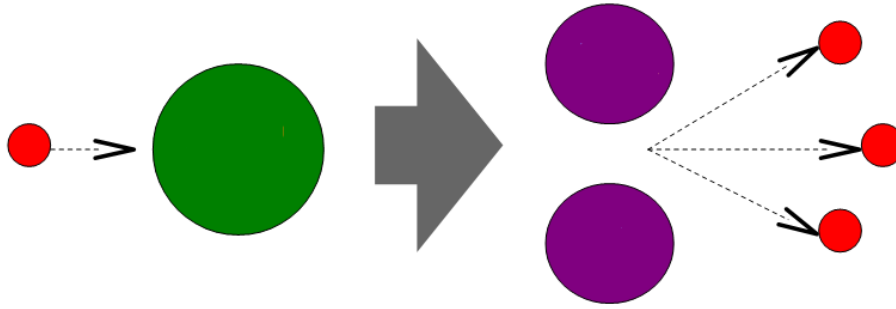
Figure 1.1: Schematic showing the process of nuclear fission. A neutron (red) collides with a fissile nucleus (green), which separates into two fission products (purple) and releases neutrons and γ radiation.

core. These are composed of neutron moderators or poisons, which absorb a portion of the free neutrons, reducing the number of fission reactions and, by extension, the power output when pushed deeper into the core. The reactor coolant may also be used as an alternative form of control, where reducing the temperature of the coolant increases its density and allows more neutrons to be absorbed.

To be viable as a nuclear fuel, a heavy element isotope must be fissile, which means it is capable of sustaining a nuclear chain reaction. These isotopes are almost exclusively actinide elements, with ^{235}U and ^{239}Pu the most commonly used. Naturally occurring uranium only contains $\sim 0.72\%$ ^{235}U, compared to 99.28% ^{238}U [9]. While ^{238}U can undergo an induced fission reaction, the majority of neutrons it emits do not have sufficient energy to induce further reactions. Therefore, the fuel is typically enriched to 3.5–5% ^{235}U, with the exact proportion depending on the requirements of the reactor [9].

The nuclear fuels used in modern reactors are typically metal oxides, which have higher melting points and a lower risk of burning than the pure metals that were used previously [10]. Uranium dioxide (UO_2) is currently the most commonly used fuel, but it is susceptible to oxidation, forming a wide range of other oxides, including U_3O_8 and UO_3. PuO_2 has a contrasting problem, as it readily reduced to Pu_2O_3. Mixed oxide (MOX) fuels are a more recent alternative, containing varying proportions of U and Pu oxides [9]. ThO_2 has also been shown as a promising fuel material, with greater chemical stability and natural abundance than UO_2 and PuO_2. Furthermore, the only major isotope (^{232}Th) is fertile, meaning it forms the fissile ^{235}U upon absorbing neutrons. As the fissile material is immediately used in the reactor, the risks of proliferation are reduced [11].

1.2 Oxidation of Uranium Dioxide

In UO_2, uranium is found in the U^{4+} oxidation state. However, during the processes involved in preparing the fuel, generating electricity and disposing or storing the waste, known collectively as the nuclear fuel cycle [12], it is regularly exposed to oxidising conditions. This allows a variety of uranium oxides to form, with oxidation states that include U^{4+}, U^{5+} and U^{6+} [13]. Many of these oxides are also found naturally, associated with deposits of uraninite (UO_2, also known as pitchblende). The major uranium oxides are discussed in Section 1.2.1.
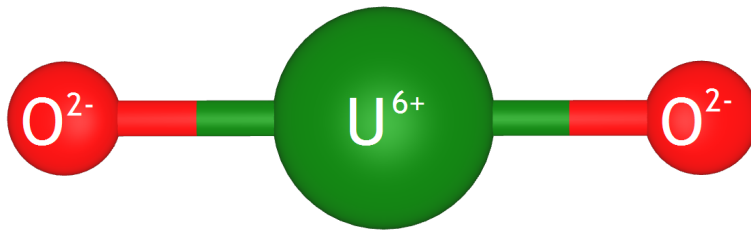
Figure 1.2: The uranyl cation, UO_2^{2+}, where U^{6+} and O^{2-} are shown as green and red spheres, respectively.

When released into the environment, uranium is commonly found in the U^{6+} oxidation state. U^{6+} often forms two strong collinear U-O bonds, 1.7–1.9 Å in length, known as uranyl bonding (Figure 1.2). In contrast to UO_2, the uranyl cation (UO_2^{2+}) is soluble in water, so it can readily contaminate soil and groundwater [14, 15], which poses risks to the environment and to the health of humans and animals [16–18] and requires regular monitoring [4, 5, 19]. One commonly used method of remediation is the immobilisation of UO_2^{2+} by its reaction with inorganic minerals, such as apatite ($Ca_5(PO_4)_3(OH,F)$), forming a variety of uranyl minerals [6, 20–28]. Uranyl minerals also occur naturally as secondary minerals, formed by the weathering of pitchblende deposits [29]. These minerals are introduced in Section 1.2.2, with more specific details on selected minerals in Chapter 6.

1.2.1 The Uranium-Oxygen System

The uranium-oxygen system is complex [30], with a large number of intermediate oxides forming between UO_2 (U^{4+}) and UO_3 (U^{6+}). The phase diagram is reproduced in Figure 1.3 from a publication by Hoekstra *et al.* [30]. UO_2 crystallises in a cubic fluoride structure, which is retained for the oxides up to $UO_{2.5}$ (U_2O_5). Four phases of U_2O_5 have been reported, with α-, β- and γ-U_2O_5 described as adopting the fluorite structure. In contrast, the structures of δ-U_2O_5, U_3O_8 and UO_3 are found to adopt layered structures.
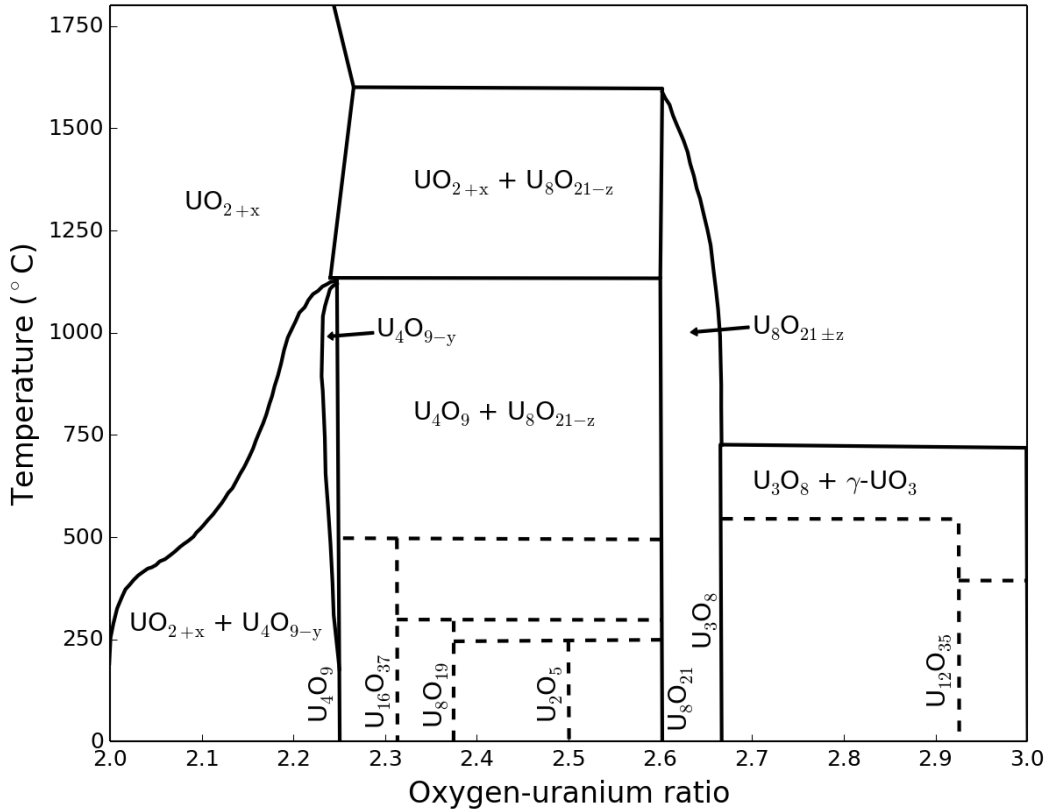
Figure 1.3: Reproduction of the phase diagram for the binary uranium oxygen system between UO_2 and UO_3 stoichiometries, as published by Hoekstra *et al.* [30].

U_3O_8 and UO_3 are the most stable uranium oxides [31, 32] and have both been studied as feasible nuclear fuels [33].

The cubic fluorite structure of UO_2 [34] (Figure 1.4.a) has been reported to incorporate oxygen hyperstoichiometry (UO_{2+x}) with very little change in structural properties. The clustering of oxygen interstitials is well known in UO_{2+x}. The first type of defect cluster described for UO_{2+x} was the Willis cluster [35–37] (Figure 1.4.b), in which interstitial oxygen ions displace lattice oxygen ions, producing additional interstitial ions and oxygen vacancies. A second cluster arrangement proposed for UO_{2+x} is known as the cuboctahedral cluster [38–40] (Figure 1.4.c), where a cube of oxygen lattice sites become vacant and are replaced by a cuboctahedral cage-like structure of oxygen interstitials, of which four are in excess of the perfect UO_2 stoichiometry. Another group of defect clusters are the split interstitials [41–44], which consist of an oxygen vacancy and three oxygen interstitials in an equilateral triangle arrangement. The structures of U_4O_9 and U_3O_7 have been described as a cubic fluorite UO_2 supercell with periodic arrangements of defect clusters [45].
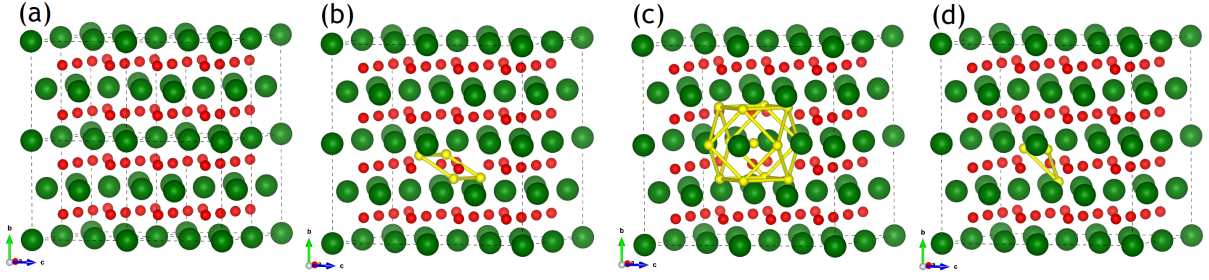
Figure 1.4: a) The crystal structure of UO_2, b) the 2:2:2 Willis cluster, c) the cubocta-hedral cluster and d) the split di-interstial cluster. Green and red represent the uranium and oxygen ions, respectively, while yellow represents the interstitials. The dashed black lines represent the unit cells.

U_2O_5 ($UO_{2.5}$) is known to be the stoichiometry at which the cubic fluorite based oxides transition to the layered structures. Atomic coordinates are only available for the layered orthorhombic structure of δ-U_2O_5 [46] (Figure 1.5.a), but the experimentally determined densities have indicated that α-, β- and γ-U_2O_5 adopt fluorite type structures [30]. Experiments originally suggested that a mixture of U^{4+} and U^{6+} exist in U_2O_5 [47], but a more recent XPS study has suggested that all uranium ions are in the U^{5+} oxidation state [48], which has been supported by computational work [12, 49]. The relative paucity of experimental information on U_2O_5 arises from the difficulty in stabilising it; previous computational studies have shown it is thermodynamically unstable [50].

U_3O_8 is the kinetically stable oxidation product of UO_2 [31]. It adopts a similar layered structure to δ-U_2O_5, but as it is significantly more stable, it has been studied more extensively than any other uranium oxide, with the exception of UO_2. Of the three known polymorphs, α-U_3O_8 is the most common [40] (Figure 1.5.b), but β-U_3O_8 forms after heating and slowly cooling the α polymorph [51], suggesting that these phases are in competition at room temperatures. In contrast, γ-U_3O_8 has been reported to form under high pressure conditions [40, 52]. The focus of Chapter 4 is on simulating the vibrational properties of the α and β phases, so more detailed structural information is provided there.

UO_3 has been reported as the thermodynamic oxidation product of UO_2 [32]. There are seven reported crystalline polymorphs and one amorphous phase [30, 53], of which the γ polymorph is the most stable (Figure 1.5.c). Two of the more common structures, α- and β-UO_3, have been described as defective [54, 55], demonstrating that pure stoichiometric phases are difficult to synthesise experimentally. The structural and vibrational properties of α-, β-, γ-, δ- and η-UO_3 are discussed in Chapter 5.
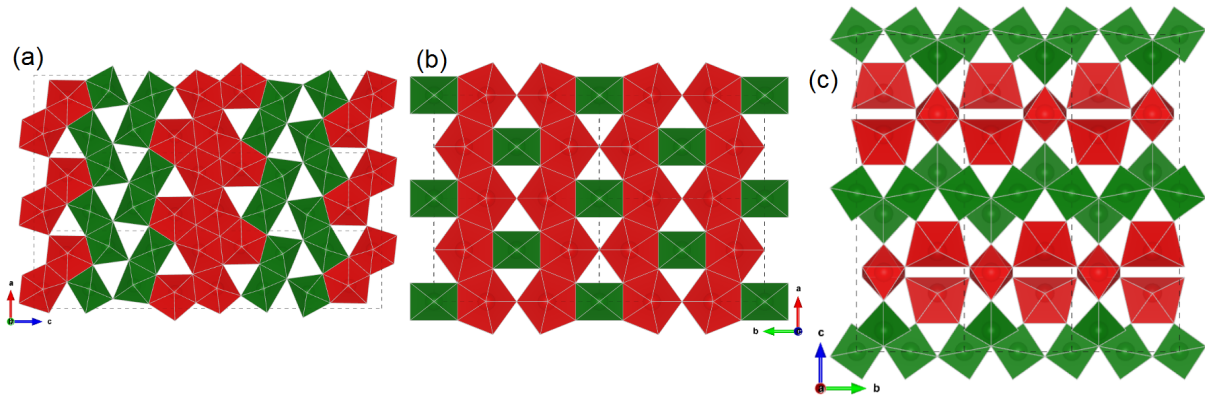
Figure 1.5: The layers found in a) δ-U_2O_5 and b) α-U_3O_8 and a cross section of the layers in γ-UO_3. For each structure, red and green polyhedra represent symmetrically distinct uranium environments.

1.2.2 Uranyl Minerals

Over 200 uranyl minerals have been reported [56]; however, in many cases aspects of their structure, composition, stability or occurrence are not fully characterised. The known structures may be arranged into five categories, based on their topology: structures based on isolated polyhedra; finite clusters; chains of polyhedra; 2D sheet structures and 3D frameworks. The minerals studied in this investigation are autunite, torbernite, zeunerite, nováčekite, andersonite, schröckingerite, johannite, natrozippeite, uranophane, cuprosklodowskite, kasolite and compreignacite. The majority of these minerals adopt a 2D sheet of polyhedra, with the exception of the uranyl carbonate minerals andersonite and schröckingerite, which are based around finite clusters of UO_2 and CO_3 polyhedra.

In addition to their topological differences, uranyl minerals may be categorised based on their composition. The minerals in this study are uranyl phosphates, arsenates, carbonates, sulphates, silicates and hydrates. Uranyl phosphates are the largest and most diverse category of uranyl minerals, with the majority adopting either the autunite or phosphuranylite type sheet structure [56]. The autunite minerals are particularly common, adopting the general formula $M(UO_2)_2(XO_4)_2 \cdot nH_2O$, where M is a cation (e.g. Cu^{2+} or Mg^{2+}), X is P, As or V and n is the number of water molecules. [57] The sheet is comprised of uranyl and phosphate polyhedra, while the divalent cations and water are found in the interlayer space. Many uranyl minerals have a variable level of hydration, which depends on their physical environment. For autunite minerals, the dehydrated forms are typically referred to as meta-autunite minerals [58]. This propensity to dehydrate means that intrusive experimental methods may change the sample as it is observed, therefore, low impact analytical techniques are valuable. Uranyl minerals are

described in more detail in Chapter 6, while autunite minerals are the focus of Chapter 7.

1.3 Analysis of Uranium Containing Minerals

The unambiguously identification of an unknown mineral sample in a forensic investigation requires the application of multiple techniques, including mass spectrometry (MS), scanning electron microscopy (SEM), energy-dispersive X-ray spectroscopy (EDX) and X-ray diffraction (XRD). However, some information can be obtained rapidly, allowing a provisional assignment to be made. First, a visual inspection of the sample provides the colour and morphology of any crystals, in addition to the presence of associated minerals. Second, vibrational spectra can be rapidly obtained, providing information on its structure or composition, without causing significant damage or changing the sample [59, 60]. Of particular value is Raman spectroscopy, which can be performed on a sample without prior preparation and, with the addition of an optical microscope, can study very small sample sizes, even dust particles [61]. Furthermore, handheld Raman devices have been developed, allowing samples to be analysed *in situ*, which is especially valuable for investigations where the samples are fragile or difficult to transport [62, 63]. Consequently, Raman has proven to be a valuable technique for initial detection and screening of unknown samples.

Each mode in the Raman and IR spectra directly corresponds to the vibration of one or more bonds, with the frequency (typically plotted as wavenumber, $\bar{\nu}$, in cm^{-1}) affected by the nature and strength of the bonds. Consequently, the vibrational spectra of different crystal structures provide unique fingerprints. Furthermore, Raman and IR spectroscopies have different selection rules, so both techniques are typically used to obtain a complete picture of the vibrational properties. The uranyl minerals in particular contain a variety of distinct polyions, such as PO_4^{3-}, SiO_4^{4-}, CO_3^{2-} and the uranyl cation itself (UO_2^{2+}), which all produce characteristic modes in the Raman and IR spectra. In many cases, it may be possible to predict what modes should be seen in both Raman and IR spectra, based upon the crystal structure and symmetry, while predictions of the peak positions may be made if the vibrational spectra of free ions are known (Section 1.3.2). Raman and IR spectroscopy, EDX and scanning electron microscopy (SEM) have all been utilised in this investigation and are discussed in Chapter 2.

1.3.1 Interpretation of Vibrational Spectra

Traditional methods for interpreting vibrational spectra are based around the use of group theory [64, 65]. This approach uses knowledge of the crystal symmetry and atomic coordinates to predict the set of vibrational modes, the symmetry group of each mode and whether they are Raman or IR active. The set of predicted peaks may then be used to interpret experimental Raman or IR spectra. In general, stretching modes are found at higher wavenumbers than bending modes and motions involving heavier atoms are found at lower wavenumbers. These trends may allow the spectra of structures with small or highly symmetric unit cells (e.g. UO_2 and α-UO_3) to be interpreted using group theory alone, but for larger and more complex systems, an alternative approach may be more appropriate. The interpretation may be complicated further by overlapping peaks or a deviation from perfect symmetry in the real system.

Computational modelling is a useful approach to predict the vibrational spectra of theoretically pure crystals and to interpret experimental data. Such calculations may be expensive in terms of computer resource, but they can produce both a predicted wavenumber and a vibrational motion, allowing the structural and vibrational properties to be linked. Furthermore, using the same model for multiple structures provides a base for investigating the trends in vibrational properties that result from small changes in structure or composition. This approach has been used to investigate how different proportions of phosphorus and arsenic affect the Raman and IR spectra of autunite minerals in Chapter 7.

As UO_2 has the simplest structure of all uranium oxides, it has been the subject of many computational investigations [43], including those analysing the defect clusters found in UO_{2+x}. Similarly, U_3O_8 [49] and selected phases of UO_3 [55] have been simulated in previous investigations. Few computational based investigations have focused on the less stable uranium oxides or the uranyl minerals and no studies have used DFT to predict the vibrational properties of uranyl minerals.

The two strategies used within most modern electronic structure simulation codes for calculating the vibrational modes and motions are the frozen phonon approach and density functional perturbation theory (DFPT) [66, 67]. Computation of the Raman and IR activities requires additional information: for IR, the Born effective charges need to be calculated and for Raman the dielectric response to each vibrational motion must be determined. Chapter 3 provides background information on the use of DFT, including

the calculation of vibrational properties.

1.3.2 Vibrational Properties of Free Ions

If the uranyl minerals are considered to be a sum of their individual components (i.e. the distinct polyanions and cations), it is possible to use a group theory approach to determine the set of vibrational modes associated with each component. For example, the linear uranyl cation (UO_2^{2+}) has $D_{\infty h}$ symmetry, so three fundamental vibrational modes are predicted. These are the ν_1 symmetric stretch, the ν_2 doubly degenerate bending mode and the ν_3 antisymmetric stretch. As the $D_{\infty h}$ symmetry group contains an inversion centre, the rule of mutual exclusion applies, such that the ν_1 mode is only Raman active, whereas ν_2 and ν_3 are only IR active. However, within the environment of a mineral, the uranyl cation often becomes distorted from perfect symmetry, leading to a relaxation of this rule. In literature Raman and IR spectra of aqueous uranyl ions, the positions of ν_1, ν_2 and ν_3 are typically seen around 750–900 cm^{-1}, 200–300 cm^{-1} and 850–1000 cm^{-1}, respectively.
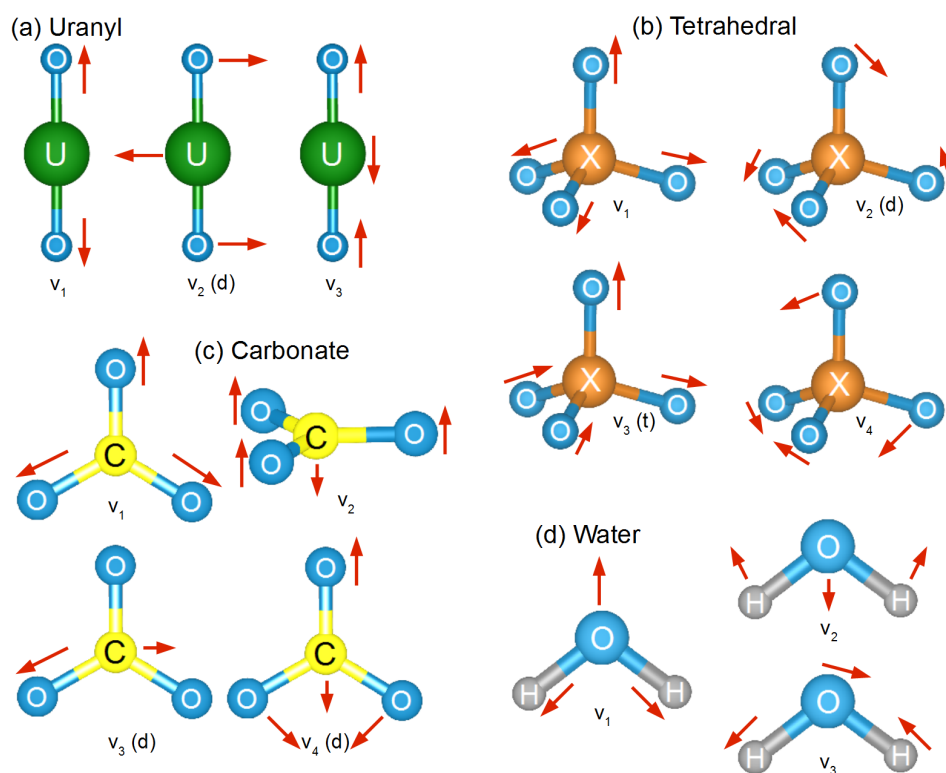
Figure 1.6: The vibrational motions predicted for (a) the uranyl cation (UO_2^{2+}), (b) polyanions with tetrahedral symmetry (XO_4), (c) the carbonate anion (CO_3^{2-}) and (d) the water molecule. Red arrows show the vector of each atom within each vibrational motion (labelled v). (d) and (t) indicate the mode is doubly or triply degenerate, respectively.

A group theory approach predicts that free tetrahedral ions (T_d symmetry) have four fundamental vibrational modes. These are the ν_1 symmetric stretch, ν_2 doubly degenerate bending mode, ν_3 triply degenerate antisymmetric stretch and ν_4 bending mode. ν_1 and ν_2 are predicted to be only Raman active, whereas ν_3 and ν_4 are both Raman and IR active. Literature positions for these vibrational modes in the four tetrahedral ions of interest to this chapter (PO_4^{3-}, AsO_4^{3-}, SiO_4^{4-} and SO_4^{2-}) are presented in Table 1.1.

Table 1.1: The positions seen in literature Raman and IR spectra for the symmetric stretch (ν_1), antisymmetric stretch (ν_3) and bending modes (ν_2 and ν_4) of the tetrahedral ions of interest in this chapter.

Ion	ν_1 (cm^{-1})	ν_2 (cm^{-1})	ν_3 (cm^{-1})	ν_4 (cm^{-1})	Ref(s)
PO_4^{3-}	938	420	1017	567	[68–70]
AsO_4^{3-}	780–815	320–350	780–830	380–450	[71–73]
SiO_4^{4-}	819	340	956	527	[74]
SO_4^{2-}	950–1020	350–560	1040–1280	560–680	[75]

In addition to the tetrahedral polyanions, two minerals in this investigation contain carbonate (CO_3^{2-}) anions. CO_3^{2-} has D_{3h} symmetry and four fundamental vibrational modes are predicted using group theory. These are ν_1 symmetric stretching mode, the ν_2 out-of-plane bending, the ν_3 doubly degenerate antisymmetric stretching mode and the ν_4 doubly degenerate in-plane bending mode. The ν_1, ν_2, ν_3 and ν_4 modes have been found around 1060–1100 cm^{-1}, 800–900 cm^{-1}, 1400 cm^{-1} and 680–700 cm^{-1}, respectively, in previously published vibrational spectra of uranyl carbonates [76, 77].

All uranyl minerals in this investigation contain water molecules, with some also containing hydroxyl ions. The ν_1 symmetric and ν_3 antisymmetric stretching modes are typically observed between 2900–3700 cm^{-1} (the hydroxyl O-H stretch is also seen here) and the ν_2 bending mode between 1590–1700 cm^{-1} [78]. These positions are typically at lower wavenumbers if there is more hydrogen bonding in the structure. As the quantity of water molecules in uranyl minerals is generally variable, these peaks have not been considered in this investigation, with the focus on peaks corresponding to the uranyl cation and polyanions that may allow the minerals to be distinguished.

1.4 Aims of Thesis

The first objective of this thesis is to investigate how vibrational properties vary for different uranium oxides and uranyl minerals. To this end, a selection of uranyl minerals from Cornwall were studied with Raman spectroscopy in Chapter 6 and the most

significant peaks and trends are noted. Furthermore, any differences to previously published spectra are described, as this may provide opportunities to differentiate samples from different locations. The observed trends and variations could contribute to a future database on radioactive materials, which would be a valuable tool for forensic and environmental studies, where samples need to be rapidly identified.

The second major aim of this investigation is to determine whether computational techniques can be used to simulate vibrational properties and interpret features of experimental Raman and IR spectra. In Chapters 4 and 5, the Raman and IR spectra are simulated for the structural models of U_3O_8 and UO_3, developed by Brincat *et al.* [49, 55], and then compared against experimental spectra [79, 80]. In Chapter 7, models of four autunite minerals are discussed, with the goal of interpreting the experimental Raman and IR spectra.

The final goal of this investigation is to use computational techniques to probe how changes in structure and composition affect the vibrational properties, including the characteristic uranyl symmetric stretching mode, the position of which varies in different materials. This is presented in Chapter 7 by modelling a series of autunite minerals with systematic changes in composition, then simulating the vibrational properties of each. The observed trends are then applied to the experimental spectra of samples with a known composition, to determine if information about the composition can be obtained. The position of the uranyl symmetric stretching mode is also considered for many uranium oxides and the differences are discussed.

Chapter 2

Experimental Theory and Methodology

The vibrational properties of uranium materials is the primary focus of this investigation, so the theory and experimental details of infrared (IR) and Raman spectroscopy is described in Section 2.1. Scanning electron microscopy (SEM) and energy-dispersive X-ray spectroscopy (EDX) were also used to study the samples, so these techniques are discussed in Section 2.2. Section 2.3 notes some general safety concerns related to the samples.

2.1 Vibrational Spectroscopy

Vibrations can be induced in systems when they interact with electromagnetic radiation of an appropriate frequency. Vibrational spectroscopy is employed to study this interaction and provide information about the bonding within the molecule, including bond strengths, bond lengths, force constants and dissociation energies [81].

The three strategies for collecting vibrational spectra are emission, absorption and Raman spectroscopy [81]. In emission spectroscopy, the system transitions from an excited vibrational state to the ground state, emitting the difference in energy as a photon, which is detected. Absorption spectroscopy works by irradiating the sample with a range of frequencies and determining the frequencies that are absorbed. The absorbed radiation causes the molecule to transition to a more excited vibrational state. In Raman experiments, a monochromatic incident source is used and the radiation scattered from the surface of the sample is detected.

A typical potential energy curve for the vibration of a diatomic molecule is given in Figure 2.1.a [81], where V is the potential energy and R is the bond distance. At bond distances close to the equilibrium (R_e), the potential energy curve may be represented by a parabola, where

$$V = \frac{1}{2}k(R - R_e)^2 \tag{2.1}$$
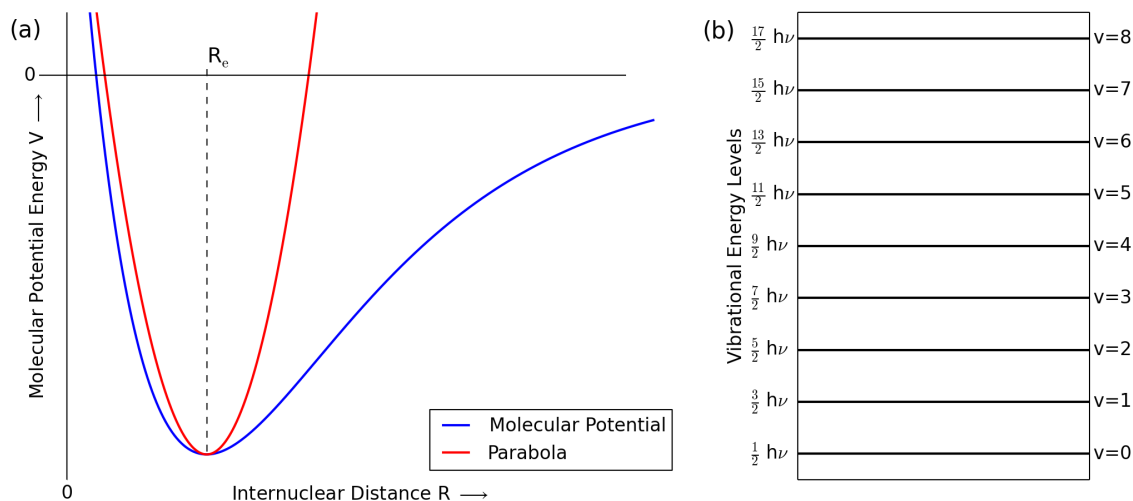
Figure 2.1: a) A parabola (red) can be used to approximate a molecular potential energy curve (blue) close to the equilibrium bond distance (R_e) [81]. b) The vibrational energy levels of a harmonic oscillator, which have a uniform separation of $h\nu$.

and k is the bond force constant. The energy levels (E_v) of a parabolic potential, in which the oscillations are harmonic, are

$$E_v = (v + \frac{1}{2})h\nu, \tag{2.2}$$

where v is the vibrational quantum number ($v = 0, 1, 2, ...$), h is Planck's constant,

$$\nu = \frac{1}{2\pi}\sqrt{\frac{k}{\mu}} \quad \text{and} \quad \mu = \frac{m_A m_B}{m_A + m_B}. \tag{2.3}$$

μ is known as the effective mass (or reduced mass), while m_A and m_B are the masses of the two atoms forming the diatomic molecule.

The vibrational energy levels of a harmonic oscillator are shown in Figure 2.1.b [81] and have a uniform separation of $h\nu$. IR and Raman spectra are typically reported in terms of wavenumber ($\bar{\nu}$, measured in cm^{-1}), which is related to the frequency $\nu = c\bar{\nu}$ (where c is the speed of light), so the separation can also be written as $hc\bar{\nu}$. The specific selection rule for vibrational spectroscopy states that a transition between energy levels can only occur if $\Delta v = \pm 1$, which means that the change in energy (ΔE) for any allowed vibrational transition is ΔE=$hc\bar{\nu}$. Therefore, in absorption spectroscopy, only photons with an energy that matches ΔE can be absorbed by the molecule [81, 82]. In general, vibrations of bonds with a higher force constant (k) and bonds between lower mass atoms (lower μ) lead to larger wavenumber modes. For example, the vibrational spectra of organic molecules are typically recorded between 600–4000 cm^{-1}, whereas the modes

of bonds involving metal ions are often observed between 200–400 cm^{-1}.

At room temperature, the ground state ($v = 0$) is typically the only occupied vibrational energy level, meaning the $v = 0 \rightarrow 1$ transition is the most significant [81, 82]. However, in situations where molecules are initially at more excited vibrational energy levels, the parabolic approximation provides a poorer representation of the actual potential energy curve. This vibrational motion is described as anharmonic, because the restoring force is not proportional to the increase in bond length. One consequence of anharmonicity is that the spacing between energy levels becomes smaller at high excitation. Furthermore, the specific selection rule may be broken, as it was derived from the harmonic oscillator, so transitions where $\Delta v = +1, +2, ...$, known as overtones, may be found in the spectra.

Polyatomic molecules and crystalline solids contain multiple bonds, which leads to a large number of combined vibrational modes. A molecule with N atoms has $3N - 6$ modes of vibration if it is non-linear, or $3N - 5$ modes if it is linear [81]. Each mode is known as a normal mode and is described as a synchronous motion of atoms that can be excited independently of other normal modes. These motions may be localised in a small group of atoms or may encompass the entire system. Normal modes behave in a similar manner to the harmonic oscillator, with vibrational energy levels as described in Equation 2.2. In these cases, the effective mass depends upon the relative contribution of each atom to the vibration and the force constant depends on the extent of bending and stretching motions within the mode. In general, stretching modes are found at higher wavenumbers because the motions involve a significant distortion of the electron density located within the bond, which does not occur during bending vibrations.

Raman and IR spectroscopy are the two techniques used in this investigation to measure the vibrational spectra [81, 82]. The IR spectra were collected using absorption spectroscopy. Both methods follow the specific selection rule for vibrational spectroscopy, but have different gross selection rules, meaning that the techniques can provide complementary information.

2.1.1 Infrared Spectroscopy

Infrared (IR) spectroscopy is the traditional method for recording vibrational spectra. It is performed as absorption spectroscopy, where a sample is irradiated by a range of frequencies and the absorption at each frequency is monitored [81, 82]. In some IR spectrometers, this is achieved by scanning sequentially with radiation of different fre-

quencies, while most modern spectrometers irradiate the sample with many wavelengths simultaneously, then use a Fourier transform to deconvolute the spectrum.

An incident photon can only be absorbed by the sample if its energy matches the transition between vibrational energy levels (ΔE=hc$\bar{\nu}$) and it obeys the gross selection rule for absorption spectroscopy. The gross selection rule states that the electronic dipole moment of the molecule must change during the vibration [81, 82]. This can be exemplified using the symmetric and antisymmetric stretching modes of the free uranyl cation (UO_2^{2+}, Figure 2.2). The initial dipole moment of a UO_2^{2+} cation with two equivalent U-O bonds is zero. During the symmetric stretch, a simultaneous extension or compression of the two U-O bonds occur, which retains the overall dipole moment of zero, meaning this vibration is IR inactive. In contrast, the antisymmetric stretch involves one bond extending and the other compressing, generating a temporary dipole moment and meaning this mode is IR active.
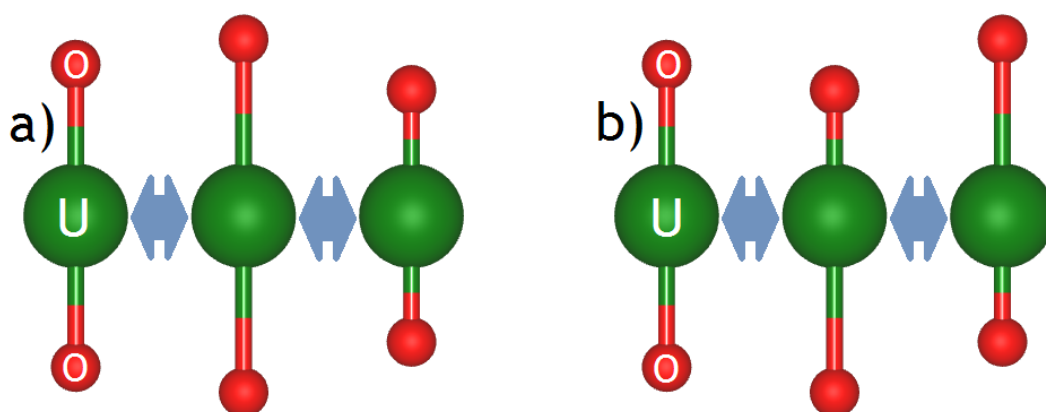
Figure 2.2: The uranyl a) symmetric and b) antisymmetric stretching motions. Uranium and oxygen atoms are represented by green and red spheres, respectively.

IR spectrometers conventionally collect data by transmitting the incident radiation through the sample and detecting the proportion of each frequency that has not been absorbed. The absorption (A) of light can be related to the concentration of absorbing species (c) by the Beer-Lambert Law [81],

$$A = \log\left(\frac{I_0}{I_t}\right) = \epsilon c l, \tag{2.4}$$

where I_0 and I_t are the intensities of incident and transmitted light, l is the path length and ϵ is the molar absorption coefficient. ϵ is dependent upon the frequency of incident radiation and is at a maximum at frequencies that correspond to a vibrational energy

level transition.

One drawback in using transmission IR spectroscopy to study solid materials is that the samples must be crushed into a powder or pellet that is thin enough for the radiation to pass through. However, this can be circumvented by using an attenuated total reflectance (ATR) geometry, which relies on the property of total internal reflection to reflect the light that is not absorbed within a crystalline window that is in contact with the sample. This allows a solid or liquid sample to be studied without prior preparation and avoids potential problems with strong attenuation of the IR signal. In order to reflect the IR signal, the ATR crystal must be composed of a material with a higher refractive index than the sample under investigation. Typical materials used include germanium, zinc selenide and diamond.

Experimental IR Methodology

The IR spectra in this investigation were collected using a Perkin-Elmer spectrometer equipped with a diamond coupler and set in the attenuated total reflection (ATR) configuration. All wavelengths in the 650–4000 cm^{-1} region were scanned simultaneously and a Fourier transform (FTIR) was used to deconvolute the data. The resolution of the instrument was ± 10 cm^{-1}.

2.1.2 Raman Spectroscopy

In Raman spectroscopy, the monochromatic incident radiation is directed through the sample, but only light scattered from collisions with molecules at the surface are detected [81, 82]. The majority of collisions between photons and molecules are elastic, meaning the scattered photons have the same energy as the incident photons. However, approximately 1 in 10^7 collisions are inelastic, with some energy transferred between the photon and molecule. This process is known as Raman scattering. It is the low probability of inelastic scattering that necessitates the use of high intensity lasers in Raman experiments.

The energy transferred in Raman scattering corresponds to the difference between vibrational energy levels, $\Delta E = hc\bar{\nu}$ [81, 82]. However, this only corresponds to a fraction of the initial energy of the photon, so the change in energy (reported as a wavenumber, $\bar{\nu}$) is measured. This energy change is known as the Raman shift and is often small, necessitating the use of a monochromatic incident radiation source.

In a Raman experiment, each scattered photon may retain the same energy, lose energy to molecules in the sample or gain energy from the sample [81, 82]. When photons are scattered elastically and have the same energy as the incident radiation, it is known as Rayleigh scattering; the Rayleigh line is found at zero on the Raman spectrum. In collisions where incident photons lose energy, the molecule increases to a more excited vibrational energy level ($\Delta v = +1$). The corresponding peaks on the Raman spectrum are known as Stokes lines and are traditionally reported as a positive Raman shift. In contrast, anti-Stokes lines correspond to collisions where the molecule moves to a less excited vibrational energy level ($\Delta v = -1$) and the scattered photon has more energy than the incident radiation. Anti-Stokes lines are reported as a negative Raman shift, but have the same magnitude of shift as the corresponding Stokes lines. However, as the majority of molecules are in the ground state vibrational energy under ambient conditions, anti-Stokes lines are typically weaker than Stokes lines, so only the latter are reported.

The gross selection rule for Raman spectroscopy is that vibrations must change the molecular polarisability [81, 82]. Polarisability describes how easily the electron cloud can be distorted and while it is difficult to determine directly, the electron density can provide an indication. To illustrate, the uranyl symmetric and antisymmetric stretching modes may be considered (Figure 2.2). The symmetric stretching mode is Raman active and involves a simultaneous extension or compression of the two U-O bonds, leading to a change in electron density. In contrast, the antisymmetric stretching mode involves one U-O bond extension and one compression, resulting in no overall change in electron density and no Raman activity.

2.1.3   Porto Notation

A Raman experiment may be described using Porto's notation, $k_I(e_I e_S)k_S$, which describes the directions of propagation k and polarisation e of the incident I and scattered S light [83, 84]. For example, a Raman experiment in which incident light follows the z-axis of the crystal coordinates and is polarised in the x-direction, then scattered light polarised in the y-direction is detected in the reverse z-direction, is described as $Z(XY)\bar{Z}$. Raman experiments may be parallel polarised (e.g. $Z(XX)\bar{Z}$), cross-polarised (e.g. $Z(XY)\bar{Z}$) or unpolarised (e.g. $Z(UU)\bar{Z}$), in which case the Raman intensity is a sum of the intensities for the parallel and cross polarised experiments.

2.1.4 Raman Tensors

The intensity (I) of a mode in the Raman spectrum is largely dependent upon three factors [84],

$$I \propto \left| e_j^S \cdot R_{jk,l} \cdot e_k^I \right|^2 . \tag{2.5}$$

e_k^I and e_j^S are vectors that represent the polarisation direction of incident and scattered light, respectively. $R_{jk,l}$ is a Raman tensor, which determines the amplitude of the scattered waves and is unique to each vibrational mode, l.

Every Raman tensor is composed of nine elements, which may be zero or non-zero and some non-zero elements may be equivalent to others [84]. Non-zero and equivalent elements of a Raman tensor are distinct to the symmetry label of a vibration, for example, the Raman tensor for an A_{1g} mode in a tetragonal crystal symmetry is

$$\begin{pmatrix} a & 0 & 0 \\ 0 & a & 0 \\ 0 & 0 & b \end{pmatrix}, \tag{2.6}$$

where a and b are non-equivalent and non-zero elements. Non-zero and non-equivalent elements in a Raman tensor can be determined from group theory if the crystal and vibrational symmetries are known. An example for calculating the Raman activity in a backscattered parallel polarised Raman experiment ($Z(XX)\bar{Z}$) for the mode which has the Raman tensor given in Equation 2.6 is

$$I = \begin{pmatrix} 1 & 0 & 0 \end{pmatrix} \begin{pmatrix} a & 0 & 0 \\ 0 & a & 0 \\ 0 & 0 & b \end{pmatrix} \begin{pmatrix} 1 \\ 0 \\ 0 \end{pmatrix} = a. \tag{2.7}$$

In an equivalent unpolarised Raman experiment ($Z(UU)\bar{Z}$), the Raman activity is the sum of Raman intensities for the parallel and cross polarised ($Z(XY)\bar{Z}$) experiments.

As the Raman intensity depends on the polarisation of incident and scattered light and the Raman tensor, studying the crystal from alternative orientations may result in different Raman activities for the same mode. If the polarisation of the incident radiation is known, this can provide the shape of the Raman tensor and allow the symmetry label to be assigned to some modes.

2.1.5 The Rule of Mutual Exclusion

It has been noted in the previous sections that the uranyl symmetric stretch is Raman active and the uranyl antisymmetric stretch is IR active, but neither mode is found in both spectra. This is a result of the rule of mutual exclusion, which applies to molecules with a centre of inversion as a symmetry element and prevents coincidences between its IR and Raman spectra [82]. As the uranyl cation has a centre of inversion, this rule applies. Other polyions, such as the tetrahedral PO_4^{3-} anion, do not have centres of inversion, therefore, some of the modes may be both Raman and IR active.

2.1.6 Experimental Raman Methodology

The Raman spectra presented in this investigation were recorded using a Renishaw inVia Raman spectrometer. Three lasers were used to excite the spectra: 785 nm (Renishaw, diode laser, 370 mW at source), 532 nm (Renishaw, diode laser, 380 mW at source) and 325 nm (KIMMON, He-Cd laser, 270 mW at source). A different diffraction grating was also used for each source, resulting in spectral resolutions of ± 0.2, ± 1.2 and ± 5 cm^{-1} for the 785, 532 and 325 nm lasers, respectively. The microscope objectives used to collect the scattered light were $\times 5$ and $\times 50$ long-focus objectives (LEICA) for the 532 and 785 nm lasers and a $\times 15$ long-focus fused silica objective (THORLABS) designed for the 325 nm laser. The spectrometer was calibrated for the 532 and 785 nm lasers using the 520 cm^{-1} line of silicon, while the 1332 cm^{-1} peak of a cubic diamond was used to calibrate for the 325 nm laser. To obtain spectra with a good signal-to-noise ratio, the acquisition time and number of accumulations were varied. Furthermore, more than 95% of the laser power was typically attenuated to prevent damage to the surface of the sample. Data was acquired using the Renishaw WiRE software package, while a custom Python script, written by J. Skelton, was used to fit peaks to the spectra (Appendix A) [85].

2.2 Scanning Electron Microscopy and Energy-Dispersive X-ray spectroscopy

Scanning Electron Microscopy (SEM) is a technique that may be used to produce images of a surface, with a possible resolution better than 1 nm. This is performed by directing a beam of electrons at the sample, which then interact with the atoms, producing a variety of different signals that can be detected. The two most common imaging modes involve collecting secondary electrons (SE) and backscattered electrons (BSE) and are

used to study topology and composition, respectively.

Secondary electrons are low energy (<50 eV) electrons ejected from atoms after an inelastic collision and are detected orthogonal to the incident beam. The relatively low energy of these particles mean that only surface atoms are studied, while electrons from the bulk cannot escape the sample. Steep surfaces and edges increase the number of electrons that can be detected, increasing the brightness of these surface features in SE images. This leads to well defined images with a large depth of field, allowing surface features smaller than 1 nm to be examined.

Backscattered electrons are high energy electrons from the incident beam that elastically scatter from atoms in the sample and are detected above the sample. As heavy elements scatter electrons more readily than lighter atoms, the former appear brighter in a BSE image, allowing the distribution of different compositions to be examined. One downside to BSE is that electrons emerging from deeper in the sample can be detected, reducing the image resolution. Many modern SEM machines compensate for this by employing both SE and BSE detectors.

In conventional SEM experiments, the surface of the sample must be electrically conducting and grounded, to prevent both charge and heat from building at the surface. This is straightforward for metal samples, which just require cleaning and mounting before study. In contrast, non-conductive samples must be coated with an electrically conducting material, such as gold, chromium or graphite. Heavy metals may also be used to coat samples studied in secondary electron experiments, increasing the number of collisions and improving the signal-to-noise ratio for elements with a low atomic number. An alternative is to set the SEM to low voltage or vacuum mode, which allow the charge to dissipate before it heats the surface of the sample.

Energy-dispersive X-ray (EDX) spectroscopy is often performed in conjunction with SEM experiments. It is performed by directing a beam of charged particles, such as electrons, or X-rays, onto the surface of a sample. When an incident particle or photon collides with an atom, it excites an inner shell electron, which is ejected from the atom and leaves an electron hole in its place. An electron from an outer shell then fills this hole, releasing the energy of this transition as an X-ray, which is detected. As the transition energy is characteristic to the electronic structure of the element, each atom has a distinct fingerprint of peaks in the EDX spectrum, allowing the composition to be measured.

A number of factors can affect the accuracy of an EDX experiment. X-rays are emitted in all directions, so not all escape the sample and are detected. The more material that an X-ray has to pass through, the more likely it will be reabsorbed by other molecules and the chance of it escaping and being detected is lowered. Furthermore, some elements have transitions with similar energies, so some peaks may overlap, making their assignment difficult.

2.2.1 Experimental SEM and EDX Methodology

The SEM images and EDX spectra in this investigation were collected using a JEOL 6480 LV Scanning Electron Microscope, equipped with an Oxford Instruments INCA X-act silicon drift detector. SEM images were generated using both secondary and backscattered electrons, providing images that described the topology and the location of heavy elements. EDX spectra were collected using the INCA softwareand optimised using a copper standard and internally stored empirical standards were used to determine the ratios of atoms in each mineral, accurate to $\pm 1\%$ [86]. Samples were studied as single crystals or aggregates and fixed to an aluminium mount using carbon tape (Agar Scientific), then dried in a dessicator for 24 hours. The analysis was performed under low vacuum ($\sim$45 Pa), preventing the build up of charge on the surface of the sample and the subsequent heat damage. This also allowed the samples to be studied without coating them with a conductive material.

A number of limitations were associated with collecting quantative EDX data in this investigation. First, the percentages of carbon and oxygen were always higher than anticipated from the chemical formula; the former likely results from the carbon tape used to secure the samples, but both may be related to contaminants on the surface of the sample. An additional difficulty is the close association of the uranyl mineral samples with the host rock, resulting in the detection of certain elements, including silicon, aluminium and iron, that would not be expected by the chemical formula.

2.3 Practical Considerations

The two primary health risks presented by the uranyl mineral samples studied in this investigation were the toxicity and radioactivity of uranium. Standard personal safety equipment was employed to handle the materials, including a lab coat, goggles and gloves. Contamination and dose meters were also available to help determine the risk posed by the samples, while a personal radiation monitor was used to track the dose accumu-

lated over time. The contamination meter was also available to check the workspace for spillages of radioactive material after finishing an experiment. The samples were stored in separate airtight bags within a locked metal cupboard, which was found to block all radioactivity from the samples, lowering the risk to others using the laboratory.

For the majority of mineral samples, the dose was measured as less than 5 μSv/h, with the largest doses measured for uranophane and compreignacite, which were both below 20 μSv/h. This low level of radiation meant that small spillages of material could be disposed with standard waste. The university exposure limit for ionising radiation is 1 mSv per year, whereas the overall dose detected by the personal radiation monitor was insignificant.

One further safety consideration was the possible presence of radon gas formed from the decay of uranium within the minerals. Therefore, the sample containers were opened inside a fume cupboard, to prevent inhalation of accumulated radon.

Long term storage of the uranyl mineral samples also had to be considered, as they are known to be susceptible to dehydration in warm and dry conditions. However, the water content was not a major focus of this investigation and since previous studies by Frost *et al.* have shown that no significant structural deviations occur below 400 °C [58, 70, 87, 88], storage at room temperature was considered suitable.

Chapter 3

Computational Theory and Methodology

Computational modelling has been a major part of this investigation; the methodology is described in this chapter. First, quantum theory is introduced (Section 3.1). Sections 3.2 and 3.3 focus on the theory and implementation of density functional theory (DFT), which has been the primary computational technique used for this study. Section 3.4 describes the energy minimisation procedure, which has been used extensively in our calculations. As the main goals of this investigation involve the vibrational properties of uranium materials, the methods used to compute vibrational modes and motions and the corresponding IR and Raman activities are given in Section 3.5. Lastly, Section 3.6 provides specific details on the methods and software used in this investigation, in addition to the relevant parameters required for the simulations.

Two major approaches may be used to model chemical systems: quantum mechanics (QM) explicitly simulates the electronic structure, while classical techniques represent the interatomic forces as a set of functions, known as potentials. As electrons are explicitly represented in QM calculations, the largest systems that may be represented are smaller than those that may be studied in classical methods. However, QM methods allow properties depending on the electronic structure to be predicted. The basis of quantum theory is given in Section 3.1. Two commonly used QM methods are Hartree-Fock (HF) and density functional theory (DFT); the latter is the primary technique used in this investigation, so it is described in detail in Section 3.2.

3.1 Quantum Theory

The primary difference between quantum and classical mechanics approaches to simulating atomic systems is that electrons are explicitly represented in the former, but not in the latter [89]. This has the advantage of allowing properties that depend on the electronic structure to be derived, but limits the size of the systems that can be simulated. According to the Heisenberg uncertainty principle, the position and momentum of a quantum particle, such as an electron, cannot be known simultaneously. Therefore,

an electron is typically described using a wavefunction (Ψ), which represents how it is distributed across space [81]. The probability of finding an electron within a specific region of space may be obtained by integrating Ψ^2 over that volume.

The Schrödinger equation [81, 89],

$$i\hbar\frac{\partial\Psi(\mathbf{r},t)}{\partial t} = \hat{H}\Psi(\mathbf{r},t), \tag{3.1}$$

describes how the quantum state of a quantum system, represented by its wavefunction Ψ, changes with respect to time t and spacial coordinates $\mathbf{r}$. $\hat{H}$ is the Hamiltonian operator, which is applied to the wavefunction in order to determine the energy of a quantum system. It is comprised of kinetic $\hat{T}$ and potential $\hat{V}$ energy components,

$$\hat{H} = \hat{T} + \hat{V}. \tag{3.2}$$

In situations where the Hamiltonian does not depend on time, the wavefunction may be separated into spacial ($\varphi(\mathbf{r})$) and temporal ($\phi(t)$) parts, $\Psi(\mathbf{r},t) = \varphi(\mathbf{r})\phi(t)$ [81, 89]. The Schrödinger equation can then be rewritten in the time independent form,

$$\hat{H}\Psi(\mathbf{r}) = E\Psi(\mathbf{r}), \tag{3.3}$$

where E is the energy eigenvalue. Mathematically, an infinite number of combinations of E and Ψ can be used to satisfy the Schrödinger equation, but only some wavefunctions are physically accepted, depending on the restrictions of the system. Consequently, only specific values of energy are allowed.

Exact solutions to the Schrödinger equation cannot be found for any system with three or more interacting particles (i.e. larger than the hydrogen atom), so many sophisticated methods have been developed to find approximate solutions. These include the Hartree-Fock method (HF) and density functional theory (DFT), which is a major part of this investigation and described in Section 3.2.

The energy of a system with multiple nuclei and electrons can be represented as a sum of kinetic and potential parts,

$$E = T_\text{n} + T_\text{e} + V_\text{n-n} + V_\text{n-e} + V_\text{e-e}. \tag{3.4}$$

T_n and T_e are the kinetic energy contributions of the nuclei and electrons, respectively, while the V terms arise from the potential energy acting between each type of particle. The Born-Oppenheimer approximation [81, 89, 90] allows the energy to be separated further, into a sum of nuclear and electronic components, $E_{total} = E_{nuclear} + E_{electronic}$. This is due to the significant difference in mass between nuclei and electrons, as the electrons can react to any change in the positions of the nuclei almost instantaneously. Hence, the electronic energy is comprised of the kinetic and potential energy of the electrons moving in the potential field of the fixed nuclei and the electron-electron repulsions.

Hartree-Fock Method

The Hartree-Fock method is a strategy for approximately determining the wavefunction and energy of a quantum many-body system in a stationary state. An exact solution cannot be found for many-body systems, but the variation theorem states that the energy calculated by an approximated wavefunction will always be greater than that calculated by the exact wavefunction [89]. Consequently, a lower energy solution may be considered more accurate than a higher energy solution. The lowest energy configuration may be considered as being in an energy minimum, at which point the first derivative of the energy is zero. The Hartree-Fock equations are obtained by imposing this condition on the expression for energy.

In the Hartree-Fock approach, the N-electron wavefunction is replaced by N single-electron wavefunctions, known as Hartree-Fock orbitals. The aim is to locate a set of electronic wavefunctions that correspond to the lowest energy configuration [89]. To accomplish this, each electron is treated individually, operating under the effect of a combined potential. This potential encompasses the nuclear-electron interactions and the interactions between the electron of interest and an average of all remaining electrons in the system. The electron-electron interactions consist of both Coulombic and exchange components; these interactions, alongside the nuclear-electron interactions, contribute to an effective one-electron Hamiltonian operator, also known as the Fock operator, that may be used to find solutions to the Hartree-Fock orbitals.

The strategy for solving the Hartree-Fock system is known as a self-consistent field (SCF) approach [89]. To start, a trial set of solutions to the Hartree-Fock orbitals are generated and used to obtain the Coulomb and exchange operators. The Hartree-Fock equations can then be solved, providing a new set of orbitals for the next iteration. In this way, the energy of the system is reduced until the orbital occupations no longer change and the energy has reached a minimum.

Calculations that use the full Hartree-Fock approach are known as *ab initio* and are fully theoretical simulations [89]. However, these calculations are very computationally expensive, so some parameters may be approximated, fitted to empirical data or other fully *ab initio* calculations. Another drawback is that Hartree-Fock fails to treat the electron correlation effects, potentially leading to large deviations from experimental data. Correlation effects have been incorporated into a number of other approaches, such as Møller-Plesset perturbation theory [91], which are known as post-Hartree methods.

3.2 Density Functional Theory (DFT)

Density functional theory (DFT) is a quantum mechanical method used to simulate the electronic structure of many-body atomic systems. In contrast to the Hartree-Fock approach, the full wavefunction of an N-electron system is not calculated in DFT; the total energy and other properties of the system are instead determined from the electron density distribution as a function of the electronic coordinates $\rho(\mathbf{r})$ [89]. The first formulation of DFT was the Thomas-Fermi model [92, 93], in which the kinetic energy density T_{TF} is approximated using a non-interacting electron gas of uniform density. An electron exchange functional was added later by Dirac [94], which satisfies the Pauli exclusion principle [95] by changing the sign of the total wavefunction if a pair of electrons are interchanged. However, errors remained in the approximation of kinetic and exchange energies, while neither approach accounted for the electron correlation energy, which arises from quantum entanglement and prevents the quantum states of electrons from being described independently.

3.2.1 The Hohenberg-Kohn Theorems

All modern DFT calculations depend upon two theorems formalised and proven by Hohenberg and Kohn [96]. The first demonstrated that the electron density uniquely defines the ground state energy and other properties of a system [89]. The second describes a functional that uses the electron density to calculate the total energy ($E[\rho(\mathbf{r})]$),

$$E[\rho(\mathbf{r})] = \int V_{\text{ext}}(r)\rho(\mathbf{r})dr + F[\rho(\mathbf{r})] = E_{\text{ne}}[\rho(\mathbf{r})] + F[\rho(\mathbf{r})], \quad (3.5)$$

where the first term ($E_{\text{ne}}[\rho(\mathbf{r})]$) arises from the interaction of the electrons with an external potential $V_{\text{ext}}(r)$, typically resulting from Coulomb interactions with the nuclei. $F[\rho(\mathbf{r})]$ is known as the Hohenberg-Kohn functional and is comprised of the kinetic energy of the electrons ($T_{\text{e}}[\rho(\mathbf{r})]$), the interelectronic Coulomb interactions ($J[\rho(\mathbf{r})]$) and

non-classical contributions from electron exchange and correlation ($E_{\text{ncl}}[\rho(\mathbf{r})]$),

$$F[\rho(\mathbf{r})] = T_{\text{e}}[\rho(\mathbf{r})] + J[\rho(\mathbf{r})] + E_{\text{ncl}}[\rho(\mathbf{r})]. \tag{3.6}$$

3.2.2 The Kohn-Sham Equations

Following the Hohenberg-Kohn theorems, Kohn and Sham developed a stategy for utilising them [97]. Combining Equations 3.5 and 3.6 gives an expression for the total energy of an N-electron system [89],

$$E[\rho(\mathbf{r})] = E_{\text{ne}}[\rho(\mathbf{r})] + T_{\text{e}}[\rho(\mathbf{r})] + J[\rho(\mathbf{r})] + E_{\text{ncl}}[\rho(\mathbf{r})]. \tag{3.7}$$

As noted, the terms $E_{\text{ne}}[\rho(\mathbf{r})]$ and $J[\rho(\mathbf{r})]$ are readily defined as classical Coulomb interactions, whereas the remaining terms cannot be easily defined.

To determine the electronic kinetic energy $T_{\text{e}}[\rho(\mathbf{r})]$, the Kohn-Sham scheme defines a reference system of non-interacting electrons, which have an identical electron density to the real system and move through an effective external potential V_{Ref}. This allows the total wavefunction to be represented as a Slater determinant comprised of single electron wavefunctions, φ_i, known as Kohn-Sham orbitals. For each electron, the orbital with the lowest energy solution can be found independently,

$$\left[-\frac{1}{2}\frac{\partial^2}{\partial \mathbf{r}^2} + V_{\text{Ref}}(\mathbf{r}) \right] \varphi_i(\mathbf{r}) = \epsilon_i \varphi_i(\mathbf{r}), \tag{3.8}$$

where ϵ_i is the energy of the orbital. The kinetic energy of the non-interacting reference system can then be defined as

$$T_{\text{Ref}}[\rho(\mathbf{r})] = -\frac{1}{2}\sum_{i=1}^{N} \int \varphi_i(\mathbf{r})\frac{\partial^2 \varphi_i(\mathbf{r})}{\partial \mathbf{r}^2} d\mathbf{r}, \tag{3.9}$$

where the electron density is in the ground state,

$$\rho(\mathbf{r}) = 2\sum_{i=1}^{N/2} |\varphi_i(\mathbf{r})|^2. \tag{3.10}$$

Equation 3.7 can then be modified to describe the energy of the Kohn-Sham system,

$$E_{\text{KS}}[\rho(\mathbf{r})] = E_{\text{ne}}[\rho(\mathbf{r})] + T_{\text{Ref}}[\rho(\mathbf{r})] + E_{\text{ee}}[\rho(\mathbf{r})] + E_{\text{xc}}[\rho(\mathbf{r})]. \tag{3.11}$$

The exchange and correlation energies are grouped into the $E_{\text{xc}}[\rho(\mathbf{r})]$ term, known as the exchange-correlation functional, along with the remaining kinetic energy $(T_{\text{corr}}[\rho(\mathbf{r})])$, which arises from the correlation effects between electrons,

$$E_{\text{xc}}[\rho(\mathbf{r})] = T_{\text{corr}}[\rho(\mathbf{r})] + E_{\text{ncl}}[\rho(\mathbf{r})]. \tag{3.12}$$

The final requirement is to generate an effective external potential $V_{\text{Ref}}(\mathbf{r})$ that produces the same electron density in the non-interacting system as in the real system. At the ground state energy, the electron density is at a minimum energy configuration. Therefore, the calculated energy corresponding to any trial electron density $\bar{\rho}(\mathbf{r})$ will be higher than the true ground state energy, unless $\bar{\rho}(\mathbf{r})$ is the same as the ground state electron density $\rho(\mathbf{r})$. This allows an expression to be developed for the reference potential in terms of the interacting system,

$$V_{\text{Ref}}(\mathbf{r}) = V_{\text{ext}}(\mathbf{r}) + \int \frac{\rho(\mathbf{r}')}{|\mathbf{r} - \mathbf{r}'|} d\mathbf{r}' + V_{\text{xc}}(\mathbf{r}), \tag{3.13}$$

where $V_{xc}(r)$ is the exchange-correlation potential,

$$V_{\text{xc}}(\mathbf{r}) = \frac{\delta E_{\text{xc}}}{\delta \rho(\mathbf{r})}. \tag{3.14}$$

The system can then be solved self-consistently by generating an initial set of Kohn-Sham orbitals, using them to produce an effective potential (Equation 3.13), which is then used to minimise the energy of the orbitals within the non-interacting system (Equation 3.9). The minimised orbitals can then be used to generate a new effective potential and the process is continued until the system reaches convergence (subsequent iterations no longer change).

3.2.3 Approximate Exchange-Correlation Functionals

In the Kohn-Sham DFT scheme, the remaining uncertainties from electron exchange and correlation have been grouped into the exchange-correlation potential, $E_{\text{xc}}[\rho(\mathbf{r})]$. This functional is only known exactly for the free electron gas, but the choice of approximation can influence the success of the model [89]. These approximations can be fully theoretical or semi-empirical. The simplest approach is known as the local density approximation (LDA), which is a theoretical approximation. A commonly used extension of LDA is known as the generalised gradient approximation. Other types of functionals also exist, such as hybrid functionals, which combine the exchange energy from Hartree-Fock with

a correlation contribution from either *ab initio* or empirical sources.

The Local Density Approximation

The local density approximation (LDA) is based on the uniform gas model [96], in which all electrons are evenly distributed through space [89]. The total exchange-correlation energy $E_{\text{xc}}[\rho(\mathbf{r})]$ can then be found by integrating over all space,

$$E_{\text{xc}}^{\text{LDA}}[\rho(\mathbf{r})] = \int \rho(\mathbf{r})\epsilon_{\text{xc}}[\rho(\mathbf{r})]d\mathbf{r}, \tag{3.15}$$

where $\epsilon_{\text{xc}}[\rho(\mathbf{r})]$ is the exchange-correlation energy per electron, in the uniform electron gas. In LDA, it is assumed that for a small volume around point $\mathbf{r}$ in the system of interest, the electron density is constant and $\epsilon_{\text{xc}}[\rho(\mathbf{r})]$ is identical to that of the homogeneous electron gas with the same density. Values of $\epsilon_{\text{xc}}[\rho(\mathbf{r})]$ for uniform electron gases of most densities have been accurately determined [98]. One drawback to this approach is that the functional only depends on the local electron density around each point and is not influenced by long range effects. Furthermore, the LDA cannot accurately represent the electron density in systems where it changes significantly within a small volume [99].

Modern LDA functionals can be applied to spin polarised systems, in an approach known as the local spin density approximation (LSDA),

$$E_{\text{xc}}^{\text{LSDA}}[\rho_\alpha(\mathbf{r}), \rho_\beta(\mathbf{r})] = \int d\mathbf{r}\rho(\mathbf{r})\epsilon_{\text{xc}}(\rho_\alpha(\mathbf{r})\rho_\beta(\mathbf{r})), \tag{3.16}$$

where $\rho_\alpha(\mathbf{r})$ and $\rho_\beta(\mathbf{r})$ are the electron densities of the two opposing electron spin states, which sum to the total electron density of the system $\rho(\mathbf{r})$ [100].

The exchange-correlation energy is comprised of exchange and correlation components. A commonly used expression for the exchange component is [94]

$$E_{\text{x}}^{\text{LDA}}[\rho(\mathbf{r})] = -\frac{3}{4}\left(\frac{3}{\pi}\right)^{\frac{1}{3}} \int \rho(\mathbf{r})^{\frac{4}{3}}d\mathbf{r}. \tag{3.17}$$

The correlation component is less readily defined and in most modern LDA functionals this is fitted to data from high accuracy simulations of the uniform electron gas [98, 101, 102].

The Generalised Gradient Approximation

Despite its relative simplicity, LDA often performs well, but in some situations it is inadequate. The generalised gradient approximation (GGA) improves upon LDA exchange-correlation functional by adding a correction that depends on the gradient of electron density at each point, allowing inhomogeneous chemical systems to be represented more accurately,

$$E_{\mathrm{xc}}^{\mathrm{GGA}}[\rho(\mathbf{r})] = \int \rho(\mathbf{r}) \epsilon_{\mathrm{xc}} \left(\rho(\mathbf{r}), \left| \frac{\partial \rho(\mathbf{r})}{\partial \mathbf{r}} \right| \right) d\mathbf{r}. \tag{3.18}$$

As with LDA, the GGA exchange-correlation functional may be separated into exchange and correlation contributions [89]. One commonly used correction to the exchange functional was proposed by Becke [103, 104] and includes an empirical parameter that was fitted to experimental data for noble gas atoms. The PW91 functional [105] uses the same form, but is modified to remove the dependence on the empirical parameter. The correlation functional proposed by Lee, Yang and Parr is also widely used [106] and is often used in combination with Becke's exchange correction, known as the BLYP functional. The functional used in this investigation, the Perdew-Burke-Ernzerhof (PBE) functional [107], corrects the exchange energy using a rational function with computationally determined components. This approach typically causes the binding energies to be underestimated in the simulations, resulting in greater lattice parameters and volumes compared to experimental data. To counteract this overestimation for densely packed solids, a revision of the PBE functional was developed, known as PBEsol [108]; however, this approach predicts other properties less accurately, such as the dissociation energies. Another variation of the GGA functionals, known as meta-GGA functionals, use the second derivative of the electron density to improve the prediction of the lattice parameters and band gaps [109, 110].

Hybrid Functionals

One advantage that DFT has over Hartree-Fock theory is that correlation effects are readily incorporated, while including it in Hartree-Fock significantly increases the required computational resources [89]. However, the Hartree-Fock treatment of the exchange contribution to the energy is considered exact. The addition of correlation energy from DFT to the energy from Hartree-Fock calculations or empirical sources is the basis of hybrid functionals, such as PBE0 [111], B3LYP [106, 112] and HSE [113]. Hybrid functionals can improve the prediction of atomisation energies, bond lengths and vibrational frequencies.

3.2.4 DFT +U

One notable issue with DFT is in how it treats transition metal or actinide oxides that contain some ions with partially filled d- or f-orbitals, such as NiO and UO_2 [114–116]. For these systems, the most common exchange-correlation functionals (e.g. LDA and GGA) predict the electrons to be delocalised, in contrast to the insulating properties observed experimentally [117, 118]. This originates from the strong Coulomb repulsions between the localised d- or f-electrons, which are not adequately described by most exchange-correlation functionals [119]. Furthermore, the lattice constants and binding energies of these systems are typically underestimated and overestimated, respectively [120].

The behaviour of the strongly correlated electrons may be represented using the Hubbard model [121], in which electrons can only move between atomic sites (by tunneling) if they have sufficient energy to overcome the Coulomb repulsions from other electrons on the neighbouring site [118]. To determine the energy contribution of these electrons, the Hubbard Hamiltonian is used, which is comprised of a kinetic energy term allowing electron tunneling and a Coulomb repulsion term with a strength dictated by the Hubbard parameter U. When implemented in DFT, this approach is known as DFT +U, in which the total energy of a system (E_{DFT+U}) becomes

$$E_{DFT+U} = E_{DFT} + E_U. \tag{3.19}$$

E_{DFT} is the energy calculated using a standard exchange-correlation functional and E_U is a contribution that involves the interelectronic interactions modelled with the Hubbard Hamiltonian. It should be noted that the Hubbard correction is only applied to strongly localised electrons, with the remainder simulated using the standard DFT approach.

Two of the most widely used implementations of DFT +U are the Liechtenstein [122] and Dudarev [114, 115] schemes. The first approach uses two parameters to calculate E_U, known as the effective on-site Coulomb and exchange interactions, U and J, respectively [118]. The second approach is a simplified formulation of the first, which disregards J, but typically replaces U with an effective value $U_{eff} = U - J$. Values of U and J are often tuned so that they can reproduce the desired properties from experimental data, such as the band gap. The parameters used for uranium in this investigation are $U = 4.50$ eV and $J = 0.54$ eV and were derived from X-ray photoelectron spectroscopy (XPS) experiments on UO_2 [123, 124].

3.3 Implementation of DFT

In addition to the theoretical treatment of DFT detailed in Section 3.2, there are a number of practical considerations involved when using DFT to study solid state crystal structures. These concepts are introduced in this section and include periodic boundary conditions, reciprocal space, plane waves, Bloch's theorem, k-points and pseudopotentials.

3.3.1 Periodic Boundary Conditions

Routine DFT simulations are limited to ~ 200 atom systems, which presents a problem in representing real systems of $\sim 10^{23}$ atoms. Periodic boundary conditions are employed to simulate large systems using a small number of particles, by generating images of the unit cell in all directions [89]. Hence, the particles within the primary unit cell experience forces as if they were within a bulk structure. The coordinates of particles within the replicated unit cells are found by adding or subtracting multiples of the lattice parameters and each replicated particle performs the same motion as the one in the initial unit cell. Therefore, if a particle leaves the boundaries of the initial cell, a corresponding image enters from the opposing boundary. An example of this effect is given in Figure 3.1, which demonstrates periodic boundary conditions in two dimensions. A drawback to simulating large systems in this way is that fluctuations of the system with a greater wavelength than the length of the unit cell cannot be represented. Furthermore, the long-range interactions can cause some long-range ordering to be imposed on the system. Nevertheless, periodic boundary systems have been used successfully in many DFT simulations of crystalline systems.

3.3.2 The Reciprocal Lattice

The reciprocal lattice is a representation of the real (direct) lattice in reciprocal space (k-space) that is important in electronic structure calculations of periodic systems. The reciprocal lattice vectors ($\mathbf{a}^*$, $\mathbf{b}^*$ and $\mathbf{c}^*$) can be obtained from X-ray diffaction experiments [89]; an inverse Fourier transform can then be applied to transition between the reciprocal and direct lattice parameters ($\mathbf{a}$, $\mathbf{b}$ and $\mathbf{c}$). The relationship between the direct and reciprocal lattice vectors is

$$\mathbf{a}^* = 2\pi \frac{\mathbf{b} \times \mathbf{c}}{\mathbf{a} \cdot \mathbf{b} \times \mathbf{c}}; \quad \mathbf{b}^* = 2\pi \frac{\mathbf{a} \times \mathbf{c}}{\mathbf{b} \cdot \mathbf{a} \times \mathbf{c}}; \quad \mathbf{c}^* = 2\pi \frac{\mathbf{a} \times \mathbf{b}}{\mathbf{c} \cdot \mathbf{a} \times \mathbf{b}}. \tag{3.20}$$
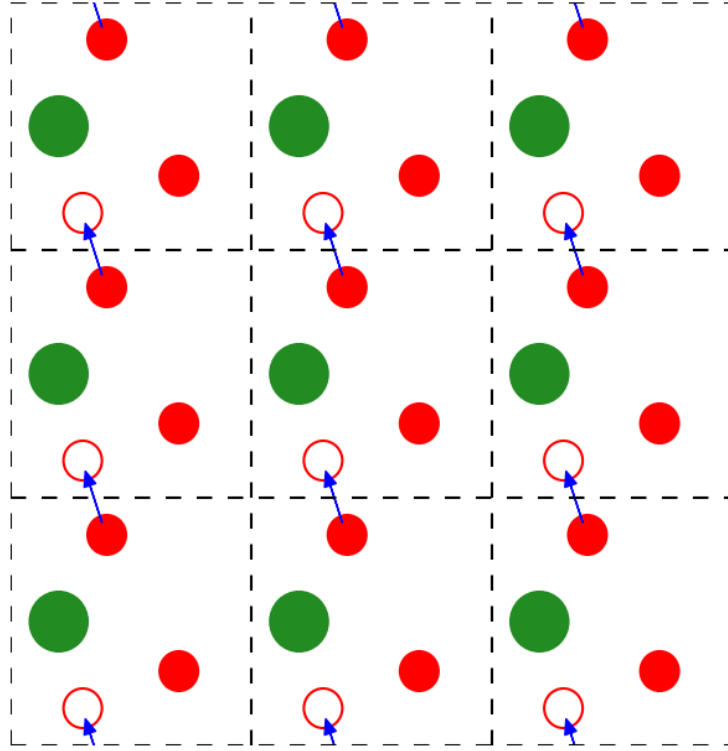
Figure 3.1: A schematic to show periodic boundary conditions in two dimensions, where green and red spheres represent atoms and the dashed black line represents the unit cell boundaries. The central unit cell is replicated in all directions and the atom images within the replicated cells perform the same motions as those in the original cell. When an atom leaves the unit cell (represented by the blue arrow), an image of the same atom enters from the opposing boundary.

$\mathbf{a}$, $\mathbf{b}$ and $\mathbf{c}$ have units of $\frac{1}{\text{length}}$, which means that larger unit cells have smaller reciprocal lattices.

As with the real space lattice, the reciprocal lattice is comprised of multiple symmetrically equivalent units. The smallest symmetrically inequivalent unit is known as the primitive cell and, in the reciprocal lattice, this is known as the first Brillouin zone. The first Brillouin zone is useful in electronic structure calculations of periodic systems because the wavefunction can be completely characterised within this volume.

3.3.3 Plane Waves, Bloch's Theorem and k-Points

A plane wave is a wave of constant frequency with parallel wavefronts (planes where the wave has the same value) normal to the vector of propagation (Figure 3.2) [89]. Bloch's theorem states that the wavefunction of an electron in a periodic potential may be expressed as the product of a plane wave and a periodic function with the same

periodicity as the unit cell ($f_n(\mathbf{r})$), known as a Bloch wave,

$$\Psi_n(\mathbf{r}) = e^{i\mathbf{k}\cdot r} f_n(\mathbf{r}), \tag{3.21}$$

where $\Psi_n(\mathbf{r})$ is the wavefunction of electron n at coordinates $\mathbf{r}$, $\mathbf{k}$ is the wave vector that represents the direction and frequency of the plane wave within the first Brillouin zone and i is the imaginary unit.

The periodic function provides a basis set of plane waves between all equivalent lattice points in other primitive cells [89]. However, in practice the number of plane waves may be reduced, as those with greater wave vectors have higher kinetic energy and contribute less to the wavefunction. Therefore, a cut-off energy is specified for the calculation and plane waves with a higher kinetic energy are discarded. An appropriate cut-off energy may be determined by convergence testing, in which several calculations with different cut-off energies are performed. Values below the optimum cut-off will change the calculated energy significantly, whereas the energy will not change for values above the cut-off.
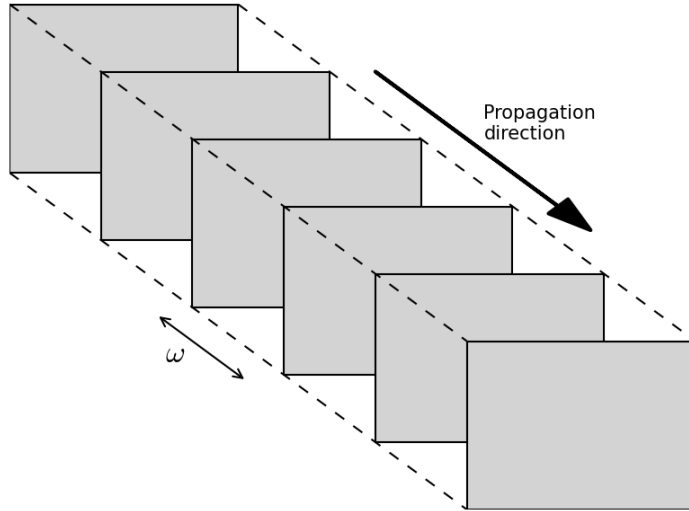
Figure 3.2: A plane wave, where wavefronts (in-phase planes) are normal to the direction of propagation. In a Bloch wave, the periodicity ω is equivalent to the periodicity of the unit cell.

As the form of the wavefunction is continuous, at two nearby points in reciprocal space the value is very similar [89]. Therefore, the wavefunction can be evaluated at a discrete set of points, each of which represent a small volume of reciprocal space. These points are known as k-points and the value of the wavefunction at each is multiplied by a weighting factor, which is related to the volume it represents. A denser set of k-points

will result in a more accurate calculation, but it is also more computationally demanding. Convergence testing may be performed to determine the most computationally efficient k-point density. The distribution of k-points must also be considered. The Monkhorst-Pack scheme is a popular method, distributing k-points evenly throughout the first Brillouin zone and typically centered at the middle of the reciprocal lattice (Γ-point) [125]. This has the advantage that many k-points are related by symmetry, futher reducing the number of positions that must be evaluated. The homogeneous distribution of k-points is represented by

$$k = x_1 a^* + x_2 b^* + x_3 c^*, \tag{3.22}$$

where,

$$x_i = \frac{1}{n_i} \quad \text{and} \quad l = 1, ..., n_i. \tag{3.23}$$

n_i is known as the folding parameter and dictates the density of the k-point grid in direction i. There are three directions, corresponding to the reciprocal lattice vectors a^*, b^* and c^*, meaning three folding parameters are reported ($n_1 \times n_2 \times n_3$). In conducting materials, more k-points need to be evaluated, so a larger folding parameter is required. In contrast, insulating materials require a smaller folding parameter. Furthermore, to maintain a consistent k-point density, systems with larger unit cells, which have smaller reciprocal lattice cells, require a smaller folding parameter.

3.3.4 Pseudopotentials

In most chemical systems, valence electrons typically contribute to bonding and other properties, while core electrons remain unaffected by the environment [89]. Therefore, DFT simulations commonly consider the core electrons as part of the nuclear potential and only explicitly represent the valence electrons. However, the wavefunctions of valence electrons oscillate rapidly near the atomic core, meaning that a large number of plane waves are required to accurately represent this behaviour, increasing the computational expense of the calculation. This is further compounded in simulations of heavy elements, which contain more core electrons, resulting in more oscillations of the valence electron wavefunctions. A common technique to overcome this problem is to replace the strong potential within the core region with a weaker one, known as a pseudopotential.

A pseudopotential is a potential function that represents how valence electrons interact with the combined nucleus and core electrons [89, 126]. Inside the core region, the pseudopotential gives wavefunctions with far fewer oscillations, but does not change the form of wavefunctions outside the core region. This approach reduces the number of

plane waves required to represent the wavefunction and, by extension, the computational expense. An example of how a wavefunction changes under the influence of the real potential and the pseudopotential is shown in Figure 3.3.
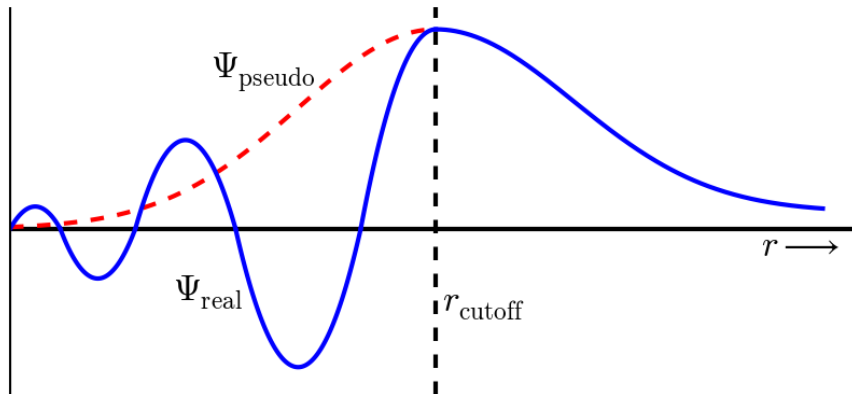
Figure 3.3: Examples of wavefunctions Ψ acting under a real potential and a pseudopotential [127]. Outside the core region ($r > r_{\text{cutoff}}$) both wavefunctions have the same form, but within the core region ($r < r_{\text{cutoff}}$) the wavefunction under the psudopotential (Ψ_{pseudo}) has fewer nodes than the one under the real potential (Ψ_{real}).

Most pseudopotentials are derived from *ab initio* calculations that include all the electrons, but some are fitted to empirical data. In either case, the pseudopotential must then reproduce the behaviour and properties of the valence electrons in the full calculation [89]. The two main types of pseudopotential are known as norm-conserving and ultrasoft. Ultrasoft pseudopotentials require fewer plane waves, which improves the efficiency of the calculation, whereas norm-conserving pseudopotentials maintain the same valence electron density within the core region as the all-electron calculation and are more transferrable. Therefore, the choice of pseudopotential depends on the requirements of the calculation [99, 128]. Systems with lighter elements are generally better represented by norm-conserving pseudopotentials, because the valence electrons are closer to the core, while ultrasoft pseudopotentials may be used for heavier elements. In this work, the projector augmented wave (PAW) method [129] is used, which reduces the number of plane waves required in the same way as ultrasoft potentials and allows all-electron properties to be calculated from the smoother wavefunctions.

3.4 Simulation Methods

Within both classical and quantum mechanical simulations, there are three primary techniques used: energy minimisation, also known as geometry optimisation or mechanical minimisation (MM), molecular dynamics (MD) and Monte Carlo (MC) [89]. In all three

procedures, the atomic coordinates are iteratively adjusted to generate new sets of co-ordinates. In energy minimisation, successive iterations are performed to reduce the potential energy of the system and locate stable configurations, where the energy is at a minimum. One major application for energy minimisation procedures is in validating the computational model, which can be done by comparing the minimised properties, often structural parameters, to the experimentally obtained values. Energy minimisation procedures have been used extensively in this investigation and are detailed in Section 3.4.1. In molecular dynamics, the positions and velocities are updated at each step according to Newton's equations of motion. This provides a trajectory, which describes how different variables change over time and can be used to provide thermodynamic averages over all time steps. In Monte Carlo simulations, each new configuration is generated by randomly moving some of the atoms in the current structure. The new configuration is then accepted or rejected according to Boltzmann's equation. Desired properties are calculated for each accepted configuration and used to obtain the average of that property over all configurations.

3.4.1 Energy Minimisation

The potential energy of a chemical system is dependent on the coordinates (degrees of freedom) of its component atoms [89]. This relationship between energy and atomic co-ordinates is typically referred to as the potential energy surface. Positions of minimum energy on the surface correspond to stable configurations of atoms. The configuration with the lowest energy is known as the global minimum, but higher energy minima often exist and are known as local minima. The purpose of energy minimisation procedures is to identify a minimum energy configuration by iteratively adjusting the atomic coordinates.

The start of any energy minimisation procedure is to select an initial structure, which is often obtained from experimental data, such as X-ray crystallography [89]. An algorithm is then used to locate the nearest energy minimum, which may be the global or a local minimum; the minimum found may be influenced by the initial configuration.

An energy minimum is located where the first derivative of the potential energy is zero and the second derivatives are positive values [89]. The first and second derivatives are a vector corresponding to the forces acting upon each atom and a matrix of force constants known as the Hessian matrix, respectively. These derivatives may also be used to increase the efficiency of a minimisation algorithm. The first derivative may be used
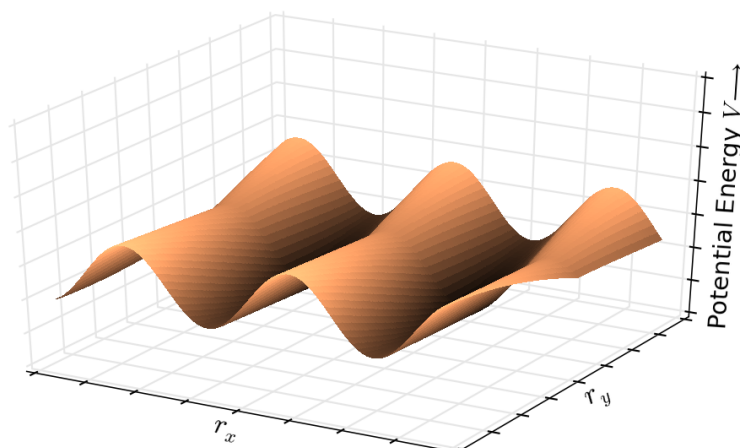
Figure 3.4: An example of a potential energy surface, where r_x and r_y represent two different degrees of freedom. The objective of an energy minimisation procedure is to adjust the degrees of freedom such that the potential energy is at a minimum.

to indicate the direction of the energy minimum, while the second derivative can be used to estimate its location. The latter is performed by approximating the potential energy surface as a quadratic function, which is very efficient when close to a minimum energy, but poorer where the approximation is less valid. In contrast, first derivative methods are typically more robust when used further from the minimum, but can be less efficient when the minimum is located in a narrow valley.

The choice of minimisation algorithm primarily depends on the size of the system, the availability of computer resources and storage and the distance from an energy minimum. Calculation of the Hessian matrix in second derivative methods requires significant memory, so these methods are typically reserved for systems with relatively small numbers of atoms [89]. First derivative methods are less computationally intensive, so can be used for larger systems, but they tend to be less efficient, requiring more steps to minimise. They are also more robust, so these are typically used to start a calculation, while second derivatives are used closer to the energy minimum. Four types of minimisation algorithm are discussed in this section: the steepest descent and conjugate gradient approaches are first derivative methods while the Newton-Raphson and quasi-Newton approaches are second derivative methods.

Steepest Descent Minimisation

The steepest descent method calculates the first derivative of the potential energy (g_i) at the current position on the energy surface [89]. This indicates the direction of the

energy minimum ($s_i = -g_i$), which is used to update the atomic coordinates ($\mathbf{r}_i$),

$$\mathbf{r}_{i+1} = \mathbf{r}_i + a_i s_i. \tag{3.24}$$

In some implementations, the magnitude of each step (a_i) starts with a predetermined value, but is increased with successive decreases in energy and lowered if the energy increases. An alternative approach is to use a line search procedure, where three positions along the vector determined by the gradient are found, such that the outer positions are at higher energies than the central position. This means that an energy mimimum is bracketed by the outer points, so the bracketed region is iteratively reduced until the minimum is located. Following the line search, a second procedure must be performed orthogonal to the first to find the minimum energy configuration. In general, using an arbitrary step method requires more iterations than the line search, but the latter is more computationally intensive.

The direction of adjustment in a steepest descent approach is determined by the largest interatomic forces acting upon the structure, meaning this method is particularly good at relieving the highest energy features of the configuration [89]. Furthermore, the method is robust, so can be used with configurations that are far from the energy minimum. Therefore, steepest descent is a very useful strategy to begin an energy minimisation procedure. However, the number of steps required to reach a minimum using this approach can be larger, particularly when the energy minimum is located within a narrow valley on the energy surface. In this situation, the algorithm often oscillates between points on the slope either side of the minimum until the step size has been sufficiently reduced.

Conjugate Gradient Minimisation

The conjugate gradients minimisation procedure begins with a steepest descent step [89]. Each subsequent iteration uses both the calculated first derivative of the potential energy (g_i) and the direction of the previous step (s_{i-1}) to determine the direction of the next displacement [130, 131],

$$s_i = -g_i + \gamma_i s_{i-1}. \tag{3.25}$$

γ_i is a scalar constant, originally given as

$$\gamma_i = \frac{g_i \cdot g_i}{g_{i-1} \cdot g_{i-1}}, \tag{3.26}$$

but a number of other variations also exist. Inclusion of the direction from previous iterations allows the conjugate gradient method to locate a minimum more efficiently than the steepest descent approach.

Newton-Raphson Minimisation

The Newton-Raphson method is the simplest minimisation procedure that uses the second derivative of the energy, known as the Hessian matrix, which provides information about the curvature of the potential energy surface [89, 132]. The first derivative of the potential energy (g_i) at configuration j can be written as

$$g_j = g_i + (\mathbf{r}_j - \mathbf{r}_i)W_i, \tag{3.27}$$

where $\mathbf{r}_i$ and W_i are the atomic coordinates and Hessian matrix at for iteration i. Assuming the potential energy surface is a purely quadratic function, the Hessian will be the same for all positions on the energy surface ($W_i = W_j$). At the lowest energy configuration, the first derivative of the energy is known to be zero ($g_j = 0$), so the minimum energy configuration ($\mathbf{r}_j$) may be directly calculated as

$$\mathbf{r}_j = \mathbf{r}_i - \frac{g_i}{W_i} = \mathbf{r}_i - g_i \cdot W_i^{-1}, \tag{3.28}$$

where W_i^{-1} is the inverted Hessian matrix. However, the energy surface is only approximately quadratic close to the energy minimum, so multiple iterations of calculating and inverting the Hessian must be performed. These procedures require significant computer memory, particularly for larger systems, limiting the Newton-Raphson approach to smaller systems. Furthermore, this method can fail for configurations further from the energy minimum, where the quadratic approximation is not valid.

A number of variations of Newton-Raphson exist, primarily designed to avoid calculating the Hessian matrix every iteration [89]. One approach is to use the same Hessian for multiple steps, recalculating it at intervals. An alternative is the quasi-Newton methods, which only calculate the first derivative, but construct the Hessian with successive steps. Block-diagonal Newton-Raphson techniques instead only move one atom each iteration, so only a 3×3 Hessian matrix must be inverted at each step; however, this is less efficient in situations where the motions of two or more atoms are closely related.

Quasi-Newton Minimisation

Quasi-Newton minimisation procedures are an adaption of the Newton-Raphson approach, but instead of calculating and inverting the Hessian matrix at every iteration, the inverse Hessian is built up gradually over successive steps [89]. At each step, a new set of atomic coordinates can be determined as in Equation 3.28, but using the current approximated inverse Hessian W_i^{-1},

$$\mathbf{r}_{i+1} = \mathbf{r}_i - g_i \cdot W_i^{-1}, \tag{3.29}$$

where $\mathbf{r}_i$ and g_i are the current positions and first derivative, respectively.

A number of formulae exist for updating the Hessian at each iteration, including the Davidon-Fletcher-Powell (DFP) [130], Broyden-Fletcher-Goldfarb-Shanno (BFGS) [133–136] and RMM-DIIS [137] approaches. The DFP formula is

$$W_i^{-1} \approx W_{i-1}^{-1} + \frac{\delta r \times \delta r}{\delta r \cdot \delta g} - \frac{(W_{i-1}^{-1} \cdot \delta g) \times (W_{i-1}^{-1} \cdot \delta g)}{\delta g \cdot W_{i-1}^{-1} \cdot \delta g}, \tag{3.30}$$

where δr and δg represent the difference between the current and previous atomic coordinates and first derivatives, respectively [89]. Other methods also incorporate information from earlier iterations [138].

Quasi-Newton procedures are particularly common in quantum mechanical calculations, as they can be more efficient than first derivative methods, but are not as computationally expensive as the Newton-Raphson approach [89].

Convergence Criteria

In simulations of chemical systems, determining the precise location of a minimum is rarely possible. Convergence criteria are used to terminate a calculation once the configuration is sufficiently close to the energy minimum [89]. One simple strategy is to monitor the difference in energy between successive steps and to stop the calculation when the energy difference is below a specified threshold. A similar approach may be taken by assessing the change in atomic coordinates at each step. Another consideration is the force acting upon each atom (the first derivative of the energy), which should be close to zero at an energy minimum.

In quantum mechanical minimisations, the electronic structure must also be minimised

for each iteration of atomic (ionic) coordinates. Therefore, convergence criteria must be provided for both ionic and electronic minimisation procedures.

When the vibrational properties (Section 3.5) are calculated after the energy minimisation procedure, the convergence criteria must be particularly rigorous. This is because some methods used to perform the latter involve calculating the change in energy after displacing some atoms within the system. The difference in energy between the minimised and displaced structures is small, so the convergence criteria for the minimisation procedure must be smaller.

Constant Volume and Constant Pressure Minimisations

Two major implementations of energy minimisation are typically used: constant volume and constant pressure. In constant volume, the unit cell dimensions are fixed, while the atomic coordinates are adjusted to minimise the forces using the chosen algorithm. The constant pressure approach performs the same procedure, then alters the lattice vectors to minimise the bulk lattice strain.

3.5 Calculation of Vibrational Properties

Two of the primary goals of this investigation were to use simulated data to interpret experimental Raman and IR spectra and to systematically study how a change in structure or composition affects the vibrational properties of uranium minerals. The first step to calculating the vibrational properties is to construct a force constant matrix, which describes how the system responds to each atom displacing from its equilibrium position. This may be achieved using either the finite displacement approach (Section 3.5.1) or density functional perturbation theory (DFPT, Section 3.5.2). The vibrational frequencies and associated motions can then be calculated. The relative infrared (IR, Section 3.5.3) and Raman (Section 3.5.4) activities may subsequently be determined.

A concerted motion of atoms in a chemical system that can be independently excited is known as a normal mode [89]. Each normal mode is approximated as a harmonic oscillator, in which small displacements from the equilibrium configuration increase the total energy of the system. This energy change can be very small, so before simulating the vibrational properties the structure must be energy minimised with rigorous convergence criteria.

The force constant matrix calculated in finite displacement or DFPT simulations is the

second derivative of the total energy of the system, also known as the Hessian matrix (W) [89]. It is the same Hessian matrix used during Newton-Raphson energy minimisation. To determine the vibrational frequencies, the Hessian matrix must be converted into an equivalent matrix of mass-weighted force constants (D),

$$D = M^{-\frac{1}{2}} W M^{-\frac{1}{2}}, \tag{3.31}$$

where M is a $3N \times 3N$ matrix containing the atomic masses. All elements of M are zero, except those on the leading diagonal, which correspond to the masses of each atom. The mass of each atom must be incorporated because a force of a particular magnitude has a different effect on atoms with a larger mass than atoms with a smaller mass. D is then diagonalised to obtain a set of eigenvalues and eigenvectors. The frequency ν_n of each normal mode may be calculated from the corresponding eigenvalue λ_n,

$$\nu_n = \sqrt{\frac{\lambda_n}{2\pi}}, \tag{3.32}$$

while the eigenvectors describe the motion of each atom during the vibration.

In cases where the system is not in a stable energy minimum, some displacements will not contain a restoring force. The corresponding normal modes have an imaginary component, so are commonly described as imaginary modes. The imaginary mode may be used to obtain a more energetically stable configuration, by adjusting the atomic coordinates in the directions indicated by the eigenvectors.

3.5.1 The Frozen Phonon Approach

One strategy used to populate the force constant matrix W is the frozen phonon or finite displacement approach. Individual elements of the matrix,

$$W_{ij}^{\alpha\beta} = -\frac{\partial F_i^{\alpha}}{\partial R_j^{\beta}}, \tag{3.33}$$

describe how the force F acting on atom i in direction α is affected by the change in coordinates R of atom j in direction β [139]. Therefore, these elements may be obtained by systematically displacing individual atoms from their equilibrium position by a finite distance and calculating the forces acting upon every atom in the resulting system [140, 141]. At the equilibrium configuration, the forces acting upon every atom should be zero, so any new forces emerge from the atomic displacements. The Hellmann-

Feynman theorem may be used to determine the forces acting upon each atom [140],

$$F_i = -\int \rho(\mathbf{r}) \frac{\partial \nu_i(\mathbf{r} - \mathbf{R}_i)}{\partial \mathbf{R}_i} d\mathbf{r} - \frac{\partial E_N(\{\mathbf{R}\})}{\partial \mathbf{R}_i}, \tag{3.34}$$

where $\rho(\mathbf{r})$ is the electron density corresponding to atomic configuration $\{R\}$, R_i represents the coordinates of atom i, E_N is the nuclear electrostatic energy and $\nu_i(\mathbf{r} - \mathbf{R}_i)$ represents the Coulomb interaction between nucleus i and the electrons. Figure 3.5 shows a supercell of UO_2, with a single displaced atom highlighted.
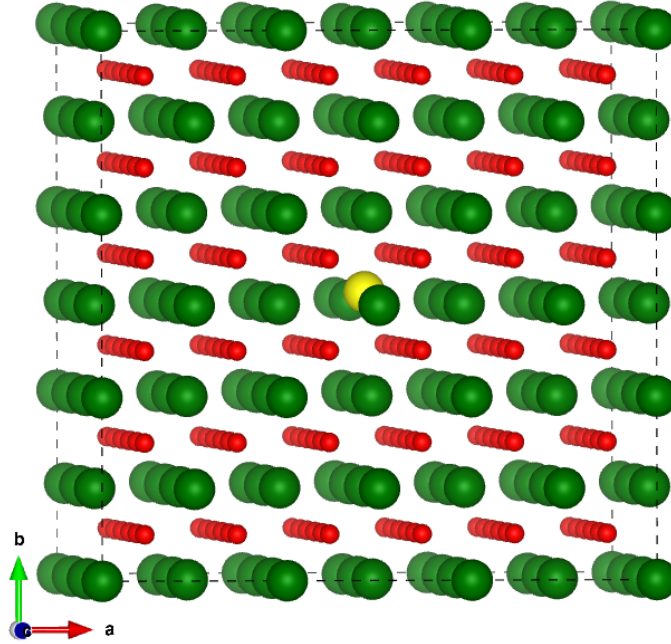
Figure 3.5: An example of a displaced structure in the frozen phonon simulation of the UO_2 supercell, where the displaced uranium atom is shown as a yellow sphere. The other uranium atoms and the oxygen atoms are shown as green and red spheres, respectively.

The primary advantage of using the frozen phonon approach is that no specialised computer code is required to perform it; it may be implemented on any software that calculates the force or energy of a system [139]. Furthermore, the calculation may be modularised, with individual displaced structures analysed in independent simulations and the force constant matrix constructed afterwards [142]. Modular calculations may be performed in parallel, reducing the time required to obtain the vibrational properties. The calculation time may be further reduced by employing the symmetry elements of the unit cell, as some displacements may be symmetrically equivalent and provide the same results.

One drawback to performing frozen phonon calculations is that the displacement of one atom may affect all atoms within the periodic image of the primitive cell, including

the image of the displaced atom [141]. This is particularly prominent for systems with small unit cells. To prevent this, simulations are performed on supercell structures, with dimensions large enough that the interatomic forces on the equivalent image atoms are insignificant [139]. This approach increases the size of the system under investigation, which also increases the computational expense of the calculation.

An important consideration when performing a frozen phonon calculation is the magnitude of the atomic displacements. An appropriate displacement for heavier atoms is larger than that of lighter atoms, but if the displacement is too large for the latter then it may no longer be properly represented by the harmonic oscillator. The default values used by codes that implement the frozen phonon approach are typically ∼0.01 Å [142, 143].

3.5.2 Density Functional Perturbation Theory

The second strategy used to calculate the force constant matrix is known as density functional perturbation theory (DFPT) [144, 145]. In this method, an explicit expression for the force constants is found by differentiating the force with respect to the atomic coordinates, as in Equation 3.33. This expression is dependent upon the electron density $\rho(\mathbf{r})$ and how it is affected by a distortion of the atomic coordinates [139, 140]. The latter is evaluated in DFPT by approximating Equation 3.10 as a linear function,

$$\frac{\partial \rho(\mathbf{r})}{\partial \mathbf{R}_i} = 4 \sum_{n=1}^{N/2} \varphi_n^*(\mathbf{r}) \frac{\partial \varphi_n(\mathbf{r})}{\partial \mathbf{R}_i}, \tag{3.35}$$

where φ_n are the Kohn-Sham orbitals. The linear response for each Kohn-Sham orbital also need to be evaluated, which can be performed by linearising Equation 3.8,

$$(H_{\text{Ref}} - \epsilon_n) \frac{\partial \varphi_n(\mathbf{r})}{\partial \mathbf{R}_i} = -\left(\frac{\partial V_{\text{Ref}}(\mathbf{r})}{\partial \mathbf{R}_i} \frac{\partial \epsilon_n}{\partial \mathbf{R}_i} \right) \varphi_n(\mathbf{r}), \tag{3.36}$$

where H_{Ref} is the Hamiltonian for an electron under effective potential V_{Ref} and ϵ_n is the corresponding energy eigenvalue. These equations may be solved self-consistently, in a similar manner to the Kohn-Sham equations in Section 3.2.2, while linearising Equation 3.13 provides an expression for updating the the effective potential response $\frac{\partial V_{\text{Ref}}(\mathbf{r})}{\partial \mathbf{R}_i}$. In this approach, the matrix obtained is known as the dynamical matrix; this may be transformed into the Hessian by performing a Fourier transform.

One of the major advantages to the DFPT approach is that it is flexible and may be

45

applied to evaluate the response of many properties, including phonons and polarisability, that results from perturbations to the atomic coordinates, electric field or other variables. In addition, the perturbations are infinitesimal, so the harmonic oscillator approximation remains valid. Furthermore, this method does not require a supercell to be generated, as in the frozen phonon approach, so the overall computational expense may be lower than the latter. The primary disadvantage compared to the frozen phonon approach is that implementating DFPT requires specialised DFT code, which is not readily parallelised.

3.5.3   Simulation of Infrared Activities

As noted in Section 2.1.1, the gross selection rule for IR spectroscopy states that a vibrational mode is IR active if it causes a change in the overall dipole moment [81, 82]. The relative intensity of each IR active mode I_ν^{IR} may be determined based on how the overall polarisation of the structure P changes with respect to the displacement of atoms during the vibration [146],

$$I_\nu^{\mathrm{IR}} = \sum_\alpha \left| \sum_{i,\beta} Z_{i,\alpha,\beta}^* \epsilon_{i,\nu,\beta} \right|^2, \tag{3.37}$$

where $\epsilon_{i,\nu,\beta}$ is the normalised vibrational eigenvector of atom i in cartesian direction β during normal mode ν, calculated in the previous frozen phonon or DFPT simulation. $Z_{i,\alpha,\beta}^*$ is an element of the Born effective charge tensor,

$$Z_{i,\alpha,\beta}^* = \frac{\Omega}{|e|} \frac{\partial P_\alpha}{\partial R_{i,\beta}}, \tag{3.38}$$

which describes how a displacement in direction β of atom i affects the overall polarisation in direction α [147]. Ω is the unit cell volume and e is the elementary charge.

The Born effective charge tensor may be obtained using a finite displacement or DFPT approach, in a similar manner to how the force contants were calculated. Indeed, the Born tensors may be determined alongside the force constants, reducing the overall cost of the calculation.

3.5.4   Simulation of Raman Activities

The relative Raman intensity I_ν^{Raman} of each vibrational mode is given by [84],

$$I_\nu^{\mathrm{Raman}} \propto \left| e_j^S \cdot R_{jk,\nu} \cdot e_k^I \right|^2. \tag{3.39}$$

$R_{jk,\nu}$ is the Raman tensor of normal mode ν, which describes how the amplitude of the Raman scattered wave depends on the polarisation direction of the incident and scattered light, represented by the vectors e_k^I and e_j^S, respectively. Therefore, a Raman tensor must be constructed for each unique normal mode. This may be achieved by calculating the linear response of the electric polarisability χ_{jk} that results from atomic displacements $\mathbf{u}_\nu$, using a similar DFPT approach to that for determining the force constants and Born effective charge tensors,

$$R_{\nu,jk} = \left| \frac{\partial \chi_{jk}}{\partial \mathbf{u}_\nu} \right|^2. \tag{3.40}$$

The major difference in calculating the Raman tensors compared to the force constants and Born effective charge tensors is that a different tensor is required for each normal mode, meaning the frozen phonon or DFPT calculation must be performed beforehand. Consequently, calculation of the Raman tensors can be computationally expensive, depending on the size of the system and the number of normal modes that need to be investigated.

In systems where the preferred crystal geometry and the polarisations of the incident and scattered light are known, Equation 3.39 may be used to directly calculate the relative Raman intensities of each normal mode (Section 2.1.4). This was the approach used to study the Raman activities for the autunite minerals saléeite, torbernite, nováčekite and zeunerite. However, for polycrystalline and liquid samples, no preferred orientation exists. A well established approximation is commonly used to calculate the Raman intensities for an average of orientations in an assumed 90° scattering geometry [148],

$$I_\nu^{Raman} = 45\alpha^2 + 7\beta_2, \tag{3.41}$$

where

$$\alpha = \frac{R_{11} + R_{22} + R_{33}}{3} \tag{3.42}$$

and

$$\beta_2 = \frac{((R_{11} - R_{22})^2 + (R_{11} - R_{33})^2 + (R_{22} - R_{33})^2)^2 + 6(R_{12}^2 + R_{13}^2 + R_{23}^2)}{2}. \tag{3.43}$$

This approximation is used in the vasp_raman.py code [149] and has been utilised for calculating the Raman intensities of UO_2, U_3O_8 and UO_3, which are known to exist as polycrystalline deposits.

3.6 Computational Details

At the start of this project, a number of trial calculations on uranyl carbonates and phosphates were performed using classical techniques. These were implemented in the METADISE [150] and GULP [151] codes and utilised potentials derived by Kerisit and Liu [152], Rabone and de Leeuw [153] and de Leeuw and Parker [154]. However, the complexity of the possible oxidation states and mineral compositions meant that the primary focus of this project became the application of DFT.

In this investigation, the VASP code [155, 156] (version 5.3.5) has been used extensively for DFT calculations. The PBE exchange-correlation functional [107] was used, which is a formulation of the generalised gradient approximation (GGA). Pseudopotentials were implemented with the projector augmented wave (PAW) method [129] and convergence testing demonstrated that a plane wave cut-off energy of 500 eV was sufficient. Each calculation used an automatically generated Monkhorst-Pack k-point mesh, centered around the Γ-point [125]. To represent the strong localisation of f-electrons at uranium atom sites, DFT +U was implemented using the Dudarev scheme [115], with values of $U = 4.50$ eV and $J = 0.54$ eV ($U_{\text{eff}} = 3.96$ eV) derived from X-ray photoelectron spectroscopy (XPS) experiments on UO_2 [123, 124]. This DFT +U set-up has been recently used to investigate a range of binary uranium oxides. [43, 49, 55]

The primary computational method used was energy minimisation, which is directly implemented within the VASP code. This procedure took initial crystal structure data from previously published experimental investigations. The constant pressure approach was used, which allowed the atomic positions and the unit cell volume and shape to change. Furthermore, the minimisation was not constrained by maintaining the unit cell symmetry. A conjugate gradients method was typically used to begin the procedure, while the quasi-Newton algorithm RMM-DIIS [137] was applied closer to the energy minimum. Convergence criteria were chosen to be rigorous, as the minimised structure was then used to calculate the vibrational properties. The criteria were 10^{-6} eV/atom for electronic relaxation and 0.01 eV/Å for ionic relaxation. Molecular dynamics (MD) was also performed in VASP for a small number of procedures, to locate appropriate starting configurations for water molecules where no experimental data for hydrogen atoms was available.

Both the frozen phonon approach [139–141] and density functional perturbation theory (DFPT) [139, 140, 144, 145] were used to calculate the vibrational frequencies and their

corresponding eigenvectors in this investigation. These methods are implemented within the VASP code, but the frozen phonon approach was also performed using the Phonopy code [142], which generates a set of displaced crystal structures, uses VASP to calculate the energies and forces for each, then diagonalises the force constant matrix to obtain the vibrational modes. The default atomic displacements for the frozen phonon method in VASP and Phonopy are 0.015 Å [143] and 0.01 Å [142], respectively.

The Born effective charge tensors, used to calculate the IR intensity of each vibrational mode, were generated during the DFPT procedure within the VASP code. A script was then employed to calculate the IR intensities from the computed eigenvectors, using Equation 3.37. To evaluate the Raman activities, a Raman tensor was generated for each vibrational mode after the initial frozen phonon or DFPT calculation. These simulations were implemented using the vasp_raman.py code [149], which also used VASP to calculate the elements of the Raman tensor.

The majority of DFT simulations were performed on the UK national high performance computing (HPC) service ARCHER, provided by UoE HPCx Ltd, Cray Inc and NAG Ltd at the University of Edinburgh. Its predecessor, HECToR, was also used for some earlier work. Access to both systems was provided via our membership of the UK's HPC Materials Chemistry Consortium (MCC), which is funded by EPSRC (EP/F067496 and EP/L000202). Other calculations were performed on the University of Bath's HPC facilities Aquila and Balena. The simulations were typically run using 6–12 nodes and optimised with the NPAR and KPAR settings in VASP. Calculation of the vibrational frequencies within VASP often took 24–48 hours on 6–12 nodes, but the Raman simulations were task farmed on ∼400 nodes for 2–3 hours. The Raman simulations were ideal candidates for task farming as they involved running a large number of very similar calculations, which finished in approximately the same amount of computer time.

Structural figures were generated using the VESTA program [157], while the motions corresponding to each vibrational mode were analysed and drawn using POVRAY [158]. Plots were generated using the Python module matplotlib [159].

Chapter 4

Triuranium Octaoxide U$_3$O$_8$

U$_3$O$_8$ has been described as the kinetic oxidation product of UO$_2$ [31]. Its inherent stability makes it the second most widely studied uranium oxide in the nuclear fuel cycle, after UO$_2$ [40]. Indeed, the viability of both U$_3$O$_8$ and UO$_3$ as nuclear fuels has recently been investigated, which have the potential to avoid the need for ^{235}U enrichment [33]. Three polymorphs of U$_3$O$_8$ have been reported [40, 51, 160], of which the α and β structures are stable under ambient conditions and γ-U$_3$O$_8$ is the high pressure form [49]. A brief literature review on U$_3$O$_8$ is given in Section 4.1. The computationally determined structural properties of α and β-U$_3$O$_8$ have been previously reported by Brincat *et al.* [49] and are detailed in Section 4.2. The focus of this investigation is on calculating the vibrational properties, which are reported in Section 4.3.

4.1 U$_3$O$_8$ Background

U$_3$O$_8$ is often found as an oxidation product of UO$_2$ at different stages of the nuclear fuel cycle [13, 31]. It has also been reported to form during the reduction or decomposition of UO$_3$ [32, 161]. The oxidation of UO$_2$ to U$_3$O$_8$ is accompanied by an increase in volume of approximately 36%, potentially leading to stress or damage to the fuel rods [31]. Consequently, the reactivity of UO$_2$, particularly the oxidation process, has been the focus of many experimental [31, 40, 162–164] and computational [43, 165, 166] investigations.

A variety of techniques, including neutron and X-ray diffraction, have been used to characterise the structures of α-U$_3$O$_8$ [160, 167–170], β-U$_3$O$_8$ [51, 171] and γ-U$_3$O$_8$ [172]. α-U$_3$O$_8$ was reported to crystallise in the $Amm2$ [160] and $C222$ space groups, β-U$_3$O$_8$ in the $Cmcm$ [51] and $P2_1/m$ [171] space groups and γ-U$_3$O$_8$ in the $P\bar{6}2m$ space group [172]. Experimental investigations have shown that U$_3$O$_8$ (UO$_{2.67}$) can accomodate considerable variation in composition, retaining the structure with oxygen loss down to UO$_{2.61}$ [79]. Thermodynamic studies indicate that α-U$_3$O$_8$ is the most common polymorph under ambient conditions and may be formed by heating UO$_2$ up to 900 K in dry air [40]. β-U$_3$O$_8$ is considered the high temperature polymorph and can be formed by heating α-U$_3$O$_8$ to 1623 K in air and then slowly cooling to room temperature [51]. γ-U$_3$O$_8$ is described as the high pressure polymorph and is reported to form after heating α-

U_3O_8 to 473–573 K at high oxygen partial pressure (∼16 kbar) [40, 52, 173]. Recent DFT+U simulations predict that α- and β-U_3O_8 are competitive at low temperatures, suggesting that the polymorph formed is dependent upon the synthesis conditions [49]. The structures of each phase are described in more detail in Section 4.2.

The electronic properties, including the binding energies [174], band gap [175, 176] and the nature of bonding [177, 178] have been studied using XPS, electron spin resonance spectroscopy, XANES and a range of other techniques. Two distinct assignments have been given for the distribution of valence states within the structure, with older investigations suggesting a 2:1 ratio of U^{6+}:U^{4+} [47, 179] and newer studies indicating a 2:1 ratio of U^{5+}:U^{6+} [48, 180]. Computational techniques have also been employed to determine the preferred configuration, with initial potential-based and DFT simulations using an averaged charge of $U^{5\frac{1}{3}+}$ showing the best agreement with experimental structures [181, 182]. However, the U^{5+}/U^{6+} configuration was supported by more recent DFT+U calculations [32, 49, 183].
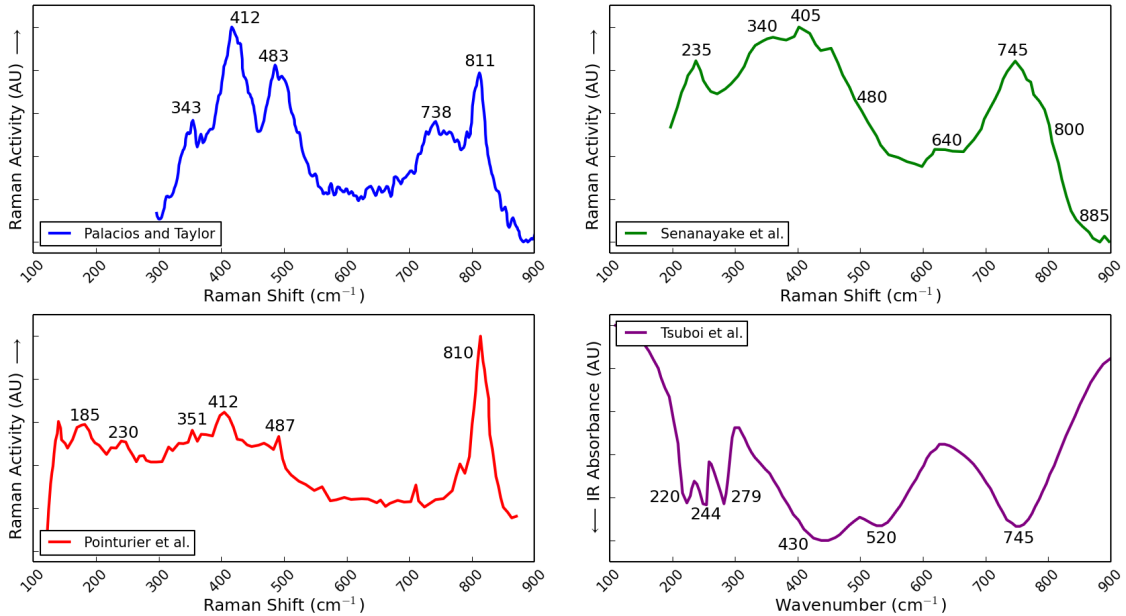
Figure 4.1: Reproductions of previously published experimental Raman spectra of U_3O_8 by Palacios and Taylor [65], Senanayake *et al.* [163] and Pointurier *et al.* [184], and an IR spectrum by Tsuboi *et al.* [64]. The intensity and absorption axes are given in arbitrary units.

The present investigation is focused on simulating the vibrational properties of U_3O_8, including determination of the Raman and IR activities for each mode. Previously published Raman and IR spectra are reproduced in Figure 4.1 [64, 65, 163, 184], while those

reported by Allen *et al.* [79, 80, 185, 186] are given alongside the simulated spectra in Figure 4.4. The modes have been conventionally assigned using a simple model proposed by Ohwada and Soga, based on two non-interacting uranium environments and combined with a group theory analysis of the two clusters [79, 187]. The first environment was treated as octahedral UO_2, while the second is the hexagonal bipyramid in α-UO_3. Although the simplicity of this model may be useful, two major issues arise. First, this model assumes that U_3O_8 adopts a U^{4+}/U^{6+} oxidation state configuration, with no strategy for accomodating the U^{5+} environments expected from more recent experiments. Second, vibrations that involve multiple uranium environments are not predicted. In contrast, the DFT simulations used in this investigation allow vibrations that encompass multiple uranium environments within the unit cell and does not fix the oxidation states. Approximate positions and relative intensities for each peak are also calculated with DFT, whereas the original model relies upon experimental spectra of UO_2 and UO_3.

4.2 Structures and Models

Previously reported experimental studies show that α- and β-U_3O_8 crystallise in the $C222$ [160] and $Cmcm$ [51] space groups, respectively. However, individual layers of U_3O_8 are equivalent in both phases, with a 2:1 ratio of pentagonal bipyramidal (UO_7) and distorted octahedral (UO_6) type environments (Figures 4.3a and b). The variation is in the stacking of adjacent layers, in addition to the distribution of uranium oxidation states within the structure.

The distribution of uranium oxidation states in α- and β-U_3O_8 were determined using the calculated magnetisation values for each uranium ion; U^{6+} and U^{5+} are known to have magnetisation values of 0 and 1, respectively. This approach was also utilised by Brincat *et al.* [49]. An alternative strategy would be to use the calculated charge distribution; however, uncertainties arise when formally assigning bonding electrons to specific ions. In contrast, the uranium ions have a magnetisation whereas oxygen ions do not, hence, these values allow a clearer assignment to be made.

In α-U_3O_8, adjacent layers are aligned (Figure 4.2a), such that equivalent uranium environments form a chain perpendicular to the layers. All UO_7 environments contain uranium in the U^{5+} oxidation state, while U^{6+} ions occupy the UO_6 environments (Figure 4.3a). Consequently, adjacent U^{6+} ions compete for axial oxygen atoms, meaning all axial the U-O bonds are approximately 2.10 Å in length and uranyl bonds cannot
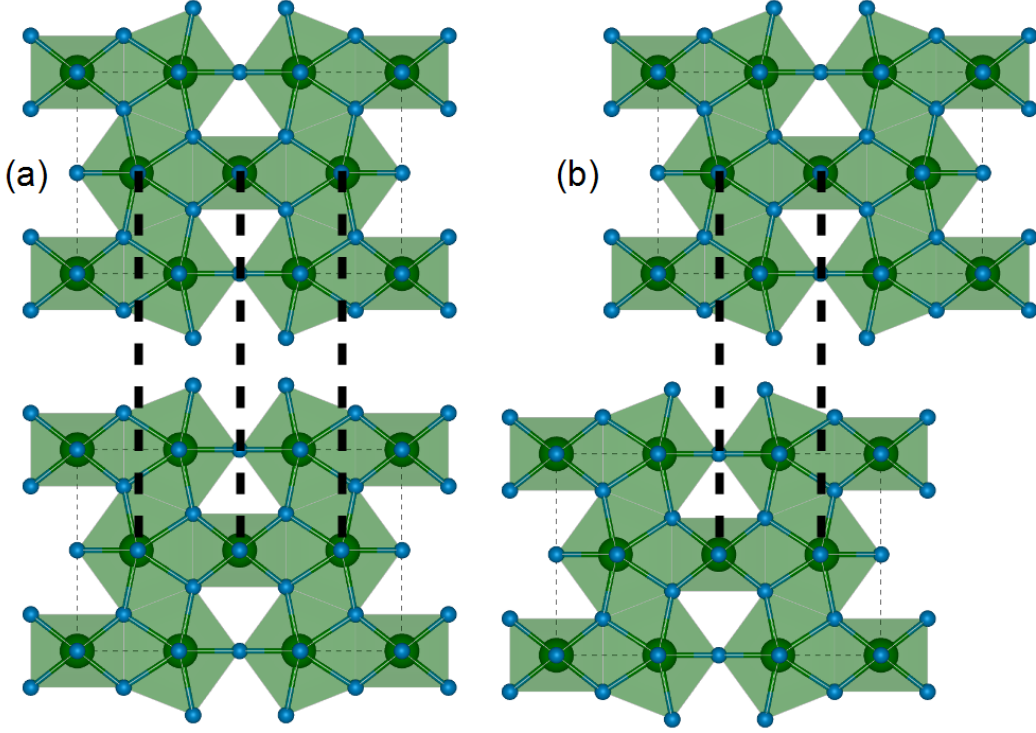
Figure 4.2: The stacking of adjacent layers in (a) α-U_3O_8 and (b) β-U_3O_8; dashed black lines connect uranium polyhedra that share oxygen vertices. Equivalent environments share vertices in adjacent layers in α-U_3O_8 whereas every second layer in β-U_3O_8 is offset by a third of the unit cell in the b-direction.

form. In contrast, adjacent layers in β-U_3O_8 are offset by a third of the unit cell in the b-direction (Figure 4.2b), so equivalent environments do not overlap and uranyl bonding can form. In this structure, the U^{6+} ions are located in UO_7 environments and form uranyl bonds ($\sim$1.91 Å), while the remaining UO_7 and UO_6 environments contain uranium in the U^{5+} oxidation state (Figure 4.3b). As the $U^{5+}O_6$ environments are adjacent to the uranyl bonded environments, these axial U-O bonds are longer to compensate ($\sim$2.32 Å). The equatorial U-O bonds in both environments are similar in both α- and β-U_3O_8; all bond distances are provided in Figures 4.3c and d.

It should be noted that the experimentally determined unit cell of α-U_3O_8 that was minimised by Brincat *et al.* [55] only comprised a single layer, whereas two layers constitute in a single unit cell of β-U_3O_8. When simulating vibrational properties for the latter structure, a number of motions were found to involve both layers and the bonds connecting them. Therefore, a supercell of α-U_3O_8 was generated, to allow interlayer vibrations to be investigated. This supercell retained the characteristic layers observed in both U_3O_8 phases, in addition to the distribution of U^{5+} and U^{6+} ions found in the
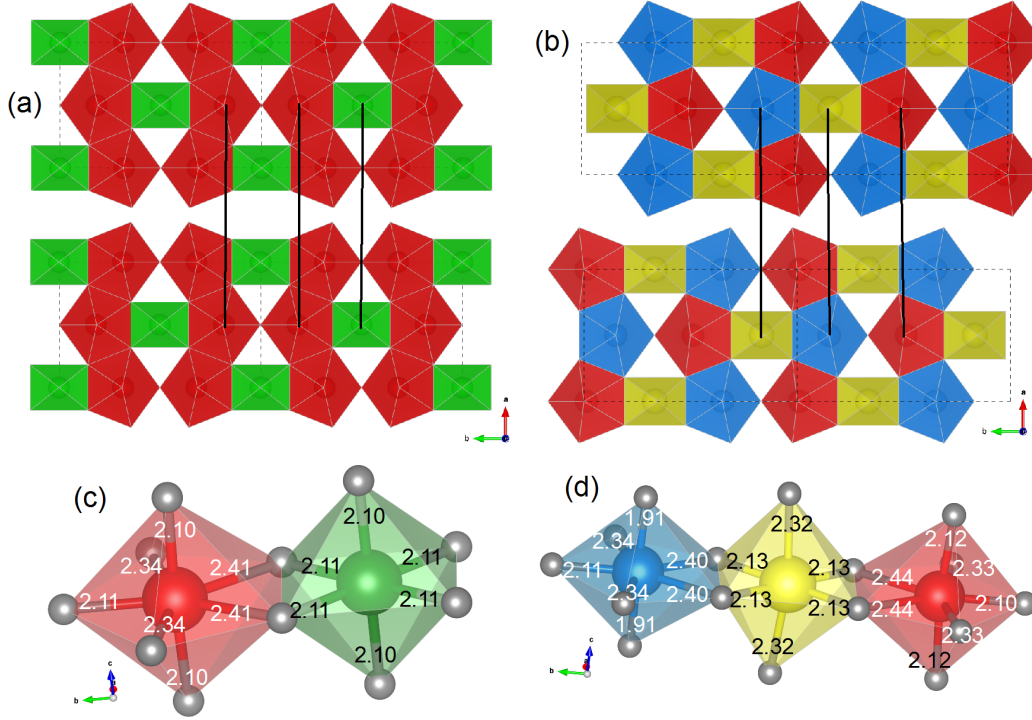
Figure 4.3: The layers in (a) α-U_3O_8 and (b) β-U_3O_8; solid black lines connect uranium polyhedra that share oxygen vertices and dashed black lines represent the unit cell. The uranium environments in (c) α-U_3O_8 and (d) β-U_3O_8; U-O distances are given in Å. Red polyhedra represent $U^{5+}O_7$ environments, green polyhedra represent $U^{6+}O_6$, blue polyhedra represent $U^{6+}O_7$ and yellow polyhedra represent $U^{5+}O_6$.

original α-U_3O_8 structure. The bond distances in Figure 4.3c and the structural parameters and vibrational properties presented in Section 4.3 correspond to this supercell structure. Other supercell structures of α-U_3O_8 were also minimised, which did not retain the U^{5+}/U^{6+} distribution and instead contained some U^{6+} ions in the UO_7 environment. All of these systems were found to be higher in energy and, since calculating the vibrational properties is computationally expensive, the properties of these systems were not predicted.

For both α- and β-U_3O_8, the unit cell volume and shape were fully relaxed without constraining the symmetries. The electronic and ionic convergence criteria were 1×10^{-6} eV/atom and 0.01 eV/Å, respectively, and testing demonstrated that 500 eV was a sufficient cutoff energy [49]. A Γ-centered k-point mesh of 4 x 2 x 4 was used for both phases.

Table 4.1: A comparison between experimental and relaxed (DFT) structural parameters for α and β-U_3O_8. The parameters for both the single unit cell and the supercell of α-U_3O_8 are presented. The volume per uranium ion has been presented, to allow for a comparison across all structures.

	α-U_3O_8			β-U_3O_8	
	Expt. [160]	DFT_{single}	$DFT_{supercell}$	Expt. [51]	DFT [49]
a (Å)	6.70	7.22	7.23	7.07	7.21
b (Å)	11.95	11.59	11.59	11.45	11.65
c (Å)	4.14	4.20	8.40	8.30	8.45
$\alpha=\beta=\gamma$ (°)	90.0	90.0	90.0	90.0	90.0
Vol./U (Å^3)	55.30	58.67	58.70	55.98	59.08
Space Group	C222	Cmmm	Cmmm	Cmcm	Cmcm

4.3 Results and Discussion

The minimisation procedure performed on α- and β-U_3O_8 resulted in structures with slightly overestimated lattice parameters compared to those determined experimentally, but the increase in volume remained less than 7%. U-O bond distances were also found to be overestimated, which resulted in calculated vibrational modes being at lower wavenumbers than corresponding experimental peaks. This discrepancy is a known effect of the DFT functional used [107, 115]. Experimental [51, 160] and simulated structural parameters for the two phases are given in Table 4.1.

The simulated Raman and IR spectra of α- and β-U_3O_8 are given in Figure 4.4, alongside previously published spectra by Allen *et al.* [79, 80]. To facilitate the discussion, the high, middle and low wavenumber regions of the spectra are discussed separately: 680–820 cm^{-1}, 360–550 cm^{-1} and <360 cm^{-1}, respectively. The motions observed for each mode are noted in Tables 4.2 and 4.2 for α- and β-U_3O_8, respectively. For clarity, each vibration is separated into the effective motion at each uranium environment (UO_6 and UO_7). This approach is similar to that described by Ohwada and Soga, [187], where motions of the UO_6 and UO_7 were interpreted using non-interacting environments of UO_2 octahedra and α-UO_3 hexagonal bipyramids, except that here the environments may interact. Figure 4.5 illustrates the different motions observed and the labels assigned in this figure (i.e. A1, B1 etc.) correspond to those given in the discussion and Tables 4.2 and 4.3.
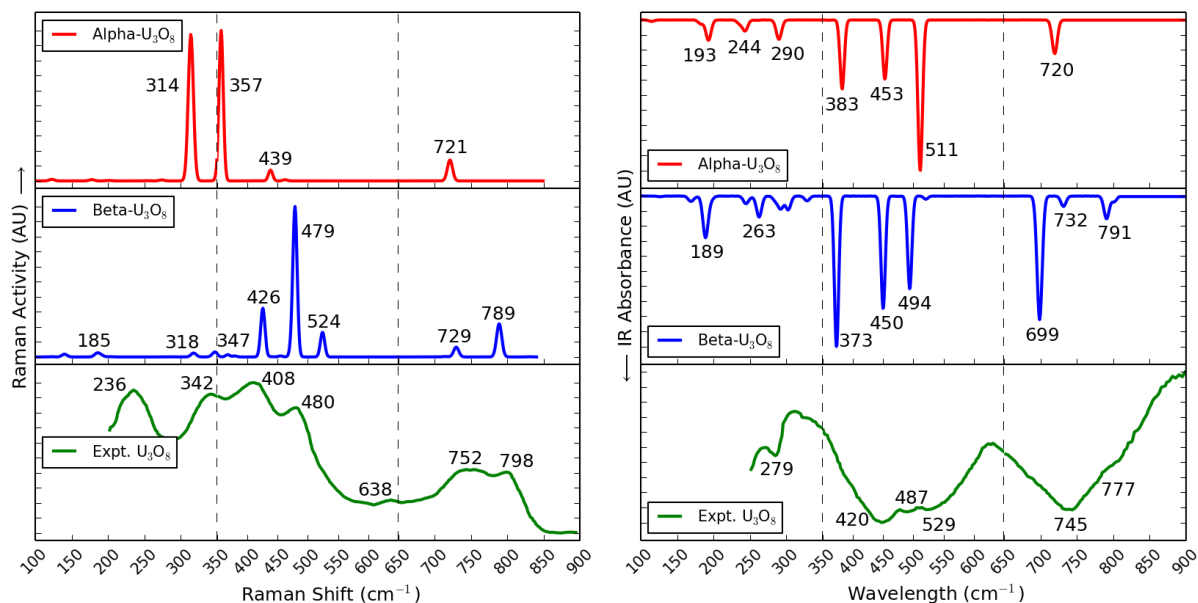
Figure 4.4: The simulated Raman (left) and IR (right) spectra of α- and β-U_3O_8 and experimental spectra reproduced from data published by Allen *et al.* [79, 80]. Peak positions are annotated in cm^{-1}, while the intensity and absorption axes are given in arbitrary units.

High Wavenumber Region

The high wavenumber region (680–820 cm^{-1}) of the simulated Raman and IR spectra of α-U_3O_8 are dominated by peaks at 721 and 720 cm^{-1}, respectively. These correspond to combination modes of equatorial stretching (Figure 4.5, A3 and B7) and scissoring (A4 and B6) across both uranium environments. In β-U_3O_8, the presence of two distinct UO_7 environments results in a greater number of combination modes. Furthermore, the axial uranyl bonds in the $U^{6+}O_7$ environments produce characteristic symmetric stretching modes (B1 and B2) in the Raman and IR spectra at 789 and 802 cm^{-1}, respectively, as well as an antisymmetric stretching mode (B8) at 699 cm^{-1} in the IR spectrum. The lack of uranyl bonding in the structure of α-U_3O_8 precludes the presence of equivalent modes in its spectra. The observed uranyl vibrations are complex and include additional equatorial motions in other environments (A2 and B3). The modes at 732 and 729 cm^{-1} only contain vibrations involving the longer equatorial bonds (A2, A3, B5, B3 and B4), so are found at lower wavenumbers than the combination modes. Although the U-O stretching modes assigned here agree with the conventional assignment of this region, based on Ohwada and Soga's model [187], the complex motions are different and emphasise that the two environments cannot be treated as non-interacting units.

Table 4.2: The Raman and IR active modes in the simulated spectra of α-U_3O_8. The labels correspond to the motions of environments shown in Figure 4.5. *Eq* indicates the equatorial plane of the environment and *ax* represents the axial vector.

Freq (cm^{-1})	Activity (R/IR)	UO_6 (U^{6+}) motion	UO_7 (U^{5+}) motion
721	R	A3) Eq sym str	B6) Eq scissor
720	IR	A4) Eq scissor	B7) Eq sym str
515	IR	A4) Eq scissor	B9) Eq sym str
513	IR	A5) Ax antisym str	B8) Ax antisym str
511	IR	A5) Ax antisym str	B8) Ax antisym str
463	R	A7) Eq antisym str	B13) Eq scissor
453	IR	A9) Eq antisym str	B14) Eq twist
439	R	A10) Eq scissor	B15) Eq scissor
383	IR	A11) Eq rocking	B16) Eq O translate
357	R	A8) Eq twisting	B18) Eq scissor
314	R	A13) Ax + Eq bending	B22) Ax + Eq bending
290	IR	A16) Eq bending	B23) Eq bending
244	IR	A14) Ax bending	B21) Ax bending
236	IR	—	B10) Eq U-O bend
193	IR	A18) Eq rocking	B26) Eq bending
183	IR	A20) Ax translate	B28) U translate
178	R	—	B28) U translate
123	R	—	B28) U translate
115	IR	A20) Ax translate	B28) U translate

The modes in the high wavenumber region of the simulated Raman spectrum of β-U_3O_8 (789 and 729 cm^{-1}) show good agreement to those observed at 752 and 798 cm^{-1} in experimental Raman spectra of U_3O_8 [65, 79, 163, 184]. The mode at 721 cm^{-1} in the simulated spectrum of α-U_3O_8 also corresponds well to the experimentally observed mode at 752 cm^{-1}. Similar observations may be made for the IR modes in this region, as a strong and broad peak is observed in experimental spectra at 745 cm^{-1}, with a shoulder at 777 cm^{-1} [64, 185], that could correspond to the peaks in simulated β-U_3O_8 at 699 and 791 cm^{-1}. The simulated spectrum of α-U_3O_8 also contains a peak at 720 cm^{-1} that may correspond to the experimental 752 cm^{-1} peak. The presence of peaks in the experimental spectra that may be attributed to uranyl stretches suggests that β-U_3O_8 is be the dominant phase, or that an alternative configuration containing uranyl bonds exists.

Middle Wavenumber Region

The middle wavenumber region (360–550 cm^{-1}) of the simulated IR spectra for both α- and β-U_3O_8 are dominated by three strong modes, which appear to be characteristic of

Table 4.3: The Raman and IR active modes in the simulated spectra of β-U_3O_8. The labels correspond to the motions of environments shown in Figure 4.5. *Eq* indicates the equatorial plane of the environment and *ax* represents the axial vector.

Freq (cm^{-1})	Activity (R/IR)	UO_6 (U^{5+}) motion	UO_7 (U^{5+}) motion	UO_7 (U^{6+}) motion (uranyl)
802	IR	A1) Ax sym str	B1) Ax sym str + eq str	B1) Ax sym str + eq str
791	IR	A2) Eq rocking	B2) Ax sym str	B3) Eq Scissor
789	R	A1+2) Sym str + rocking	B3) Eq Scissor	B2) Ax sym str
732	IR	A3) Eq sym str	B3) Eq Scissor	B4) Eq Scissor
729	R	A2) Eq rocking	B5) Eq sym str	B3) Eq Scissor
699	IR	A5) Ax antisym str	—	B8) Ax antisym str
524	R	A2) Eq rocking	B9) Eq sym str	B9) Eq sym str
521	IR	A2) Eq rocking	B9) Eq sym str	B9) Eq sym str
494	IR	—	B8) Ax antisym str	B10) Eq U-O bend
479	R	A1+6) Sym str + scissor	B11) Eq antisym str	B12) Sym str + scissor
474	R	A7) Eq antisym str	B13) Eq scissor	B13) Eq scissor
450	IR	A9) Eq asym str	B14) Eq twist	B14) Eq twist
426	R	A10) Eq scissor	B13) Eq scissor	B15) Eq scissor
373	IR	A11) Eq rocking	B17) Eq scissor	B16) Eq O translate
347	R	A12) Eq rocking	B17) Eq scissor	B17) Eq scissor
329	IR	A13) Ax + Eq bending	B19) Ax + Eq bending	B19) Ax + Eq bending
318	R	A14) Ax bending	B20) Eq bending	B21) Ax bending
303	IR	A14) Ax bending	B21) Ax bending	B21) Ax bending
293	IR	A15) Eq wagging	B23) Eq bending	B24) Eq wagging
287	IR	A15) Eq wagging	B23) Eq bending	B19) Ax + Eq bending
285	IR	A14) Ax bending	B25) Bend + twist	B25) Bend + twist
263	IR	A14) Ax bending	B21) Ax bending	B28) U translate
245	IR	A14) Ax bending	B21) Ax bending	B21) Ax bending
196	IR	A17) U translate	—	B28) U translate
189	IR	A18) Eq rocking	B26) Eq bending	B26) Eq bending
189	IR	A19) Eq bend + ax twist	B27) Ax twist	B27) Ax twist
185	R	A20) Ax translate	B28) U translate	B28) U translate
169	IR	A19) Eq bend + ax twist	B27) Ax twist	B27) Ax twist
140	R	A17) U translate	B28) U translate	B28) U translate

the U_3O_8 layers. The highest wavenumber modes are seen at 511 and 513 cm^{-1} for α-U_3O_8 and 494 cm^{-1} for β-U_3O_8 and primarily correspond to axial antisymmetric stretches (Figure 4.5, A5 and B8). The second modes are at 453 and 450 cm^{-1} for α- and β-U_3O_8, respectively, and involves an equatorial antisymmetric stretch in the UO_6 environments (A9) coupled with a twist in the UO_7 environments (B14). The third modes involve a rocking motion in UO_6 (A11) and an in-plane equatorial bending in UO_7 environments (B17 or B16) and are observed at 383 and 373 cm^{-1} in α- and β-U_3O_8, respectively. These three peaks demonstrate a general trend within this region, with stretching modes at higher wavenumbers, bending modes at lower wavenumbers and combined modes

between. Three peaks were also seen experimentally at 420, 487 and 529 cm^{-1} [64, 185]. The 420 and 529 cm^{-1} peaks were conventionally assigned to equatorial stretching in the UO_6 and UO_7 environments, respectively, while the 487 cm^{-1} peak was attributed to a combination of lower wavenumber modes [64, 185, 186]. The relative intensities of these modes in the simulated spectrum of β-U_3O_8 and the experimental spectrum decrease with increasing wavenumber, whereas α-U_3O_8 does not follow the same trend. This supports the assignment of β-U_3O_8 as the dominant phase.

The simulated Raman spectrum of β-U_3O_8 shows three distinct modes in the middle wavenumber region at 426, 474/479 and 524 cm^{-1}. These modes correspond to equatorial bending and stretching motions (A2, A6, A10, B9, B11 and B15), while the strong 479 cm^{-1} peak also involves a uranyl symmetric stretch (A1 and B12). In contrast, the simulated Raman spectrum of α-U_3O_8 only contains two low intensity peaks in the middle region at 439 and 463 cm^{-1}, which correspond to the same motions as the 426 and 474 cm^{-1} modes in β-U_3O_8. In this region, the experimental Raman spectra demonstrate similarities to the simulated β-U_3O_8 spectrum, containing three broad peaks at 342, 408 and 480 cm^{-1} [65, 79, 163, 184]. The conventional assignment of these modes were equatorial stretching motions, which agrees with the simulations, but does not account for the uranyl stretching modes.

Low Wavenumber Region

The vibrational motions in the low wavenumber region (<340 cm^{-1}) of the simulated Raman and IR spectra almost exclusively correspond to bending motions (Figure 4.5, A14, A18, B19, B20 and B23–B27). These modes in this region are typically of lower intensity compared to those in the high and middle regions, with the exception of the peaks at 314 and 357 cm^{-1} in the Raman spectrum of α-U_3O_8. The corresponding motions are equatorial in-plane bending (A18 and B18) and combined axial and equatorial out-of-plane bending modes (A13 and B22), respectively. The experimental Raman and IR spectra contain significant peaks in this region, at 236 cm^{-1} [65, 79, 163, 184] and 279 cm^{-1} [64, 185, 186], respectively. These were conventionally assigned to bending modes, which agrees with the simulations, but does not account for interactions between uranium environments.

4.4 Conclusions

Density functional theory (DFT) simulations have been utilised to investigate the vibrational properties of α- and β-U_3O_8. Both phases are comprised of equivalent layers, with
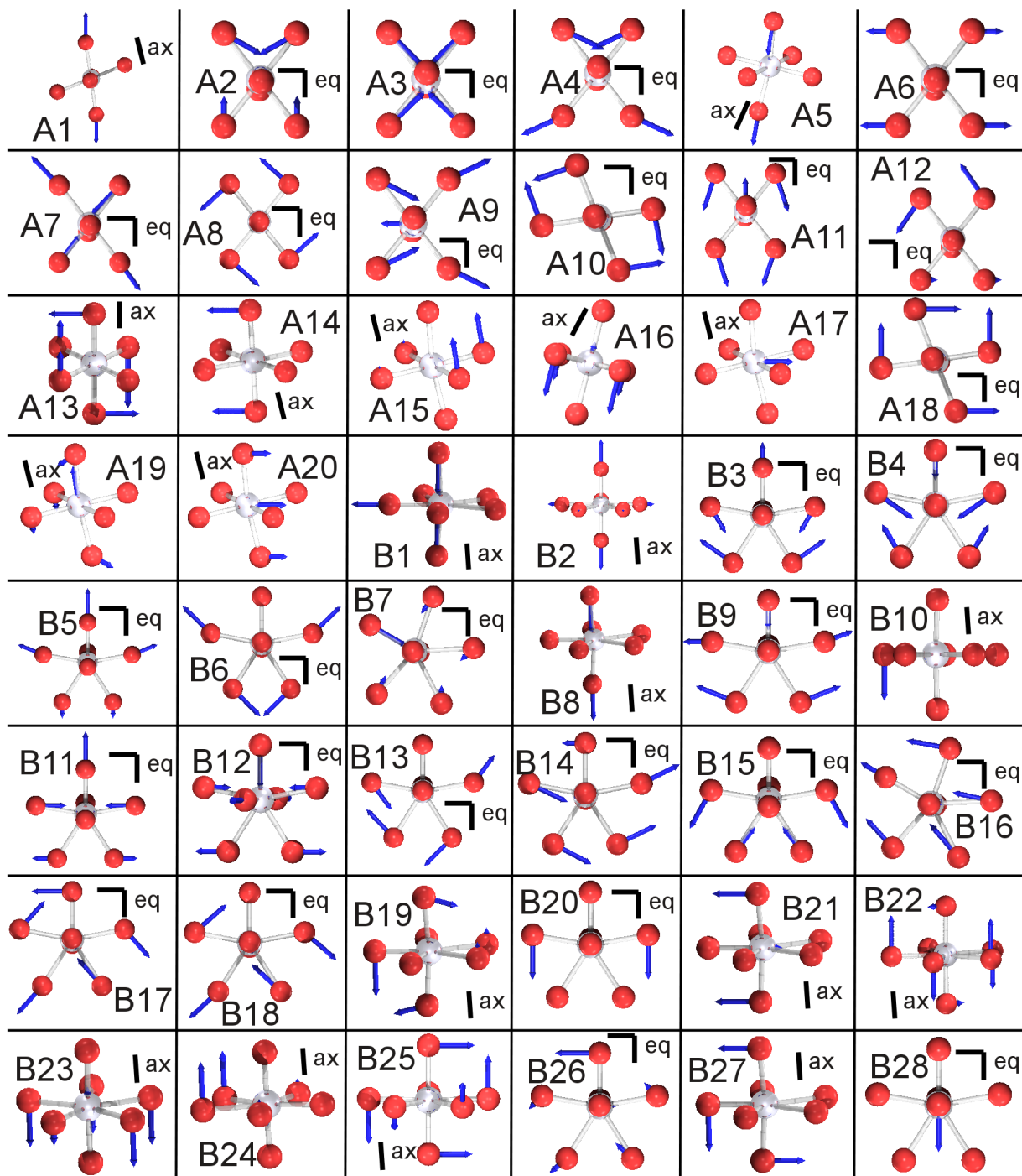
Figure 4.5: Vibrations of the UO_6 (A) and UO_7 (B) clusters in the polymorphs of U_3O_8. Depending on the orientation of the cluster, either the equatorial plane (*eq*) or axial vector (*ax*) is labelled. These images are referenced in Tables 4.2 and 4.3.

differences in the spectral features emerging from the stacking of successive layers. One major advantage of computational simulations is the ability to directly compare spectral features with the structure and individual environments. These simulations have shown that the majority of vibrational modes in both phases of U_3O_8 involve motions in every environment. Therefore, the conventional model of non-interacting UO_2 and α-UO_3 units [187] was determined to insufficiently represent the vibrational properties.

Three distinct modes were found in the 360–550 cm^{-1} region of both α- and β-U_3O_8 simulated IR spectra, as well as the experimental U_3O_8 IR spectrum. This indicates that these peaks are characteristic of the U_3O_8 layered structure and may be used to distinguish it from other uranium oxide materials. One of the major features that may be used to discriminate between the two phases is the presence of uranyl bonding in β-U_3O_8, which is able to form due to the rotation of adjacent layers. The high wavenumber region (680–820 cm^{-1}) of β-U_3O_8 contains multiple Raman active modes, where only a single mode was seen in α-U_3O_8. This results partly from inequivalent UO_7 environments and partly from uranyl bonding in β-U_3O_8. A further difference is in the middle wavenumber region (360–550 cm^{-1}) of β-U_3O_8, where three modes are observed, corresponding to uranyl stretching motions. In contrast, α-U_3O_8 only contains weak modes in this region. The experimental Raman spectra show similar peaks to the simulated spectrum β-U_3O_8, suggesting that this phase is dominant, that both phases form in association, or that an alternative configuration exists, where adjacent layers do not overlap and uranyl bonds can form.

Chapter 5

Uranium Trioxide UO$_3$

UO$_3$ is an oxidation product of UO$_2$, forming in natural uranium deposits as well as within the nuclear fuel cycle [12]. Seven crystalline phases have been reported for UO$_3$, in addition to an amorphous phase [30, 53, 55], and it has been noted that the formation of different polymorphs is dependent on the method used to produce them [188]. Therefore, a strategy for distinguishing these phases would be of great value to forensic and environmental science investigations. However, it can be difficult to synthesise stoichiometric samples for experimental study because UO$_3$ exhibits hypostoichiometry [189]. Further difficulties in synthesising a single stoichiometric sample arise from the ready formation of multiple polymorphs [188, 190, 191] and hydrolysis products [52, 192, 193]. In this chapter, density functional theory (DFT) is used to simulate the structures and vibrational properties of five stoichiometric UO$_3$ phases, which are compared against experimental spectra. The primary goal of this study is to determine whether Raman and IR spectroscopy may be used to distinguish between the polymorphs.

The five UO$_3$ polymorphs studied in this chapter are α-, β-, γ-, δ- and η-UO$_3$; the syntheses of two additional phases, ϵ-UO$_3$ [194, 195] and ζ-UO$_3$ [189, 190] have been reported, but the atomic coordinates have not been resolved for these structures. A review of literature for the five phases of interest to this study is given in Section 5.1. This investigation utilises the DFT models prepared by Brincat *et al.* [55] and the major structural features of each phase are described in Section 5.2, alongside some computational details. The simulated Raman and IR spectra are given in Section 5.3, alongside published IR data [80] and unpublished Raman spectra provided by Allen for the same samples. The syntheses for the minerals studied by Allen are described briefly in Appendix B.

5.1 Review of UO$_3$ Literature

γ-UO$_3$

The most stable polymorph of UO$_3$ under ambient conditions is γ-UO$_3$ [32, 161]. This phase is also the most thermodynamically stable binary uranium oxide. As such, it may be synthesised by heating other UO$_3$ polymorphs to 723 K in 40 atm O$_2$, or by burning
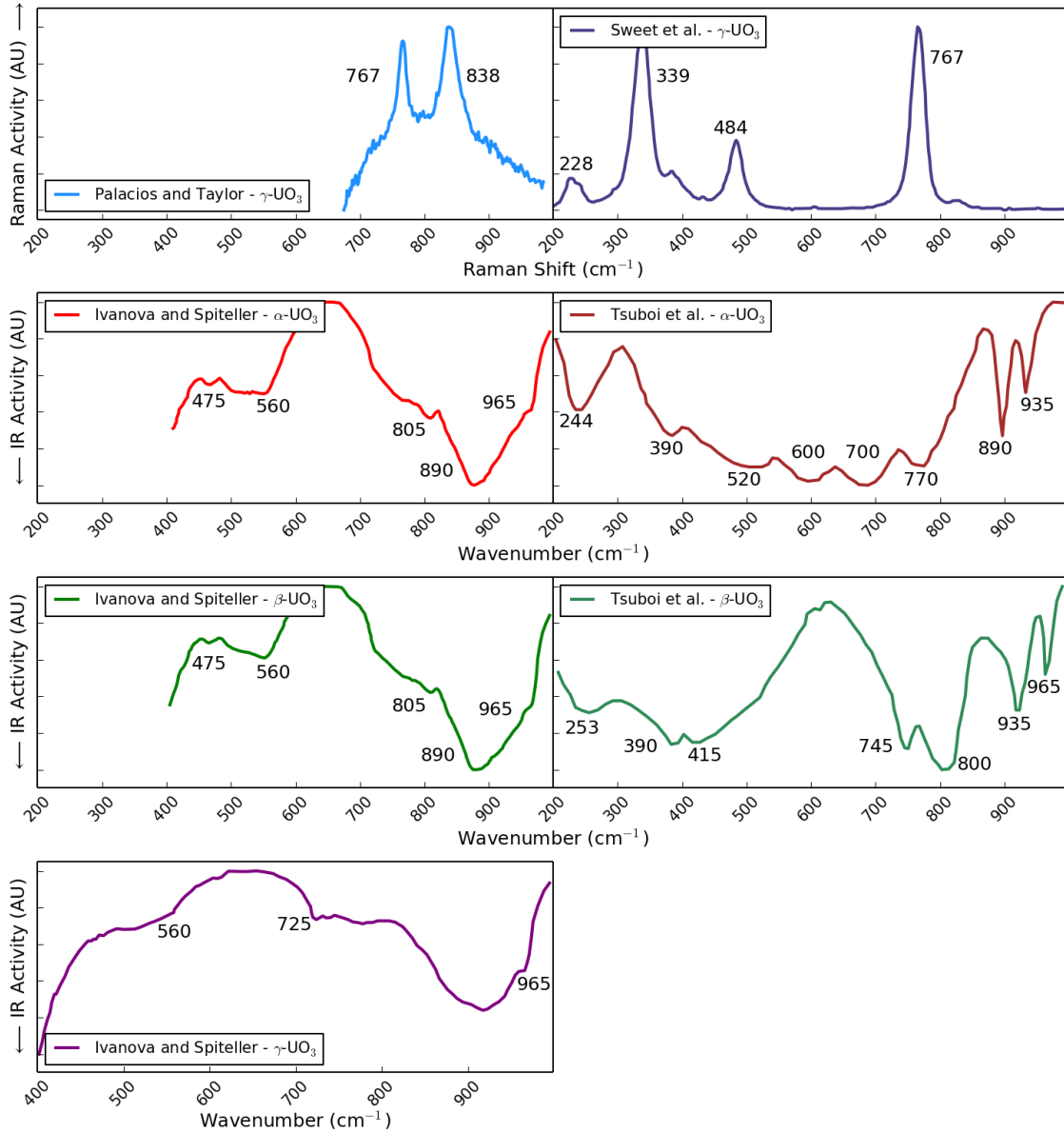
Figure 5.1: Reproductions of previously published literature spectra: the Raman spectra of γ-UO$_3$ by Palacios and Taylor [65] and Sweet *et al.* [188], the IR spectra of α-, β- and γ-UO$_3$ by Ivanova and Spiteller [196], and the IR spectra of α- and β-UO$_3$ by Tsuboi *et al.* [64]. The intensity and absorption axes are plotted on an arbitrary scale.

uranyl nitrate hexahydrate in air at 673–873 K [197]. XRD experiments performed by Engmann found that it adopted a tetragonal $I4_1$ structure [198], while Loopstra later identified two closely related structures, tetragonal $I4_1$ and orthorhombic $Fddd$, observed above 373 K and below 293 K, respectively [199]. A computational investigation by He *et al.* used LSDA+U to simulate the $I4_1$ polymorph and found the volume to be well reproduced, but did not publish any further structural information [176]. More recently, Brincat *et al.* performed GGA+U simulations on both $I4_1$ and $Fddd$ modifi-

cations of γ-UO$_3$, finding the structural and energetic properties to be near identical on relaxation [55].

As the most stable polymorph, several authors have presented Raman [65, 188] and IR [80, 196] spectra of γ-UO$_3$. The new Raman spectra presented in this chapter were collected by Allen and correspond to the same samples for which the IR and XPS spectra have been published [200]. A number of differences became apparent when comparing the experimental spectra of equivalent phases from different literature sources. For example, the Raman spectrum of γ-UO$_3$ collected by Palacios and Taylor [65] and Sweet *et al.* [188] (Figure 5.1) have a strong peak at 767 cm^{-1}, while an additional peak at 838 cm^{-1} is only found in the former. In contrast, the unpublished spectrum by Allen (Figure 5.7) is dominated by a strong peak at 690 cm^{-1} and smaller peaks at 820 and 830 cm^{-1}. These differences may arise from variations in the stoichiometry, the level of hydration or the presence of other uranium oxide phases, which may result from different synthesis conditions, such as temperature, humidity or oxygen pressure. Furthermore, some features of the spectra may be inconsistent if different excitation wavelengths or powers were used to collect the Raman data, if ATR geometry was used for the IR spectra or if different standards were used to calibrate the spectrometer. These differences emphasise that a standardised procedure is necessary when collecting vibrational spectra, particularly when this data is compared against simulations.

The γ-UO$_3$ model used in this chapter was the $I4_1$ structure minimised by Brincat *et al.* [55]. It has been used to simulate the vibrational properties of γ-UO$_3$, including the vibrational modes and corresponding Raman and IR activities. A description of the γ-UO$_3$ structure and some pertinant computational details are provided in Section 5.2.1.

δ-UO$_3$

δ-UO$_3$ may be synthesised by hydrothermally reacting the γ- phase, then heating the resultant β-UO$_3$(OH)$_2$ to 648 K. This polymorph has been reported to crystallise in the $Pm\bar{3}m$ space group, in a structure equivalent to ReO$_3$ [191]. Every uranium ion is located in a perfectly octahedral environment, therefore, it is the most successfully simulated polymorph using a variety of DFT functionals [55, 176, 182, 201].

While the IR spectrum of δ-UO$_3$ has been published by Allen and Holmes [80], no Raman spectrum for this phase has been published. Therefore, the spectrum provided by Allen is considered the only Raman spectrum available for δ-UO$_3$ (Figure 5.8). It should be noted that a group theory analysis of the δ-UO$_3$ structure found three triply degenerate

vibrations, $2T_{1u}$ and T_{2u}, of which the first two are IR active, but none are Raman active. This is in direct contrast to the experimental Raman spectrum collected by Allen, so the $Pm\bar{3}m$ structure minimised by Brincat *et al.* [55] has been expanded to a supercell. Details of the original and expanded structures are described in Section 5.2.2. The supercell structure was used to determine the vibrational properties of δ-UO$_3$.

α-UO$_3$

α-UO$_3$ is usually synthesised by heating uranyl peroxide to $\sim$673–773 K [202]. It has been described as being structurally similar to α-U$_3$O$_8$, with uranium deficiencies. Zachariasen first characterised it as hexagonal $P\bar{3}m1$ using XRD [170]; however, further refinements indicated $C2mm$ [203] or $C222$ [54]. It was noted that the experimental densities of these samples were significantly lower than the theoretical density, hence, Greaves concluded that the structure was not stoichiometric and $\sim$12% of uranium lattice sites were vacant [54]. The structural parameters of the stoichiometric $P\bar{3}m1$ modification have been well represented in previous simulations [55, 176, 201] and Brincat *et al.* found it to be more energetically stable than the $C2mm$ structure [55]. Consequently, it is the $P\bar{3}m1$ structure minimised by Brincat *et al.* that has been used in this chapter to evaluate the vibrational properties of α-UO$_3$. The structural properties of this polymorph are presented in Section 5.2.3.

The vibrational properties of α-UO$_3$ were first investigated by Tsuboi *et al.*, who used a combination of IR spectroscopy and group theory [64]. A group theory approach predicts four IR active modes with symmetry labels $2A_{2u}$ and $2E_u$, which were observed in the experimental spectra. Two Raman active modes were also predicted, A_{1g} and E_g, the positions of which were inferred by Tsuboi *et al.* based on the high wavenumber combination modes in the IR spectrum. More recently, the IR spectrum has been collected by Ivanova *et al.* [196] and Allen and Holmes [80], while a Raman spectrum was provided by Allen for this investigation. A comparison of the literature spectra is presented in Figure 5.1 and the simulated spectra from this work are given in Section 5.3.3.

β-UO$_3$

β-UO$_3$ is the most complex UO$_3$ polymorph studied, crystallising in a $P2_1$ monoclinic unit cell with five distinct uranium environments [204, 205]. Its synthesis has been reported as the calcination of ammonium diuranate in air at 732–773 K; lower temperatures instead form γ-UO$_3$. The first computational investigation of β-UO$_3$ was performed by Brincat *et al.*, who found that relaxation of the structure resulted in significant changes

to some bond lengths and uranium environments [55]. Indeed, the relaxed bond lengths were more consistent with those seen for other uranium oxides. This suggests that β-UO_3 is a defective structure. The relaxed structural properties are described in Section 5.2.4 and the vibrational properties are presented in Section 5.3.4.

Tsuboi *et al.* published the IR spectrum of β-UO_3; however, due to the complexity of the structure, they were unable to provide a group theory analysis and interpretation of the peaks [64]. IR spectra were also published by Ivanova *et al.* [196] and Allen and Holmes [80], while the only available Raman spectrum is that provided by Allen for this investigation.

η-UO_3

η-UO_3 was first identified by Siegel *et al.*, who noted the polymorph is formed at 1373 K and 30 kbar, but did not present a detailed synthesis [53]. The calculated and measured density is higher than the other phases (8.86 gcm^{-1} [30]), which fits with its description as the high pressure polymorph. XRD found this phase to adopt an orthorhomic $P2_12_12_1$ structure, with all uranium ions in a puckered pentagonal bipyramidal environment [53]. This structure has been reproduced well in simulations by Pickard *et al.* [201] and Brincat *et al.* [55], with the latter investigation also showing this is the highest density phase, confirming the high pressure description.

No experimental Raman or IR spectra are available for η-UO_3, so the vibrational properties presented in this chapter are considered predictive (Section 5.3.5). Nevertheless, the relaxed structural parameters and bond lengths (detailed in Section 5.2.5) are very close to the experimentally determined properties, supporting the quality of this prediction.

5.2   Structures and Models

5.2.1 γ-UO_3

γ-UO_3 is the most thermodynamically stable polymorph of UO_3 below 10 atm pO_2 [161]. It has been described as crystallising in both $Fddd$ and $I4_1$ space groups [198, 199]. However, Brincat *et al.* reported these to be modifications of the same structure, with near identical lattice parameters, bond lengths and energies after minimisation [55]. Therefore, the smaller $I4_1$ system has been used in this investigation (Figure 5.2). The structural properties do not change significantly upon minimisation, with both symmetry and uranium coordination retained and the bond lengths remain within ± 0.1 Å of the

experimental distances. Two distinct uranium environments are present in this structure, a distorted octahedron (environment 1) and a distorted dodecahedron (environment 2). However, the distorted dodecahedra environment contains two longer U-O distances (>2.8 Å), so these have not been considered as bonds in this investigation. Both environments contain collinear uranyl bonds (U-O bond distance 1.7–1.9 Å), which produce characteristic bands in both Raman and IR spectra [206]. It is notable that the uranyl oxygens in environment 1 are also coordinated to the adjacent uranium ion, whereas the uranyl oxygens in environment 2 remain uncoordinated. It is therefore possible that water molecules will coordinate to environment 2 when γ-UO_3 is hydrated, changing the nature of the uranyl bond. The remaining four oxygen atoms (O_{eq}) are found within the equatorial plane, at longer distances (2.23–2.34 Å).
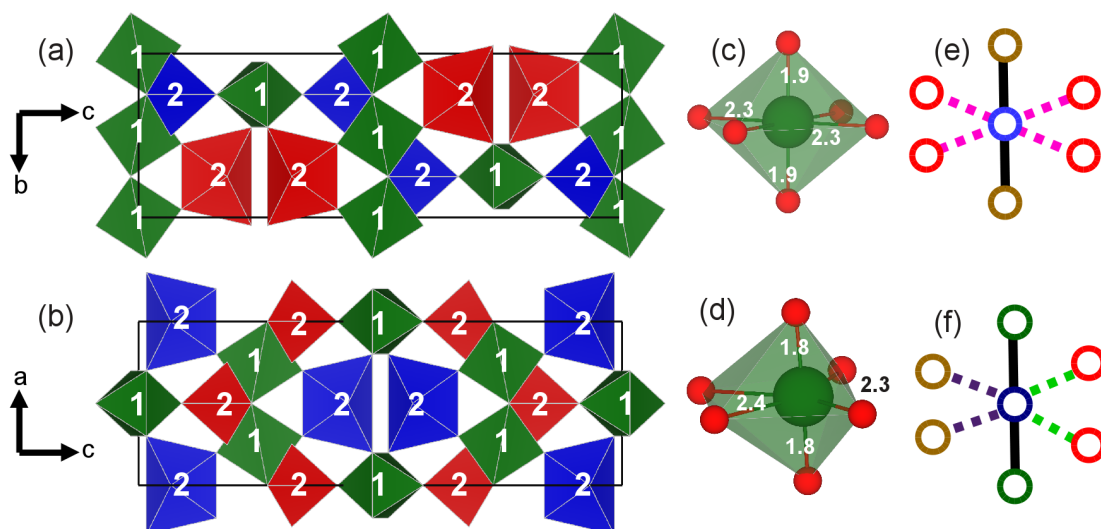
Figure 5.2: (a and b) Two orientations of the minimised unit cell of $I4_1$ γ-UO_3, with the two distinct environments labelled. (c and d) Uranium environments 1 and 2, with bond distances labelled (Å). The experimental structure of γ-UO_3 is very similar, with all U-O bond distances within 0.1 Å of the minimised distances. (e and f) Schematics of environments 1 and 2, where the blue, green, red and brown circles represent uranium, axial oxygens and two types of equatorial oxygens, respectively, the solid black line represents the shorter U-O bond and the dashed pink, purple and green lines represent the longer U-O bonds.

DFT calculations of γ-UO_3 were performed using VASP 5.3.5 and parallelised over 20 nodes (480 cores) on ARCHER using KPAR 20 and NPAR 3 settings. The Γ-centered k-point mesh used was 6 x 6 x 4 (76 irreducible k-points), the same as that used by Brincat *et al.* [55].

5.2.2 δ-UO$_3$

The experimental structure of δ-UO$_3$ was reported to crystallise in the Pm$\bar{3}$m space group, with a single symmetrically distinct uranium environment and one distinct oxygen environment. [191] The structure minimised by Brincat *et al.* [55] maintains this symmetry; each uranium is in a perfectly octahedral environment, with U-O bond lengths of 2.10 Å. However, the simulated vibrational spectrum for this structure does not contain any Raman active modes, which directly disagrees with the experimental spectrum. This suggests that the δ-UO$_3$ system cannot be accurately represented using the 4-atom unit cell, necessitating the use of a larger cell. A 16-atom supercell has been minimised, which exhibits a rotation of the octahedral uranium environments, similar to that observed in perovskite CaMnO$_3$ [207]. As a result, three distinct pairs of collinear U-O bonds distances emerge in each environment: a uranyl-like 1.90 Å bond and two longer bonds (2.11 and 2.35 Å). The lattice energy of the 16-atom structure was calculated and compared against the values for all five polymorphs presented by Brincat *et al.* [55]. The 16-atom structure was found to be 0.16 eV more stable per uranium than the 4-atom structure and 0.03 eV less stable per U than γ-UO$_3$, the most stable polymorph. This is a significant increase in the relative stability of the delta phase, further emphasising that it needs to be re-examined experimentally.

The unit cells and uranium environments for both 4- and 16-atom structures are illustrated in Figure 5.3, while structural and elastic parameters are given in Table 5.1. The elastic constants (C$_{xy}$) were calculated using the finite displacement method and the bulk modulus (B) was determined by averaging the first nine values (C$_{11}$:C$_{33}$). Brincat *et al.* observed that UO$_3$ phases containing uranyl bonding have a bulk modulus below 100 GPa [55], which holds true for the 16-atom system of δ-UO$_3$ (67 GPa). This is because the uranyl bond is very strong and rigid, weakening the surrounding U-O bonds and making the system overall less resistant to compression (i.e. a lower bulk modulus).

DFT calculations of δ-UO$_3$ were performed using VASP 5.3.5 and parallelised over 8 nodes (192 cores) on ARCHER using KPAR 8 and NPAR 3 settings. The Γ-centered k-point mesh used for the 4-atom system was 12 x 12 x 12 (868 k-points), as used by Brincat *et al.* [55], while the 16-atom system was modelled using a k-point mesh of 11 x 5 x 11 (303 k-points).
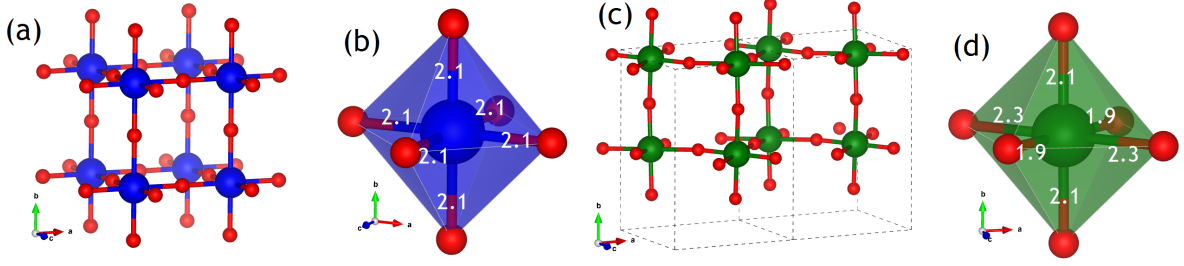
Figure 5.3: (a) The lattice and (b) uranium coordination environment of the 4-atom unit cell of δ-UO$_3$. (c) The lattice and (d) uranium coordination environment of the 16-atom unit cell of δ-UO$_3$. The unit cell is given as a dashed black line in the lattice images and bond distances are given in Å for the uranium environment diagrams.

Table 5.1: Comparison of the structural and elastic properties in the 4- and 16-atom unit cells of δ-UO$_3$.

	Lattice Parameters					
System	a (Å)	b (Å)	c (Å)	$\alpha = \gamma$ (°)	β (°)	Symmetry [†]
4-atom	4.196	4.196	4.196	90.00	90.00	Pm$\bar{3}$m (221)
16-atom	10.411	6.008	8.433	90.00	144.70	C2/c (15)
	Elastic Constants (GPa)					
	C_{11}	C_{22}	C_{33}	C_{12}	C_{13}	C_{23}	C_{44}
4-atom	387.6	-	-	33.2	-	-	27.3
16-atom	124.4	261.1	124.8	-20.5	93.6	-25.3	20.1
	C_{55}	C_{66}	C_{16}	C_{26}	C_{36}	C_{45}	B
4-atom	-	-	-	-	-	-	151
16-atom	20.1	97.3	1.8	6.4	1.4	0.1	67

† Tolerance = 0.01 Å

5.2.3 α-UO$_3$

The experimental and relaxed crystal structures of α-UO$_3$ (space group P$\bar{3}$m1) are shown in Figure 5.4. Each uranium ion is located in an 8-coordinate distorted hexagonal bipyramidal environment, where two oxygen ions are bound by short collinear bonds (O$_{ax}$) and the remaining six are displaced above and below the equatorial plane (O$_{eq}$). Upon relaxation, the O$_{eq}$ atoms are closer to the equatorial plane and the U-O$_{eq}$ bonds are shorter. Nevertheless, the space group of the relaxed structure remains the same as the experimental structure.

DFT calculations of α-UO$_3$ were performed using VASP 5.3.5 and parallelised over 1 node (24 cores) on ARCHER using the default KPAR and NPAR settings. The Γ-centered k-point mesh used was 5 x 5 x 5 (39 k-points), equivalent to that used by Brincat *et*

69
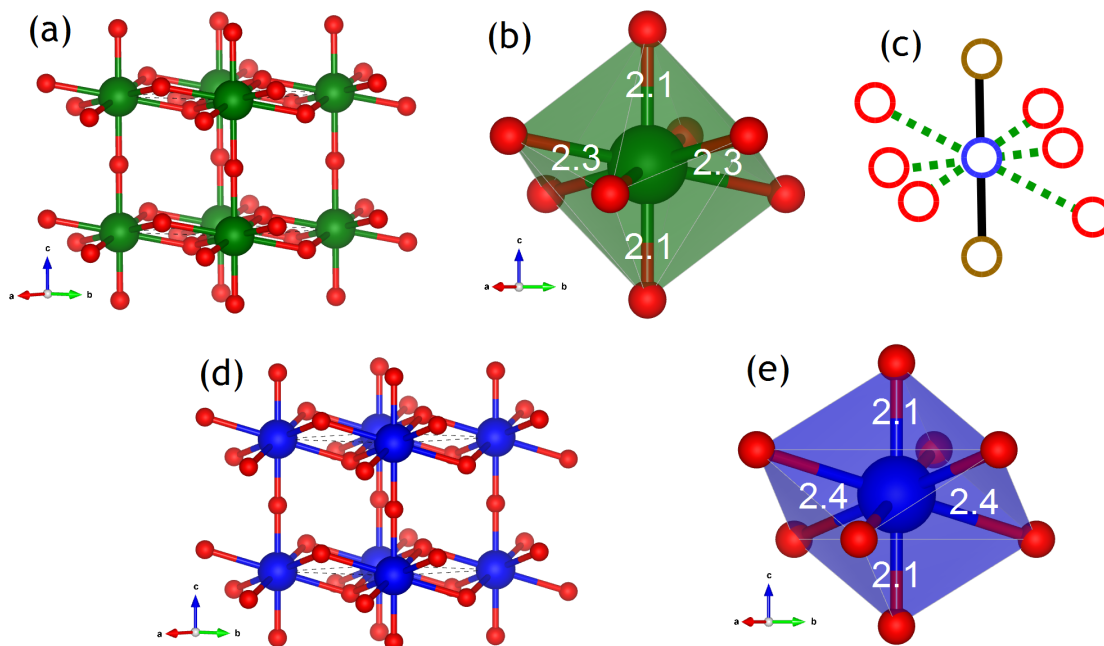
Figure 5.4: (a) The lattice and (b) uranium environment of the minimised α-UO$_3$ structure. (c) The schematic representation of the minimised uranium cluster, where the blue, red and brown circlesrepresent uranium, equatorial oxygen and axial oxygen ions, respectively. The solid black line represents the shorter U-O$_{ax}$ bonds and the dashed green line represents the longer U-O$_{eq}$ bonds. (d) The lattice and (e) uranium environment of the experimental α-UO$_3$ structure. The unit cell is given as a dashed black line in the lattice diagrams and U-O bond distances are given in Å for the uranium environment diagrams.

al. [55].

5.2.4 β-UO$_3$

The structure of β-UO$_3$ was experimentally determined to crystallise in the P2$_1$ space group [204, 205], with five distinct uranium environments and fifteen unique oxygen sites (Figure C.7). Four uranium ions are located in an irregular 7-fold coordination, with one or two short U-O bonds (1.5–1.8 Å) and five or six longer bonds (2.1–2.8 Å) [55]. The other uranium environment is a distorted octahedron, with six bonds between 1.7–2.2 Å. The distortions present in these environments preclude the formation of collinear uranyl bonding.

The relaxed structure of β-UO$_3$ [55] was found to be more homogeneous than the experimental one, but it retains the P2$_1$ symmetry and five distinct uranium sites. Collinear uranyl bonding emerges in environments 1, 4 and 5 (Figure 5.5), each of which also
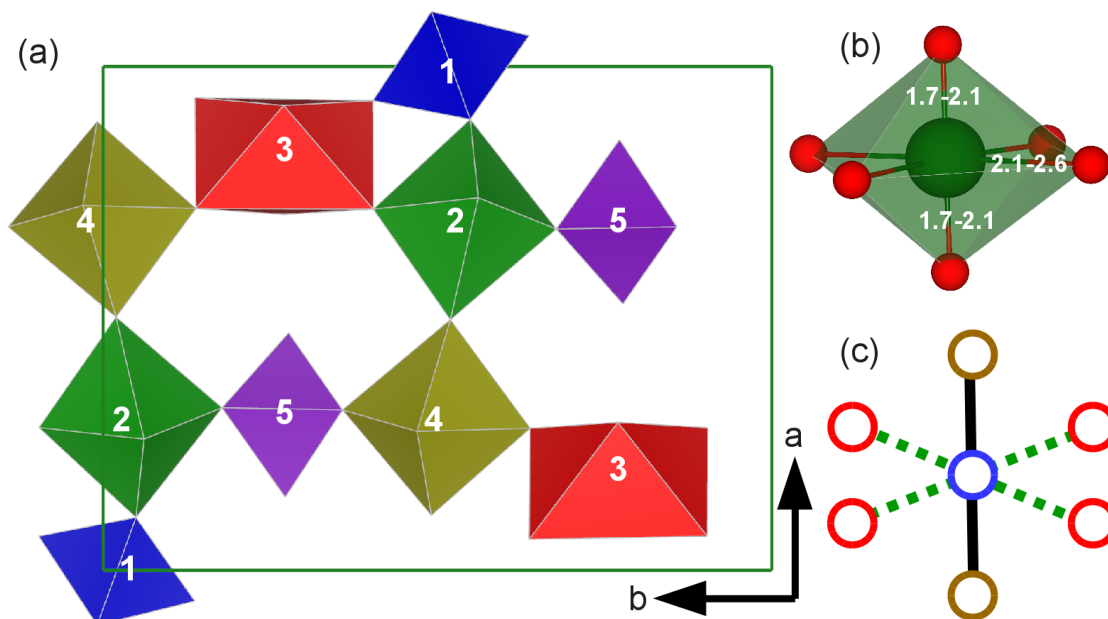
Figure 5.5: (a) The minimised unit cell of β-UO$_3$, with each environment labelled and (b) a representative uranium environment, with bond distance ranges given in Å. (c) A schematic representation of the uranium environments in the minimised β-UO$_3$ structure, where blue, red and brown circles represent the uranium and two oxygen environments, respectively, the solid black line represents the uranyl-like bonds and the dashed green lines represent the longer U-O bonds.

contains four U-O bonds 2.2–2.6 Å in length. The remaining environments are closer to octahedral symmetry, with six U-O bonds between 1.9–2.2 Å.

DFT calculations of β-UO$_3$ were performed using VASP 5.3.5 and parallelised over 4 nodes (96 cores) on ARCHER using KPAR 4 and the default NPAR settings. The Γ-centered k-point mesh used was 4 x 4 x 8 (54 k-points), equivalent to that used by Brincat *et al.* [55].

5.2.5 η-UO$_3$

η-UO$_3$ has been described as the high pressure phase of UO$_3$ and reported to crystallise in the P2$_1$2$_1$2$_1$ space group [53]. The unit cell contains four formula units, with each uranium ion located in a 7-fold puckered pentagonal bipyramidal environment (Figure 5.6). Both space group and uranium environment are retained upon minimisation [55]. Uranyl bonding is also present in the structures, with U-O lengths of 1.85 and 1.80 Å experimentally and 1.84 and 1.82 Å when relaxed.

71
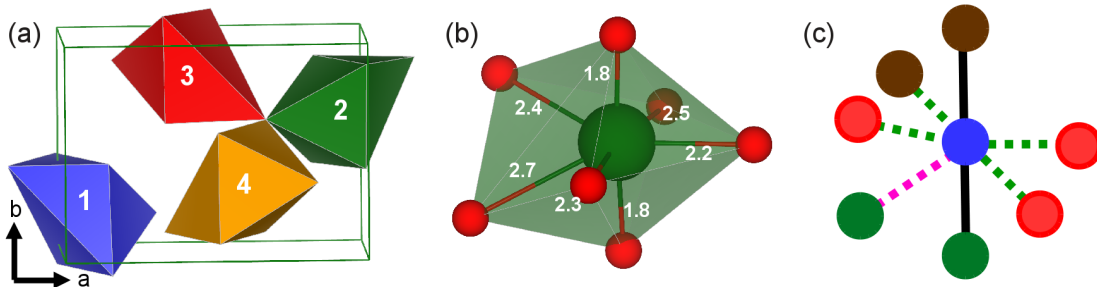
Figure 5.6: (a) The four uranium environments in a unit cell of η-UO_3. (b) The uranium environment, with bond lengths labelled in Å and (c) a schematic representation of the same, where the uranium environment is represented by a blue circle, the three oxygen environments are represented by brown, green and red circles, the collinear uranyl bonds ($\sim$1.8 Å) are represented by solid black lines, bonds between 2.0–2.5 Å are represented by dashed green lines and the longest bonds (2.7 Å) are represented by dashed pink lines.

DFT calculations of η-UO_3 have been performed using VASP 5.3.5 and parallelised over 2 nodes (48 cores) on ARCHER using the default KPAR and NPAR settings. The Γ-centered k-point mesh used was 6 x 7 x 7 (64 k-points), equivalent to that used by Brincat *et al.* [55].

5.3 Results and Discussion

5.3.1 γ-UO_3

The structural similarities between experimental and minimised γ-UO_3 support the validity of the simulation. Bands in the simulated Raman and IR spectra agree with the majority of peaks in each experimental spectrum [65, 80, 188, 196]. This indicates that the simulations can reproduce the vibrational fingerprint of stable polymorphs well, allowing the spectral and structural features to be linked. The simulated and experimental Raman and IR spectra of γ-UO_3 are presented in Figure 5.7. Figures C.1 and C.2 detail each vibrational motion within the spectrum of this phase.

It should be noted that some differences were observed between the experimental Raman spectra of γ-UO_3 taken by Allen and other previously published spectra [65, 188]. These differences are likely to have arisen from variations in the synthetic and analytical procedure used by each author, suggesting that these systems contain multiple phases or contain a significant number of defects. For detailed comparisons between experimental studies and modelling, it would be useful to see a standardised experimental procedure and a more detailed analysis of the phases present and the extent of stoi-
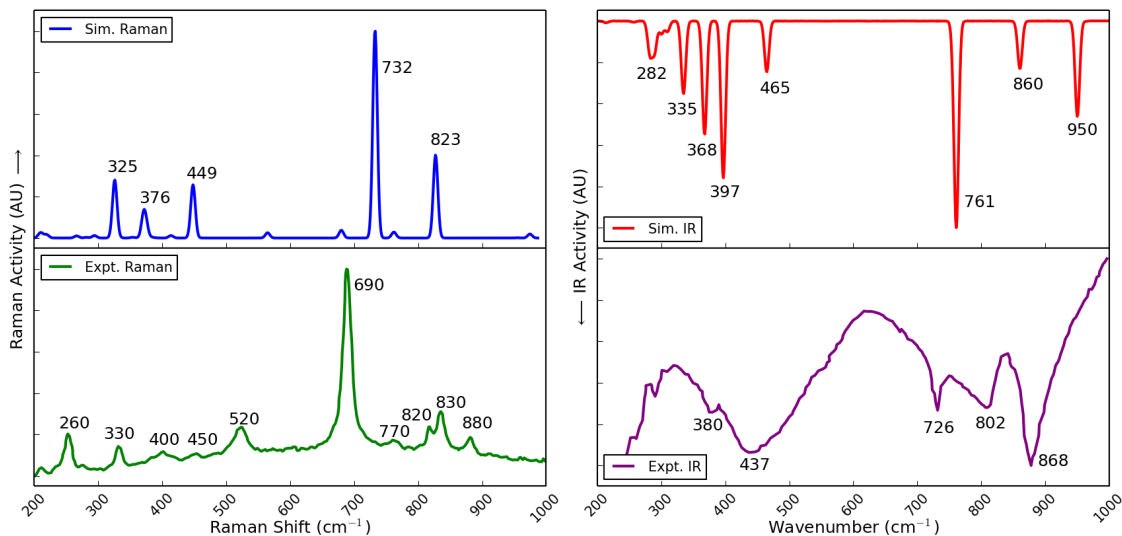
Figure 5.7: The experimental and simulated Raman and IR spectra of γ-UO$_3$. Experimental Raman and IR spectra of γ-UO$_3$ show good agreement to previously published spectra [65, 188, 196]. The experimental IR spectrum has been published by Allen *et al.* [80]. The intensity and absorption axes are plotted on an arbitrary scale. An analysis of the vibrational modes in this spectrum is given in Figures C.1 and C.2.

chiometry. In Allen's γ-UO$_3$ spectrum, the strongest peak is seen at ∼690 cm^{-1}, while a much smaller peak is seen at 770 cm^{-1} and three distinct peaks are found at 820, 830 and 890 cm^{-1}. In contrast, previously published spectra show strong peaks at 767 cm^{-1} and 838 cm^{-1} [65, 188]. As UO$_3$ is known to form a number of hydration products, the three peaks at 820, 830 and 890 cm^{-1} in Allen's spectrum may be attributed to those, while the peaks at 690 and 770 cm^{-1} correspond to the uranyl symmetric stretches at 732 and 823 cm^{-1}, respectively, in the simulated spectrum. An alternative explanation is that the strong peak at 690 cm^{-1} peak in Allen's spectrum corresponds to a contaminant material. This means that the simulated uranyl stretches at 732 and 823 cm^{-1} would correspond to the 770 cm^{-1} peak and the 820, 830 and 890 cm^{-1} group, respectively. The presence of multiple modes corresponding to the 823 cm^{-1} simulated peak may be explained by the coordination of water to the free uranyl oxygen in environment 2 (Figure 5.2), which would change the bond strength and thus peak position. This coordination is not possible in environment 1 because the uranyl oxygen ions are also equatorial oxygen ions in environment 2.

For an aqueous uranyl cation with collinear U-O bonds the symmetric and antisymmetric stretching modes are only Raman and IR active, respectively. However, the strongest mode in the simulated IR spectrum of γ-UO$_3$ is a complex mode at 761 cm^{-1} with contributions of symmetric and antisymmetric stretches from different environments.

This emphasises the need to consider each band as a vibration that encompasses the entire structure and not just the motions within a single environment. The peak at 726 cm^{-1} in Allen and Holmes' spectrum [80] may be attributed to this mode.

Peaks within the low wavenumber region (<550 cm^{-1}) are normally bending modes and have a lower intensity compared to peaks at higher wavenumbers. The broad band seen in the experimental IR spectrum at 437 cm^{-1} [80] likely corresponds to the low intensity bending modes in the 250–500 cm^{-1} region of the simulated IR spectrum of γ-UO$_3$.

5.3.2 δ-UO$_3$
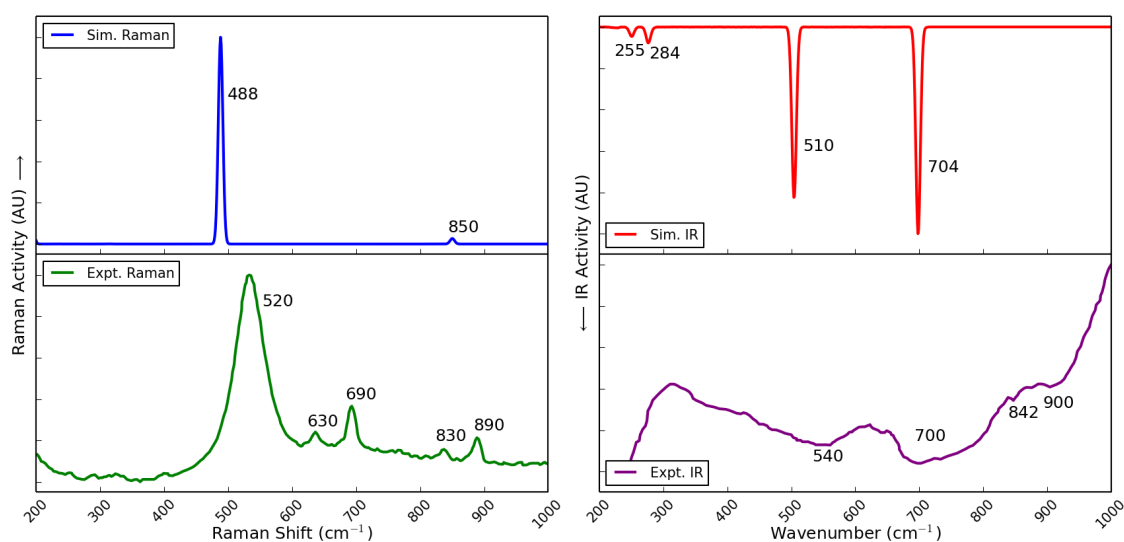
Figure 5.8: The experimental and simulated Raman and IR spectra of the distorted C2/c structure of δ-UO$_3$. No previous Raman spectra have been published for this phase. The experimental IR spectrum has been published by Allen *et al.* [80]. The intensity and absorption axes are plotted on an arbitrary scale. An analysis of the vibrational modes in this spectrum is given in Figure C.3 and Table C.3.

As noted in Section 5.2.2, the simulated spectra for the 4-atom δ-UO$_3$ structure did not contain any Raman active modes, which directly contradicts the experimental Raman spectrum provided by Allen. In contrast, the simulated Raman spectrum of the 16-atom unit cell showed good agreement to the experimental spectrum, supporting the validity of the distorted structure. This structure also contains short uranyl-like bonds, which produce characteristic modes in the vibrational spectra. The simulated and experimental Raman and IR spectra of δ-UO$_3$ are presented in Figure 5.8, while Figure C.3 and Table C.3 detail each vibrational motion within the spectrum of this phase.

The experimental and simulated Raman spectra δ-UO$_3$ are dominated by peaks at 520

and 488 cm^{-1}, respectively. This band in the simulated spectrum is attributed to the uranyl symmetric stretching mode. The lower wavenumber compared to aqueous uranyl cations may be explained by the infinite chain of U-O bonds, which weakens the uranyl-like bonds in this structure. A similar explanation can be made for the uranyl anti-symmetric stretching mode at 704 cm^{-1} in the simulated spectrum, which is observed as a broad band at $\sim$700 cm^{-1} in Allen's IR spectrum and a lower intensity mode at $\sim$690 cm^{-1} in the corresponding Raman spectrum. A broad band is also observed in the experimental IR spectrum at $\sim$540 cm^{-1}, which may be attributed to the antisymmetric stretching motion of the longer (2.1 Å) O-U-O bonds seen at 504 cm^{-1} in the simulated spectrum. The correlation between experimental and simulated spectra supports the existence of the distorted δ-UO$_3$ structure, which may be proven by future structural investigations.

5.3.3 α-UO$_3$
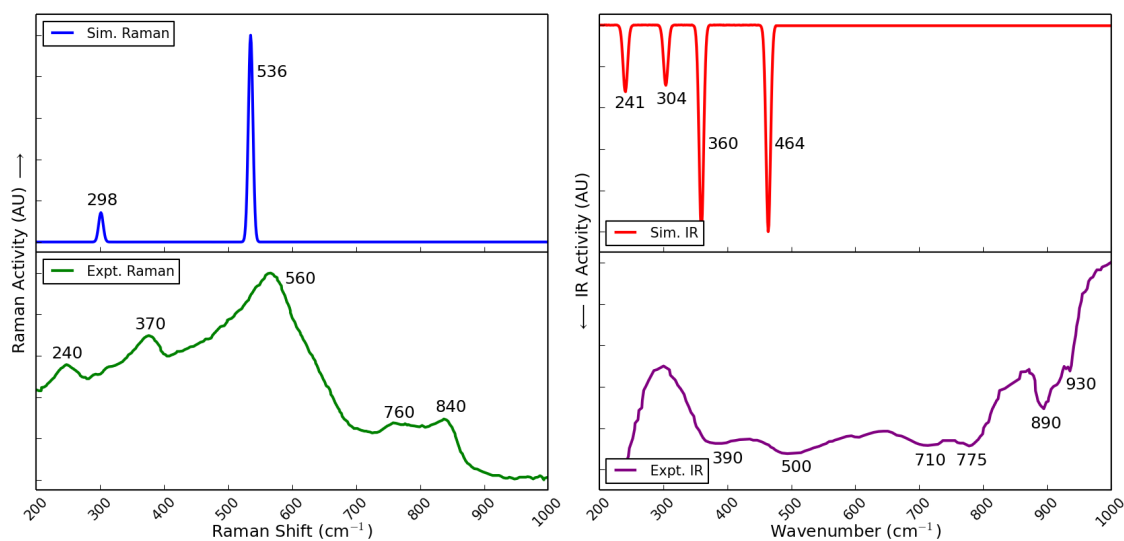
Figure 5.9: The experimental and simulated Raman and IR spectra of α-UO$_3$. The experimental IR spectrum has been published by Allen *et al.* [80] and shows good agreement to other experimental data [64, 196]. The Raman active peaks also agree with those predicted by Tsuboi *et al.* [64]. The intensity and absorption axes are plotted on an arbitrary scale. An analysis of the vibrational modes in this spectrum is given in Figure C.4 and Table C.4.

The minimised crystal structure for α-UO$_3$ retains the same space group as the experimental equivalent, P$\bar{3}$m1 [170]. The most notable structural differences are a shortening of the equatorial U $-$ O$_{eq}$ bonds and less distortion of the O$_{eq}$ ions from the equatorial plane. The simulated Raman and IR spectra contain peaks in similar positions to those seen experimentally, which supports the quality of the model. However, the structure of

α-UO$_3$ is known to be defective, so it may be inferred that the non-stoichiometry causes a shortening in the U $-$ O$_{eq}$ bonds. The simulated and experimental Raman and IR spectra of α-UO$_3$ are presented in Figure 5.9, while Figure C.4 and Table C.4 detail each vibrational motion within the spectrum of this phase.

The experimental Raman spectrum of α-UO$_3$ provided by Allen is dominated by a broad peak at $\sim$560 cm^{-1}. This band is assigned to the simulated mode at 536 cm^{-1}, which corresponds to a U $-$ O$_{eq}$ stretching motion. The E_g symmetry label attributed to this motion is equivalent to the interpretation given by Tsuboi *et al.* [64], who estimated this mode to be at 545 cm^{-1} based on the combination modes in the IR spectrum. The Raman peak at $\sim$240 cm^{-1} in Allen's spectrum and the 244 cm^{-1} IR peak seen by Tsuboi *et al.* both show good agreement to the simulated mode at 241 cm^{-1}, which corresponds to a O$_{ax}$ $-$ U $-$ O$_{ax}$ bending mode. It is possible that this peak became Raman active due to deviation from perfect stoichiometry.

The peaks observed around 890 cm^{-1} in the experimental IR spectra published by Allen and Holmes [80] and Tsuboi *et al.* [64] do not correspond to any bands in the simulated spectra. It is possible is that these peaks correspond to low level contamination by another phase, such as γ- or β-UO$_3$, which contain modes in this region.

5.3.4 β-UO$_3$

The minimised structure of β-UO$_3$ retains the P2$_1$ space group and five symmetrically distinct uranium environments found in the experimental structure [204, 205]. One difference is the greater homogeneity in the environments of the simulated structure, which all adopt a distorted octahedral coordination [55]. Uranyl-like bonding also emerges in three sites, resulting in characteristic uranyl stretching modes in the simulated vibrational spectra. Similar modes are also present in the experimental spectra, despite the lack of uranyl bonding reported. Simulated and experimental Raman and IR spectra of β-UO$_3$ are presented in Figure 5.10, while Figures C.5 and C.6 show the motions for each vibration within the spectrum of this phase.

β-UO$_3$ contains five symmetrically distinct uranium environments, which can perform different motions at a single frequency. These are described here as complex vibrations and are exemplified by the strong Raman active modes in the 680–878 cm^{-1} region of the simulated spectrum, attributed to combinations of uranyl symmetric and antisymmetric stretching modes. These modes may correspond to the strong bands in Allen's
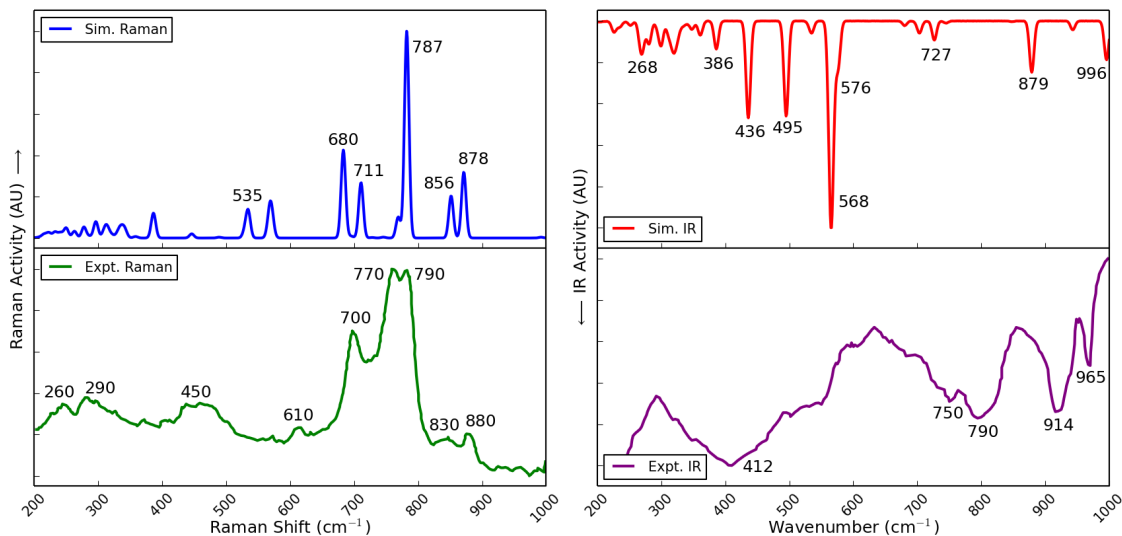
Figure 5.10: The experimental and simulated Raman and IR spectra of β-UO$_3$. No previous Raman spectra have been published for this phase. The experimental IR spectrum has been published by Allen *et al.* [80]. The intensity and absorption axes are plotted on an arbitrary scale. An analysis of the vibrational modes in this spectrum is given in Figures C.5 and C.6.

experimental spectrum at $\sim$700, 770 and 790 cm^{-1}. Another example is the strongest IR active mode in the simulated spectrum, observed at 568 cm^{-1}. This band involves the antisymmetric stretching of collinear O-U-O bonds and the bending of other U-O bonds.

Overall, there is less agreement between both structural and vibrational properties for experimental and simulated β-UO$_3$ compared to the other phases studied in this chapter. Brincat *et al.* suggested that these differences arise from disorder in the structure [55]. As the simulations correspond to a β-UO$_3$ structure with perfect stoichiometry, it is possible that the simulated spectra represent a stoichiometric sample well, but experimental samples may be stabilised by non-stoichiometry. Further computational studies may be performed to assess how defects in this structure affect the vibrational properties, improving the comparison to experimental data; however, this is not the aim of this chapter. Nevertheless, the presence of peaks in the experimental spectra that appear similar to simulated uranyl stretching modes suggest that uranyl bonding is present experimentally, perhaps to compensate for vacancies within the crystal structure.
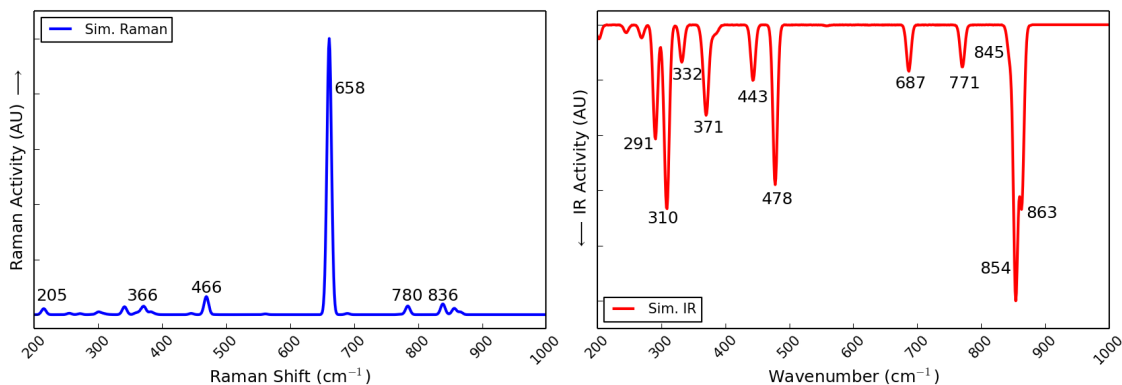
Figure 5.11: The simulated Raman and IR spectra of η-UO$_3$. No experimental spectra are available for this phase; however, the structural parameters were well reproduced in the simulation. The intensity and absorption axes are plotted on an arbitrary scale. An analysis of the vibrational modes in this spectrum is given in Figures C.8 and C.9.

5.3.5 η-UO$_3$

The space group of both experimental and minimised structures of η-UO$_3$ is P2$_1$2$_1$2$_1$ and the seven coordinate uranium environments, including uranyl-like bonds, are maintened after relaxation. These observed similarities suggest that the vibrational properties are also well reproduced; however, since no experimental Raman or IR spectra are available, these simulations are purely predictive. The simulated Raman and IR spectra are presented in Figure 5.11, while Figures C.8 and C.9 show the motions corresponding to each vibrational mode.

The simulated spectra of η-UO$_3$ display many trends observed for the other UO$_3$ phases. Uranyl symmetric stretching modes are found in the 658–780 cm^{-1} region, antisymmetric stretches are within the 836–863 cm^{-1} region and bending modes are below 400 cm^{-1}. The symmetric stretch is at a lower wavenumber than that observed for γ-UO$_3$, resulting from the uranyl oxygen ions coordinating to neighbouring uranium ions, weakening the uranyl bonds. However, these U-O interactions are at a significant distance ($>$2.5 Å) and do not form an extended chain of bonds, so the peak is not found as low as the corresponding mode in δ-UO$_3$.

A single unit cell of η-UO$_3$ contains four uranium environments, all symmetrically equivalent but capable of independent vibrations. For every vibrational mode in the simulated spectra, all environments undertake the same motion, but different environments may vibrate in- or out-of-phase with one another. This often affects the Raman and IR activities for each mode, which depend on the changes in polarisability and dipole moment,

respectively, that occur for the entire structure. For example, some modes expected to be Raman active (e.g. uranyl symmetric stretching mode) may instead be IR active.

5.3.6 Characteristic Uranyl Vibrations in UO_3 Polymorphs

Uranyl-like bonding has been found in the minimised structures of β, γ, δ and η-UO_3. Consequently, characteristic uranyl symmetric stretching modes have been observed in the simulated Raman spectra for these phases. In free uranyl cations, the symmetric stretch is typically found in the 750–900 cm^{-1} region; however, the exact position depends upon the local environment around the uranyl cation. In the simulated spectra of different UO_3 phases, the uranyl symmetric stretching mode has been found between 478–878 cm^{-1} (Table 5.2); the environments that give rise to different shifts are discussed here.

Table 5.2: The uranyl symmetric stretching modes in the simulated Raman and IR spectra for the different uranium environments in four phases of UO_3. The frequency of each symmetric stretch is given alongside the uranium coordination number and U-O bond distances for the environments.

Phase	β-UO_3			γ-UO_3		δ-UO_3	η-UO_3
Environment	1	4	5	1	2	—	—
U Coordination	6	6	6	6	6	6	7
U-O bond distance (Å)	1.81	1.76	1.76	1.87	1.78	1.90	1.83
Symmetric stretching mode frequencies (cm^{-1})	856	856	878	732	823	478	780
	787	787			860		771
	535				761		687
							658

The effect of different local environments on the uranyl symmetric stretching mode position may be described using the two distinct uranium sites in γ-UO_3. The first environment contains a uranyl group in which the uranyl oxygen ions are each coordinated to a second uranium ion, which weakens the uranyl bond and results in a uranyl symmetric stretching vibration at 732 cm^{-1}. In the second environment, the uranyl oxygen ions are not coordinated to other ions, so the corresponding stretching mode is found at 823 cm^{-1}. Similar shifts are seen in some environments of β-UO_3, for which the uranyl symmetric stretching modes are observed between 680–878 cm^{-1}, and η-UO_3, which produces a stretch at 658 cm^{-1}. The lowest wavenumber uranyl symetric stretching mode is found at 488 cm^{-1} in the spectrum of δ-UO_3. Within the structure, an extended chain of U-O bonds exist, so every uranyl oxygen ions is also strongly coordinated to a second uranium ion. Therefore, the uranyl bonds are weakened significantly, which lowers the wavenumber of the stretching mode.

The trend observed across the UO_3 phases that contain uranyl bonding is that the position of the uranyl symmetric stretching mode in the spectrum shifts to a lower wavenumber when the bond is weakened. A weakening of the uranyl bond has been shown to occur when uranyl oxygen ions are coordinated to additional uranium ions. As a consequence, the strongly coordinated oxygen ions in the δ-UO_3 structure result in the lowest uranyl symmetric stretching mode, while the free oxygen ions in γ-UO_3 produce the highest symmetric stretching mode.

5.4 Conclusions

In this chapter, vibrational properties have been simulated for α-, β-, γ-, δ- and η-UO_3, using density functional theory (DFT) and initial structures that were minimised by Brincat *et al.* [55]. The simulated spectra were compared against unpublished experimental Raman data, provided by Allen, and experimental IR data published by Allen and Holmes [80]. Of note, no Raman spectra have been previously published for β- and δ-UO_3, so this is new data. Futhermore, no experimental spectra are available for η-UO_3, but since the structure is well reproduced, the simulated spectra are considered good predictions. Creating an extensive database of experimental and simulated properties for every phase of UO_3 would be valuable to forensic and environmental investigations. It would allow unknown materials to be identified and, since the phase of UO_3 is dependent upon the conditions it was formed under, may allow the origin of an unknown sample to be determined. In addition, a number of discrepancies were found between different experimental spectra, which may arise from the presence of multiple phases; confidence in the simulated spectra would provide a means to investigate what is present in a mixed sample.

One of the most significant obervations was for the 4-atom structure of δ-UO_3: the simulated spectrum showed no Raman activity, in contrast to the experimental spectrum. An alternative distorted 16-atom simulated unit cell was instead found to produce a set of Raman active modes with good agreement to the experimental spectrum. Therefore, an experimental revision of the δ-UO_3 structure may be valuable.

The simulated spectra of the stable γ-UO_3 phase were found to show good agreement to experimental spectra, whereas spectra for the structures that changed significantly when minimised (α- and β-UO_3) were less well reproduced. The latter phases have been reported as defective [54, 55], so it follows that simulations of the stoichiometric structure do not accurately reproduce experimental data. However, some similarities are found,

such as the presence of strong experimental peaks in the region where uranyl stretching modes are observed in the simulated Raman spectrum of β-UO$_3$. This indicates that uranyl bonding is present in the structure, despite it not being detected experimentally.

In the spectra of δ- and η-UO$_3$, the uranyl symmetric stretching modes are found at lower wavenumbers compared to β-UO$_3$, which results from neighbouring environments coordinating to the uranyl oxygen ions, weakening the uranyl bond. Separate uranyl stretches were also observed for γ-UO$_3$, where one uranyl environment is constrained, but the second is not.

One discrepancy in the simulated spectra is the peak positions, which are always shifted relative to their experimental counterparts. This is an established effect of the DFT functional used, so changing functional may improve the comparison for phases with a well reproduced structure. However, this would not be an improvement for phases where the structure is less well represented; for an improvement in these cases, the non-stoichiometric structure would have to be simulated.

A major advantage of using computational methods to investigate vibrational properties is the ability to determine the motion for each mode in the spectrum. This is particularly valuable for larger phases, with multiple uranium environments per unit cell. In the cases of β- and γ-UO$_3$, there are symmetrically distinct uranium environments, which allow different types of vibration to occur at a single frequency. An example of this is the combined symmetric and antisymmetric stretching mode at 879 cm^{-1} in β-UO$_3$. In contrast, η-UO$_3$ and the 16-atom unit cell of δ-UO$_3$ contain symmetrically equivalent uranium environments, which always undertake the same vibration, but may perform them in- or out-of-phase. In both cases, the Raman or IR activity depends upon the overall motion across the structure, emphasising the need to consider the structure as a whole and demonstrating the value of computational techniques in analysing vibrational properties.

Chapter 6

A Raman Investigation of Uranyl Minerals from Cornwall

Raman spectroscopy has proven to be a powerful tool for distinguishing between uranyl minerals [29, 208–210]. The focus of this chapter is to investigate the possibility of using Raman for nuclear forensic research. The minerals studied are uranyl minerals, which are named for the uranyl cation (UO_2^{2+}) they contain, where uranium exists in the U^{6+} oxidation state. The cation forms from the weathering of uranium oxides, both from natural deposits and products from the nuclear fuel cycle [29]. Its solubility and mobility means that soil and water contamination presents a significant risk to the health of humans and animals in the area [14–18]. However, the cation is susceptible to reaction with many inorganic materials, which immobilise the cation by forming uranyl minerals [6, 20–28].

Over 200 uranyl minerals have been observed in nature, where the exact composition of the sample is dependent on the chemical environment [56]. Many of these minerals adopt a layered structure, including the majority studied in this chapter, but others are comprised of clusers or 3D frameworks. The relationship between local conditions and the uranyl minerals formed presents a valuable opportunity for nuclear forensics, as knowledge of the minerals formed, their composition and even the host rock may be combined to build a unique dataset pertaining to the sample's origin. For this investigation, a selection of uranyl minerals from Cornwall, UK were collected by Elton and Hooper [211–213] and studied using Raman and EDX spectroscopy. A list of these samples and corresponding chemical formulae taken from the literature is given in Table 6.1. In this chapter, the possibility of using Raman to distinguish between different uranyl minerals is discussed. To accomplish this, a consistent procedure (Section 2.1.6) was used to collect and analyse Raman data for all samples. The research presented here has been published in RSC Advances, in an article entitled *'A Raman Spectroscopic Study of Uranyl Minerals from Cornwall'* [206]. Before discussing the results, it is useful to consider previously published literature pertaining to the concepts discussed in this chapter.

Table 6.1: The uranyl mineral samples investigated in the present study. The majority of samples were collected from locations in Cornwall, UK. Chemical formulae from literature sources are given for each mineral.

Mineral Name	Literature Formula	Provenance
Autunite	$Ca(UO_2)_2(PO_4)_2 \cdot 11H_2O$ [214, 215]	Merrivale Quarry, Tavistock [†] [216]
Torbernite	$Cu(UO_2)_2(PO_4)_2 \cdot 12H_2O$ [217]	Bunny Mine, Stenalees, St. Austell [218]
Zeunerite	$Cu(UO_2)_2(AsO_4)_2 \cdot 12H_2O$ [219]	Wheal Gorland, Redruth [218]
Nováčekite	$Mg(UO_2)_2(AsO_4)_2 \cdot 10H_2O$ [220]	Wheal Edward, St. Just [212, 221]
Phosphuranylite	$Ca(UO_2)_3(PO_4)_2(OH)_2 \cdot 6H_2O$ [221]	Wheal Edward, St. Just [221]
Andersonite	$Na_2Ca(UO_2)(CO_3)_3 \cdot 6H_2O$ [222]	Geevor Mine, Pendeen [213, 221]
Schröckingerite	$NaCa_3(UO_2)(CO_3)_3(SO_4)F \cdot 10H_2O$ [223]	Geevor Mine, Pendeen [213, 221]
Johannite	$Cu(UO_2)_2(OH)_2(SO_4)_2 \cdot 8H_2O$ [224]	Geevor Mine, Pendeen [213]
Natrozippeite	$Na_5(UO_2)_8(SO_4)_4O_5,(OH)_3 \cdot 8H_2O$ [225]	Geevor Mine, Pendeen [221]
Uranophane	$Ca(UO_2)_2(SiO_3OH)_2 \cdot 5H_2O$ [226]	Wheal Edward, St. Just [211]
Cuprosklodowskite	$Cu(UO_2)_2(SiO_3OH)_2 \cdot 6H_2O$ [227]	West Wheal Owles, St. Just [211]
Kasolite	$Pb(UO_2)(SiO_4) \cdot H_2O$ [228]	Loe Warren Zawn, St. Just [229]
Compreignacite	$K_2(UO_2)_6O_4(OH)_6 \cdot 7H_2O$ [230]	West Wheal Owles, St. Just [211]

[†] Merrivale Quarry is located in the county of Devon, UK.

6.1 Review of Literature on Uranyl Minerals

In this section, the major structural features of each group of uranyl minerals are described, in addition to a review of the literature pertaining to structural and vibrational properties. The most extensive set of investigations using Raman spectroscopy have been performed by Frost *et al.* [29, 208–210], which include low temperature studies [57] and investigations into the dehydration process [58, 70, 87, 88]. They used a consistent procedure when collecting Raman data, which is necessary if a comparison is to be made between different samples. As the crystal structures adopted by uranyl minerals are comprised of subunits, specifically the uranyl cation and a variety of polyanion groups, previous spectra have been interpreted as a combination of bands arising from the component polyions. Therefore, the vibrational properties of aqueous ions have been presented in Section 1.3.2. The position of the uranyl symmetric stretching mode has also been linked to the length of the uranyl bond by the Bartlett and Cooney relation, described in Section 6.1.1.

Autunite Group of Uranyl Phosphates and Arsenates

The largest and most diverse type of uranyl minerals are the uranyl phosphates and arsenates [56, 231, 232]. These minerals may be separated into subcategories based upon the topology of the layers, the most significant being the autunite minerals, also known as the uranyl micas [219, 220, 233, 234]. Autunite minerals have been shown

as promising candidates for immobilisation of the uranyl cation in contaminated sites, due to their comparatively low solubility [25–28, 235, 236]. Therefore, understanding the chemical processes of these minerals is of great value to studies involving nuclear forensics and environmental remediation.

Autunite minerals adopt a layered structure, with uranium square bipyramidal environments sharing equatorial vertices with phosphate or arsenate tetrahedra [69, 214, 237–240] (Figure 6.1). Charge compensating cations and water molecules are found in the interlayer space. These minerals adopt the general formula $M(UO_2)_2(XO_4)_2 \cdot nH_2O$, where M are the cations, X is P or As and n represents the number of water molecules. The level of hydration is variable and depends upon the local conditions. In a fully hydrated autunite mineral, $n \approx 10$ or 12, whereas the dehydrated equivalents, known as metaautunite minerals, are typically $n \approx 8$ or 6 [69, 241, 242]. This propensity for dehydration necessitates the use of low impact analytical techniques, such as Raman spectroscopy, that don't change the hydration level during observation.
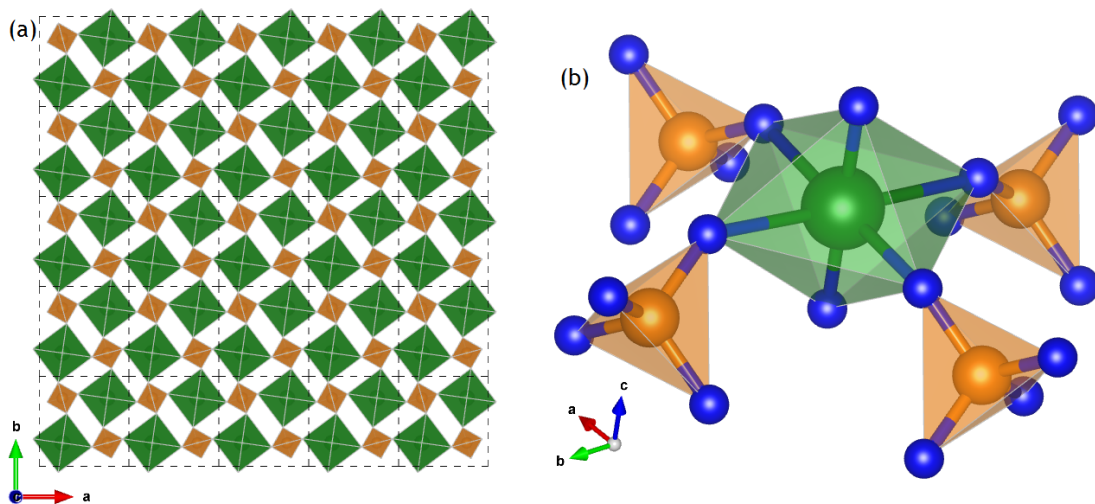
Figure 6.1: a) The characteristic autunite layered structure, found in autunite, torbernite, zeunerite, saléeite and nováčekite. b) The uranium environment in autunite minerals. Green, orange and blue represent uranium, phosphorus and oxygen, respectively.

As noted, the autunite group of minerals is diverse, containing a range of uranyl phosphates, including torbernite [217], saléeite [243], autunite [214, 215] and sabugalite [233], as well as uranyl arsenates, such as zeunerite [219], nováčekite [220], metauranospinite [244] and metakirchheimerite [245]. Autunite minerals are also widespread, with samples originating in Australia, the Czech Republic, France, America, the UK [69], Portugal [236] and the Congo [14]. The minerals described in this chapter all originated from mines in Cornwall, UK, with the exception of autunite, which was collected in

the neighbouring county of Devon. The chemical formula and provenance for all uranyl minerals studied in this chapter are given in Table 6.1.

The infrared spectra of many autunite minerals has been collected by a number of authors [59, 73, 238–240, 246–248]. Čejka *et al.* commented that the oxyanions within uranyl minerals lend them to vibrational spectroscopy [238]. More recently, Frost *et al.* utilised Raman spectroscopy to study a selection of autunite minerals [57, 69, 244, 249, 250]. The major bands found in the Raman spectra were uranyl symmetric stretches in the 809–833 cm^{-1} region, and phosphate antisymmetric stretches in the 957–1093 cm^{-1} region. Some difficulty was noted when interpreting the arsenate equivalents, as the arsenate symmetric and antisymmetric stretches overlap with the uranyl symmetric stretch. Further investigations also used Raman to study the dehydration processes involved in the formation of metaautunite minerals [58, 70, 87, 88]. Raman spectroscopy has also been performed on synthetic samples of autunite minerals metatorbernite, metauranocircite ($Ba(UO_2)_2(PO_4)_2 \cdot nH_2O$) and a mixed phase by Sánchez-Pastor *et al.* [251]. The first Raman spectrum of the uranyl arsenate mineral nováčekite was published in the paper corresponding to this chapter [206].

Phosphuranylite Group of Uranyl Phosphates and Arsenates

The second most common group of uranyl phosphate and arsenate minerals are those with the phosphuranylite sheet structure [252]. There are 16 minerals in this group with known crystal structures, including bergenite, phurcalite, dewindtite, dumontite, phosphuranylite and yingjiangite [231, 232, 253, 254].

The phosphuranylite layered topology is more complex than that seen for the autunite group; here, uranium is found in pentagonal and hexagonal bipyramids (Figure 6.2a and c), which share edges with phosphate (or arsenate) tetrahedra and O^{2-} anions [56, 252, 255–259]. Further uranium polyhedra are present in square bipyramids that connect adjacent layers (Figure 6.2b and d), meaning all three types of uranyl coordination environments are present [231, 260, 261]. Charge compensating cations (Ca^{2+} and K^+ in phosphuranylite) and water are located in channels within the framework.

The composition of phosphuranylite appears to be variable, with multiple chemical formulae reported:

- Demartin *et al.* [255] reported $(K,Ca)(H_3O)_3(UO_2)_7(PO_4)_4O_4 \cdot 8H_2O$;
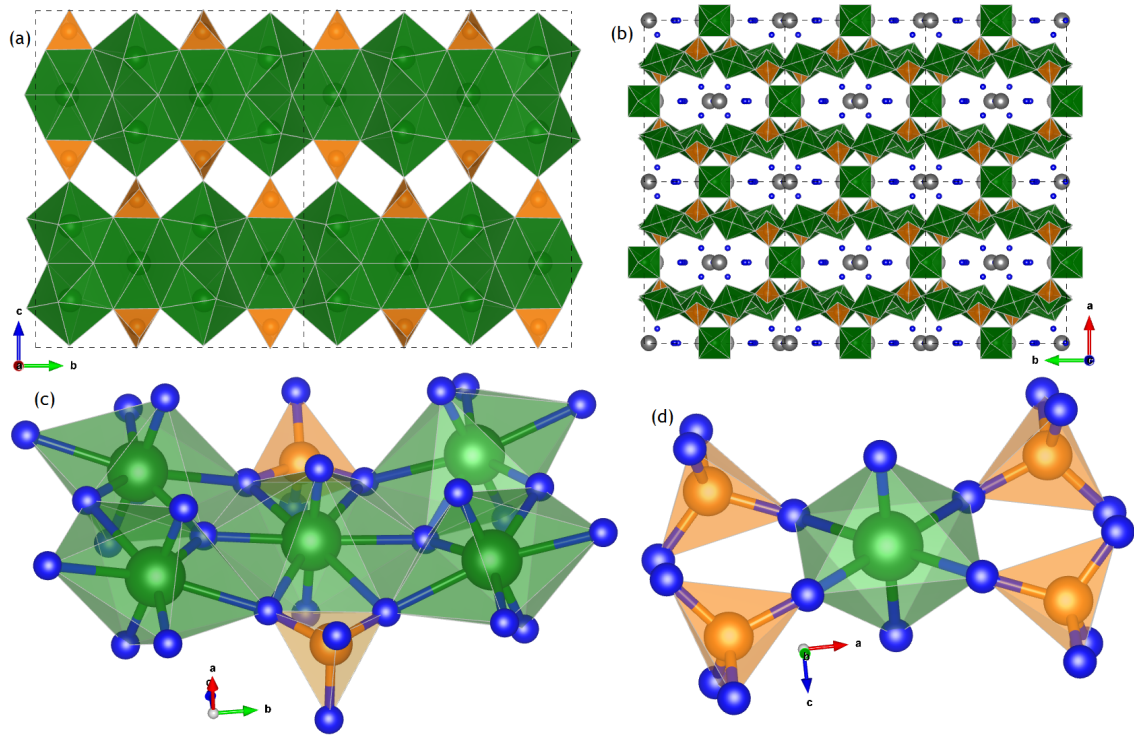
Figure 6.2: (a and b) Two views of the phosphuranylite layered structure. c) The hexagonal and pentagonal bipyramidal environments and d) the square bipyramidal environments found in phosphuranylite. Green, orange, blue and grey represent uranium, phosphorus, oxygen and calcium, respectively.

- Piret *et al.* [262] reported $Ca(UO_2)_7(PO_4)_4(OH)_4 \cdot 12H_2O$;

- Zhang *et al.* [260] reported $(K_2,Ca)(UO_2)_7(PO_4)_4(OH)_6 \cdot 6H_2O$;

- Ryback and Tandy [221] reported $Ca(UO_2)_3(PO_4)_2(OH)_2 \cdot 6H_2O$.

The sample described by Ryback and Tandy was collected from Wheal Edward, St. Just, Cornwall, UK, which is the same mine that the sample used in this study was taken from. Therefore, the representative formula provided in Table 6.1 corresponds to Ryback and Tandy's formula. A similar mineral, yingjiangite, has been described by a number of authors $(K_{1.3}Ca_{0.7}(UO_2)_6(PO_4)_4(OH)_{2.7} \cdot 8H_2O)$ [253, 256, 260]; however, the similarities in structure and composition have led to suggestions that yingjiangite and phosphuranylite are identical [263, 264].

A number of authors have investigated the vibrational properties of phosphuranylite and yingjiangite using IR spectroscopy [256, 265, 266]. A more recent set of studies by Frost *et al.* has provided the Raman spectra for samples of phosphuranylite [267], dumontite [268], bergenite [68] and phurcalite [269]. The investigation of phosphuranylite

86

included three samples, originating from Minerva Heights and Saddle Ridge Mine in South Australia and Ruggles Mine in the USA [267]. The Raman spectra for the Saddle Ridge Mine and Ruggles Mine samples were dominated by uranyl symmetric stretching modes in the 812–847 cm^{-1} region and phosphate antisymmetric stretching modes in the 1000–1056 cm^{-1} region. However, differences were found in the Raman spectrum taken for the Minerva Heights sample, in which the uranyl and phosphate stretching modes were in the 805–815 cm^{-1} and 992–1016 cm^{-1} regions, respectively. This corroborates the variability observed in the composition of phosphoruranylite and emphasises the need to study samples from a variety of locations.

Uranyl Tricarbonates

Uranyl carbonate minerals may be categorised based on the number of carbonate anions (CO$_3^{2-}$) within each formula unit [56]. For example, rutherfordine is a uranyl monocarbonate [61], zellerite is a uranyl dicarbonate [270] and voglite is a uranyl tricarbonate [77]. The uranyl tricarbonates are the most thoroughly studied actinyl (VI) carbonate solids [271, 272]; the two uranyl carbonate minerals described in this chapter, andersonite and schröckingerite, are both uranyl tricarbonates. The samples studied here were collected from Geevor Mine, Cornwall, UK, but uranyl carbonates from other locations, including the Czech Republic and USA have been investigated [77, 270]. Furthermore, many uranyl carbonates have been synthesised [273–275]. Table 6.1 contains the chemical formulae for both andersonite and schröckingerite.

Uranyl tricarbonates are characterised by uranium in a hexagonal bipyramidal environment, where the equatorial vertices belong to the three bidentate carbonate anions (UO$_2$(CO$_3$)$_3$) [276–279]. The uranyl tricarbonate clusters in andersonite form a complex framework (Figure 6.3a), connected by cation polyhedra (Na and Ca) [222]. In contrast, schröckingerite is a multi-anion mineral (Figure 6.3b), composed of layers of UO$_2$(CO$_3$)$_3$, SO$_4$ and NaO$_6$ [223]. Water molecules are found within channels in andersonite and the interlayer space in schröckingerite, held in place by hydrogen bonding [222, 231, 280, 281].

The IR spectrum of many uranyl carbonates, including andersonite and schröckingerite, have been extensively studied [275, 277, 280, 282–285]. More recently, Frost *et al.* have performed Raman spectroscopy on samples of andersonite [286] and schröckingerite [76], both from the USA, in addition to rutherfordine [61], zellerite [270], voglite [77], liebigite [287], kamotoite-(Y) [288] and wyartite [289]. The Raman spectrum of andersonite was found to be dominated by the uranyl symmetric stretch at 831 and 832 cm^{-1} and the carbonate symmetric stretch at 1080 and 1092 cm^{-1} [286]. Equivalent modes in
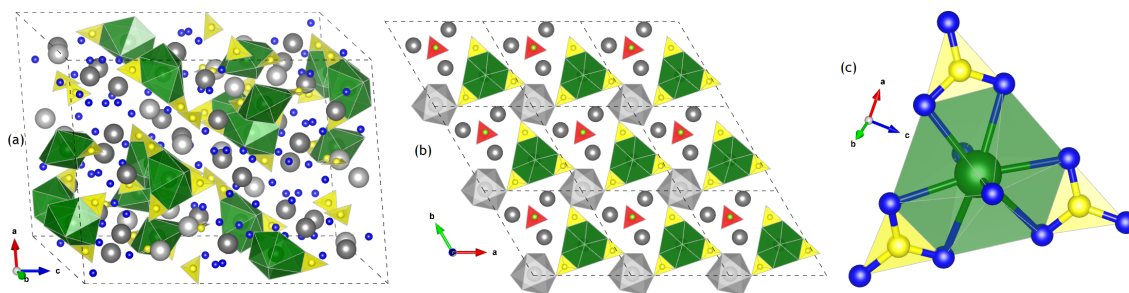
Figure 6.3: a) The complex framework structure in andersonite and b) the layered structure found in schröckingerite. c) The uranyl tricarbonate cluster found in both environments. Green, yellow, blue, red, pale green and grey represent uranium, carbon, sulphur, oxygen, fluorine and the divalent cations (Ca and Na), respectively.

schröckingerite were found at 815 and 1092 cm^{-1}, respectively, while the sulphate anion gives rise to an additional symmetric stretch at 983 cm^{-1} [76].

Uranyl Sulphates

The two uranyl sulphate minerals studied in this chapter are johannite and natrozippeite (also known as sodium zippeite). Table 6.1 includes chemical formulae for both minerals. Natrozippeite is the most common member of the zippeite group of uranyl sulphates, which includes the minerals potassium zippeite [290], pseudojohannite and magnesium-zippeite [75]. Natrozippeite has been found in the Czech Republic [291, 292] and Switzerland [293], while the sample studied in this chapter originated from Geevor Mine, Cornwall, UK [294]. The sample of johannite used in this chapter was also collected from Geevor Mine, but it has also been identified in Saint Agnes, Cornwall and Australia [295].

The uranium ions in johannite are all found in an identical pentagonal bipyramidal environment (Figure 6.4a and c), where three vertices are shared with sulphate tetrahedra and the remaining two are hydroxide anions that act as bridges between pairs of uranyl polyhedra [56, 224, 295]. These groups form a layered structure, with copper cations coordinating to uranyl oxygen atoms in adjacent layers. This structure and composition have been confirmed for both natural and synthetic samples [296–299].

Zippeite minerals also contain uranyl pentagonal bipyramidal environments (Figure 6.4b and d), but here two equatorial vertices are shared with sulphate tetrahedra and the remainder are coordinated to oxygen or hydroxide anions [56]. These layers are topologically identical in every zippeite mineral [225, 237, 281] and always contain a 2:1 ratio of U:S [75, 225, 300]. However, the exact distribution of O^{2-} and OH$^-$ anions in the layer can vary, allowing the sheets to accomodate cations with different charges in
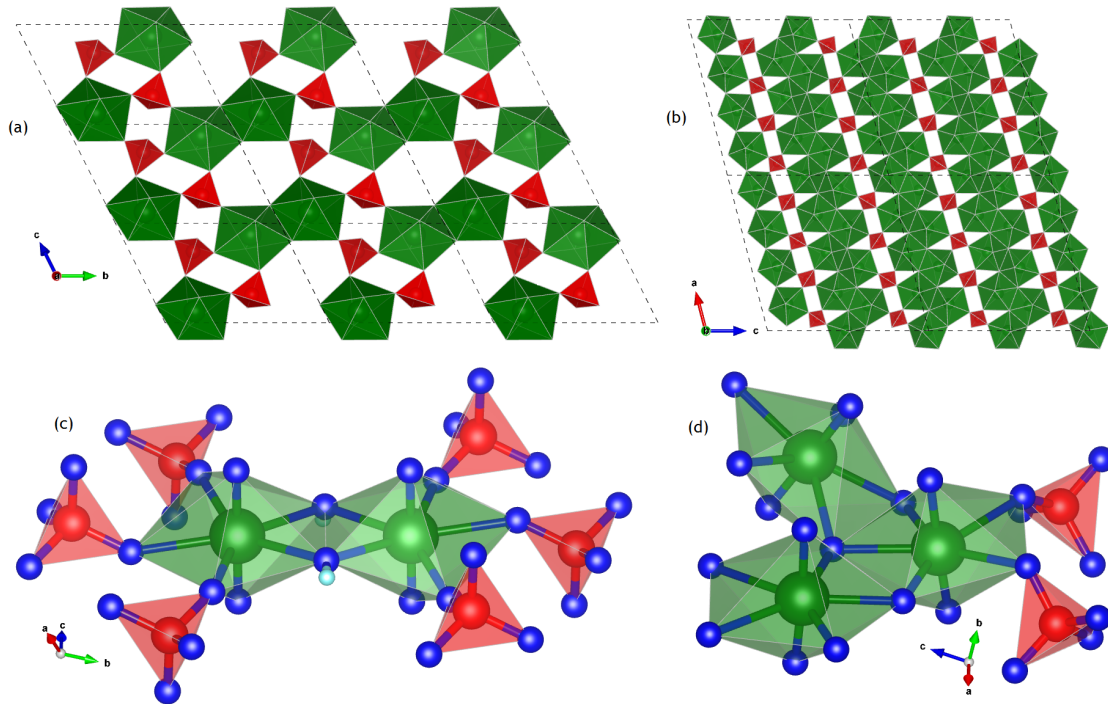
Figure 6.4: The layered structures found in a) johannite and b) natrozippeite. The uranium environments in c) johannite and d) natrozippeite. Green, red and blue represent uranium, sulphur and oxygen, respectively.

the interlayer (e.g. K^+, Na^+, Mg^{2+} and Zn^+) [301]. It has also been noted that the proportion of interlayer cations in zippeite minerals is always lower than expected [302], possibly resulting from the relatively large interlayer, which is primarily held together by a hydrogen bonding network [225]. The original chemical formula given for natural and synthetic natrozippeite was $Na_4[(UO_2)_6(SO_4)_3(OH)_{10}]\cdot 4H_2O$ [303], while a more recent synthetic study found the formula to be $Na_5(H_2O)_{12}[(UO_2)_8(SO_4)_4O_5(OH)_3$ [225]. As the sample in this investigation was collected from a naturally occurring deposit, the former formula is presented in Table 6.1.

The IR spectra have been published for johannite [296, 304] and a number of natural and synthetic zippeite samples [266]. Frost *et al.* have applied Raman spectroscopy to the study of johannite from St. Agnes, Cornwall, UK [295], natrozippeite from Happy Jack Mine, USA [300], pseudojohannite [75] and uranopilite [305]. The Raman spectrum of potassium zippeite has also been presented by Plášil *et al.* [306]. Characteristic uranyl symmetric stretching modes were observed at 786 and 811 cm^{-1} for johannite and in the 823–841 cm^{-1} region for natrozippeite [295, 300]. Bands corresponding to the symmetric and antisymmetric stretch of the sulphate polyanion were found at 1042 and 1090–1147 cm^{-1}, respectively, for both johannite and natrozippeite.

Uranophane Group of Uranyl Silicates

The mineral uranophane has been described as one of the most common uranium minerals, after uraninite [307]. Indeed, minerals with the uranophane layered topology have been shown to form from the alteration of spent nuclear fuel under the conditions found in a geological repository [308–311]. These minerals are of further importance as the structure may incorporate a number of other radionuclides, such as Np, Cs or Sr [312–314], potentially controlling the release of radionuclides into the environment surrounding the repository [315–317].

Within the uranophane layers, uranium is found in a pentagonal bipyramidal environment (Figure 6.5), which shares equatorial verices with three silicate tetrahedra and an edge with a fourth anion [56, 226, 318, 319]. This provides a 1:1 ratio of U:Si. The silicate anion in most uranophane minerals has been described as acidic (SiO_3OH), with the hydroxyl group oriented into the interlayer space [246, 266, 272, 320] and participating in the hydrogen bonding that links the layers [231, 237, 321]. An exception is the mineral kasolite, which instead contains SiO_4^{4-} anions [228]. Charge compensating cations (Ca^{2+}) and water are located in the interlayer space, held by interatomic forces [226].
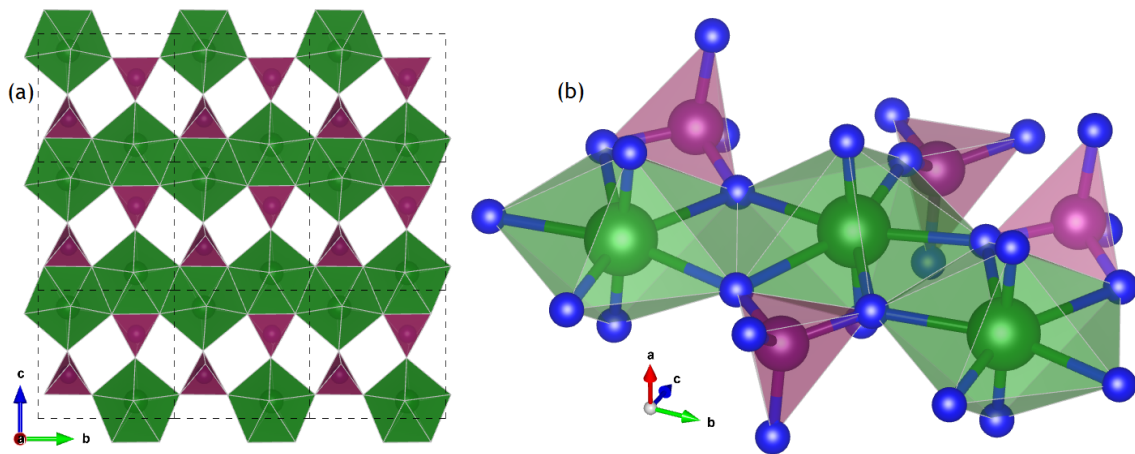
Figure 6.5: a) The layered structure and b) the uranium environment found in the uranophane minerals. Green, purple and blue represent uranium, silcon and oxygen, respectively.

It should be noted that uranophane forms two polymorphs [231]. The polymorph of interest here is α-uranophane, whereas β-uranophane adopts a different structure. In addition to α-uranophane [226], the minerals kasolite [228] and cuprosklodowskite [227] are studied in this chapter. The chemical formulae for all three minerals are given in Table 6.1. Other members of the uranophane group include sklodowskite, boltwoodite and oursinite [237, 281]. These minerals have been located in the USA, Congo [307], Australia

and Namibia [78], while the samples studied in this chapter originated from West Wheal Owles, Wheal Edward and Loe Warren Zawn in St. Just, Cornwall, UK [211, 229]. A number of synthetic uranyl silicates have also been described [322, 323].

IR spectra have been reported for a selection of natural uranyl silicates and synthetic equivalents [324], as summarised by Čejka [266]. The Raman spectra have also been published [78, 325], with an investigation by Frost *et al.* studying uranophane (with traces of boltwoodite) from the USA and Congo [307]. The characteristic uranyl symmetric stretching mode is typically found between 750–850 cm^{-1} for uranyl silicates, with reported values of $\sim$797, 787–812 and 759 cm^{-1} for uranophane, cuprosklodowskite and kasolite, respectively [78]. The silicate symmetric stretching mode was also observed in the Raman spectra at 961, 974 and 904 for uranophane, cuprosklodowskite and kasolite, respectively.

Uranyl Oxide Hydrates

The mineral compreignacite, studied in this chapter (chemical formula in Table 6.1), is a rare uranyl oxide hydrate [211, 326–328], found to form from the oxidation of UO_2 in spent nuclear fuel [308, 310, 315, 329]. It has also been observed as a product of the transformation of schoepite ($UO_3 \cdot 2.25H_2O$), another uranyl oxide hydrate [330, 331], while other investigations have found products like compreignacite form from the interaction of uranyl ions and synthetic zeolites [328]. Compreignacite is also suspected to incorporate other actinide elements, such as Cs, which may control their release into the local environment [315].

The layered structure seen in compreignacite and several other uranyl oxide hydrate minerals (Figure 6.6) is topologically similar to α-U_3O_8 (Figure 4.3), with uranium ions in a 2:1 ratio of pentagonal bipyramidal and square biyramidal environments [56, 230, 231, 332–334]. The equatorial vertices are a combination of O^{2-} and OH^- anions, with the exact distribution affecting the net charge of the layers and allowing the sheet to accomodate interlayer cations of various charges. Adjacent layers are held together through hydrogen bonding, which also determines the mobility of interlayer cations [281].

In addition to compreignacite and schoepite [335, 336], the α-U_3O_8 type layered topology is found in the minerals becquerelite [237, 337], billietite [338–340], curite [322, 341, 342] and vandendriesscheite [321]. A synthetic mineral, known as metaschoepite ($UO_3 \cdot 2H_2O$), has also been studied [343].
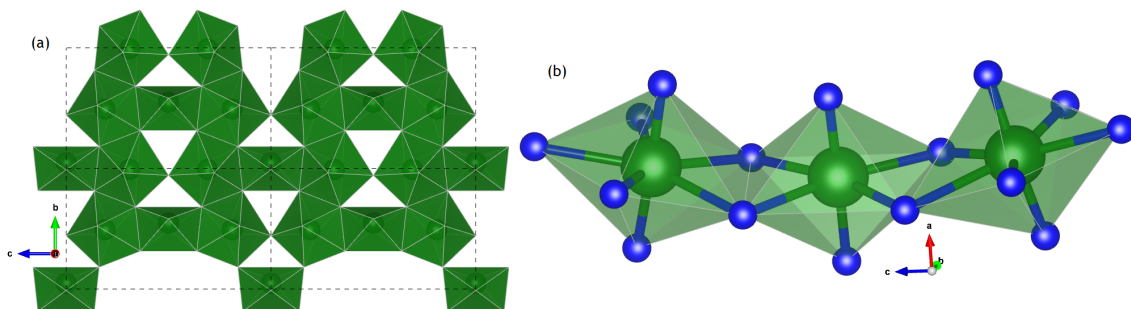
Figure 6.6: a) The layered structure and b) the square and pentagonal bipyramidal uranium environments found in the uranophane minerals. Green and blue represent uranium and oxygen, respectively. Note that the layered structure in compreignacite is equivalent to that found in U_3O_8 (Figure 4.3).

The IR spectra of compreignacite, becquerelite and schoepite and a number of synthetic phases have been presented [304, 344–347], while a variety of phases in the UO_3-H_2O system have been reviewed by Hoekstra and Siegel [348]. The Raman spectra of schoepite and a synthetic compreignacite equivalent have also been published [266, 349–351]. More recently, Frost *et al.* have performed Raman spectroscopy on a sample of compreignacite from Margna Mine, France [29], as well as on samples of becquerelite, billietite, curite, schoepite and vandendriesscheite from Australian sources [352]. The characteristic uranyl symmetric stretching mode was observed at 824 and 848 cm^{-1} for compreignacite [29]. While no polyanion groups are present in compreignacite, several modes were found in the 153–778 cm^{-1} region and attributed to the vibrations of a variety of subunits comprised of uranium, oxygen and hydrogen (e.g. U_3O and UOH). The sample of compreignacite studied in this chapter was collected from West Wheal Owles, Cornwall, UK [211].

6.1.1 The Bartlett and Cooney Relation

The Raman spectra of uranyl minerals are typically dominated by the uranyl symmetric stretching mode ($\nu_1(UO_2)^{2+}$). This peak may be found between 750–900 cm^{-1}, but the exact position varies with the strength and length of the uranyl bond and, by extension, the local chemical environment. The Bartlett and Cooney relation [353],

$$R_{\text{UO}} = 106.5[\nu_1(UO_2)^{2+}]^{-\frac{2}{3}} + 0.575 \text{ Å}, \tag{6.1}$$

was established to allow the length of a uranyl bond (R_{UO}) to be estimated from the position of the uranyl symmetric stretching mode seen in the Raman spectrum. This is particularly valuable when crystallographic techniques are unavailable or cannot be used to study a sample.

6.2 Results

The majority of uranyl mineral samples investigated were collected from Cornwall, UK, by Elton and Hooper, who used a combination of X-ray powder diffraction and EDX to identify the samples [211–213]. Table 6.1 shows the names, a chemical formula taken from literature sources and the provenance for each mineral sample. In Section 6.2.1, a physical description is provided for the mineral samples, alongside photographs. The EDX data collected in this investigation is presented and discussed in Section 6.2.2. The Raman spectra are then presented for each set of uranyl minerals. The uranyl and polyanion vibrations are of primary interest, hence, the 100-1200cm^{-1} region of each spectrum is illustrated. As discussed in Section 6.1, Frost *et al.* have published the Raman spectra of many uranyl minerals, so this information was used to verify the identity of the corresponding samples in this investigation. The trends observed for the uranyl and polyanion vibrations are the focus of Sections 6.3.1 and 6.3.2, respectively. Spectra obtained with different excitation wavelengths were found to produce varying proportions of background noise and fluorescence, so the spectrum presented for each mineral was chosen to minimise these effects. A discussion on spectra obtained using different wavelengths is given in Section 6.3.3. Multiple spectra were obtained for each sample and average values of peak positions are presented in the tables of Appendix D. The most relevant features are described in this section.

6.2.1 Physical Description

A short description of the observable physical features for each mineral sample studied in this chapter is given in this section, with photographs given in Figure 6.7. Brief comments on each crystal's habit are also made, based on SEM images, presented in Figure 6.8. The SEM images were collected as described in Section 2.2.

The sample of autunite from Merrivale Quarry, Tavistock, Devon, UK, appears as fine, yellow crystals on a white, grey and black host rock, which is ∼6 cm in diameter (Figure 6.7.a). Individual crystals are observed in the SEM in a foliated (layered) square plate habit, ∼100 μm across (Figure 6.8.a).

The sample of torbernite from Bunny Mine, Stenalees, St. Austell, Cornwall, UK, appears as green, tabular crystals, ∼600 μm across, on a grey and brown host rock, which is ∼11 cm in diameter (Figure 6.7.b). A foliated tabular crystal habit is observed in the SEM, with individual crystals ∼600 μm across (Figure 6.8.b).
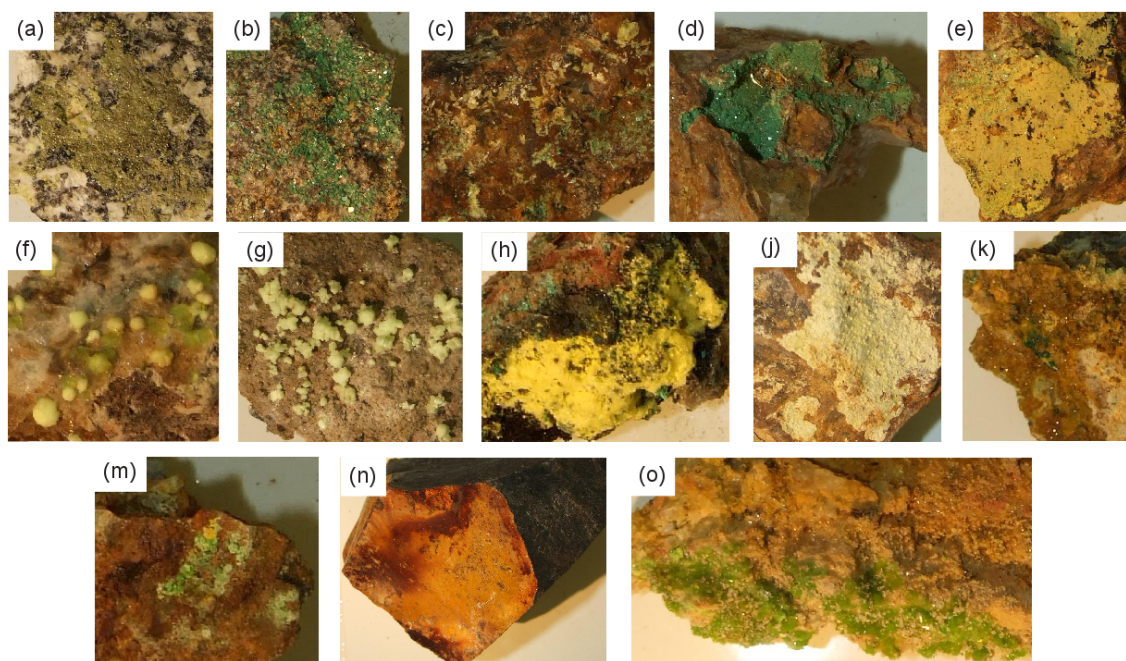
Figure 6.7: Photographs of the mineral samples studied in this chapter: a) yellow crystals of autunite; b) green crystals of torbernite; c) yellow flakes of nováčekite; d) green crystals of zeunerite; e) yellow crust of phosphuranylite; f) yellow aggregates of andersonite; g) pale yellow aggregates of schröckingerite; h) yellow crust of natrozippeite; j) yellow crust of uranophane; k) dark yellow crystals of compreignacite; m) pale green crystals of cuprosklodowskite; n) orange-red crust of kasolite and o) green crystals of johannite. The majority of samples are ∼4–7 cm in size.

The sample of nováčekite from Wheal Edward, St. Just, Cornwall, appears as yellow and green flakes on a black and brown host rock, which is ∼5 cm in diameter (Figure 6.7.c). The crystal habit appears as foliated plates in the SEM, ∼600 μm across (Figure 6.8.c).

The sample of zeunerite from Wheal Gorland, Redruth, Cornwall, appears as fine green crystals on a light brown host rock, which is ∼7 cm in diameter (Figure 6.7.d). Individual crystals appear in a foliated tabular habit, at least 300 μm across (Figure 6.8.d).

The sample of phosphuranylite from Wheal Edward appears as a yellow crust on a brown rock, which is ∼7 cm across (Figure 6.7.e). Individual crystals appear in a columnar (long, slender prisms) habit, ∼30 μm long, when observed in the SEM (Figure 6.8.e). Fine, green crystals are also found associated with the mineral.

The minerals andersonite and schröckingerite from Geevor Mine, Pendeen, Cornwall, appear as yellow aggregates on a brown host rock, ∼4 cm in diameter (Figure 6.7.f and

94
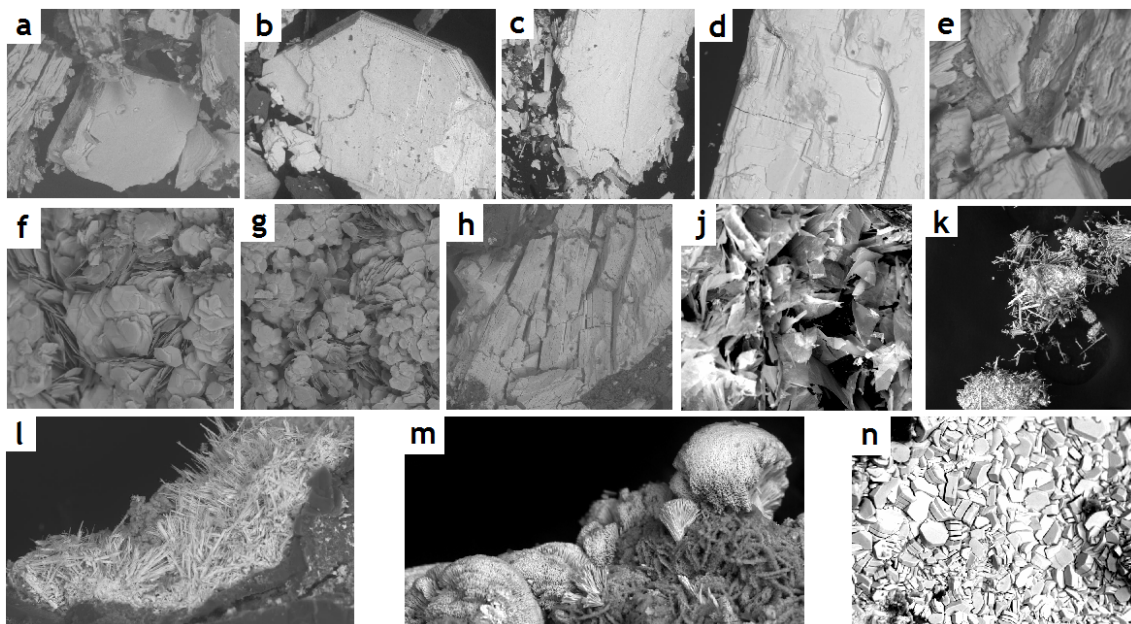
Figure 6.8: SEM images of the minerals studied in this chapter: a) autunite at x200; b) torbernite at x110; c) nováčekite at x220; d) zeunerite at x350; e) phosphuranylite at x650; f) andersonite at x160; g) schröckingerite at x200; h) johannite at x120; j) natrozippeite at x400; k) uranophane at x120; l) cuprosklodowskite at x350; m) kasolite at x500 and n) compreignacite at x500.

g). A thin, transparent layer of gypsum crystals are also found, associated with both minerals. SEM images of both minerals show tabular habits, ∼50–100 μm across (Figure 6.8.f and g).

The sample of johannite from Geevor Mine appears as pale green crystals on a yellow-brown host rock, which is ∼5 cm in diameter (Figure 6.7.o). It appears as foliated tabular crystals in the SEM, ∼100 μm across (Figure 6.8.h).

The sample of natrozippeite from Geevor Mine occurs as a yellow crust on a black and brown host rock, which is ∼7 cm in diameter (Figure 6.7.h). Aggregates of plate-like crystals (lenticular) are observed in the SEM, ∼50 μm in size (Figure 6.8.j). Small, green crystals are found in association with this sample, but these did not present any uranyl peaks in the Raman spectrum.

The sample of uranophane from Wheal Edward appears as a pale yellow crust on a light brown host rock, which is ∼6 cm in diameter (Figure 6.7.j). Individual crystals are seen to adopt a columnar habit in the SEM, ∼50 μm long (Figure 6.8.k). This sample is also associated with a black vein of pitchblende.

Table 6.2: The atomic percentages obtained from an EDX analysis for the uranyl minerals in this chapter

Mineral Name	Atomic Percentage (±1%), averaged over multiple spectra												
	U	O	P	As	Si	S	Cu	Ca	Mg	Na	K	Pb	F
Autunite	7.5	81.1	5.9	0.8	-	-	-	3.7	-	-	-	-	-
Torbernite	8.3	80.3	7.6	0.2	-	-	3.7	-	-	-	-	-	-
Nováčekite	6.3	86.8	0.9	3.8	-	-	-	-	2.2	-	-	-	-
Zeunerite	8.4	80.0	1.7	6.3	-	-	3.6	-	-	-	-	-	-
Phosphuranylite	8.7	77.5	5.5	0.4	-	-	-	3.8	-	-	2.2	-	-
Andersonite	3.2	74.4	-	-	-	4.1	-	9.6	-	3.2	-	-	5.5
Schröckingerite	4.9	69.5	-	-	-	4.1	-	13.7	-	2.6	-	-	5.1
Johannite	6.1	80.4	-	-	2.0	5.6	4.2	-	-	-	-	-	-
Natrozippeite	12.2	77.1	-	-	-	5.6	-	-	-	5.1	-	-	-
Uranophane	7.5	80.7	-	-	7.7	-	-	3.0	-	-	-	-	-
Cuprosklodowskite	7.3	77.1	1.5	1.4	9.2	-	2.6	-	-	-	-	-	-
Kasolite	7.1	76.4	-	-	7.0	-	-	-	-	-	-	6.8	-
Compreignacite	12.1	80.7	-	-	1.9	3.0	-	-	-	-	2.3	-	-

The sample of kasolite from Low Warren Zawn, St. Just, appears as an orange-red crust on one face of a large grey host rock, ∼12 cm in diameter (Figure 6.7.n). It adopts a fibrous crystal habit (extremely slender prisms), observed to be ∼40 μm long in the SEM (Figure 6.8.m).

The samples of compreignacite and cuprosklodowskite from West Wheal Owles, St. Just, are present as associated minerals on a brown, black and grey host rock (Figure 6.7.k and m). Compreignacite occurs as dark yellow crystals, in a blocky crystal habit ∼10–20 μm in size (Figure 6.8.n). Cuprosklodowskite occurs as green crystals in a fibrous habit, ∼50 μm long (Figure 6.8.l).

6.2.2 EDX Analysis

EDX spectra were collected for the uranyl minerals investigated in this chapter using the method described in Section 2.2. Table 6.2 shows the atomic percentages obtained using EDX for each mineral, averaged over 2–4 individual spectra. In general, only minerals with an atomic percentage above 1% are reported, with those of lower concentration considered as contaminants or components of the host rock. Also, the percentage of carbon is not presented, as the proportion was always found to be very high. This is likely a result of carbon in the host rock and the carbon tape used to mount the samples. In general, collecting EDX spectra for the mineral samples is challenging and only provides limited information; however, when additional data is available, valuable

Table 6.3: The chemical composition taken from literature sources and an estimate from the EDX analysis for the minerals in this chapter.

Mineral	Literature Composition	Estimate from EDX
Autunite	$Ca(UO_2)_2(PO_4)_2 \cdot 11H_2O$ [214, 215]	$Ca(UO_2)_2(PO_4)_{1.6}(AsO_4)_{0.2}$
Torbernite	$Cu(UO_2)_2(PO_4)_2 \cdot 12H_2O$ [217]	$Cu_{0.9}(UO_2)_2(PO_4)_{1.8}$
Nováčekite	$Mg(UO_2)_2(AsO_4)_2 \cdot 10H_2O$ [220]	$Mg_{0.7}(UO_2)_2(PO_4)_{0.3}(AsO_4)_{1.2}$
Zeunerite	$Cu(UO_2)_2(AsO_4)_2 \cdot 12H_2O$ [219]	$Cu_{0.9}(UO_2)_2(PO_4)_{0.4}(AsO_4)_{1.5}$
Phosphuranylite	$Ca(UO_2)_3(PO_4)_2(OH)_2 \cdot 6H_2O$ [221] $(K,Ca)(H_3O)_3(UO_2)_7(PO_4)_4O_4 \cdot 8H_2O$ [255]	$K_{0.7}Ca_{1.3}(UO_2)_3(PO_4)_{1.9}$
Andersonite	$Na_2Ca(UO_2)(CO_3)_3 \cdot 6H_2O$ [222]	$NaCa_3(UO_2)(SO_4)_{1.3}F_{1.7}$
Schröckingerite	$NaCa_3(UO_2)(CO_3)_3(SO_4)F \cdot 10H_2O$ [223]	$Na_{0.5}Ca_{2.8}(UO_2)(SO_4)_{0.8}$
Johannite	$Cu(UO_2)_2(OH)_2(SO_4)_2 \cdot 8H_2O$ [224]	$Cu_{1.4}(UO_2)_2(SO_4)_{1.8}$
Natrozippeite	$Na_5(UO_2)_8(SO_4)_4O_5,(OH)_3 \cdot 8H_2O$ [225]	$Na_{2.5}(UO_2)_6(SO_4)_{2.7}$
Uranophane	$Ca(UO_2)_2(SiO_4)_2 \cdot 5H_2O$ [226]	$Ca_{0.8}(UO_2)_2(SiO_4)_{2.1}$
Kasolite	$Pb(UO_2)(SiO_4) \cdot 2H_2O$ [228]	$Pb(UO_2)(SiO_4)$
Cuprosklodowskite	$Cu(UO_2)_2(SiO_4)_2 \cdot 6H_2O$ [227]	$Cu_{0.7}(UO_2)_2(SiO_4)_{2.5}$
Compreignacite	$K_2(UO_2)_6O_4(OH)_6 \cdot 7H_2O$ [230]	$K_{1.2}(UO_2)_6$

conclusions may be made.

Table 6.3 presents the literature chemical formula for each mineral, in addition to a formula estimate based on the EDX data. The EDX estimate has been normalised to integer values of uranium atoms. In most cases, the presence and proportion of atoms is similar to that expected based on literature data [211–213, 221]; however, there are some discrepancies. The water content has not been reported, as hydrogen cannot be observed in the EDX spectrum and the hydration state of the samples may change as a result of the experiment.

The proportion of uranium to polyanion tends to be slightly higher than expected, with the exception of the silicate minerals. These observations may be a result of both elements existing at low concentrations in the host rocks. A similar explanation may be made for the concentration of copper in johannite being higher than expected, as the area around Geevor Mine has been mined for copper. In contrast, the samples of natrozippeite, uranophane, cuprosklodowskite and compreignacite are cation deficient. This has been observed for many zippeite minerals [302] and explained as the ready diffusion of cations through the large interlayer space.

6.2.3   Autunite Group of Phosphate and Arsenate Minerals

The autunite minerals analysed in this investigation were identified from EDX spectra as the uranyl phosphates autunite and torbernite and the uranyl arsenates nováčekite and zeunerite. In most cases, both phosphorus and arsenic were present in the mineral samples, suggesting that both isostructural phosphate and arsenate minerals exist in close association or that mixed crystal structures are present in the sample. Therefore, the name assigned for each sample was based on the phosphorus to arsenic ratio determined from the EDX spectrum. Prior to this investigation [206], no Raman spectra were found in the literature for nováčekite, so the spectrum for this sample has been compared against that for its phosphate analogue, saléeite. The spectra are presented in Figure 6.9 and compare well to previously published spectra [69, 70, 87]. The spectrum of nováčekite also follows the trends seen for the other autunite minerals. All peaks in the autunite minerals' Raman spectra are given in Tables D.1–D.4.

The 785 nm excitation source was found to produce Raman spectra for autunite and nováčekite with little fluorescence, whereas the 532 nm source typically produced a significant amount and hence prevented some peaks from being observed. In contrast, the spectra obtained for torbernite and zeunerite had little fluorescence under all three lasers (325, 532 and 785 nm), although the peaks in torbernite were better resolved using the 532 nm laser. One issue with the 325 nm excitation wavelength is that no modes were visible in the bending region of the Raman spectrum (below 600 cm^{-1}) for any mineral, whereas the other lasers showed these peaks.

The Raman spectrum of each autunite mineral was dominated by the uranyl symmetric stretching mode ($\nu_1(\text{UO}_2)^{2+}$), seen at 830 cm^{-1} in autunite, 825 cm^{-1} in torbernite, 817 cm^{-1} in nováčekite and 821 cm^{-1} in zeunerite. In the 785 nm spectra of the phosphate minerals autunite and torbernite, a low intensity shoulder was also observed. The uranyl antisymmetric stretch ($\nu_3(\text{UO}_2)^{2+}$) is seen around 900 cm^{-1} in the majority of spectra, which suggests that the uranyl cations in the minerals no longer retain the perfect $D_{\infty h}$ symmetry observed for free uranyl cations. The uranyl bending mode ($\nu_2(\text{UO}_2)^{2+}$) is seen in the 200–300 cm^{-1} region of the 532 and 785 nm Raman spectra, but is absent in the 325 nm spectra.

The Raman spectra for both autunite and torbernite show a strong peak corresponding to the phosphate antisymmetric stretching mode ($\nu_3(\text{PO}_4)^{3-}$) around 1000 cm^{-1}. In some spectra, it is instead found as two separate bands, most notably in the 785 nm
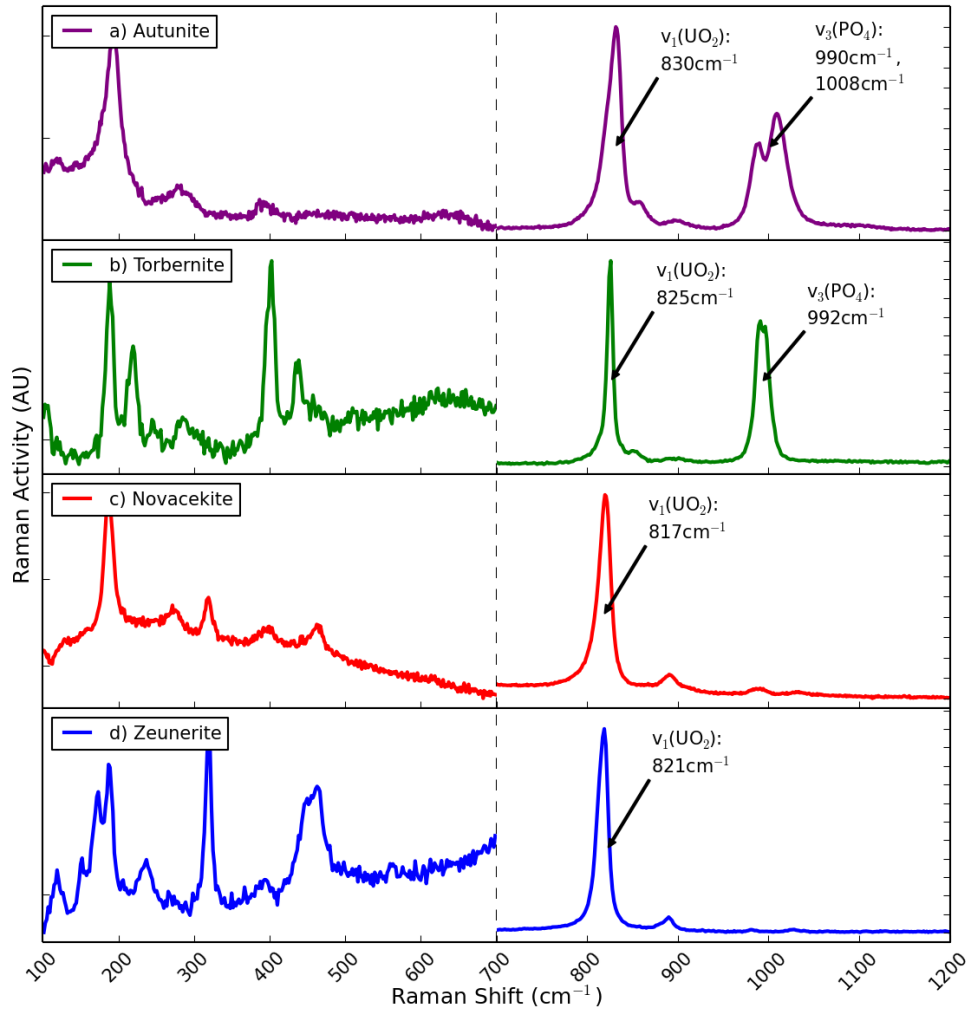
Figure 6.9: Representative Raman spectra of a) autunite (785 nm excitation laser), b) torbernite (532 nm), c) nováčekite (785 nm) and d) zeunerite (532 nm) mineral samples. The 100–700cm^{-1} regions have been rescaled by a) ×5, b) ×12, c) ×4 and d) ×18, to emphasise the bands in this region. The excitation laser wavelengths shown were determined to be the optimum for each mineral. The major peaks are annotated, while all bands are listed in Tables D.1–D.4.

spectrum of autunite. This splitting may result from the polyanion losing tetrahedral symmetry. In the spectrum of nováčekite, a low intensity peak is also found around 1000 cm^{-1}, but this can be explained by the low proportion of phosphorus detected in the EDX spectrum.

The phosphate symmetric stretching mode ($\nu_1(\mathrm{PO}_4)^{3-}$), expected between 930–950 cm^{-1}, is absent in the autunite and torbernite spectra. The exact cause is unknown, but its absence has been previously reported by Frost *et al.* [57].

The phosphate and arsenate bending modes were observed as low intensity bands in the 300-650 cm^{-1} region of the Raman spectra collected using 532 and 785 nm excitation sources. In general, the arsenate bending modes are found at lower wavenumbers than the phosphate equivalents.

6.2.4 Phosphuranylite

The EDX spectrum collected for phosphuranylite in this study has a very similar U:P ratio (3:1.9) to that reported by Ryback and Tandy for a sample from Wheal Edward (3:2) [221]. However, both potassium and calcium are found, as described by Demartin *et al.* [255] and Zhang *et al.* [260].
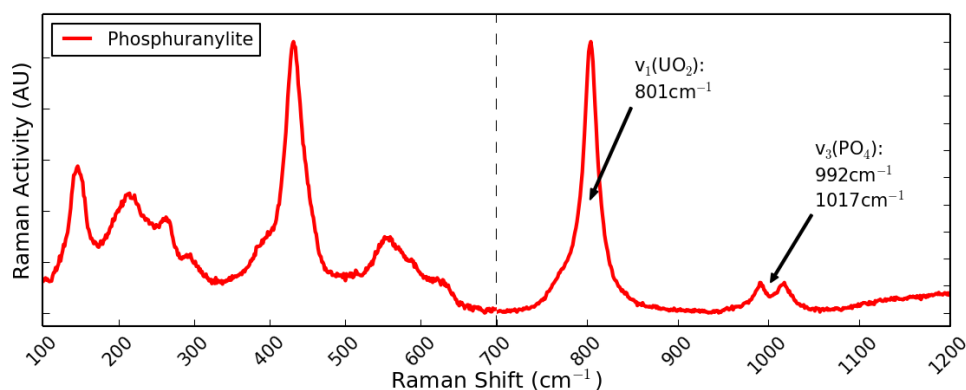
Figure 6.10: A representative Raman spectrum of the mineral phosphuranylite (785 nm excitation laser). The 100–700cm^{-1} region has been rescaled by $\times 2$, to emphasise the bands in this region. The 785 nm excitation source produced the best spectrum. The major peaks are annotated, while all bands are listed in Table D.5.

The best excitation wavelength for collecting Raman spectra of phosphuranylite was found to be 785 nm, as the fluorescence was minimal and the resolution of many peaks is better than with other wavelengths (Figure 6.10). Indeed, the only visible mode in the 325 nm spectrum corresponds to the uranyl symmetric stretch and in the 532 nm spectrum the phosphate antisymmetric stretch ($\nu_3(PO_4)^{3-}$) is very low intensity. All peaks are given in Table D.5.

The strongest Raman active mode in the spectrum of phosphuranylite is the uranyl symmetric stretch ($\nu_1(UO_2)^{2+}$), seen at 801 cm^{-1}. This spectrum bears similarities to a previously published spectrum of phosphuranylite from Minerva Heights, Australia [267], for which the $\nu_1(UO_2)^{2+}$ mode was found at 768, 793, 805 and 815 cm^{-1}. However, the spectra collected for other samples of phosphuranylite differed, with the $\nu_1(UO_2)^{2+}$ modes for a sample from Saddle Ridge Mine, Australia at 816, 837, 843 and 847 cm^{-1} and for

a sample from Ruggles Mine, USA at 817, 832 and 841 cm^{-1} [267]. The uranyl bending mode was found in some 785 nm spectra around 216 cm^{-1}, but no peaks were found to correspond to the uranyl antisymmetric stretch, which may be expected at $\sim$900 cm^{-1}.

The $\nu_3(PO_4)^{3-}$ mode was found at $\sim$1000 cm^{-1} in the Raman spectra of phosphuranylite. In some 785 nm spectra, this split into two bands at 992 and 1017 cm^{-1}. As noted for the autunite minerals, the phosphate symmetric stretch ($\nu_1(PO_4)^{3-}$) was not observed in the Raman spectrum. A strong mode $\sim$435 cm^{-1} in 532 and 785 nm spectra has been interpreted as the phosphate bending mode ($\nu_2(PO_4)^{3-}$).

6.2.5 Uranyl Carbonates

The EDX spectra of the uranyl carbonate minerals andersonite and schröckingerite cannot be used to accurately determine the proportion of carbon in the samples, as carbon was found to be very abundant in all mineral samples studied. This may be explained by its presence in the host rocks and the carbon tape used to hold the samples in place. A further issue with the andersonite sample is the proportion of calcium, is significantly higher than expected, while fluorine and sulphur are found but not part of the literature composition. These observations may be explained by the presence of transparent
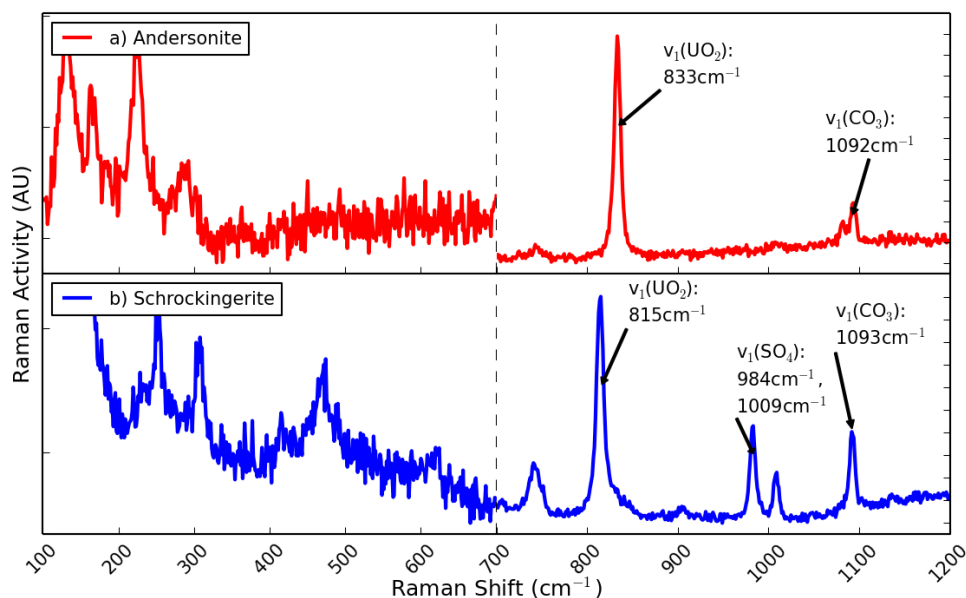
Figure 6.11: Representative Raman spectra of the uranyl carbonate minerals a) andersonite (785 nm excitation laser) and b) schröckingerite (785 nm). The 100–700cm^{-1} regions have both been rescaled by ×5, to emphasise the bands in this region. The 785 nm excitation source was found to be the optimum for both minerals. The major peaks are annotated, while all bands are listed in Tables D.6 and D.7.

gypsum crystals ($CaSO_4$), which were reported by Elton and Hooper [213], and possibly fluorspar (CaF_2), which is a common component of host rocks.

No significant differences were found between the three excitation wavelengths for the Raman spectra of andersonite and schröckingerite (Figure 6.11). Some fluorescence was observed in the 532 nm spectra, but the peaks remained distinct. All peaks are given in Tables D.6 and D.7.

The uranyl symmetric stretching mode ($\nu_1(UO_2)^{2+}$) dominates the Raman spectra of both carbonate minerals and is seen at 833 cm^{-1} in andersonite and 815 cm^{-1} in schröckingerite. These values show close agreement to the peaks observed in published spectra [76, 286]. An additional low intensity shoulder is also seen for schröckingerite. The uranyl antisymmetric stretch is seen in some spectra as a low intensity band $\sim$900 cm^{-1}, but no uranyl bending modes have been consistently identified.

The Raman spectra of both andersonite and schröckingerite contain a carbonate symmetric stretch at 1092 cm^{-1}, with a lower wavenumber shoulder observed in andersonite. Carbonate bending modes are also observed at $\sim$743 cm^{-1}. The schröckingerite spectrum also contains a sulphate symmetric stretch at 984 cm^{-1} and a second band at 1009 cm^{-1} in the 532 and 785 nm spectra.

6.2.6   Uranyl Sulphates

Johannite

The EDX spectrum obtained for the sample of johannite agrees well with the composition reported in the literature, where the atomic percentages of U and S are equivalent [295]. It differs from the other uranyl mineral samples in that the cation concentration is higher than expected from the chemical formula. As copper has been mined in many locations in Cornwall, it is likely present in the host rock.

There were no significant differences between the three excitation wavelengths when collecting Raman spectra of johannite, with the exception of the bending modes not being observed in the 325 nm spectrum.

The Raman spectrum of johannite was dominated by the uranyl symmetric stretch at 836 cm^{-1} (Figure 6.12). This is significantly different to the peaks reported by Frost *et al.* for a sample collected from St. Agnes, Cornwall (756, 788 and 812 cm^{-1}) [295]. The
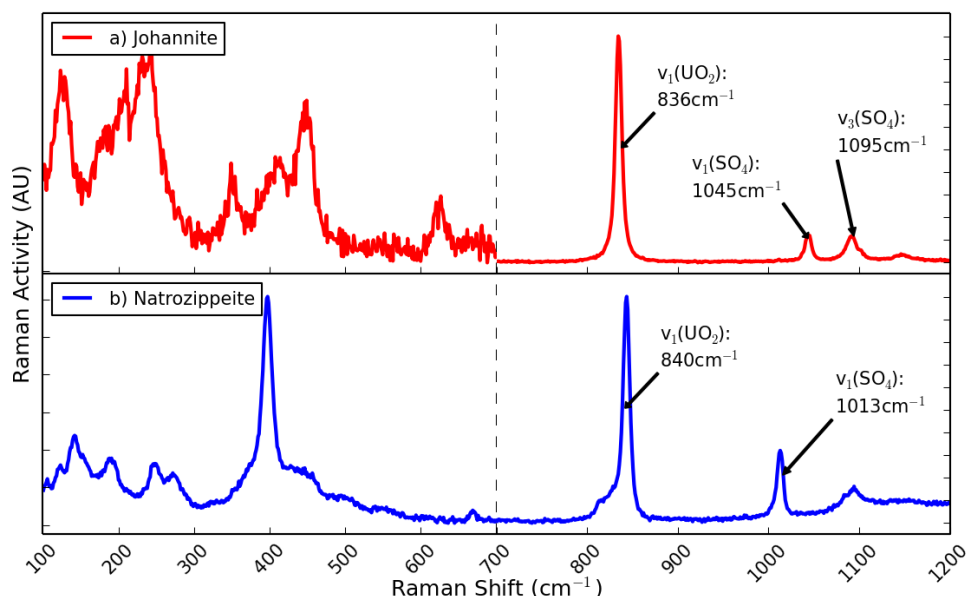
Figure 6.12: Representative Raman spectra of the uranyl sulphate minerals a) johannite (785 nm excitation laser) and b) natrozippeite (785 nm). The 100–700cm^{-1} regions have been rescaled by a) ×20 and b) ×2, to emphasise the bands in this region. The 785 nm excitation source was found to provide the best spectrum for both minerals. The major peaks are annotated, while all bands are listed in Tables D.8 and D.9.

variation is likely due to differences in the mineral composition. The uranyl antisymmetric stretch was not seen in the Raman spectrum; however, low intensity modes were seen in the 532 and 785 nm spectra corresponding to the uranyl bending mode.

The sulphate stretching modes were observed at 1045 and 1095 cm^{-1} region of the 532 and 785 nm spectra. In the 532 nm spectrum, the 1095 cm^{-1} peak also has a shoulder. Some spectra contain a low intensity mode at 1012 cm^{-1}. Sulphate bending modes are also found as low intensity bands in the 350–500 cm^{-1} region.

Natrozippeite

The EDX spectrum for natrozippeite from Geevor mine demonstrates the 2:1 U:S ratio and a sodium deficiency, which are well known features of zippeite minerals.

The 785 nm excitation source was found to provide Raman spectra with little background fluorescence (Figure 6.12), whereas 532 nm spectra contained large fluorescence bands. Spectra obtained using the 325 nm laser were typically weak and noisy and only contained the uranyl symmetric stretching mode.

The uranyl symmetric stretching mode in natrozippeite was seen as an asymmetric peak at $\sim$840 cm^{-1}. The asymmetry indicates the presence of multiple bands, which agrees with the peaks observed at 813, 823, 834, 840 and 841 cm^{-1} in a published spectrum [300]. No uranyl antisymmetric stretching mode was present, but a low intensity mode at $\sim$250 cm^{-1} may correspond to the uranyl bending mode.

A sulphate symmetric stretching mode was identified at 1013 cm^{-1} and a sulphate bending mode was observed at 397 cm^{-1}.

6.2.7 Uranyl Silicates

The EDX spectra obtained for the uranyl silicate minerals showed a composition that agreed with the expected chemical formulae. The only notable deviation is the proportion of silicon, which was found to be higher than anticipated, but this may be attributed to the host rock.

All silicate minerals produced good spectra using the 532 and 785 nm excitation wavelengths; however, a stronger signal was obtained for cuprosklodowskite with the 532 nm laser and some background fluorescence was found in the 532 nm spectrum of uranophane. No bending modes were visible in the 325 nm spectra, but the most significant stretching modes were observed.

Raman spectra of the uranyl silicates (Figure 6.13) were dominated by the uranyl symmetric stretching mode ($\nu_1(\mathrm{UO_2})^{2+}$), which was found at a lower wavenumber than previous minerals. The $\nu_1(\mathrm{UO_2})^{2+}$ mode was seen as a sharp peak at $\sim$800 cm^{-1} in uranophane, as a broader, asymmetric peak at $\sim$792 cm^{-1} in cuprosklodowskite and as a sharp peak at $\sim$760 cm^{-1} in kasolite. Low intensity modes were observed for the uranyl antisymmetric stretching mode in the 850–920 cm^{-1} region and for the uranyl bending mode in the 200–300 cm^{-1} region.

The silicate antisymmetric stretching modes have been assigned to peaks in the 939–974 cm^{-1} region of all three silicate minerals. In the 532 and 785 nm spectra of kasolite, this mode resolves into two peaks. The silicate symmetric stretching modes were not observed for any uranyl silicate mineral, but low intensity bands in the 350–550 cm^{-1} region have been assigned to the silicate bending modes.
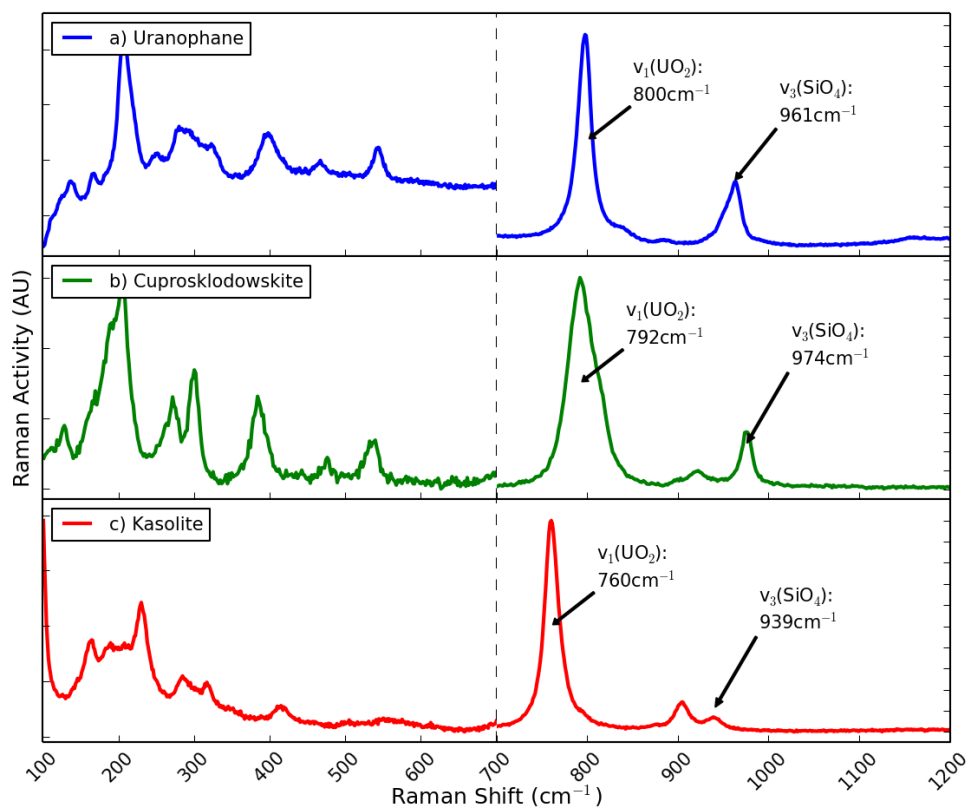
Figure 6.13: Representative Raman spectra of the uranyl silicate minerals a) urano-phane (785 nm excitation laser), b) cuprosklodowskite (532 nm) and c) kasolite (785 nm). The 100–700cm^{-1} regions have been rescaled by a) ×3, b) ×4 and c) ×3, to emphasise the bands in this region. The excitation laser wavelengths shown were determined to be the optimum for each mineral. The major peaks are annotated, while all bands are listed in Tables D.10– D.12.

6.2.8   Uranyl Oxide Hydrates

The EDX spectrum of compreignacite shows a significantly lower proportion of potassium than expected, suggesting a cation deficiency. However, this observation may be a result of excess uranium in associated minerals or the host rock. No assessment of the layer composition can be made from EDX, as it is constructed from oxygen, which appears as very abundant in the EDX, and hydrogen, which does not appear at all.

Both 532 and 785 nm excitation wavelengths provided good Raman spectra for com-preignacite, although a low level of fluorescence was seen in the 532 nm spectrum. Peaks in the 325 nm spectrum tended to be significantly weaker.

The most significant peak seen in the Raman spectra of compreignacite (Figure 6.14) is the uranyl symmetric stretch, visible at ∼834 cm^{-1}. A smaller peak or shoulder is also
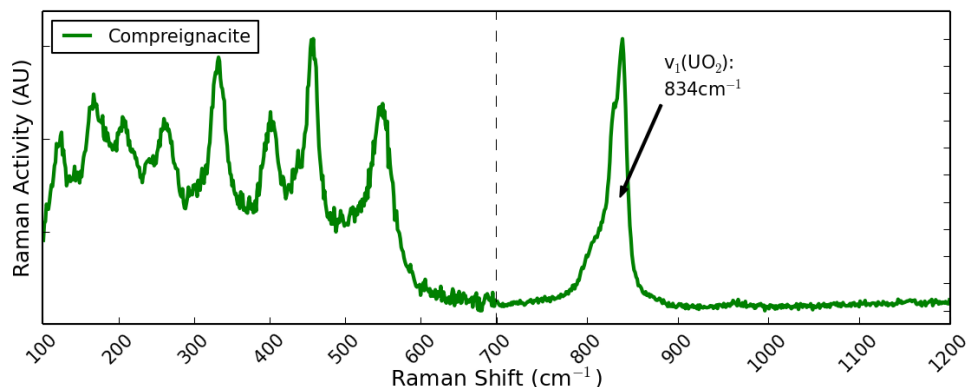
Figure 6.14: A representative Raman spectrum of the uranyl hydrate mineral compreignacite (785 nm excitation laser). The 100–700cm^{-1} region has been rescaled by ×3, to emphasise the bands in this region. The 785 nm excitation source was found to produce the best spectrum. The major peaks are annotated, while all bands are listed in Table D.13.

observed at ∼804 cm^{-1} in the 785 nm spectrum or ∼858 cm^{-1} in the 325 nm spectrum. Other bands were seen in the 532 and 785 nm spectra, most consistently at 549, 460, 402, 329 and 204 cm^{-1}. The 204 cm^{-1} peak may be attributed to the uranyl bending mode, while the others may be assigned to the bending and stretching of equatorial uranium-oxygen interactions.

6.3 Discussion

Raman spectra have been collected for a selection of uranyl minerals originating from Cornwall, UK. In this section, the trends observed in the position of the uranyl symmetric stretching modes are discussed (Section 6.3.1), the peaks corresponding to the polyanions in each mineral are described (Section 6.3.2) and an analysis of the different excitation wavelengths is given (Section 6.3.3).

6.3.1 The Uranyl Symmetric Stretching Mode

The most prominent peak in most Raman spectra of uranyl minerals is the uranyl symmetric stretch ($\nu_1(UO_2)^{2+}$). This peak is seen in the 750–900 cm^{-1} region, but the exact position was shown to vary for different minerals, providing a possible strategy for discriminating between them. Table 6.4 contains the measured $\nu_1(UO_2)^{2+}$ peak positions and literature values for comparison. The standard error is also given, which was calculated by dividing the standard deviation of all the spectra for that sample by the square root of the number of spectra. Most peak positions observed in this investigation show good agreement with the corresponding literature values. The main discrepancies are in

the spectra of johannite and compreignacite and may be due to a variation in sample composition.

The charge on the polyanions coordinated to the uranyl cation in the equatorial plane were found to influence the position of the uranyl symmetric stretching mode ($\nu_1(UO_2)^{2+}$). Polyanions with a more negative charge (e.g. SiO_4^{4-}) shift $\nu_1(UO_2)^{2+}$ to a lower wavenumber compared to less negatively charged polyanions (e.g. SiO_4^{4-}). Differences in structure may also have an effect on $\nu_1(UO_2)^{2+}$, arising from the nature and coordination of the cations and water in the interlayer space.

The uranyl antisymmetric stretching and bending modes were observed in many spectra within the 850–950 cm^{-1} and 200–300 cm^{-1} regions, respectively. In contrast to the symmetric stretch, these modes were typically low intensity (they should be IR active and Raman inactive) and the position did not shift across the series of minerals.

Table 6.4: The uranyl symmetric stretching modes observed in this investigation are displayed, alongside a standard error calculated for each set of spectra. The poly-anions that coordinate to the equatorial plane of the uranyl group are given for each mineral. Published values are also shown. An estimation of the U-O bond distance (R_{UO}) is made from the uranyl symmetric stretch using the Bartlett and Cooney relation (Equation 6.1) [353].

Mineral Name	Equatorial Poly-anion(s)	This study (cm^{-1})	Std. Error	Literature (cm^{-1})	Estimated R_{UO} (Å)
Kasolite	SiO_4^{4-}	760.4	0.2	759 [78]	1.85
Cuprosklodowskite	SiO_3OH^{3-}	791.8	0.4	787 [78]	1.82
Uranophane	SiO_3OH^{3-}	800.0	0.3	797; [78] 796; 797; 794 [307]	1.81
Phosphuranylite	PO_4^{3-} and O^{2-}/OH^-	801.1	0.9	805; 847; 844 [267]	1.81
Schröckingerite	CO_3^{2-}	815.3	0.2	815 [76]	1.80
Saléeite	PO_4^{3-}	—	—	833; [69] 827 [70]	—
Nováčekite	AsO_4^{3-}	817.5	0.3	—	1.79
Zeunerite	AsO_4^{3-}	821.0	0.6	818 [87]	1.79
Torbernite	PO_4^{3-}	826.0	0.3	826 [69]	1.78
Autunite	PO_4^{3-}	829.6	0.5	833 [69]	1.78
Andersonite	CO_3^{2-}	833.5	0.1	830 [286]	1.78
Compreignacite	O^{2-} and OH^-	834.0	0.7	848 [29]	1.78
Johannite	SO_4^{2-} and OH^-	835.6	0.2	812 [295]	1.78
Natrozippeite	SO_4^{2-} and O^{2-}/OH^-	840.1	0.7	841 [300]	1.77

The $\nu_1(UO_2)^{2+}$ peak in the autunite group of minerals was observed in the 817–830 cm^{-1} region. It was found at a higher wavenumber for the phosphate samples than for the arsenate samples. The measured position of nováčekite and the literature position of saléeite were significantly different, indicating the minerals may be distinguished in this way; however, there was little difference in the measured positions for torbernite and zeunerite, preventing an identification using this trend alone.

The $\nu_1(UO_2)^{2+}$ peak for the mineral phosphuranylite is found at a lower position (801 cm^{-1}) compared to the autunite minerals, despite the phosphate dominant composition. This may be attibuted to the different uranyl environments in phosphuranylite, as square, pentagonal and hexagonal bipyramids are present, which affect the local charge around the cation differently. Furthermore, some uranyl cations are also coordinated to O^{2-} or OH^- anions in the equatorial plane. Differences in the proportion of each anion may cause the $\nu_1(UO_2)^{2+}$ peak to shift in samples from different locations, as observed by Frost *et al.* [267]. In their investigation, one sample from Minerva Heights, Australia had a similar Raman spectrum to the one described in this chapter ($\nu_1(UO_2)^{2+}$ at 805 cm^{-1}), whereas the other two samples from Saddle Ridge Mine, Australia and Ruggles Mine, USA were significantly different ($\nu_1(UO_2)^{2+}$ at 847 and 844 cm^{-1}, respectively), stressing the importance of studying samples from a variety of locations.

The uranyl silicate minerals in this investigation adopt the uranophane sheet structure, in which the uranyl cations are coordinated by four silicate anions in the equatorial plane, with an equatorial coordination of five. The $\nu_1(UO_2)^{2+}$ peaks are observed in the 790–800 cm^{-1} region for uranophane and cuprosklodowskite, whereas the equivalent peak for kasolite is found at 760 cm^{-1}. The positions seen in this study show good agreement with those previously reported [78, 307]. A possible explanation for the difference in peak position is that the silicate groups in uranophane and cuprosklodowskite are SiO_3OH^{3-}, which provide a less charged environment compared to the SiO_4^{4-} groups in kasolite.

The uranyl cations in johannite and natrozippeite are both found in pentagonal bipyramidal environments, where the equatorial vertices are shared with sulphate, O^{2-} and OH^- anions. A similar arrangement is also found in compreignacite, with the exception that all equatorial vertices are O^{2-} or OH^- anions. These anions have a lower charge than those found in the other uranyl minerals, resulting higher wavenumber $\nu_1(UO_2)^{2+}$ peaks. However, these peaks in the spectra for johannite and compreignacite show significant deviation from published literature values [29, 295], which may result from the variable composition and local charge in different samples.

The $\nu_1(\mathrm{UO_2})^{2+}$ peak positions in andersonite and schröckingerite, the uranyl tricarbonate minerals, are found at 833 and 815 cm^{-1}, respectively. The equatorial uranyl environment in both minerals is equivalent, with three edge-sharing carbonate anions forming a hexagonal bipyramidal coordination environment. Therefore, the difference in peak position must result from other aspects of the mineral structure. In andersonite, the mineral forms a complex framework structure, which is significantly different to the layered structures seen in the other uranyl minerals described in this chapter. In contrast, uranyl cations in the schröckingerite structure may be coordinated by F$^-$ anions in the axial direction, weakening the U-O bonds and lowering the wavenumber of the $\nu_1(\mathrm{UO_2})^{2+}$ peak.

6.3.2 The Poly-anion peaks

The polyanions that exist in the structure of uranyl minerals have their own distinct set of associated vibrational modes. These bands can act as a fingerprint, allowing the ions present in the structure to be identified.

The phosphate antisymmetric stretching mode ($\nu_3(\mathrm{PO_4})^{3-}$) was seen as a strong peak or pair of peaks in the 990–1020 cm^{-1} region of the Raman spectrum for uranyl phosphate minerals. Phosphate bending modes have also been identified in the 370–480 cm^{-1} (ν_2) and 560–660 cm^{-1} (ν_4) regions for many spectra collected with a 532 or 785 nm laser. The phosphate symmetric stretch (ν_1) has been reported as absent in previous Raman investigations of autunite minerals [57], which is confirmed in this investigation. The exact cause of this absence remains unknown.

The arsenate symmetric ($\nu_1(\mathrm{AsO_4})^{3-}$) and antisymmetric ($\nu_3$) stretching modes were not observed in the Raman spectra of the arsenate members of the autunite group. However, the expected position for these peaks is in the 810–840 cm^{-1} region and Frost *et al.* have suggested that these peaks overlap with the uranyl symmetric stretching mode [57]. This absence provides a strategy for distinguishing between phosphate and arsenate members of the autunite group of minerals, as the $\nu_3(\mathrm{PO_4})^{3-}$ peak is seen for the phosphate minerals, but no peaks are seen in the same region of the Raman spectrum for the arsenate minerals. The arsenate bending modes (ν_2 and ν_4) are typically observed as low intensity bands in the 320–470 cm^{-1} region.

The characteristic vibrational modes of the silicate anion adopt a different fingerprint to the phosphate and arsenate groups. The silicate antisymmetric stretching mode

$(\nu_3(SiO_4)^{4-})$ is a strong band observed in the 930–980 cm^{-1} region, while the symmetric stretch (ν_1) is absent, but may coincide with the uranyl symmetric stretch. Low intensity bending modes have been seen in the 390–480 cm^{-1} (ν_2) and 500–580 cm^{-1} (ν_4) regions.

All four sulphate vibrational modes are typically visible in the Raman spectra of the uranyl sulphate minerals in this study. The sulphate symmetric ($\nu_1(SO_4)^{2-}$) and antisymmetric (ν_3) stretching modes are observed as strong modes in the 980–1050 cm^{-1} and 1080–1150 cm^{-1} regions, respectively. The bending modes are often seen as low intensity modes in the 370–500 cm^{-1} (ν_2) and 480–670 cm^{-1} (ν_4) regions. The range in peak position is broader for the sulphate minerals than those in other polyanions, which may be due to the differences in sulphate environment found in the three uranyl minerals studied. In johannite and natrozippeite, sulphate anions are coordinated to the equatorial plane of the uranyl group, whereas those in schröckingerite are closer to the axial uranyl oxygens.

The carbonate symmetric mode ($\nu_1(CO_3)^{2-}$) was observed in the 1080–1100 cm^{-1} region of the Raman spectrum for the minerals andersonite and schröckingerite. The antisymmetric stretch (ν_3) was not visible in this study, but has been previously observed in the 1370–1410 cm^{-1} region. A carbonate bending mode has been observed in the 690–750 cm^{-1} region (ν_4), but the ν_2 bending mode, expected within the same region as the uranyl symmetric stretch, was not seen. It is possible that the two bands overlap.

6.3.3 Choice of Excitation Wavelength

An important consideration when collecting the Raman spectra of uranyl minerals is the wavelength chosen for exciting the sample. Certain wavelengths may result in a spectrum where the bands of interest are overwhelmed by fluorescence. Furthermore, the diffraction grating, chosen for the wavelength used, affects the resolution of the spectrum. Portable Raman devices typically only contain a single laser, so a wavelength that consistently produces good quality spectra must be chosen.

The uranyl cation produces fluorescence bands in the 450–600 nm region [354]. This explains the strong background signal observed in the 532 nm spectra of some minerals, such as natrozippeite (Figure 6.15a-c). In contrast, the spectra produced using the 325 and 785 nm excitation lasers typically had little fluorescence. The 785 nm spectra also had a high resolution (± 0.2 cm^{-1}), making it the best choice of excitation wavelength for
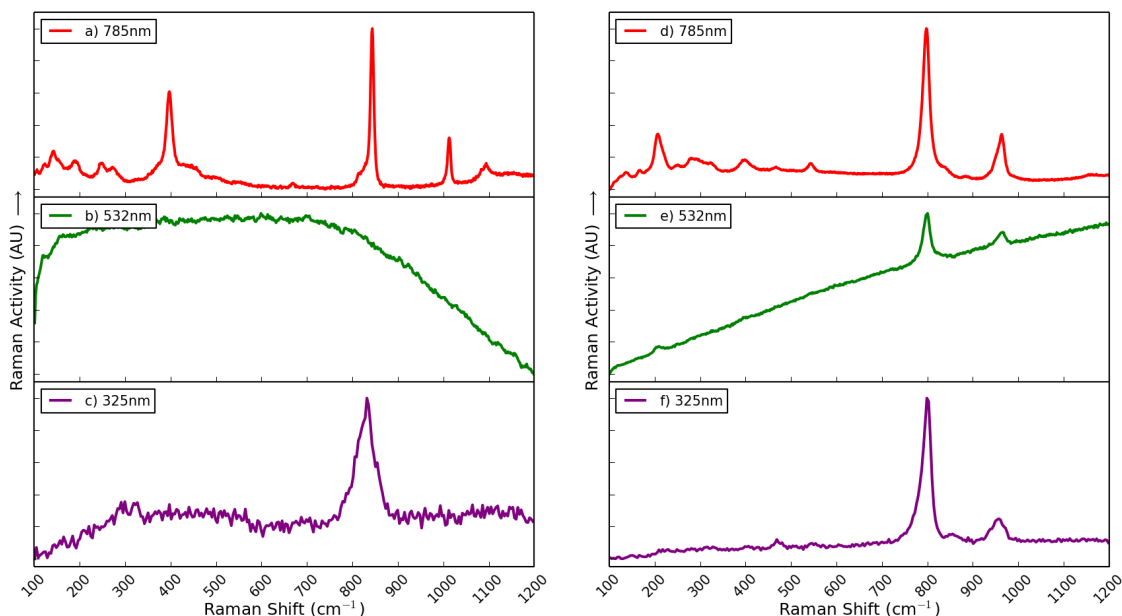
Figure 6.15: A comparison of the spectra obtained using the three excitation wavelengths for the uranyl sulphate mineral natrozippeite (a–c) and the uranyl silicate mineral uranophane (d–f).

these minerals. In cases where little background fluorescence was observed in the 532 nm spectrum (e.g. torbernite, Figure 6.16b), this wavelength also provided high resolution spectra (± 1.2 cm^{-1}). The lowest resolution spectra were obtained using the 325 nm laser (± 5.0 cm^{-1}), which prevented some low intensity modes from being observed, notably those attributed to bending motions.

The most significant fluorescence was observed in the 532 nm spectra of natrozippeite (Figure 6.15b), compreignacite and phosphuranylite. This is most significant for natrozippeite, where the Raman bands are completely overwhelmed by fluorescence. These minerals always produced good Raman spectra with the 785 nm excitation laser, whereas the 325 nm spectra were typically weak, only displaying the uranyl symmetric stretch.

Fluorescence was also a concern in the 532 nm spectra of the minerals autunite, nováčekite and uranophane (Figure 6.15d–f), but it did not overwhelm the Raman bands. Bands in the 325 nm spectra were seen with low intensity, but in these minerals the stretching modes were clearly visible. The best excitation wavelength was found to be 785 nm.

The remaining seven minerals produced good Raman spectra with all three excitation wavelengths. In general, the 532 and 785 nm spectra were very similar (Figure 6.16), although some bands in cuprosklodowskite, torbernite and johannite were better resolved
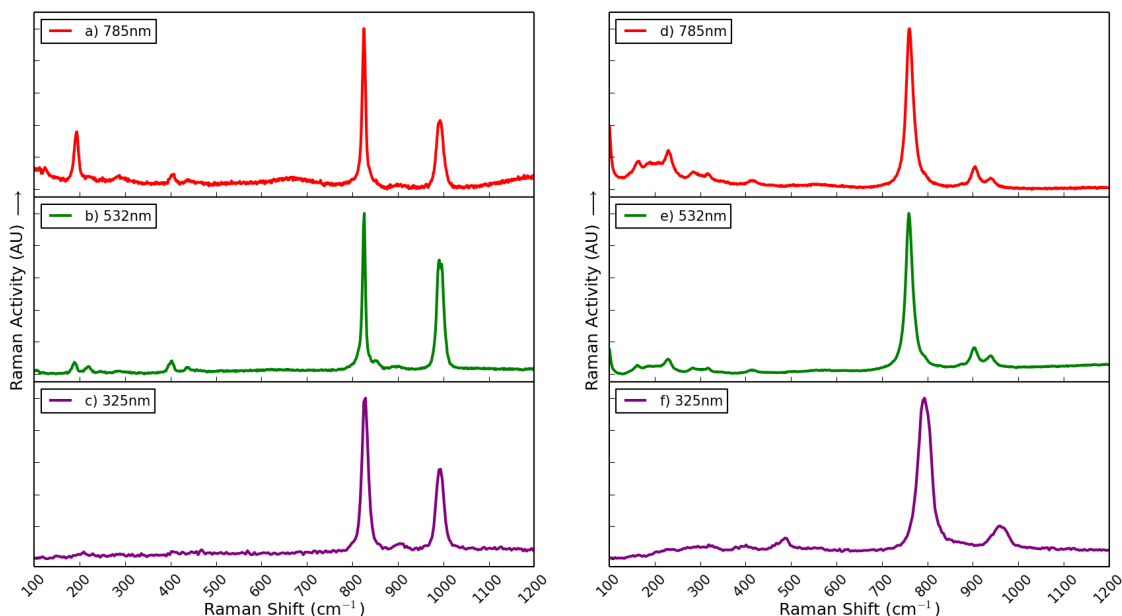
Figure 6.16: A comparison of the results obtained using the three excitation wavelengths for the uranyl phosphate mineral torbernite (a–c) and the uranyl silicate mineral kasolite (d–f).

in the 532 nm spectra. Some bands were less well resolved in the 325 nm spectra, but no stretching modes were absent.

6.4 Conclusions

Raman spectroscopy has been applied to thirteen uranyl minerals from Cornwall, UK, including the uranyl arsenate mineral nováčekite, which was not published prior to this investigation [206]. As a technique, Raman spectroscopy is fast, non-destructive and portable, which is ideal for a forensic investigation, where delicate samples may need to be studied *in situ*. Furthermore, the uranyl minerals in this study lend themselves to vibrational spectroscopic techniques, as they contain ions that produce characteristic vibrational bands and form a fingerprint for each mineral. These ions include phosphate, arsenate and silicate polyanions, as well as the uranyl cation present in all uranyl minerals. In the majority of cases, the Raman spectra agreed with previously published data; however, there were differences for some samples. This emphasises the importance of studying samples from various locations and suggests it may be possible to determine the origin of a sample by comparing its spectrum to a database of known information.

Three distinct excitation wavelengths have been used in this study: 325, 532 and 785 nm. In the minerals autunite, nováčekite, phosphuranylite, natrozippeite, uranophane and

compreignacite, the Raman spectrum collected using the 532 nm laser suffered from fluorescence; in some cases, this effect overwhelmed the Raman bands. This was not a problem for the other minerals, where both 532 and 785 nm spectra were comparable. For the majority of minerals, the 325 nm spectrum was weak and noisy, with a low resolution that meant some bands, including the bending modes, were not observed. Consequently, the 785 nm excitation source was deemed best for studying the uranyl minerals.

The uranyl cation produces a strong vibrational mode in the 750–900 cm^{-1} region of the Raman spectrum, originating from the uranyl symmetric stretch ($\nu_1(\mathrm{UO}_2)^{2+}$). The exact position of this peak has been found to vary for different samples; for nováčekite, this mode is seen at 817 cm^{-1}, whereas the corresponding peak for its phosphate analogue, saléeite, is ∼830 cm^{-1} [69, 70]. A variety of factors appear to influence the position of this peak, including the electronegativity of anions in the equatorial plane of the uranyl cation and the nature of the interlayer cations. Chapter 7 presents a computational study on the autunite group of uranyl minerals, in which the polyanion (phosphate or arsenate) is systematically varied to study the effect on the Raman and IR spectra.

Chapter 7

Simulations of the Autunite Minerals

In this chapter, density functional theory (DFT) has been used to simulate the structural and vibrational properties of a selection of autunite minerals, with the aim of assigning the peaks seen in experimental Raman and IR spectra. This is possible because the motions corresponding to each vibrational mode are calculated during the simulations. The second major aim of this investigation is to probe how the simulated vibrational spectra vary with different mineral compositions. Chapter 6 showed that the vibrational spectra may be used to distinguish between uranyl minerals, based on characteristic polyanion bands and the position of the uranyl symmetric stretching mode [206]. The latter effect is known to be directly related to the strength of the uranyl bond [355], which is influenced by the groups that coordinate around the uranyl equatorial plane. Therefore, determining the effect of different polyanions and uranium environments on the vibrational spectra of uranyl minerals and combining this information with a database of known experimental spectra would be valuable to forensic and environmental science investigations, where rapid analysis of unknown samples is essential.

The uranyl minerals chosen for this investigation are from the autunite group, which have been described in detail in Chapter 6. These minerals are ideal for a systematic investigation, as they contain isostructural phosphate and arsenate members that exhibit known differences in experimental Raman and IR spectra. The minerals simulated were the uranyl phosphates torbernite and saléeite, their respective isostructural arsenates, zeunerite and nováčekite, and five intermediate structures for each of the two series, containing different proportions and distributions of phosphorus and arsenic. The simulated vibrational spectra for the two series of minerals were used to identify a set of trends that may be used to quickly estimate the ratio of phosphorus to arsenic within experimental samples. A set of spectra for four experimental mineral samples were used as a trial to estimate the P:As ratio, with EDX data used to corroborate the composition.

Many experimental investigations of the autunite minerals have been reported and are reviewed in Chapter 6, but no computational studies have been forthcoming. However, the link between local environment and the vibrational mode has been studied for a range of uranyl complexes, so this is the focus of the review in Section 7.1. Details on

the computational models used are given in Section 7.2, while the EDX data for the experimental samples used for comparison is given in Section 7.3.

7.1 Review of Literature

In Chapter 6, the position of the uranyl symmetric stretching mode in the Raman spectrum was shown to vary in different uranyl minerals. The position of this stretching mode depends upon the uranyl bond strength, which is influenced by the local electronic environment [356]. As density functional theory (DFT) simulations explicitly model the electron density, it is ideally suited to studying this relationship. It has shown that uranyl groups which are strongly coordinated in the equatorial plane transfer electron density away from the U-O bond, weakening it [356]. The equatorial binding strength is dependent upon the nature and number of coordinated groups and has been primarily investigated using uranyl complexes. Therefore, the effect caused by different coordinated ligands on the position of the uranyl symmetric stretching mode in the Raman spectrum may be used as a strategy for distinguishing between them [355].

The coordination environment for uranyl-water complexes has been extensively studied [357–361] and found to preferentially adopt an equatorial coordination number of five. DFT studies support this configuration [360, 362–364], but also find that more basic ligands, such as OH^-, reduce this number [365–367]. Uranyl complexes with CN^-, NCS^- and F^- were also found to prefer an equatorial coordination number of five [366, 368–370]. DFT simulations of CN^- demonstrated that it preferentially coordinates to the uranyl cation through the carbon atom [367, 371, 372]. The carbonate anion (CO_3^{2-}) is another ligand that has been extensively studied in uranyl complexes. The uranyl tricarbonate cluster, $UO_2(CO_3)_3$, is among the most significant uranyl species in contaminated groundwater [271, 373], while UO_2CO_3 occurs naturally as the mineral rutherfordine. The structural properties of uranyl carbonates have been studied using DFT techniques [374–376]. The general trends observed for uranyl complexes show that an increase in coordination number and more electron donating ligands weaken the uranyl bond, which in turn reduces the wavenumber of the uranyl symmetric stretching mode [355, 377, 378].

The mobility of uranyl complexes is also an important consideration in remediation of contaminated sites. Adding certain ligands to soil, such as citrate [355], may increase the mobility of the uranyl cation, allowing it to be extracted [379, 380]. An alternative approach relies on the uranyl cation reacting with inorganic materials, such as clays,

forming immobile uranyl minerals [6, 20–28]. The diffusion and adsorption of uranyl cations and uranyl carbonate complexes onto different mineral surfaces, such as montmorillonite, quartz, beidellite, pyrophyllite, goethite and calcite, have been the subject of many potential model [152, 381–390] and DFT [391–400] investigations.

7.2 Structures and Models

Initial structures of the minerals saléeite ($Mg(UO_2)_2(PO_4)_2 \cdot 10H_2O$) and meta-torbernite ($Cu(UO_2)_2(PO_4)_2 \cdot 8H_2O$) were taken from previously published crystal structure data [243, 401]. The isostructural arsenate minerals, nováčekite and meta-zeunerite, and the intermediate structures were generated by substituting appropriate phosphorus atoms for arsenic. Meta-torbernite ($n = 8$ water molecules) was chosen as a base structure instead of torbernite ($n = 12$ water molecules) because it is also a very common mineral in uranium deposits [14, 251] and fewer water molecules reduced the number of vibrational degrees of freedom. Furthermore, the uranyl and polyanion stretching modes of primary interest to this study are typically found in the 650–1100 cm^{-1} region, which does not vary significantly between torbernite and meta-torbernite [69], whereas water vibrations tend to be at a significantly higher wavenumber. Therefore, minerals from the meta-torbernite–meta-zeunerite series have been referred to as torbernite–zeunerite throughout this chapter.

The saléeite and torbernite structures contain two formula units per unit cell. In both cases, two layers exist within the unit cell, containing two inequivalent phosphate polyanions in each. In addition to the pure phosphate and pure arsenate versions of each mineral, intermediate phases with P:As ratios of 3:1, 2:2 and 1:3 have been generated and are labelled as P_xAs_y throughout this chapter, where x and y are the relative proportions of P and As. Three distinct distributions of P_2As_2 are possible:

- Phosphate and arsenate polyanions are separated into alternating layers (P_2As_2a);

- Mixed layers of phosphate and arsenate polyanions are present and adjacent layers can be superimposed (P_2As_2b);

- Mixed layers of phosphate and arsenate polyanions are present, but adjacent layers cannot be superimposed (P_2As_2c).

Schematics showing the autunite type sheet structure, the environment of Mg^{2+} and
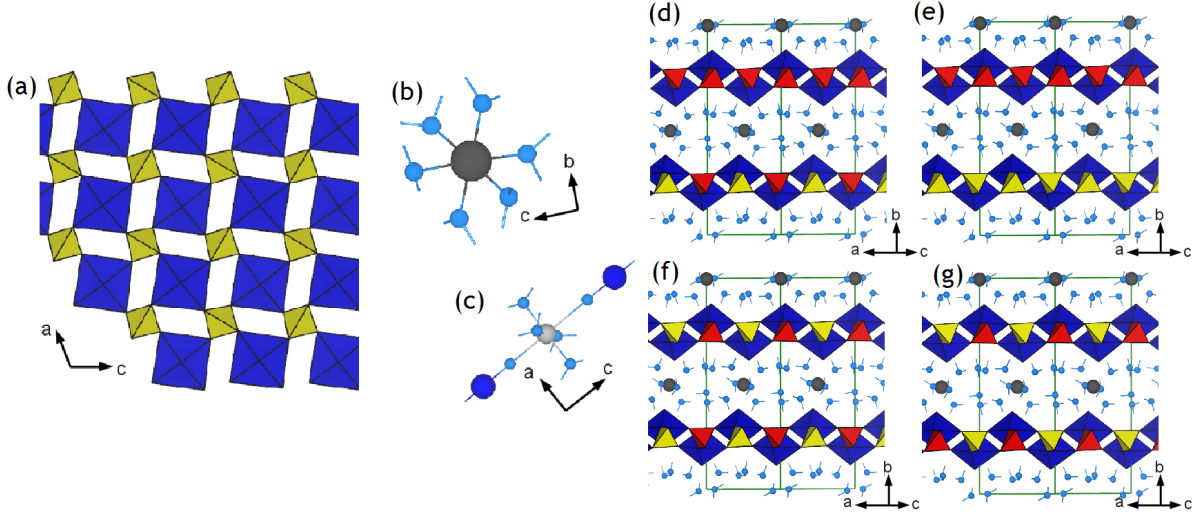
Figure 7.1: (a) The autunite sheet structure and the cation environments in (b) saléeite and (c) torbernite. The layers seen in (d) the P_3As_1 and P_1As_3 systems, (e) the P_2As_2a alternating layers structure, (f) the P_2As_2b aligned layers structure, and (g) the P_2As_2c offset layers structure. Dark blue polyhedra represent uranyl cations, while yellow and red polyhedra represent PO_4 and AsO_4, as appropriate. Mg^{2+} and Cu^{2+} are shown in grey and water molecules are shown in light blue.

Cu^{2+} cations in saléeite and torbernite, respectively, the P_1As_3 and P_3As_1 structure and each P_2As_2 configuration are presented in Figure 7.1.

For each structure, the unit cell volume and shape were fully relaxed with unconstrained symmetry. The ionic and electronic convergence criteria were 0.01 eV/$\mathring{A}$ and 1×10^{-6} eV/atom, respectively, while testing showed that a cutoff energy of 500 eV is appropriate. For the torbernite–zeunerite series, a 4 x 4 x 1 k-point mesh (10 irreducible k-points) was used, while testing showed that a 4 x 1 x 2 mesh (6 k-points) gave the same result as a 4 x 1 x 4 mesh (10 k-points) for the saléeite–nováčekite series, so the smaller number of k-points was chosen.

The energy of forming each structure (E_m) from γ-UO_3 via the reaction

$$2(\gamma\text{-}UO_3) + M_3(XO_4)_2 + n(H_2O)(s) \rightarrow M(UO_2)_2(XO_4)_2 \cdot nH_2O + 2(MO), \qquad (7.1)$$
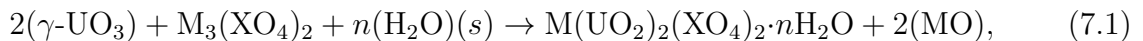
where M is the interlayer cation (Mg^{2+} or Cu^{2+}), X is P or As and n is the number of water molecules, was determined by summing the calculated lattice energies of the reactants and subtracting them from the sum of lattice energies of the products. The lattice energies for each material were calculated using the same computational settings as the autunite materials; the minimised lattice parameters and volume and the k-point

Table 7.1: The structural parameters and k-point meshes for the experimental and minimised $M_3(XO_4)_2$ and MO structures used to calculate E_m for the simulated saléeite, nováčekite, torbernite, zeunerite and mixed structures using Equation 7.1.

System	Lattice Parameters						Volume	Z
	a (Å)	b (Å)	c (Å)	α (°)	β (°)	γ (°)	(Å^3)	
Expt. $Mg_3(PO_4)_2$ [402]	7.60	8.23	5.08	90.0	94.1	90.0	316.6	2
$Mg_3(PO_4)_2$	7.73	8.34	5.12	90.0	94.2	90.0	164.8	2
$Mg_3(AsO_4)_2$ †	7.94	8.46	5.36	90.0	95.7	90.0	179.0	2
Expt. $Cu_3(PO_4)_2$ [403]	4.85	5.29	6.18	72.4	87.0	68.5	140.5	1
$Cu_3(PO_4)_2$	4.96	5.75	6.23	74.1	87.5	66.6	156.6	1
$Cu_3(AsO_4)_2$ †	5.10	5.64	6.45	71.8	86.8	67.8	162.9	1
Expt. MgO	4.22	4.22	4.22	90.0	90.0	90.0	75.0	4
MgO	4.26	4.26	4.26	90.0	90.0	90.0	77.6	4
Expt. CuO [404]	4.68	3.42	5.13	90.0	99.6	90.0	81.1	4
CuO	4.45	3.83	5.17	90.0	92.0	90.0	88.1	4

† The initial structures of $Mg_3(AsO_4)_2$ and $Cu_3(AsO_4)_2$ were adopted from the experimental structures of $Mg_3(PO_4)_2$ and $Cu_3(PO_4)_2$, respectively.

mesh used for each material is given in Table E.1. The energy used for water corresponds to the sum of the calculated energy for a single H_2O molecule in VASP and the difference between the experimentally determined enthalpies of formation of solid and gaseous H_2O. The energy for γ-UO_3 was known from Chapter 5. These values allowed the most stable P_2As_2 configurations to be determined.

The intermediate systems described in this study are mixed structures, containing an even distribution of phosphorus and arsenic. However, an alternative model for these systems contains discrete domains of the end minerals saléeite, nováčekite, torbernite and zeunerite. To investigate the relative stabilities of these two types of system, appropriate proportions of E_m for the end minerals were summed to determine the corresponding domain formation energies (E_d).

Following the successful minimisation of each structure, the vibrational modes were calculated using density functional perturbation theory (Section 3.5.2). Raman and IR activities were then calculated as described in Sections 3.5.4 and 3.5.3. As torbernite and saléeite are known to adopt preferred orientations with respect to the host rock (<001> and <010>, respectively), Equation 3.39 was used to calculate the Raman activity directly.

7.3 Experimental Samples for Comparison

The Raman and IR spectra have been collected for four autunite group minerals, with the aim of providing a trial for estimating the P:As ratio based on the trends observed in Section 7.4.2. Three of these minerals were torbernite–zeunerite samples from the same collection that was studied by Elton and Hooper [212] and described in Chapter 6. The fourth was the nováčekite sample presented in Chapter 6. Raman, IR and EDX spectra were collected using the methods described in Chapter 2 and chemical formulae and P:As ratios determined from EDX data is given in Table 7.2.

Table 7.2: Estimated chemical formulae based on EDX data for autunite mineral samples from Cornwall, UK. The formulae are normalised to the proportion of uranium and water content is not estimated. The P:As ratio is also provided.

Mineral	Provenance	Estimated formula	P:As ratio
torbernite	Old Gunnislake Mine, Calstock	$Cu_{0.8}(UO_2)_2(PO_4)_{2.0}(AsO_4)_{0.1}$	36:1
zeunerite	South Wheal Basset, Redruth	$Cu_{1.0}(UO_2)_2(PO_4)_{0.1}(AsO_4)_{1.9}$	1:25
mixed torbernite	West Wheal Owles, St. Just	$Cu_{0.9}(UO_2)_2(PO_4)_{1.2}(AsO_4)_{0.7}$	2.5:1
mixed nováčekite	Wheal Edward, St. Just	$Mg_{0.7}(UO_2)_2(PO_4)_{0.3}(AsO_4)_{1.2}$	1:3.6

7.4 Results and Discussion

Fourteen mineral structures have been simulated using DFT. These were the uranyl phosphate minerals torbernite and saléeite, the isostructural arsenate minerals zeunerite and nováčekite, respectively, and five intermediate phases for each series. The structural and vibrational properties of these minerals are presented in Sections 7.4.1 and 7.4.2, respectively, and a comparison is made to experimental spectra in Section 7.4.3.

7.4.1 Structural Parameters

The structural properties obtained from minimising the fourteen mineral structures are given in Table 7.3. Experimental values are also given for the four end members, saléeite, nováčekite, torbernite and zeunerite, which show that the structures have been well represented. The unit cell volume after minimisation is increased by less than 4% compared to the experimental structure; a volume increase is a known effect of the GGA functional. It should be noted that experimental nováčekite was described with a different

Table 7.3: A comparison of experimental and simulated structural parameters for saléeite, nováčekite, torbernite and zeunerite, in addition to the simulated stuctural parameters for the intermediate phases. The general formula for these systems is $M(UO_2)_2(XO_4)_2 \cdot nH_2O$, where M is Mg^{2+} or Cu^{2+}, X is P or As and n represents a variable number of water molecules. Two formula units are present in each unit cell for these systems. The reaction energies for forming each phase from γ-UO_3 via Equation 7.1 (E_m) and the energies for forming domains of the end minerals instead of mixed phases (E_d) are given.

Phase	Lattice Parameters						Volume	E_m	E_d
	a (Å)	b (Å)	c (Å)	α (°)	β (°)	γ (°)	(Å^3)	(eV)	(eV)
Saléeite ($Mg(UO_2)_2(PO_4)_2 \cdot 10H_2O$) – Nováčekite ($Mg(UO_2)_2(AsO_4)_2 \cdot 10H_2O$)									
Expt. P_4 [243]	6.951	19.947	9.896	90.0	135.2	90.0	967.34	—	—
Sim. P_4	7.019	19.944	10.022	89.8	135.3	90.3	986.12	-0.78	—
P_3As_1	7.057	19.984	10.079	89.7	135.4	90.4	998.89	-0.89	-0.83
P_2As_2a	7.084	20.056	10.134	89.8	135.4	90.4	1011.86	-0.93	-0.88
P_2As_2b	7.093	20.033	10.153	89.8	135.4	90.5	1013.43	-0.67	-0.88
P_2As_2c	7.087	20.062	10.142	89.8	135.4	90.3	1013.14	-0.67	-0.88
P_1As_3	7.129	20.086	10.221	89.8	135.4	90.4	1027.21	-0.93	-0.93
Sim. As_4	7.178	20.111	10.285	89.7	135.4	90.4	1042.33	-0.98	—
Expt. As_4 [405] †	7.157	20.085	10.053	90.0	134.8	90.0	1025.22	—	—
Torbernite ($Cu(UO_2)_2(PO_4)_2 \cdot 8H_2O$) – Zeunerite ($Cu(UO_2)_2(AsO_4)_2 \cdot 8H_2O$)									
Expt. P_4 [217]	6.98	6.98	17.35	90.0	90.4	90.0	845.27	—	—
Sim. P_4	7.047	7.047	17.395	90.0	90.0	90.0	863.78	-2.99	—
P_3As_1	7.084	7.084	17.423	90.0	90.0	90.0	874.24	-2.88	-2.93
P_2As_2a	7.124	7.124	17.487	90.0	90.0	90.0	887.50	-2.78	-2.86
P_2As_2b	7.122	7.122	17.486	90.0	90.0	90.0	886.99	-2.55	-2.86
P_2As_2c	7.124	7.124	17.482	90.0	90.0	90.0	887.27	-2.55	-2.86
P_1As_3	7.163	7.163	17.549	90.0	90.0	90.0	900.50	-2.74	-2.80
Sim. As_4	7.210	7.210	17.562	90.0	90.0	90.0	912.97	-2.73	—
Expt. As_4 [217]	7.109	7.109	17.416	90.0	90.0	90.0	880.27	—	—

The experimental parameters for nováčekite, metatorbernite and metazeunerite correspond to synthetic end members.

† The space group origin of experimental nováčekite (originally $P2_1/c$) [405] was changed to allow a direct comparison with the saléeite structure ($P2_1/n$) [243].

space group origin ($P2_1/c$ [405]) to saléeite ($P2_1/n$ [243]), so the origin has been changed for the former in Table 7.3, allowing the experimental structural parameters to be directly compared with the simulated parameters.

The lattice parameters for nováčekite and zeunerite are approximately 0.2 Å greater than for the corresponding phosphate minerals. This trend is also observed in the intermediate phases; however, the average distances between uranium and the oxygen atoms in the phosphate or arsenate groups remain ~2.34 Å in all structures (Figure 7.4). Therefore, to accomodate both phosphate and arsenate polyanions in the intermediate systems,

Table 7.4: A comparison of average bond distances found in saléeite, nováčekite, torbernite zeunerite and the intermediate phases. These are the P-O and As-O bonds found in the PO_4 and AsO_4 polyanions and the U-O bonds between the uranium atoms and the same polyanion oxygen ions.

Phase	Average bond distance			Phase	Average bond distance		
	P–O (Å)	As–O (Å)	U–O (Å)		P–O (Å)	As–O (Å)	U–O (Å)
	saléeite–nováčekite				torbernite-zeunerite		
P_4	1.55	—	2.34	P_4	1.56	—	2.35
P_3As_1	1.56	1.71	2.34	P_3As_1	1.56	1.71	2.35
P_2As_2a	1.56	1.72	2.34	P_2As_2a	1.56	1.71	2.35
P_2As_2b	1.56	1.71	2.34	P_2As_2b	1.56	1.71	2.35
P_2As_2c	1.56	1.71	2.34	P_2As_2c	1.56	1.71	2.35
P_1As_3	1.56	1.72	2.34	P_1As_3	1.56	1.72	2.35
As_4	—	1.72	2.33	As_4	—	1.72	2.34

there must be a deviation in the bond angles.

The energies of formation (E_m) have been calculated from Equation 7.1 for the energy minimised structures and are presented in Table 7.3. These data indicate that the most stable P_2As_2 mixed phase in both torbernite–zeunerite and saléeite–nováčekite series are P_2As_2a, in which the phosphate and arsenate polyanions are found within alternating layers of the structure. Therefore, only Raman and IR spectra corresponding to P_2As_2a are presented and discussed in this chapter; spectra for the other configurations are given in Appendix E.

The energies of forming intermediate systems comprised of distinct domains (E_d) of the end minerals saléeite, nováčekite, torbernite and zeunerite have also been calculated for each mixed system (Table 7.3). For the mixed phase saléeite–nováčekite minerals, values of E_d were found to be less negative than the corresponding values of E_m (with the exception of the P_2As_2b and P_2As_2c systems), indicating that the mixed phase minerals are more stable. In contrast, discrete domains (E_d) of torbernite and zeunerite were found to be more stable than mixed systems (E_m). However, for all mixed systems (except the P_2As_2b and P_2As_2c systems), the difference in energy between E_m and E_d was less than ± 0.1eV, suggesting that mixed phases and domains of end minerals may be competitive.

The preference for domains of torbernite and zeunerite instead of mixed phases may be rationalised by considering the volume of all four end members. saléeite, nováčekite, torbernite and zeunerite all have the same number of formula units per unit cell, but the

latter minerals have two fewer water molecules per formula unit. This may be corrected by adding 120 Å^3 to the calculated volume (the volume of a single water molecule is $\sim$120 Å^3 [406]). The corrected volumes of the phosphate minerals saléeite (986.12 Å^3) and torbernite (983.78 Å^3) are very similar, whereas the corresponding values for the arsenate minerals nováčekite (1042.33 Å^3) and zeunerite (1032.97 Å^3) are significantly different. The smaller volume indicates that the structure adopted by zeunerite is more efficiently packed than nováčekite, so defects (e.g. the intermediate phases) are less favourable. Hence, domains of the torbernite and zeunerite minerals are preferred over mixed phases, whereas the saléeite–nováčekite systems can readily accommodate mixtures.

7.4.2   Simulated Raman and IR Spectra

The simulated Raman and IR spectra for structures in the torbernite–zeunerite and saléeite–nováčekite are shown in Figures 7.2 and 7.3, respectively. As the most significant peaks are found between 650–1050 cm^{-1} in both Raman and IR spectra, only this region is displayed in this chapter. Extended spectra of the 100–1100 cm^{-1} region are provided in Appendix E for all structures, alongside tables that describe the vibrational motions calculated for each individual mode.

One notable deviation observed between experimental and simulated spectra is the shift in peak positions to a lower wavenumber in the latter. This results from the DFT functional being used and may be corrected using a scaling factor. Alternatively, a more intensive quantum mechanical technique could be employed to improve the comparison, but the size of the unit cells in this investigation mean that significant computer resources would be required. An additional difference is found in the number of peaks in simulated and experimental spectra. In simulations, every unit cell contains an identical set of environments, so every vibrational mode has a discrete value. In contrast, equialent environments in different unit cells of experimental structures often have some variation, leading to a distribution of vibrational modes. Analysis of individual modes in the simulated spectra showed that modes with similar motions tend to be found close together. The 700–850 cm^{-1} region was primarily occupied by uranyl and arsenate symmetric stretching and arsenate antisymmetric stretching modes, while the 900–1050 cm^{-1} region contains uranyl and phosphate antisymmetric stretching modes. Therefore, the labels given in Figures 7.2 and 7.3 are weighted averages for the major peaks within each of the two regions.

The uranyl symmetric stretching mode is observed in the simulated Raman spectra for
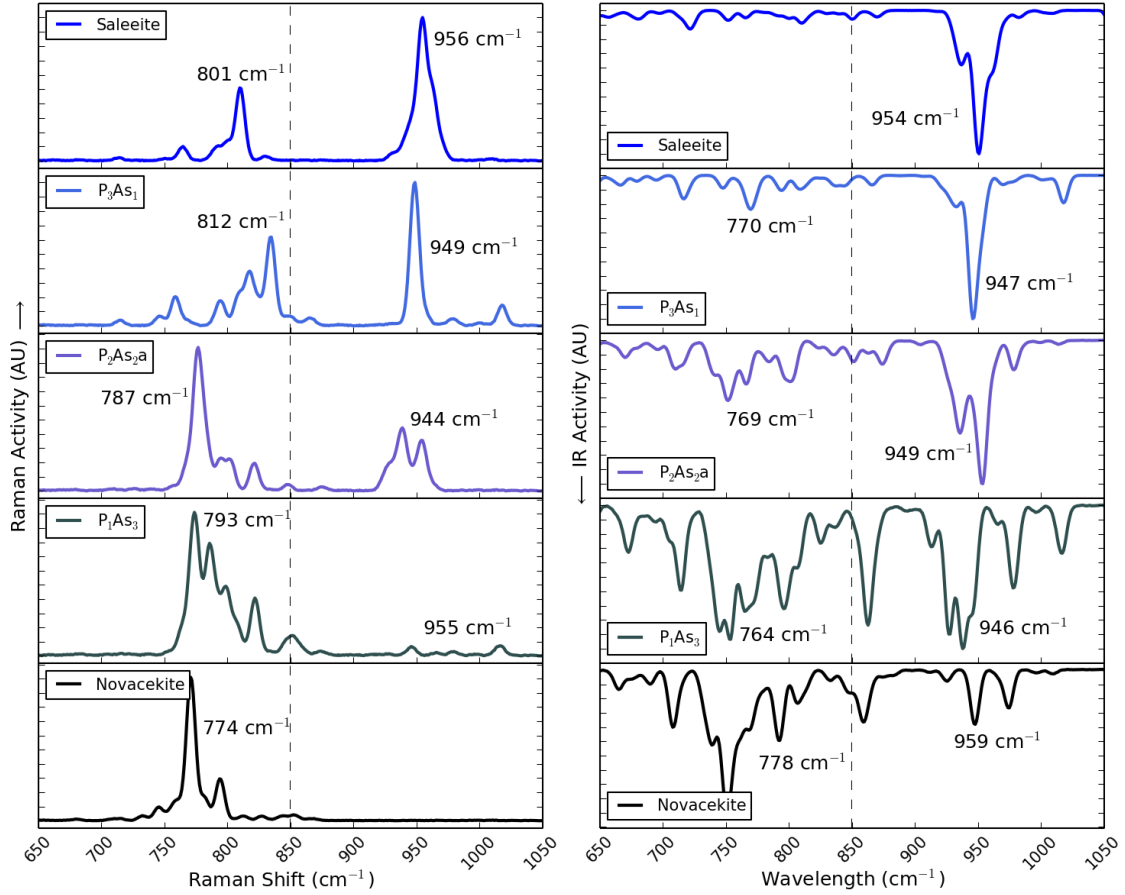
Figure 7.2: The simulated Raman (left) and IR (right) spectra for saléeite, nováčekite and the mixed P:As phases. The labels show the weighted average wavenumber of the uranyl, phosphate or arsenate modes within each region.

all structures in the 750–850 cm^{-1} region. The position of these modes are found to be higher in spectra of the phosphate end members than in the isostructural arsenate end members. This trend has also been reported for experimental spectra of autunite minerals [69, 206]. It is possible that this results from a weakening of the uranyl bond when coordinated to the larger arsenate anions (e.g. average U-O bond length 1.788 Å in saléeite, 1.792 Å in nováčekite). A further observation in experimental spectra is the broadening of the uranyl symmetric stretching mode for arsenate minerals. This has been explained as the uranyl symmetric stretch overlapping with the arsenate symmetric and antisymmetric stretching modes [69], which fits with the presence of arsenate stretches in this region. The intermediate phases for each series display a greater number of discrete peaks within this region, which may be expected, since the presence of both phosphate and arsenate groups increase the number of symmetrically distinct uranyl environments. This might also broaden the peaks in experimental spectra; a lack of significant broadening may instead indicate that the phosphate and arsenate minerals
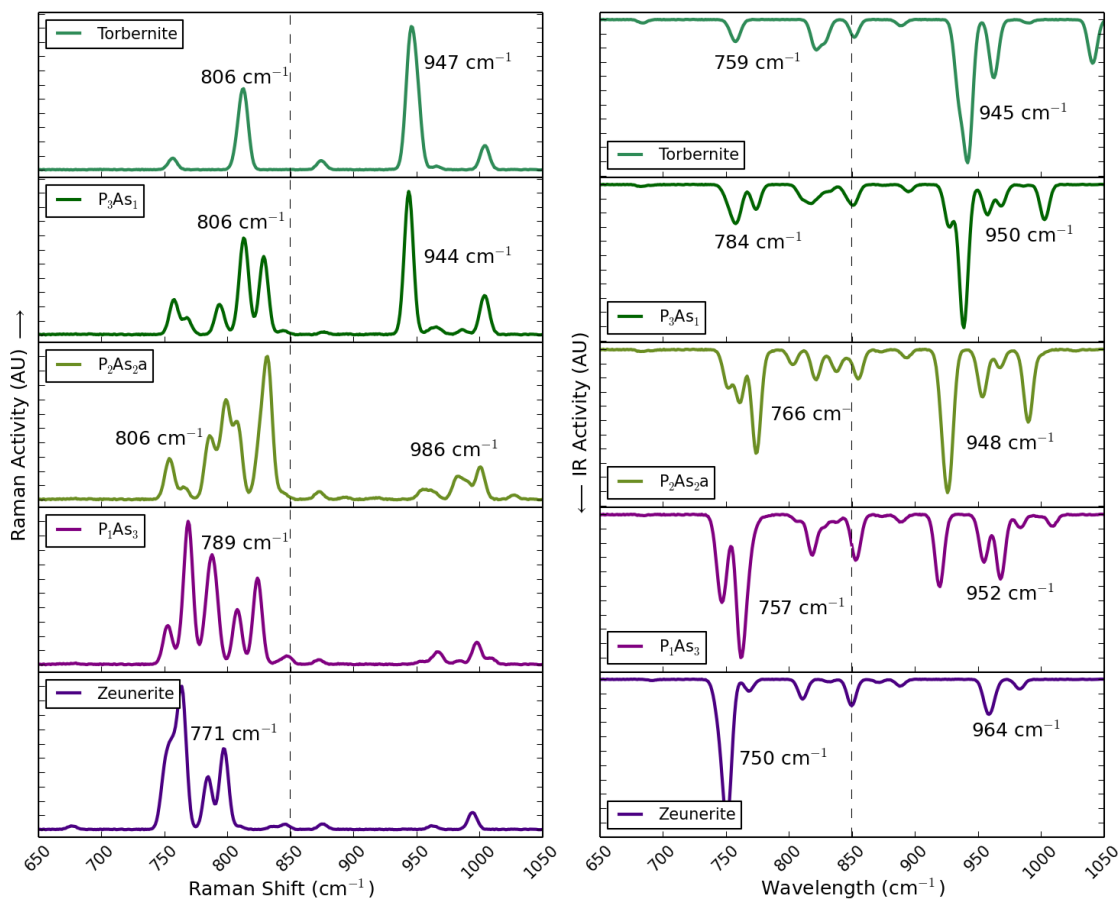
Figure 7.3: The simulated Raman (left) and IR (right) spectra for torbernite, zeunerite and the mixed P:As phases. The labels show the weighted average wavenumber of the uranyl, phosphate or arsenate modes within each region.

exist in distinct domains, rather than mixed phases.

The phosphate antisymmetric stretching mode is observed in the 940–1000 cm^{-1} region of both simulated and experimental Raman spectra for the phosphate dominant autunite minerals [206]. No peaks are observed in this region of the isostructural arsenate minerals that correspond to phosphate stretches; however, the uranyl antisymmetric stretching mode is sometimes observed as a low intensity mode here. The simulated intermediate phases also carry this trend, with the intensity of the phosphate peak diminishing with increasing arsenic content. It is observed in the P$_3$As$_1$ spectra of both series of structures, but the only P$_2$As$_2$ phase it is found in is P$_2$As$_2$a of the saléeite–nováčekite series. This structure contains phosphate and arsenate polyanions in alternating layers, suggesting that a full layer of phosphate groups are required for this peak to be observed. The phosphate symmetric stretch was found to be absent in both experimental [69, 206] and our simulated Raman and IR spectra of the autunite minerals; this mode is expected at

$\sim$920 cm^{-1}, based on the experimental spectra of aqueous phosphate ions [73]. However, the corresponding motions were located in a number of Raman and IR inactive modes. Within these modes, the phosphate symmetric stretch was only present for the phosphate ions in a single layer; therefore, the overall motion of the system does not fulfil the selection rules required to be Raman or IR active.

Two major trends are observed in the simulated IR spectra of the autunite minerals. First, the intensity of the combined uranyl and phosphate antisymmetric stretching modes (940–1050 cm^{-1}) diminish with increasing arsenic content, with only a weak uranyl antisymmetric stretching mode in zeunerite and nováčekite. Second, the combined uranyl symmetric stretch and arsenate symmetric and antisymmetric stretching modes (750–800 cm^{-1}) become more intense with a greater proportion of arsenic. This peak is most significant in spectra of zeunerite, nováčekite and the P$_1$As$_3$ phases.

7.4.3 Experimental Comparison

Experimental Raman and IR spectra are shown in Figures 7.4–7.7 for samples of torbernite, zeunerite, torbernite with some arsenic and nováčekite with some phosphorus. The trends observed in the simulated spectra (Section 7.4.2) are used to estimate the relative proportion of phosphorus and arsenic in each sample and simulated spectra for structures with a similar P:As ratio is also presented in each Figure. The P:As ratios of experimental samples were determined using EDX and are given in Table 7.2.
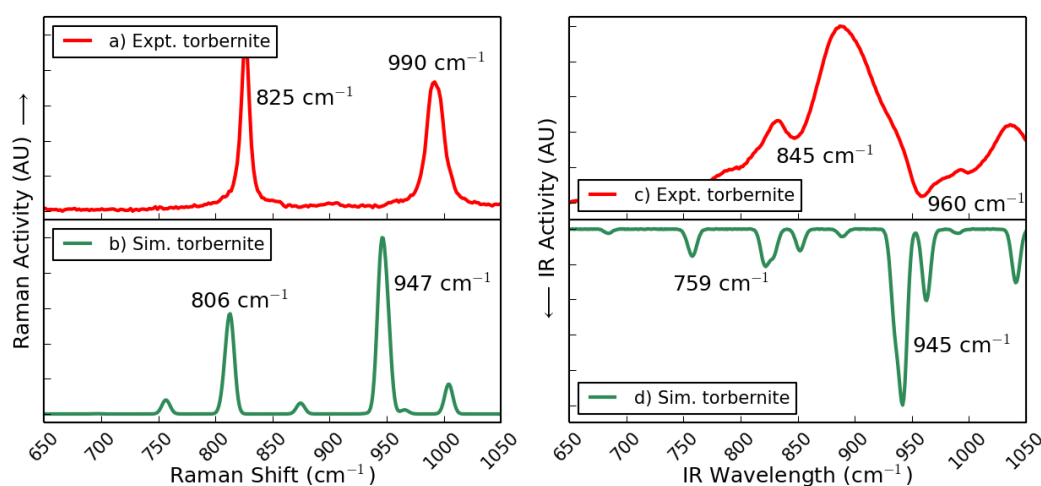
Figure 7.4: The experimental a) Raman and c) IR spectra of torbernite from Old Gunnislake Mine, collected using a 532 nm excitation laser. The P:As ratio, determined by EDX spectroscopy, is 36:1. Simulated b) Raman and d) IR spectra for the pure torbernite structure (P$_4$) is given as a comparison.
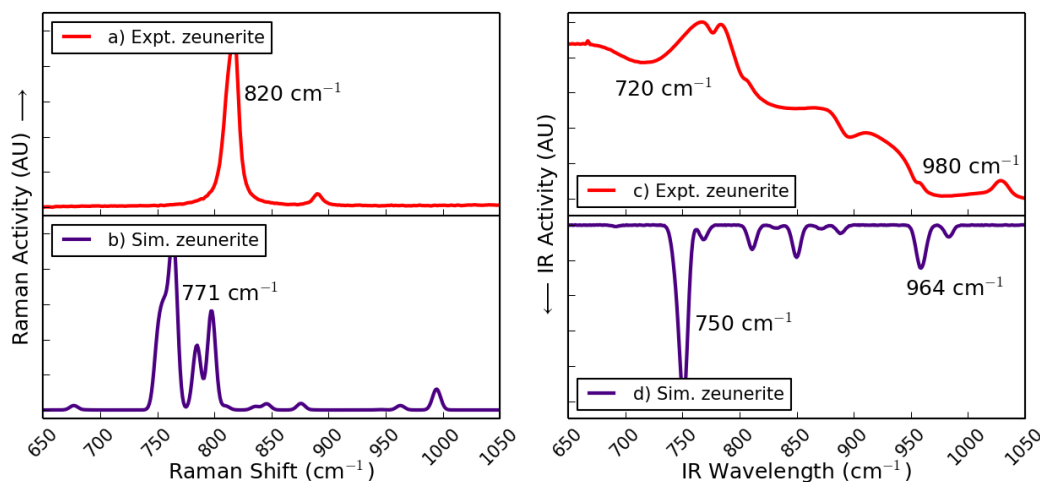
Figure 7.5: The experimental a) Raman and c) IR spectra of zeunerite from South Wheal Basset, collected using a 532 nm excitation laser. The P:As ratio, determined by EDX spectroscopy, 1:25. Simulated b) Raman and d) IR spectra for the pure zeunerite structure (As_4) is given as a comparison.

The EDX data for torbernite from Old Gunnislake Mine shows a 36:1 ratio of P:As, so it is expected to produce Raman and IR spectra similar to the simulated P_4 structure (pure torbernite). Its Raman spectrum, shown in Figure 7.4, is dominated by a sharp peak at $\sim$825 cm^{-1} and a broader peak at $\sim$990 cm^{-1}, assigned to the uranyl symmetric stretch and phosphate antisymmetric stretching modes, respectively. The relative intensities of these modes correspond well with the equivalent peaks in the simulated Raman spectra of both the torbernite and P_3As_1 structures. Similarly, the peaks at $\sim$845 and 960 cm^{-1} in the experimental IR spectrum agree well with the simulated modes at $\sim$759 and 945 cm^{-1}, the first attributed to the uranyl symmetric stretch and the latter corresponding to the phosphate antisymmetric stretching mode. Therefore, both Raman and IR spectra indicate that this sample is pure torbernite or the P_3As_1 intermediate structure, which agrees with the 36:1 P:As ratio ($P_{3.89}As_{0.11}$) determined by EDX.

EDX data for zeunerite from South Wheal Basset shows a 1:25 P:As ratio, suggesting that the Raman and IR spectra will be similar to those for the simulated As_4 structure (pure zeunerite). The Raman spectrum in Figure 7.5 is dominated by a broad peak at $\sim$820 cm^{-1}, corresponding to the combined uranyl symmetric, arsenate symmetric and arsenate antisymmetric stretching modes. This assignment is also given to the peak at $\sim$720 cm^{-1} in the IR spectrum. No peaks corresponding to the phosphate antisymmetric stretch are observed in Raman or IR spectra, but a low intensity IR mode at $\sim$980 cm^{-1} may be attributed to the uranyl antisymmetric stretch, seen at 964 cm^{-1} in the simulated spectrum. These assignments indicate that this sample is pure zeunerite or the P_1As_3
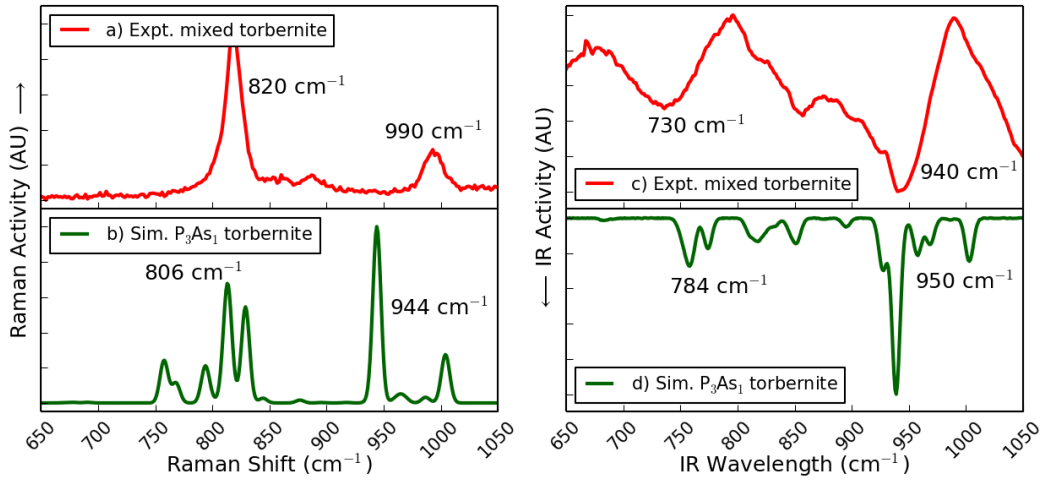
Figure 7.6: The experimental a) Raman and c) IR spectra of a mixed torbernite–zeunerite sample from West Wheal Owles, collected using a 532 nm excitation laser. The P:As ratio, determined by EDX spectroscopy, 2.5:1. Simulated b) Raman and d) IR spectra for the P_3As_1 mixed torbernite–zeunerite structure is given as a comparison.

intermediate structure, which fits with the 1:25 P:As ratio ($P_{0.15}As_{3.85}$) observed by EDX.

The EDX spectrum collected for torbernite from West Wheal Owles contains a 2.5:1 P:As ratio, suggesting the Raman and IR spectra will be similar to the simulated P_3As_1 spectra. The strongest Raman active mode in Figure 7.6 is seen at $\sim$820 cm^{-1} and is a broad band attributed to the uranyl symmetric stretch. The phosphate antisymmetric stretching mode is also present as a lower intensity band at $\sim$990 cm^{-1}, which indicates the proportion of phosphorus is greater than or equal to that of arsenic. Both observations suggest that more arsenic is present compared to the torbernite sample from Old Gunnislake Mine. This is further supported by the strength of the $\sim$730 cm^{-1} band in the IR spectrum, which corresponds to the uranyl symmetric, arsenate symmetric and arsenate antisymmetric stretches. However, the strength of the $\sim$940 cm^{-1} phosphate antisymmetric stretching mode in the IR spectrum indicates a high proportion of phosphorus is still present. These observations indicate that this sample of torbernite is a mixed structure, either P_3As_1 or P_2As_2, which agrees with the EDX determined P:As ratio of 2.5:1 ($P_{2.86}As_{1.14}$).

The sample of nováčekite from Wheal Edward has been described in Chapter 6 and was found to contain a P:As ratio of 1:3.6, suggesting the Raman and IR spectra will be similar to the simulated P_1As_3 spectra. Its Raman spectrum is shown in Figure 7.7 to be dominated by a broad peak at $\sim$820 cm^{-1}, assigned to the uranyl symmetric, arsenate symmetric and arsenate antisymmetric stretching modes. An equivalent IR active mode
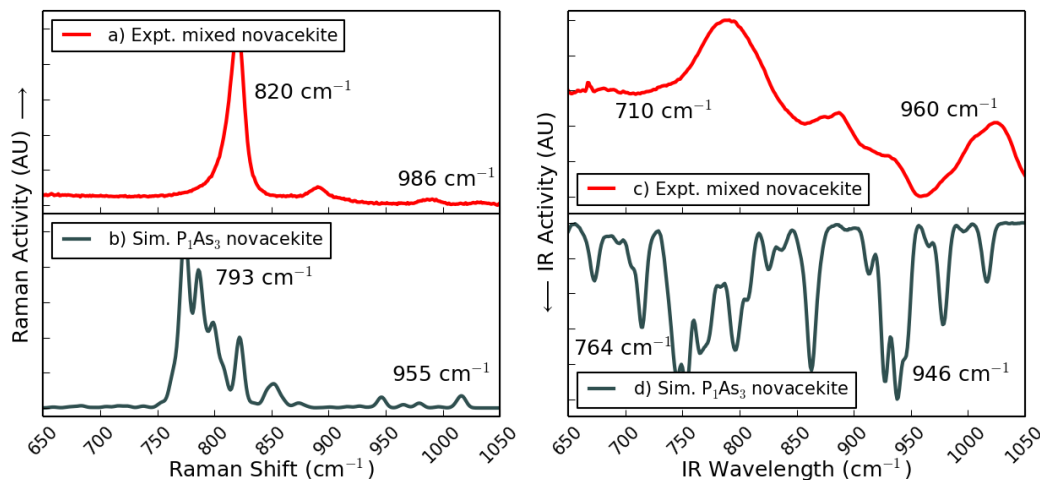
Figure 7.7: The experimental a) Raman and c) IR spectra of a mixed saléeite–nováčekite sample from West Wheal Owles, collected using a 785 nm excitation laser. The P:As ratio, determined by EDX spectroscopy, 1:3.6. Simulated b) Raman and d) IR spectra for the P_1As_3 mixed saléeite–nováčekite structure is given as a comparison.

is seen at $\sim$710 cm^{-1}, while two weaker modes are seen at $\sim$850 and 960 cm^{-1}, attributed to the arsenate symmetric stretch and a combined uranyl and phosphate antisymmetric stretch, respectively. The lack of phosphate modes in the Raman and its presence at low intensity in the IR spectrum supports a P_1As_3 assignment, which agrees with the 1:3.6 P:As ratio ($P_{0.87}As_{3.13}$) determined by EDX.

7.5 Conclusions

The structural and vibrational properties of uranyl phosphates saléeite and torbernite, the uranyl arsenates nováčekite and zeunerite and a set of intermediate structures with various proportions of phosphorus and arsenic have been successfully simulated using DFT +U methodology. The lattice parameters were well reproduced, with a resulting volume increase of <4%. The calculated formation energies for these minerals suggest that the most stable P_2As_2 mixed phase configuration is P_2As_2a, in which P and As are located in alternating layers, for both saléeite–nováčekite and torbernite–zeunerite series. Furthermore, the formation of mixed structures and discrete domains of the end minerals were found to be competitive, with only small preferences for the former in saléeite–nováčekite and the latter in torbernite–zeunerite. This is rationalised by the more efficient packing in the torbernite and zeunerite structures, which less readily accommodate defects.

One consistent deviation between experimental and simulated spectra was a shift in the

peak positions of the latter to a lower wavenumber. This is a known effect of the functional used and may be improved by applying a scaling factor. An alternative approach would be to use a more intensive quantum mechanical technique, but the computational resources required to simulate the large unit cells makes this impractical. A major advantage of using computational techniques is in linking features of the vibrational spectra to specific motions within the structure. This allows the corresponding bands in experimental spectra to be assigned to motions. It was found to be particularly valuable in complex structures containing multiple symmetrically distinct environments, as different motions may occur in each environment for a single vibrational mode.

In this investigation, the simulated spectra were used to determine a set of trends to allow the ratios of phosphorus and arsenic to be estimated for autunite minerals. The main trends observed are based on the relative intensities of two regions in both Raman and IR spectra. In the 700–900 cm^{-1} region, the peaks in both Raman and IR spectra are primarily uranyl symmetric stretches, which overlap with arsenate symmetric and antisymmetric stretches in the arsenic dominant structures. The Raman peak is found to broaden and the IR peak is more intense with increasing arsenic content. The other region is 900–1050 cm^{-1}, which includes both uranyl and phosphate antisymmetric stretching modes. In both Raman and IR spectra, the corresponding peaks are weaker with reduced phospate content, disappearing in the Raman but remaining at low intensity in the IR. This is due to the uranyl antisymmetric stretch, which is only observed in the IR spectra. These trends have been utilised to estimate the P:As ratio for a set of experimental minerals in Section 7.4.3. The estimated ratios compared well with the P:As ratio obtained by EDX for the samples, demonstrating the value of using computational techniques to predict vibrational trends and link them to structure and composition. Combining simulated and experimental data into an extensive database would be valuable for forensic or environmental science investigations, where information is needed rapidly for unidentifed samples.

Chapter 8

Conclusions and Future Work

The major conclusions of the results chapters have been summarised here, separated into four overarching areas covering the major observations and trends. The main goals outlined in Chapter 1 have been achieved: Raman spectra were collected for a selection of uranyl minerals and computational techniques were proven to be useful in the interpretation of experimental spectra and in probing how compositional variations affect the vibrational properties. Possible areas for future work have also been highlighted in the appropriate sections.

8.1   Quality of the Simulations

The simulations of U_3O_8 and UO_3, described in Chapters 4 and 5, respectively, utilised the structures previously minimised by Brincat *et al.* [49, 55], who found the majority of relaxed lattice parameters and volumes to be within 7% of the experimentally determined values. The primary exceptions were α- and β-UO_3, where the lattice parameters and U-O bond distances changed upon minimisation, supporting previous reports that these phases are non-stoichiometric and may be stabilised by the presence of defects [54, 55]. Structural parameters were also well reproduced for the four autunite group end member minerals in Chapter 7, saléeite, torbernite, nováčekite and zeunerite. For each mineral, the volume increased by <4% upon minimisation, which is a known effect of using the PBE functional.

In general, the simulated vibrational properties were found to most closely represent experimental spectra in cases where the structural parameters and local uranium environments were also well reproduced. Despite some discrepancies in the experimental spectra of γ-UO_3 (Section 5.1), the simulated Raman and IR contain bands that may correspond to the major peaks in all experimental spectra (Section 5.3). Similarly, the experimental Raman and IR spectra of U_3O_8 contain peaks that correspond well with modes in both α- and β-U_3O_8 (Section 4.3). This gives credence to the spectra predicted for η-UO_3 and other materials for which the structural properties are well reproduced but no experimental spectra are currently available.

One notable discrepancy was observed in the simulated spectra of δ-UO$_3$, which did not contain any Raman active modes, in contrast to the experimental spectrum. This prompted the use of a supercell structure with distorted uranium environments, which produced a set of Raman modes that agreed with the experimental spectrum (Section 5.3.2). Another difference between the experimental and simulated spectra was found for the autunite minerals, in which a much greater number of distinct bands were seen in the latter (Section 7.4.2). This may be rationalised because each bond distance in the experimental uranium environments can adopt a range of values, resulting in a single broad band, whereas the corresponding simulated bonds adopt a fixed value, so each vibrational mode corresponds to a distinct peak of infinitesimal width. In most cases, groups of bands within the same region of the simulated spectra were found to correspond to similar vibrational motions, allowing experimental peaks in each region to be assigned and trends to be established.

One consistent deviation between experimental and simulated spectra is a shift to lower wavenumbers in the peak positions of the latter. This is a known effect of the DFT functional used and is related to the increase in volume. The comparison may be improved by applying a scaling factor to the peak positions, but the focus of this work has been on assigning the major peaks and determining trends across multiple spectra, which has been accomplished without a scaling factor. Furthermore, defining a scaling factor for all spectra in this investigation would be difficult, as an improvement for some systems may be inappropriate for others. Using a hybrid functional or a Hartree-Fock approach may improve the comparison; however, this would require more computational resources, limiting the size of the unit cells that can be simulated. In addition, these methods would not improve the comparison between simulated and experimental spectra for structures which are known to be non-stoichiometric. A future investigation could focus on establishing the nature of the defects in these systems and incorporating them into the model.

8.2 Interpretation of Vibrational Properties

One of the major advantages of using computational techniques in this investigation is that the motions corresponding to each vibrational mode are readily available. This allows the simulated data to be utilised in assigning peaks found in the experimental Raman and IR spectra. It is particularly valuable when studying structures that contain multiple uranium environments per unit cell, as different motions may occur at each environment. In cases where all uranium environments are symmetrically equivalent, such

as δ- and η-UO$_3$, all environments perform the same motions in each mode, but may operate in- or out-of-phase (Section 5.3). β-UO$_3$ exemplifies a different type of complex vibration, as the structure contains five symmetrically distinct uranium environments that can perform different motions in the same mode. As Raman and IR activity are related to the change in dipole moment and polarisability across the entire unit cell, complex modes can result in activities that oppose those expected for the motion in a single environment. The prediction of complex modes highlights the value of using computational methods to study vibrational properties, as previous interpretations were typically based on non-interacting units [187] and could not predict vibrations that encompass the entire system.

In systems where the experimentally determined structural parameters were poorly reproduced in the simulations, the predicted spectra were also typically less well represented. However, some simulated modes were found to compare well with experimental data. This may indicate that structural features not observed experiementally, but present in the simulation, are also present in the real systems. One example of this is β-UO$_3$, which was not described with uranyl bonding, but peaks in the experimental spectra correspond well to those originating from uranyl stretches in the simulated spectra (Section 5.3.4). It is possible that uranyl bonding helps to stabilise the non-stoichiometry in this structure. Short, uranyl-like bonding is also present in the minimised 16-atom structure of δ-UO$_3$, but was not detected in experimental investigations. However, the simulated Raman spectrum of the 16-atom unit cell is dominated by a symmetric stretch of the uranyl-like bonds at 488 cm^{-1}, which agrees with the experimental peak at 520 cm^{-1} (Section 5.3.2). In contrast, the simulated spectrum of the experimentally derived 4-atom unit cell did not contain any Raman active modes, supporting the distortion in the 16-atom cell. These observations may be proven in future experimental investigations on the structures of β- and δ-UO$_3$.

The experimental Raman and IR spectra of U$_3$O$_8$ contains peaks that correspond well to those observed in simulated spectra of both α and β phases (Section 4.3). In particular, a number of modes originating from the uranyl bonding found in β-U$_3$O$_8$ suggest that this phase is the dominant one, or that both phases exist as domains within each sample. As uranyl bonding cannot exist in α-U$_3$O$_8$, due to the stacking of adjacent layers, an alternate possibility is that an intermediate configuration of layer stacking is preferred. This is another area of study for future experimental investigations on the uranium oxides.

Additional computational studies into the vibrational properties of other uranium oxides and uranyl minerals would complement an extensive database of experimental Raman and IR spectra of the same, allowing assignments to be made for peaks in the latter. Furthermore, the patterns found in both experimental and simulated spectra may allow features in samples with an unknown spectra to be identified. The structural properties of some uranium oxides have already been investigated using DFT [12], making them good initial candidates for vibrational study.

8.3   Variation in Vibrational Spectra

Previous experimental investigations of UO_3 have found that each phase forms under different conditions and may be linked to the type of reactor used. Similarly, different uranyl minerals form depending on the ions available, which can be linked to the geology of an area. This investigation has shown that the distinct uranium environments can lead to differences in the Raman and IR spectra, providing information that can be used to determine the sample origin. Therefore, an extensive database of spectra for well established samples would be a valuable tool for identifying unknown samples and their origin. This data can be complemented by using computational techniques to probe how compositional differences affect the vibrational properties.

The simulated structures of α- and β-U_3O_8 are comprised of equivalent layers, with differences arising from the stacking of adjacent layers (Section 4.2). In the simulated IR spectra of both phases, three distinct bands were observed that correspond well with a set of three modes in the experimental IR spectrum, suggesting that these bands are characteristic to the structure of the layers (Section 4.3). This indicates that U_3O_8 may be distinguished from other uranium oxides using IR spectroscopy. Futhermore, the two phases provide different Raman spectra, as the uranyl bonding in β-U_3O_8 leads to characteristic stretching modes that are not present in α-U_3O_8. The five phases of UO_3 studied in this investigation have also been shown to produce different Raman and IR spectra, arising from the varied uranium environments and bonding in each phase (Section 5.3). In addition to constructing a database for identifying unknown materials, studying the vibrational properties of other uranium oxides would provide a non-invasive strategy for following the oxidation of uranium *in situ*. This could build on existing DFT simulations of uranium oxides, such as those performed by Brincat *et al.* [12].

Experimental Raman spectra of the uranyl minerals showed the uranyl symmetric stretch in every spectrum, but variations in its position and in the presence of other characteristic

bands allowed different minerals to be distinguished (Section 6.2). The overall vibrational fingerprint arises from the combination of different polyions within the structure. For example, the Raman spectra of uranyl phosphate minerals contain a uranyl symmetric stretching mode and a phosphate antisymmetric stretching mode in the 750–850 and 950–1000 cm^{-1} regions, respectively. The Raman spectra of uranyl carbonate minerals also contain a uranyl symmetric stretching mode, while the characteristic carbonate symmetric stretch and bending modes are found at $\sim$1092 and $\sim$743 cm^{-1}, respectively.

The consistent computational approach used in this investigation allowed the variations in Raman and IR spectra resulting from a change in composition to be studied for the autunite group of minerals using DFT simulations (Chapter 7). In particular, the relative intensity of the combined uranyl and arsenate stretching modes have been shown to increase for the arsenic dominant minerals, whereas the phosphate antisymmetric stretch was found to be stronger in the phosphate minerals. These trends were used in Section 7.4.3 to estimate the relative proportions of phosphorus and arsenic in experimental samples, resulting in a good agreement to the corroborating EDX data. This suggests that further simulations of uranyl minerals could reveal other trends that can be used to distinguish between different minerals using the Raman and IR spectra. These may include systematic changes to the polyanion group, the interlayer cation, the actinyl cation or the water content, within the autunite structure or other mineral systems.

The experimental Raman spectra of some uranyl minerals, particularly johannite and phosphuranylite, displayed differences to previously published experimental spectra (Section 6.2). In the structures of the uranyl sulphate minerals johannite and natrozippeite, some of the oxygen ions coordinating to the uranium are O^{2-} and OH^{-}, but the exact proportion of each is unknown. It is likely that samples from different locations have different proportions of these ions, which could explain the observed variations in the Raman spectra. The chemical formula of phosphuranylite has also varied in different reports, suggesting that different compositions give rise to the observed variations in spectral properties. This emphasises the need to study mineral samples from different locations and indicates that hints to the origin of a sample may be found from Raman and IR spectroscopy.

8.4 Position of the Uranyl Symmetric Stretching Mode

One of the factors that makes Raman spectroscopy ideal for studying uranyl minerals and uranium oxides containing the uranyl group is the characteristic uranyl symmetric stretching mode ($\nu_1(\text{UO}_2)^{2+}$) found in the 750–900 cm^{-1} region of the spectrum. The exact position of this mode has been shown to vary, in part due to the nature of the equatorial coordination environment. Previous literature studies on uranyl complexes have indicated that an increased coordination number and more electron donating groups lead to weaker uranyl bonding, which in turn lowers the wavenumber of $\nu_1(\text{UO}_2)^{2+}$. This is exemplified in Chapter 6, where minerals with more negatively charged polyanion groups coordinating to the uranium produced lower wavenumber $\nu_1(\text{UO}_2)^{2+}$. The minerals kasolite, torbernite and natrozippeite are primarily coordinated to SiO_4^{4-}, PO_4^{3-} and SO_4^{2-} polyanions, respectively, and produce $\nu_1(\text{UO}_2)^{2+}$ modes at 760, 826 and 840 cm^{-1}. An additional difference was seen for isostructural autunite minerals containing PO_4^{3-} and AsO_4^{3-} polyanions, with a lower wavenumber $\nu_1(\text{UO}_2)^{2+}$ in the latter cases. This indicates that the larger arsenate polyanions coordinate more strongly to the uranyl cation, which weakens the uranyl bond.

The second major factor in determining the position of the $\nu_1(\text{UO}_2)^{2+}$ mode is the coordination to the uranyl oxygen ions. γ-UO$_3$ contains two symmetrically distinct uranium environments that illustrate this difference (Section 5.3.1). In environment 2, the uranyl oxygen atoms are only bound via uranyl bonding to a single uranium ion, leading to a $\nu_1(\text{UO}_2)^{2+}$ mode in the simulated spectrum at 823 cm^{-1}. In contrast, the uranyl oxygen ions in environment 1 are also coordinated to the uranium atoms in environment 2 by $\sim$2.4 Å bonds, weakening the uranyl bonding and leading to a $\nu_1(\text{UO}_2)^{2+}$ mode at 732 cm^{-1}. Similarly, the $\nu_1(\text{UO}_2)^{2+}$ mode in the simulated Raman spectrum of η-UO$_3$ is found at 658 cm^{-1}, resulting from additional coordination of the uranyl oxygen ions (Section 5.3.5). β-UO$_3$ contains five distinct uranium environments, of which three contain uranyl bonding, resulting in $\nu_1(\text{UO}_2)^{2+}$ modes ranging from 680 to 878 cm^{-1} (Section 5.3.4). The lowest wavenumber position of the $\nu_1(\text{UO}_2)^{2+}$ mode is found in the simulated Raman spectrum of 16-atom δ-UO$_3$ (Section 5.3.2). In this structure, the uranyl oxygen ions are shared with a second uranium ion at 2.3 Å, forming an extended chain of collinear U-O bonds. The associated $\nu_1(\text{UO}_2)^{2+}$ mode is observed at 488 cm^{-1}, indicating that the uranyl bonding is significantly weaker than that for β-, γ- and η-UO$_3$.

These trends have shown that the differences in uranyl environment may allow vibrational spectroscopy to be used as a tool for identifying or discriminating between uranyl based materials. This is enhanced by other differences in the Raman and IR spectra, as noted in Section 8.3, with the possibility of using this data to determine the origin of an unknown sample. The application of computational techniques allows the link between vibrational modes and structural features to be explored (Section 8.2), providing an interpretation for peaks in experimental spectra. The reproduction of experimental properties in the simulated spectra may be further improved by using more intensive methods (Section 8.1), but the majority of trends observed here would remain relevant. Collecting both experimental and simulated data into an extensive database would provide a valuable tool for use in forensic and environmental science investigations.

References

[1] Treaty on the non-proliferation of nuclear weapons. adopted and opened for signature, ratification and accession 1 July 1968, entered into force 5 March 1970, 1968.

[2] K. Mayer, M. Wallenius, I. Ray, and K-R. Lutzenkirchen. Nuclear forensic sleuths trace the origin of trafficked material. *Actinide Research Quarterly*, 4:1, 2007.

[3] C. Jégou, R. Caraballo, J. de Bondils, V. Broudic, S. Peuget, T. Vercouter, and D. Roudil. Oxidizing dissolution of spent MOX47 fuel subjected to water radiolysis: Solution chemistry and surface characterization by Raman spectroscopy. *Journal of Nuclear Materials*, 399:68 − 80, 2010.

[4] P. S. Bagus and E. S. Ilton. Theory for the XPS of actinides. *Topics in Catalysis*, 56:1121 − 1128, 2013.

[5] D. E. Crean, F. R. Livens, M. C. Stennett, D. Grolimund, C. N. Borca, and N. C. Hyatt. Microanalytical X-ray imaging of depleted uranium speciation in environmentally aged munitions residues. *Environmental Science and Technology*, 48:1467 − 1474, 2014.

[6] L. Newsome, K. Morris, and J. R. Lloyd. The biogeochemistry and bioremediation of uranium and other priority radionuclides. *Chemical Geology*, 363:164 − 184, 2014.

[7] A. Walshe, T. Prussmann, T. Vitova, and R. J. Baker. An EXAFS and HR-XANES study of the uranyl peroxides $[UO_2(\eta^2\text{-}O_2)(H_2O)_2]\cdot nH_2O$ (n=0, 2) and uranyl (oxy)hydroxide $[(UO_2)_4O(OH)_6]\cdot 6H_2O$. *Dalton Transactions*, 43:4400 − 4407, 2014.

[8] S. J. Zinkle and G. S. Was. Material challenges in nuclear energy. *Acta Materialia*, 62:735 − 758, 2013.

[9] World Nuclear Association. `www.world-nuclear.org/`. Accessed 19/05/2016.

[10] P. Nerikar, T. Watanabe, J. S. Tulenko, S. R. Phillpot, and S. B. Sinnott. Energetics of intrinsic point defects in uranium dioxide from electronic-structure calculations. *Journal of Nuclear Materials*, 384:61 − 69, 2009.

[11] F. Sokolov, K. Fukuda, and H. P. Nawada. *Thorium Fuel Cycle - Potential Benefits and Challenges.* 2005.

[12] N. A. Brincat. *Density Functional Theory Investigation of the Uranium Oxides.* PhD thesis, University of Bath, 2015.

[13] R. J. McEachern and P. Taylor. A review of the oxidation of uranium dioxide at temperatures below 400 degrees C. *Journal of Nuclear Materials*, 254:87 – 121, 1998.

[14] J. M. Astilleros, A. J. Pinto, M. A. Gonçalves, N. Sanchez-Pastor, and L. Fernandez-Diaz. In situ nanoscale observations of metatorbernite surfaces interacted with aqueous solutions. *Environmental Science and Technology*, 47:2636 – 2644, 2013.

[15] A. Abdelouas. Uranium mill tailings: Geochemistry, mineralogy and environmental impact. *Elements*, 2:335 – 341, 2006.

[16] K. S. Squibb and M. A. McDiarmid. Depleted uranium exposure and health effects in Gulf War veterans. *Philosophical Transactions of the Royal Society B-Biological Sciences*, 361:639 – 648, 2006.

[17] D. L. Stoliker, D. B. Kent, and J. M. Zachara. *Environmental Science and Technology*, 45:8733 – 8740, 2011.

[18] A. Bleise, P. R. Danesi, and W. Burkart. Properties, use and health effects of depleted uranium (DU): a general overview. *Journal of Environmental Radioactivity*, 64:93 – 112, 2003.

[19] P. S. Bagus, C. J. Nelin, and E. S. Ilton. Theoretical modeling of the uranium 4f XPS for U(VI) and U(IV) oxides. *Journal of Chemical Physics*, 139:244704 – 244717, 2013.

[20] M. J. Beazley, R. J. Martinez, P. A. Sobecky, S. M. Webb, and M. Taillefert. Uranium biomineralization as a result of bacterial phosphatase activity: Insights from bacterial isolates from a contaminated subsurface. *Environmental Science and Technology*, 41:5701 – 5707, 2007.

[21] C. C. Fuller, J. R. Bargar, J. A. Davis, and M. J. Piana. Mechanisms of uranium interactions with hydroxyapatite: Implications for groundwater remediation. *Environmental Science and Technology*, 36:158 – 165, 2002.

[22] J. S. Arey, J. C. Seaman, and P. M. Bertsch. Immobilization of uranium in contaminated sediments by hydroxyapatite addition. *Environmental Science and Technology*, 33:337 – 342, 1999.

[23] T. Ohnuki, N. Kozai, M. Samadfam, R. Yasuda, S. Yamamoto, K. Narumi, H. Naramoto, and T. Murakami. The formation of autunite ($Ca(UO_2)(PO_4)_2 \cdot nH_2O$

within the leached layer of dissolving apatite: incorporation mechanism of uranium by apatite. *Chemical Geology*, 211:1 – 14, 2004.

[24] J. L. Jerden Jr, A. K. Sinha, and L. Zelazny. Natural immobilization of uranium by phosphate mineralization in an oxidizing saprolite-soil profile: Chemical weathering of the Coles Hill uranium deposit, Virginia. *Chemical Geology*, 199:129 – 157, 2003.

[25] J. G. Catalano, J. P. McKinley, J. M. Zachara, S. M. Heald, S. C. Smith, and G. E. Brown. Changes in uranium speciation through a depth sequence of contaminated hanford sediments. *Environmental Science and Technology*, 40:2517 – 2524, 2006.

[26] Y. Arai, M. A. Marcus, N. Tamura, J. A. Davis, and J. M. Zachara. Spectroscopic evidence for uranium precipitates in vadose zone sediments at the Hanford 300-area site. *Environmental Science and Technology*, 41:4633 – 4639, 2007.

[27] D. M. Singer, J. M. Zachara, and G. E. Brown. Uranium speciation as a function of depth in contaminated hanford sediments - a micro-XRF, micro-XRD, and micro- and bulk-XAFS study. *Environmental Science and Technology*, 43:630 – 636, 2009.

[28] J. Stubbs, L. Veblen, D. Elbert, J. M. Zachara, and J. A. Davis. Newly recognized hosts for uranium in the Hanford site vadose zone. *Geochimica et Cosmochimica Acta*, 73:1563 – 1576, 2009.

[29] R. L. Frost, M. J. Dickfos, and J. Čejka. Raman spectroscopic study of the uranyl mineral compreignacite, $K_2[(UO_2)_3O_2(OH)_3]_2 \cdot 7H_2O$. *Journal of Raman Spectroscopy*, 39:1158 – 1161, 2008.

[30] H. R. Hoekstra, S. Siegel, and F. X. Gallagher. The uranium-oxygen system at high pressure. *Journal of Inorganic and Nuclear Chemistry*, 32:3237 – 3248, 1970.

[31] G. Rousseau, L. Desgranges, F. Charlot, N. Millot, J. C. Niepce, M. Pijolat, F. Valdivieso, G. Baldinozzi, and J. F. Berar. A detailed study of UO_2 to U_3O_8 oxidation phases and the associated rate-limiting steps. *Journal of Nuclear Materials*, 355:10 – 20, 2006.

[32] X. D. Wen, R. L. Martin, G. E. Scuseria, S. P. Rudin, E. R. Batista, and A. K. Burrell. Screened hybrid and DFT plus U studies of the structural, electronic, and optical properties of U_3O_8. *Journal of Physics: Condensed Matter*, 25:025501, 2013.

[33] C. V. Parks, B. D. Murphy, L. M. Petrie, and C. M. Hopper. Plutonium production using natural uranium from the front-end of the nuclear fuel cycle. Technical

Report ORNL/TM-2002/118, Oak Ridge National Laboratory, Oak Ridge, Tennessee, USA, 2002.

[34] S. A. Barrett, A. J. Jacobson, B. A. Tofield, and B. E. F. Fender. The preparation and structure of barium uranium oxide $BaUO_{3+x}$. *Acta Crystallographica Part B*, 38:2775 − 2781, 1982.

[35] B. T. M. Willis. Positions of oxygen atoms in $UO_{2.13}$. *Nature*, 197:755 − 756, 1963.

[36] B. T. M. Willis. Structures of UO_2, UO_{2+x} and U_4O_9 by neutron diffraction. *Journal De Physique*, 25:431 − 441, 1964.

[37] A. K. Cheetham, B. E. F. Fender, and M. J. Cooper. Defect structure of calcium fluoride containing excess anions .1. Bragg scattering. *Journal of Physics Part C: Solid State Physics*, 4:3107 − 3121, 1971.

[38] D. J. M Bevan, O. Greis, and J. Strahle. A new structural principle in anion-excess fluorite-related super-lattices. *Acta Crystallographica Part A*, 36:889 − 890, 1980.

[39] D. J. M. Bevan, I. E. Grey, and B. T. M. Willis. The crystal-structure of beta-U_4O_{9-y}. *Journal of Solid State Chemstry*, 61:1 − 7, 1986.

[40] L. Desgranges, G. Baldinozzi, G. Rousseau, J.-C. Niepce, and G. Calvarin. Neutron diffraction study of the in situ oxidation of UO_2. *Inorganic Chemistry*, 48:7585 − 7592, 2009.

[41] D. A. Andersson, T. Watanabe, C. Deo, and B. P. Uberuaga. Role of di-interstitial clusters in oxygen transport in UO_{2+x} from first principles. *Physical Review B*, 80:060101 − 060104, 2009.

[42] K. Govers, S. Lemehov, M. Hou, and M. Verwarft. Comparison of interatomic potentials for UO_2. Part I: Static calculations. *Journal of Nuclear Materials*, 366:161 − 177, 2007.

[43] N. A. Brincat, M. Molinari, S. C. Parker, G. C. Allen, and M. T. Storr. Computer simulation of defect clusters in UO_2 and their dependence on composition. *Journal of Nuclear Materials*, 456:329 − 333, 2015.

[44] H. Y. Geng, Y. Chem, Y. Kaneta, and M. Kinoshita. Ab initio investigation on oxygen defect clusters in UO_{2+x}. *Applied Physics Letters*, 93:201903 − 201905, 2008.

[45] G. C. Allen and P. A. Tempest. Linear ordering of oxygen clusters in hyper-stoichiometric uranium dioxide. *Journal of the Chemical Society: Dalton Transactions*, 11:2169 − 2173, 1982.

[46] L. M. Kovba and N. I. Komarevtseva. On the crystal structures of $U_{13}O_{34}$ and delta-U_2O_5. *Radiokhimiya*, 21:754 – 757, 1979.

[47] J. J. Pireaux, E. Thibaut, J. Riga, C. Tenretnoel, R. Caudano, and J. J. Verbist. Shake-up satellites in X-ray photoelectron-spectra of uranium-oxides and fluorides - band-structure scheme for uranium-dioxide, UO_2. *Chemical Physics*, 22:113 – 120, 1977.

[48] Y. A. Teterin and A. Y. Teterin. The structure of the X-ray photoelectron spectra of light actinide compounds. *Uspekhi Khimii*, 73:588 – 631, 2004.

[49] N. A. Brincat, S. C. Parker, M. Molinari, G. C. Allen, and M. T. Storr. Density functional theory investigation of the layered uranium oxides U_3O_8 and U_2O_5. *Dalton Transactions*, 44:2613 – 2622, 2015.

[50] D. A. Andersson, G. Baldinozzi, L. Desgranges, D. R. Conradson, and S. D. Conradson. Density functional theory calculations of UO_2 oxidation: Evolution of UO_{2+x}, U_4O_{9-y}, U_3O_7, and U_3O_8. *Inorganic Chemistry*, 52:2769 – 2778, 2013.

[51] B. O. Loopstra. Structure of beta-U_3O_8. *Acta Crystallographica B*, 26:656 – 657, 1970.

[52] C. A. Colmenares. The oxidation of thorium, uranium, and plutonium. *Progress in Solid State Chemistry*, 9:139 – 239, 1975.

[53] S. Siegel, H. Hoekstra, and E. Sherry. Crystal structure of high-pressure UO_3. *Acta Crystallographica*, 20:292 – 295, 1966.

[54] C. Greaves and B. E. F. Fender. The structure of α-UO_3 by neutron and electron diffraction. *Journal of the Chemical Society, Dalton Transactions*, B28:3609 – 3614, 1972.

[55] N. A. Brincat, S. C. Parker, M. Molinari, G. C. Allen, and M. T. Storr. Ab initio investigation of the UO_3 polymorphs: Structural properties and thermodynamic stability. *Inorganic Chemistry*, 53:12253 – 12264, 2014.

[56] P. C. Burns. Uranium(6) minerals and inorganic compounds: Insights into an expanded structural hierarchy of crystal structures. *Canadian Mineralogist*, 43:1839 – 1894, 2005.

[57] R. L. Frost and M. L. Weier. Raman microscopy of autunite minerals at liquid nitrogen temperature. *Spectrochimica Acta Part A*, 60:2399, 2004.

[58] R. L. Frost, J. Kristóf, M. L. Weier, and E. Horváth. Thermal decomposition of metatorbernite - a contolled rate thermal analysis study. *Journal of Thermal Analysis and Calorimetry*, 79:721 – 725, 2005.

[59] R. L. Frost, K. L. Erickson, M. O. Adebajo, and M. L. Weier. Near-infrared spectroscopy of autunites. *Spectrochimica Acta, Part A*, 61:367 – 372, 2005.

[60] D. M. L. Ho, A. E. Jones, J. Y. Goulermas, P. Turner Z. Varga, L. Fongaro, T. Fanghanel, and K. Mayer. Raman spectroscopy of uranium compounds and the use of multivariate analysis for visualization and classification. *Forensic Science International*, 251:61 – 68, 2015.

[61] R. L. Frost and J. Čejka. A Raman spectroscopic study of the uranyl carbonate rutherfordine. *Journal of Raman Spectroscopy*, 38:1488, 2007.

[62] D. Ho Mer Lin, D. Manara, Z. Varga, A. Berlizov, T. Fanghaenel, and K. Mayer. Applicability of Raman spectroscopy as a tool in nuclear forensics for analysis of uranium ore concentrates. *Radiochimica Acta*, 101:779 – 784, 2013.

[63] P. Vandenabeele, H. G. M. Edwards, and J. Jehlicka. The role of mobile instrumentation in novel applications of Raman spectroscopy: archaeometry, geosciences and forensics. *Chemical Society Reviews*, 43:2628, 2014.

[64] M. Tsuboi, M. Terada, and T. Shimanouchi. Optically active lattice vibrations of alpha-uranium trioxide. *The Journal of Chemical Physics*, 36:1301 – 1310, 1962.

[65] M. L. Palacios and S. H. Taylor. Characterization of uranium oxides using in situ micro-Raman spectroscopy. *Applied Spectroscopy*, 54:9:1372 – 1378, 2000.

[66] J. M. Skelton, E. L. da Silva, R. Crespo-Otero, L. E. Hatcher, P. R. Raithby, S. C. Parker, and A. Walsh. Electronic excitations in molecular solids: Bridging theory and experiment. *Faraday Discussions*, 177:181 – 202, 2015.

[67] P. B. Wilson and I. H. Williams. Critical evaluation of anharmonic corrections to the equilibrium isotope effect for methyl cation transfer from vacuum to dielectric continuum. *Molecular Physics*, pages 1 – 8, 2015.

[68] R. L. Frost, J. Čejka, G. A. Ayoko, and M. Weier. A Raman spectroscopic study of the uranyl phosphate mineral bergenite. *Spectrochimica Acta, Part A*, 66:979, 2007.

[69] R. L. Frost. An infrared and Raman spectroscopic study of the uranyl micas. *Spectrochimica Acta, Part A*, 60:1469, 2004.

[70] R. L. Frost and M. L. Weier. Hot-stage Raman spectroscopic study of the thermal decomposition of saléeite. *Journal of Raman Spectroscopy*, 35:299 – 307, 2004.

[71] F. K. Vansant, B. J. Van Der Veken, and H. O. Desseyn. Vibrational analysis of arsenic acid and its anions .1. description of Raman-spectra. *Journal of Molecular Structure*, 15:425 – 437, 1973.

[72] R. H. Busey and O. L. Keller. Structure of the aqueous pertechnetate ion by Raman and infrared spectroscopy. Raman and infrared spectra of crystalline $KTcO_4$, $KReO_4$, Na_2MoO_4, Na_2WO_4, $Na_2MoO_4 \cdot 2H_2O$, and $Na_2WO_4 \cdot 2H_2O$. *Journal of Chemical Physics*, 41:215 – 225, 1964.

[73] S. D. Ross. *The Infrared Spectra of Minerals*. Mineralogical Society, 1974.

[74] P. C. Zwaan, C. E. S. Arps, and E. de Grave. Vochtenite, a new uranyl phosphate mineral from Wheal Basset, Redruth, Cornwall. *Mineralogical Magazine*, 53:473, 1989.

[75] R. L. Frost, J. Plášil, J. Čejka, J. Sejkora, E. C. Keeffe, and S. Bahfenne. Raman spectroscopic study of the uranyl mineral pseudojohannite. *Journal of Raman Spectroscopy*, 40:1816, 2009.

[76] R. L. Frost, J. Čejka, G. A. Ayoko, and M. J. Dickfos. Raman spectroscopic study of the multi-anion mineral schrockingerite. *Journal of Raman Spectroscopy*, 38:1609, 2007.

[77] R. L. Frost, J. Čejka, G. Ayoko, and M. J. Dickfos. Raman spectroscopic study of the uranyl carbonate mineral voglite. *Journal of Raman Spectroscopy*, 39:374, 2008.

[78] R. L. Frost, J. Čejka, M. L. Weier, and W. Martens. Molecular structure of the uranyl silicates - a Raman spectroscopic study. *Journal of Raman Spectroscopy*, 37:538 – 551, 2006.

[79] I. S. Butler, G. C. Allen, and N. A. Tuan. Micro-Raman spectrum of triuranium octoxide, U_3O_8. *Applied Spectroscopy*, 42:901 – 902, 1988.

[80] G. C. Allen and N. R. Holmes. Characterization of binary uranium oxides by infrared spectroscopy. *Applied Spectroscopy*, 48:4:525 – 530, 1994.

[81] P. Atkins and J. de Paula. *Elements of Physical Chemistry*. Oxford University Press, Great Clarendon Street, Oxford, OX2 6DP, 4th edition, 2007.

[82] K. C. Molloy. *Group Theory for Chemists: Fundamental Theory and Applications.* Woodhead Publishing, 2004.

[83] T. C. Damen, S. P. S. Porto, and B. Tell. Raman effect in zinc oxide. *Physical Review*, 142:570 – 574, 1966.

[84] D. Wolverson. *Characterization of Semiconductor Heterostructures and Nanostructures*, chapter Raman Spectroscopy. Elsevier, 2008.

[85] A. Pallipurath, J. Skelton, S. Bucklow, and S. Elliot. A chemometric study of ageing in lead-based paints. *Talanta*, 144:977 – 985, 2015.

[86] S. R. Burgess, P. Statham, J. Holland, and Y. Chou. Standardless quantitative analysis using a drift detector, what accuracy is possible from live and reconstructed data? *Microscopy and Microanalysis*, 13:1432 – 1433, 2007.

[87] R. L. Frost, M. L. Weier, and M. O. Adebajo. Thermal decomposition of metazeunerite - a high resolution thermogravimetric and hot-stage Raman spectroscopic study. *Thermochimica Acta*, 419:119 – 129, 2004.

[88] R. L. Frost, J. Kristóf, W. N. Martens, M. L. Weier, and E. Horváth. Thermal decomposition of sabugalite - a contolled rate thermal analysis study. *Journal of Thermal Analysis and Calorimetry*, 83:675 – 679, 2006.

[89] A. R. Leach. *Molecular Modelling - Principles and Applications.* Pearson Education, 2nd edition, 2001.

[90] M. Born and J. R. Oppenheimer. On the quantum theory of molecules. *Annalen der Physik*, 84:457 – 484, 1927.

[91] C. Møller and M. S. Plesset. Note on approximate treatment for many-electron systems. *Physical Review*, 46:618 – 622, 1934.

[92] L. H. Thomas. The calculation of atomic fields. *Mathematical Proceedings of the Cambridge Philosophical Society*, 23:542 – 548, 1927.

[93] E. Fermi. Un metodo statistica per la determinazione di alcune prioriet a dell'atome. *Rend. Accad. Naz. Lincei*, 6:602 – 607, 1927.

[94] P. A. M. Dirac. Note on exchange phenomena in the Thomas-Fermi atom. *Mathematical Proceedings of the Cambridge Philosophical Society*, 26:376 – 385, 1930.

[95] W. Pauli. Über den zusammenhang des abschlusses der elektronengruppen im atom mit der komplexstruktur der spektren. *Zeitschrift für Physik*, 31:765 – 783, 1925.

[96] P. Hohenberg and W. Kohn. Inhomogeneous electron gas. *Physical Review B*, 136:B864 – B871, 1964.

[97] W. Kohn and L. J. Sham. Self-consistent equations including exchange and correlation effects. *Physical Review*, 140:1133 – 1138, 1965.

[98] D. M. Ceperley and B. J. Alder. Ground-state of the electron-gas by a stochastic method. *Physical Review Letters*, 45:566 – 569, 1980.

[99] R. M. Martin. *Electronic Structure: Basic Theory and Practical Methods*. Cambridge University Press, 2004.

[100] U. von Barth and L. Hedin. Local exchange-correlation potential for spin polarised case .1. *Journal of Physics Part C Solid State Physics*, 5:1629 – 1642, 1972.

[101] S. H. Vosko, L. Wilk, and M. Nusair. Accurate spin-dependent electron liquid correlation energies for local spin-density calculations - a critical analysis. *Canadian Journal of Physics*, 58:1200 – 1211, 1980.

[102] J. P. Perdew and A. Zunger. Self-interaction correction to density-functional approximations for many-electron systems. *Physical Review B*, 23:5048 – 5079, 1981.

[103] A. D. Becke. Density-functional exchange-energy approximation with correct asymptotic-behavior. *Physical Review A*, 38:3098 – 3100, 1988.

[104] A. D. Becke. Density-functional thermochemistry. i. the effect of the exchange-only gradient correction. *Journal of Chemical Physics*, 92:2155 – 2160, 1992.

[105] J. P. Perdew and Y. Wang. Accurate and simple analytical representation of the electron-gas correlation-energy. *Physical Review B*, 45:13244 – 13249, 1992.

[106] C. T. Lee, W. T. Yang, and R. G. Parr. Development of the Colle-Salvetti correlation-energy formula into a functional of the electron-density. *Physical Review B*, 37:785 – 789, 1988.

[107] J. P. Perdew, K. Burke, and M. Ernzerhof. Generalized gradient approximation made simple. *Physical Review Letters*, 77:3865 – 3868, 1996.

[108] J. P. Perdew, A. Ruzsinszky, G. I. Csonka, O. A. Vydrov, G. E. Scuseria, L. A. Constantin, X. L. Zhou, and K. Burke. Restoring the density-gradient expansion for exchange in solids and surfaces. *Physical Review Letters*, 100:136406 – 136409, 2008.

[109] J. W. Sun, M. Marsman, G. I. Csonka, A. Ruzsinszky, P. Hao, Y. S. Kim, G. Kresse, and J. P. Perdew. Self-consistent meta-generalized gradient approximation within the projector-augmented-wave method. *Physical Review B*, 84:035117 – 035126, 2011.

[110] J. P. Perdew, A. Ruzsinszky, G. I. Csonka, L. A. Constantin, and J. W. Sun. Workhouse semilocal density functional for condensed matter physics and quantum chemistry. *Physical Review Letters*, 103:179902 – 179905, 2009.

[111] C. Adamo and V. Barone. Toward reliable density functional methods without adjustable parameters: The PBE0 model. *Journal of Chemical Physics*, 110:6158 – 6170, 1999.

[112] A. D. Becke. Density-functional thermochemistry .3. the role of exact exchange. *Journal of Chemical Physics*, 98:5648 – 5652, 1993.

[113] J. Heyd ad G. E. Scuseria and M. Ernzerhof. Hybrid functionals based on a screened Coulomb potential. *Journal of Chemical Physics*, 118:8207 – 8215, 2003.

[114] D. L. Dudarev, G. A. Botton, S. Y. Savrasov, C. J. Humphreys, and A. P. Sutton. Electron-energy-loss spectra and the structural stability of nickel oxide: An LSDA+U study. *Physical Review B*, 57:1505 – 1509, 1998.

[115] M. R. Castell, S. L. Dudarev, C. Muggelberg, A. P. Sutton, G. A. D. Briggs, and D. T. Goddard. Surface structure and bonding in the strongly correlated metal oxides NiO and UO_2. *Journal of Vacuum Science and Technology A: Vacuum Surfaces and Films*, 16:1055 – 1058, 1998.

[116] T. Petit, B. Morel, C. Lemaignan, A. Pasturel, and B. Bigot. Cohesive properties of UO_2. *Philosophical Magazine B*, 73:893 – 904, 1996.

[117] K. Terakura, T. Oguchi, A. R. Williams, and J. Kübler. Transition-metal monoxides - band or Mott insulators. *Physical Review B*, 30:4734 – 4747, 1984.

[118] M. Cococcioni. *Correlated Electrons: From Models to Materials*, chapter The LDA+U Approach: A Simple Hubbard Correction for Correlated Ground States. Forschungszentrum Jülich, 2012.

[119] S. Hüfner. Electronic-structure of NiO and related 3d-transition-metal compounds. *Advances in Physics*, 43:183–356, 1994.

[120] O. K. Andersen, H. L. Skriver, H. Nohl, and B. Johansson. Electronic-structure of transition-metal compounds - ground-state properties of the 3d-monoxides in the atomic sphere approximation. *Pure and Applied Chemistry*, 52:93–118, 1980.

[121] J. Hubbard. Electron correlations in narrow energy bands .4. atomic representation. *Proceedings of the Royal Society of London Series A - Mathematical and Physical Sciences*, 285:542–560, 1965.

[122] A. I. Liechtenstein, V. I. Anisimov, and J. Zaanen. Density-functional theory and strong-interactions - orbital ordering in Mott-Hubbard insulators. *Physical Review B*, 52:R5467–R5470, 1995.

[123] A Kotani and T. Yamazaki. Systematic analysis of core photoemission spectra for actinide di-oxides and rare-earth sesqui-oxides. *Progree of Theoretical Physics Supplement*, 108:117–131, 1992.

[124] T. Yamazaki and A. Kotani. Systematic analysis of 4f core photoemission spectra in actinide oxides. *Journal of the Physical Society of Japan*, 60:49–52, 1991.

[125] H. J. Monkhorst and J. D. Pack. Special points for Brillouin-zone integrations. *Physical Review B*, 13:5188–5192, 1976.

[126] V. Heine. The pseudopotential concept. *Solid State Physics*, 24:1–36, 1970.

[127] M. C. Payne, M. P. Teter, D. C. Allan, T. A. Arias, and J. D. Joannopoulos. Iterative minimization techniques for ab initio total-energy calculations - molecular dynamics and conjugate gradients. *Reviews of Modern Physics*, 64:1045–1097, 1992.

[128] D. J. Singh and L. Nordström. *Planewaves, Pseudopotentials and the LAPW Method*. Springer, 2006.

[129] P. E. Blochl. Projector augmented-wave method. *Physical Review B*, 50:17953–17979, 1994.

[130] R. Fletcher and M. J. D. Powell. A rapidly convergent descent method for minimization. *Computer Journal*, 6:163–168, 1963.

[131] R. Fletcher and C. M. Reeves. Function minimization by conjugate gradients. *Computer Journal*, 7:149–154, 1964.

[132] M. J. Norgett and R. Fletcher. Fast matrix methods for calculating relaxation about defects in crystals. *Journal of Physics Part C Solid State Physics*, 3:L190 – L193, 1970.

[133] C. G. Broyden. Convergence of single-rank quasi-Newton methods. *Mathematics of Computation*, 24:365 – 382, 1970.

[134] R. Fletcher. A new approach to variable metric algorithms. *Computer Journal*, 13:317 – 322, 1970.

[135] D. Goldfarb. A family of variable-metric methods derived by variational means. *Mathematics of Computation*, 24:23 – 26, 1970.

[136] D. F. Shanno. Conditioning of quasi-Newton methods for function minimization. *Mathematics of Computation*, 24:647 – 656, 1970.

[137] P. Pulay. Convergence acceleration of iterative sequences - the case of SCF iteration. *Chemical Physics Letters*, 73:393 – 398, 1980.

[138] H. B. Schlegel. Optimisation of equilibrium geometries and transition structures. *Journal of Computational Chemistry*, 3:214 – 218, 1982.

[139] Baroni, de Gironcoli, Dal Corso, and Giannozzi. Phonons and related crystal properties from density-functional perturbation theory. *Reviews of Modern Physics*, 73:515 – 562, 2001.

[140] P. Giannozzi and S. Baroni. *Handbook of Materials Modeling*, chapter Density-Functional Perturbation Theory. Springer, 2005.

[141] Wolverton Research Group. A practical guide to frozen phonon calculations. `wolverton.northwestern.edu`. Retrieved 13/04/2016.

[142] A. Togo, F. Oba, and I. Tanaka. First-principles calculations of the ferroelastic transition between rutile-type and $CaCl_2$-type SiO_2 at high pressures. *Physical Review B*, 78:134106, 2008.

[143] G. Kresse, M. Marsman, and J. Furthmüller. VASP the guide. `cms.mpi.univie.ac.at/VASP/`. Retrieved 13/04/2016.

[144] S. Baroni, P. Giannozzi, and A. Testa. Greens function approach to linear response in solids. *Physical Review Letters*, 58:1861 – 1864, 1987.

[145] X. Gonze. Perturbation expansion of variational-principles at arbitrary order. *Physical Review A*, 52:1086 – 1095, 1995.

[146] P. Giannozzi and S. Baroni. Vibrational and dielectric properties of C60 from density functional perturbation theory. *Journal of Chemical Physics*, 100:8537 – 8539, 1994.

[147] Quantumwise. `www.quantumwise.com/documents/tutorials/latest/Polarization/index.html/chap.born.html`. Accessed 22/12/2015.

[148] D. Porezag and M. R. Pederson. Infrared intensities and Raman-scattering activities within density-functional theory. *Physical Review B*, 54:11:7830 – 7836, 1996.

[149] A. Fonari and S. Stauffer. *vasp_raman.py.* https://github.com/raman-sc/VASP/, 2013.

[150] G. W. Watson, E. T. Kelsey, N. H. de Leeuw, D. J. Harris, and S. C. Parker. Atomistic simulation of dislocations, surfaces and interfaces in MgO. *Journal of the Chemical Society: Faraday Transactions*, 92:433, 1996.

[151] J. D. Gale. GULP: A computer program for the symmetry-adapted simulation of solids. *Journal of the Chemical Society: Faraday Transactions*, 93:629 – 637, 1997.

[152] S. Kerisit and C. Liu. Molecular simulation of the diffusion of uranyl carbonate species in aqueous solution. *Geochimica et Cosmochimica Acta*, 74:4937 – 4952, 2010.

[153] J. A. L. Rabone and N. H. de Leeuw. Interatomic potential models for natural apatite crystals: Incorporating strontium and the lanthanides. *Journal of Computational Chemistry*, 27:253 – 266, 2006.

[154] N. H. de Leeuw and S. C. Parker. Modeling absorption and segregation of magnesium and cadmium ions to calcite surfaces: Introducing $MgCO_3$ and $CdCO_3$ potential models. *Journal of Chemical Physics*, 112:4326 – 4333, 2000.

[155] G. Kresse and J. Hafner. Ab-initio molecular dynamics simulation of the liquid-metal amorphous-semiconductor transition in germanium. *Physical Review B*, 49:14251 – 14269, 1994.

[156] G. Kresse and J. Furthmüller. Efficient iterative schemes for ab initio total-energy calculations using a plane-wave basis set. *Physical Review B*, 54:11169 – 11186, 1996.

[157] K. Momma and F. Izumi. VESTA: A three-dimensional visualization system for electronic and structural analysis. *Journal of Applied Crystallography*, 41:653 – 658, 2008.

[158] Persistence of Vision Pty. Ltd., Williamstown, Victoria, Australia, http://www.povray.org/. *Persistence of Vision (TM) Raytracer*, 2004.

[159] J. D. Hunter. Matplotlib: A 2D graphics environment. *Computing In Science and Engineering*, 9(3):90–95, 2007.

[160] A. F. Andresen. The structure of U_3O_8 determined by neutron diffraction. *Acta Crystallographica*, 11:612–614, 1958.

[161] E. H. P. Cordfunke and P. Aling. System UO_3 + U_3O_8: Dissociation pressure of γ-UO_3. *Trans. Faraday Soc.*, 61:50–53, 1965.

[162] G. C. Allen and R. K. Wild. Auger-spectroscopy of uranium. *Journal of the Chemical Society, Dalton Transactions*, pages 493–498, 1974.

[163] S. D. Senanayake, R. Rousseau, D. Colegrave, and H. Idriss. The reaction of water on polycrystalline UO_2: Pathways to surface and bulk oxidation. *Journal of Nuclear Materials*, 342:179–187, 2005.

[164] A. L. Tamasi, K. S. Boland, K. Czerwinski, J. K. Ellis, S. A. Kozimor, R. L. Martin, A. L. Pugmire, D. Reilly, B. L. Scott, A. D. Sutton, G. L. Wagner, J. R. Walensky, and M. P. Wilkerson. Oxidation and hydration of U_3O_8 materials following controlled exposure to temperature and humidity. *Analytical Chemistry*, 87:4210–4217, 2015.

[165] P. Maldonado, L. Z. Evins, and P. M. Oppeneer. Ab initio atomistic thermodynamics of water reacting with uranium dioxide surfaces. *Journal of Physical Chemistry C*, 118:8491–8500, 2014.

[166] T. Bo, J. H. Lan, Y. L. Zhao, Y. J. Zhang, C. H. He, Z. F. Chai, and W. Q. Shi. First principles study of water adsorption and dissociation on the UO_2 (111), (110) and (100) surfaces. *Journal of Nuclear Materials*, 454:446–454, 2014.

[167] B. O. Loopstra. Neutron diffraction investigation of U_3O_8. *Acta Crystallographica*, 17:651, 1964.

[168] B. O. Loopstra. Phase transition in alpha-U_3O_8 at 210 degrees C. *Journal of Applied Crystallography*, 3:94, 1970.

[169] B. O. Loopstra. Crystal structure of alpha-U_3O_8. *Journal of Inorganic and Nuclear Chemistry*, 39:1713–1714, 1977.

[170] W. H. Zachariasen. Crystal chemical studies of the 5f-series of elements .1. new structure types. *Acta Crystallographica*, 1:265 – 269, 1948.

[171] B. Chodura and J. Maly. A contribution to the solution of the structure of U_3O_8. *Journal of Inorganic and Nuclear Chemistry*, 7:177 – 178, 1958.

[172] W. B. Wilson. High-pressure high-temperature investigation of the uranium-oxygen system. *Journal of Inorganic and Nuclear Chemistry*, 19:212 – 222, 1961.

[173] H. R. Hoekstra, S. Siegel, L. H. Fuchs, and J. J. Katz. The uranium-oxygen system - $UO_{2.5}$ to U_3O_8. *Journal of Physical Chemistry*, 59:136 – 138, 1955.

[174] G. C. Allen, J. A. Crofts, M. T. Curtis, P. M. Tucker, D. Chadwick, and P. J. Hampson. X-ray photoelectron-spectroscopy of some uranium oxide phases. *Journal of the Chemical Society, Dalton Transactions*, pages 1296 – 1301, 1974.

[175] G. C. Allen, A. J. Griffiths, and C. W. Suckling. Electron-spin resonance-spectra of mixed oxides containing uranium and alkaline-earth metals. *Chemical Physics Letters*, 53:309 – 312, 1978.

[176] H. M. He, D. A. Andersson, D. D. Allred, and K. D. Rector. Determination of the insulation gap of uranium oxides by spectroscopic ellipsometry and density functional theory. *Journal of Physical Chemistry C*, 117:16540 – 16551, 2013.

[177] T. Vitova, K. O. Kvashnina, G. Nocton, G. Sukharina, M. A. Denecke, S. M. Butorin, M. Mazzanti, R. Caciuffo, A. Soldatov, and T. Behrends. High energy resolution X-ray absorption spectroscopy study of uranium in varying valence states. *Physical Review B*, 82:235118, 2010.

[178] A. Y. Teterin, M. V. Ryzhkov, Y. A. Teterin, K. I. Maslakov, T. Reich, and S. L. Molodtsov. Resonant emission of UO_2, U_3O_8, and UO_{2+x} valence electrons under Sr excitation near the O-4,O-5(U) absorption edge. *Journal of Structural Chemistry*, 52:295 – 303, 2011.

[179] G. C. Allen and N. R. Holmes. Mixed-valency behavior in some uranium-oxides studies by X-ray photoelectron-spectroscopy. *Canadian Journal of Applied Spectroscopy*, 38:124 – 130, 1993.

[180] K. O. Kvashnina, S. M. Butorin, P. Martin, and P. Glatzel. Chemical state of complex uranium oxides. *Physical Review Letters*, 111:253002, 2013.

[181] R. G. J. Ball and P. G. Dickens. Calculation of structural and defect properties of alpha-u_3o_8. *Journal of Materials Chemistry*, 1:105 – 112, 1991.

[182] H. Y. Geng, H. X. Song, K. Jin, S. K. Xiang, and Q. Wu. First-principles study on oxidation effects in uranium oxides and high-pressure high-temperature behavior of point defects in uranium dioxide. *Physical Review B*, 84:174115−174127, 2011.

[183] Y. Yun, J. Rusz, M.-T. Suzuki, and P. M. Oppeneer. First-principles investigation of higher oxides of uranium and neptunium: U_3O_8 and Np_2O_5. *Physical Review B*, 83:075109, 2011.

[184] F. Pointurier and O. Marie. *Spectrochimica Acta, Part B*, 65:797−804, 2010.

[185] G. C. Allen, J. A. Crofts, and A. J. Griffiths. Infrared spectroscopy of the uranium-oxygen system. *Applied Spectroscopy*, 62:273−281, 1976.

[186] G. C. Allen, I. S. Butler, and N. A. Tuan. Characterisation of uranium oxides by micro-Raman spectroscopy. *Journal of Nuclear Materials*, 144:17−19, 1987.

[187] K. Ohwada and T. Soga. Uranium-oxygen lattice-vibrations of triuranium octoxide. *Spectrochimica Acta, Part A*, 29:843−850, 1973.

[188] L. E. Sweet, T. A. Blake, C. H. Henager Jr., S. Hu, T. J. Johnson, D. E. Meier, S. M. Peper, and J. M. Schwantes. Investigation of the polymorphs and hydrolysis of uranium trioxide. *J. Radioanal. Nucl. Chem.*, 296:105−110, 2013.

[189] B. S. Girgis and N. H. Rofail. Reactivity of various UO_3 modifications in the fluorination to UF_4 by FREON-12. *Journal of Nuclear Materials*, 195:126−133, 1992.

[190] W. R. Cornman. Preparation and characterization of the polymorphs of UO_3. Technical Report TID-4500, Savannah River Laboratory, Aiken, South Carolina, 1962.

[191] M. T. Weller, P. G. Dickens, and D. J. Penny. The structure of delta-UO_3. *Polymer*, 7:243−244, 1988.

[192] V. J. Wheeler, R. M. Dell, and E. Wait. Uranium trioxide and the UO_3 hydrates. *Journal of Inorganic and Nuclear Chemistry*, 26:1829−1845, 1964.

[193] E. H. P. Cordfunke and P. C. Debets. Preparation and properties of a new monohydrate of uranium trioxide epsilon-$UO_3.H_2O$. *Journal of Inorganic and Nuclear Chemistry*, 26:1671−1677, 1964.

[194] L. M. Kovba, L. M. Vidavskii, and E. G. Lavut. Study of ϵ-UO_3. *Zhumal Strukturnoi Khimii*, 4:627−629, 1963.

[195] J. A. Johnson. *Studies of Reaction Processed for Voloxidation Methods.* PhD thesis, University of Tennessee, 2013.

[196] B. Ivanova and M. Spiteller. Uranyl-water-containing complexes: Solid-state UV-MALDI mass spectrometric and IR spectroscopic approach for selective quantitation. *Environmental Science and Pollution*, 21:1548 – 1563, 2014.

[197] H. R. Hoekstra and S. Siegel. The uranium-oxygen system - U_3O_8-UO_3. *Journal of Inorganic and Nuclear Chemistry*, 18:154 – 165, 1961.

[198] R. Engmann and P. M. de Wolff. Crystal structure of gamma-UO_3. *Acta Crystallographica*, 16:993 – 996, 1963.

[199] B. O. Loopstra, J. C. Taylor, and A. B. Waugh. Neutron powder profile studies of gamma-uranium trioxide phases. *Journal of Solid State Chemistry*, 20:9 – 19, 1977.

[200] G. C. Allen and N. R. Holmes. Surface characterization of alpha-UO_3, beta-UO_3, gamma-UO_3, and delta-UO_3 using X-ray photoelectron-spectroscopy. *Journal of the Chemical Society, Dalton Transactions*, pages 3009 – 3015, 1987.

[201] C. J. Pickard, B. Winkler, R. K. Chen, M. C. Payne, M. H. Lee, J. S. Lin, J. A. White, V. Milman, and D. Vanderbilt. Structural properties of lanthanide and actinide compounds within the plane wave pseudopotential approach. *Physical Review Letters*, 85:5122 – 5125, 2000.

[202] B. H. Kim, Y. B. Lee, M. A. Prelas, and T. K. Ghosh. Thermal and X-ray diffraction analysis studies during the decomposition of ammonium uranyl nitrate. *Journal of Radioanalytical and Nuclear Chemistry*, 293:1075 – 1083, 2012.

[203] B. O. Loopstra and E. H. Cordfunke. On structure of alpha-UO_3. *Recueil Des Travaux Chimiques Des Pays-Bas*, 85:135 – 142, 1966.

[204] P. C. Debets. The structure of beta-UO3. *Acta Crystallographica*, 21:589 – 593, 1966.

[205] P. C. Debets. Interpretation of the X-ray powder pattern of beta-UO_3. *Journal of Inorganic and Nuclear Chemistry*, 26:1468 – 1470, 1964.

[206] R. J. P. Driscoll, D. Wolverson, J. M. Mitchels, J. M. Skelton, S. C. Parker, M. Molinari, I. Khan, D. Geeson, and G. C. Allen. A Raman spectroscopic study of uranyl minerals from Cornwall. *RSC Advances*, 4:103:59137 – 59149, 2014.

[207] M. Molinari, S. C. Parker, D. A. Tompsett, F. Azough, and R. Freer. Structural, electronic and thermoelectric behaviour of CaMnO$_3$ and CaMnO$_{3-\delta}$. *Journal of Materials Chemistry A*, 2:14109 – 14117, 2014.

[208] R. L. Frost and B. J. Reddy. Raman spectroscopic study of the uranyl titanate mineral betafite. *Radiation Effects and Defects in Solids: Incorporating Plasma Science and Plasma Technology*, 165:11:868 – 875, 2008.

[209] P. L. Frost and B. J. Reddy. Raman spectroscopic study of the uranyl titanate mineral brannerite: Effect of metamictisation. *Journal of Raman Spectroscopy*, 42:691, 2011.

[210] R. L. Frost, S. J. Palmer, and J. Čejka. The application of Raman spectroscopy to the study of the uranyl mineral coconinoite Fe$_2$Al$_2$(UO$_2$)$_2$(PO$_4$)$_4$(SO$_4$)(OH)$_2$·20H$_2$O. *Spectroscopy Letters*, 44:6:381, 2011.

[211] N. J. Elton, J. J. Hooper, and G. Ryback. Compreignacite: a 2nd occurance, from St. Just, Cornwall. *Mineralogical Magazine*, 58:339 – 341, 1994.

[212] N. J. Elton, J. J. Hooper, and A. E. Jeal. Nováčekite and metanováčekite from Cornwall. *Mineralogical Magazine*, 58:513 – 514, 1994.

[213] N. J. Elton and J. J. Hooper. Andersonite and Schrockingerite from Geevor Mine, Cornwall: 2 species new to Britain. *Mineralogical Magazine*, 56:124 – 125, 1992.

[214] A. J. Locock and P. C. Burns. The crystal structure of synthetic autunite, Ca[(UO$_2$)(PO$_4$)]$_2$(H$_2$O)$_{11}$. *American Mineralogist*, 88:240 – 244, 2003.

[215] E. S. Makarov and V. I. Ivanov. The crystal structure of meta-autunite. *Doklady Akademiia Nauk SSSR*, 132:601 – 603, 1960.

[216] R. S. W. Braithwaite, B. V. Cooper, W. H. Paar, and J. E. Chisholm. Phurcalite from Dartmoor, southwest England, and its identity with 'nisaite' from Portugal. *Mineralogical Magazine*, pages 583 – 589, 1989.

[217] A. J. Locock and P. C. Burns. Crystal structures and synthesis of the copper-dominant members of the autunite and metaautunite groups: Torbernite, zeunerite, metatorbernite and metazeunerite. *Canadian Mineralogist*, 41:489 – 502, 2003.

[218] P. Golley and R. Williams. *Cornish Mineral Reference Manual*. Endsleigh Publishing, 1995.

[219] C. Frondel. Studies of uranium minerals (VII) - zeunerite. *American Mineralogist*, 36:249 – 255, 1951.

[220] C. Frondel. Studies of uranium minerals (IX) - saleeite and novacekite. *American Mineralogist*, 36:680 – 686, 1951.

[221] G. Ryback and P. C. Tandy. Eighth supplementary list of British Isles minerals (English). *Mineralogical Magazine*, 56:261 – 275, 1992.

[222] K. Mereiter. Neue kristallographische daten ueber das uranmineral andersonit. *Anzeiger der Oesterreichischer Akademie der Wissenschaften, Mathematisch-Naturwissenschaftliche Klasse*, 123:39 – 41, 1986.

[223] K. Mereiter. Crystal structure and crystallographic properties of a schröckingerite from Joachimstal. *Tschermaks Mineralogiesche und Petrographische Mitteilungen*, 35:1 – 18, 1986.

[224] K. Mereiter. Die kristallstruktur des johannits, $Cu(UO_2)_2(OH)_2(SO_4)_2 \cdot 8H_2O$. *Tschermaks Mineralogiesche und Petrographische Mitteilungen*, 30:47 – 57, 1982.

[225] P. C. Burns, K. M. Deely, and L. A. Hayden. The crystal chemistry of the zippeite group. *Canadian Mineralogist*, 41:687 – 706, 2003.

[226] D. Ginderow. Structure de l'uranophane alpha $Ca(UO_2)_2(SiO_3OH)_2 \cdot 5H_2O$. *Acta Crystallographica C*, 44:421 – 424, 1988.

[227] A. Rosenzweig and R. R. Ryan. Refinement of the crystal structure of cuprosklodowskite, $Cu[(UO_2)_2(SiO_3OH)_2] \cdot 6H_2O$. *American Mineralogist*, 60:448 – 453, 1975.

[228] A. Rosenzweig and R. R. Ryan. Kasolite, $Pb(UO_2)(SiO_4) \cdot H_2O$. *Crystal Structure Communications*, 6:617 – 621, 1977.

[229] N. J. Elton and J. J. Hooper. Widenmannite from Cornwall, England: The second world occurrence. *Mineralogical Magazine*, 59:745 – 749, 1995.

[230] P. C. Burns. The structure of compreignacite, $K_2[(UO_2)_3O_2(OH)_3]_2(H_2O)_7$. *Canadian Mineralogist*, 36:1061 – 1067, 1998.

[231] P. C. Burns. The crystal chemistry of uranium. *Reviews in Mineralogy*, 38:23 – 90, 1999.

[232] A. J. Locock, P. C. Burns, and T. M. Flynn. The role of water in the structures of synthetic hallimondite, $Pb_2[(UO_2)(AsO_4)_2](H_2O)_n$. *American Mineralogist*, 90:240 – 246, 2005.

[233] C. Frondel. Studies of uranium minerals (VIII) - sabugalite, an aluminum-autunite. *American Mineralogist*, 36:671 – 679, 1951.

[234] R. Berman. Studies of uranium minerals .23. torbernite, zeunerite and uranospherite. *American Mineralogist*, 42:905 – 908, 1957.

[235] T. Murakami, T. Ohnuki, H. Isobe, and T. Sato. Mobility of uranium during weathering. *American Mineralogist*, 82:888 – 899, 1997.

[236] A. J. Pinto, M. A. Gonçalves, C. Prazeres, J. M. Astilleros, and M. J. Batista. Mineral replacement reactions in naturally occurring hydrated uranyl phosphates from the Tarabau deposit: Examples in the Cu-Ba uranyl phosphate system. *Chemical Geology*, 312:18 – 26, 2012.

[237] P. C. Burns, M. L. Miller, and R. C. Ewing. U^{6+} minerals and inorganic phases: A comparison and hierarchy of structures. *Canadian Mineralogist*, 34:845 – 880, 1996.

[238] J. Čejka Jr., A. Muck, and J. Čejka. To the infrared-spectroscopy of natural uranyl phosphates. *Physics and Chemistry of Minerals*, 11:172 – 177, 1984.

[239] J. Čejka, J. Čejka Jr, and A. Muck. Thermal-analysis and infrared-spectra of some natural and synthetic uranium micas. *Thermochimica Acta*, pages 387 – 390, 1985.

[240] J. Čejka Jr, A. Muck, and J. Čejka. Infrared-spectra and thermal-analysis of synthetic uranium micas and their deuteroanalogues. *Neues Jahrbuch fuer Mineralogie, Monatshefte*, pages 115 – 126, 1985.

[241] A. F. Hallimond. Meta-torbernite I, its physical properties and relation to torbernite. *Mineralogical Magazine*, 19:43 – 47, 1920.

[242] K. Walenta. über die barium-uranylphosphatmineralien uranocircit I, uranocircite II, meta-uranocircit I und meta-uranocircite II von Menzenschwand im südlichen Schwarzwal. *Jahresheft des Geologischen Landesamt Baden-Württemberg*, 6:113 – 135, 1963.

[243] S. A. Miller and J. C. Taylor. The crystal structure of saleeite, $Mg(UO_2PO_4)_2 \cdot 10H_2O$. *Zeitschrift fuer Kristallographie*, pages 247 – 253.

[244] J. Čejka, J. Sejkora, R. L. Frost, and E. C. Keeffe. Raman spectroscopic study of the uranyl mineral metauranospinite Ca[(UO$_2$)(AsO$_2$)]·8H$_2$O. *Journal of Raman Spectroscopy*, 40:1786–1790, 2009.

[245] J. Plášil, J. Čejka, J. Sejkora, J. Hlousek, and U. Goliáš. New data for metakirchheimerite from Jachymov (St. Joachimsthal), Czech Republic. *Journal of Geosciences*, 54:373–384, 2009.

[246] S. V. Gevorkyan and A. S. Povarennykh. *Mineralogicheskii Zhurnal*, 2:29, 1980.

[247] J. Čejka, Z. Urbanec, J. Čejka Jr., J. Ederova, and A. Muck. Thermal and infrared-spectrum analyses of sabugalite. *Journal of Thermal Analysis*, 33:395–399, 1988.

[248] R. L. Frost, O. Carmody, K. L. Erickson, and M. L. Weier. Near-infrared spectroscopy to uranyl arsenates of the autunite and metaautunite group. *Spectrochimica Acta, Part A*, 61:1923–1927, 2005.

[249] J. Čejka, J. Sejkora, R. L. Frost, and E. C. Keeffe. Raman spectroscopic study of the uranyl mineral natrouranospinite (Na$_2$,Ca)[(UO$_2$)(AsO$_4$)]$_2$·5H$_2$O. *Journal of Raman Spectroscopy*, 40:1521, 2009.

[250] R. L. Frost, J. Čejka, and M. L. Weier. A Raman spectroscopic study of the uranyl phosphate mineral threadgoldite. *Spectrochimica Acta, Part A*, 65:797–801, 2006.

[251] N. Sanchez-Pastor, A. J. Pinto, J. M. Astilleros, L. Fernandez-Diaz, and M. A. Gonçalves. Raman spectroscopic characterization of a synthetic, non-stoichiometric Cu-Ba uranyl phosphate. *Spectrochimica Acta, Part A*, 113:196–202, 2013.

[252] A. J. Locock and P. C. Burns. The crystal structure of bergenite, a new geometrical isomer of the phosphuranylite group. *Canadian Mineralogist*, 41:91–101, 2003.

[253] J. W. Anthony, R. A. Bideaux, K. W. Bladh, and M. C. Nichols. *Handbook of Mineralogy*, volume 5. Mineral Data Publishing: Tiscon, Arizona, 2003.

[254] L. V. Kobets and D. S. Umreiko. Uranium phosphates. *Uspekhi Khimii*, 52:897–921, 1983.

[255] F. Demartin, V. Diella, S. Donzelli, C. M. Gramaccioli, and T. Pilati. The importance of accurate crystal structure determination of uranium minerals .I. phosphuranylite KCa(H$_3$O)$_3$(UO$_2$)$_7$(PO$_4$)O$_4$·8H$_2$O. *Acta Crystallographica B*, B47:439–446, 1991.

[256] Z. Chen, H. Yushu, and G. Xiaofa. *Acta Mineralogica Sinica*, 10:102, 1990.

[257] D. P. Shashkin and G. A. Sidorenko. Study of crystalline-structure of phosphuranylite $Ca[(UO_2)_3(PO_4)_2(OH)_2]\cdot 6H_2O$. *Doklady Akademiia Nauk SSSR*, 220:1161 – 1164, 1975.

[258] G. Wappler and G. Shubert. *Gessel Geol.*, 14:257, 1969.

[259] F. Mazzi, C. L. Garavelli, and F. Rinaldi. *Atti Società Toscana di Scienze Naturali*, A65:135, 1958.

[260] J. Zhang, A. Wan, and W. Gong. *Yan. Kuang. Zac.*, 11:178, 1992.

[261] R. L. Frost, M. L. Weier, T. Bostrom, J. Čejka, and W. Martens. Molecular structure of the uranyl mineral zippeite - an XRD, SEM and Raman spectroscopic study. *Neues Jahrbuch fur Mineralogie, Abhandlungen*, 181:271 – 279, 2005.

[262] P. Piret and J. Piret-Meunier. Chemical-composition and crystal-structure of phosphuranylite, $Ca(UO_2)[(UO_2)_3(OH)_2(PO_4)_2]_2\cdot 12H_2O$. *European Journal of Mineralogy*, 3:69 – 77, 1991.

[263] J. M. V. Coutinho and D. Atencio. Phosphuranylite from Minas Gerais, Brazil and its identity with yingjiangite. 4th *International Mineralogy in Museums Conference*, page 35, 2000.

[264] J. Plášil, J. Sejkora, J. Čejka, R. Škoda, and U. Goliáš. Supergene mineralization of the Medvedín uranium deposit, Krkonoše Mountains, Czech Republic. *Journal of Geosciences*, 54:15 – 56, 2009.

[265] J. Sejkora, F. Veselovsky, and V. Srein. The supergene mineralization of uranium occurrence Ryzoviste near Harrachov (Krkonose Mts., Czech Republic). *Sbornik Narodniho Muzea v Praze Rada B Prirodni Vedy*, 50:55 – 91, 1994.

[266] J. Čejka. Infrared spectroscopy and thermal analysis of the uranyl minerals. *Reviews in Mineralogy*, 38:521 – 622, 1999.

[267] R. L. Frost, J. Čejka, and G. Ayoko. Raman spectroscopic study of the uranyl phosphate minerals phosphuranylite and yingjiangite. *Journal of Raman Spectroscopy*, 39:495, 2008.

[268] R. L. Frost and J. Čejka. Raman spectroscopic study of the uranyl phosphate mineral dumontite. *Journal of Raman Spectroscopy*, 40:591, 2009.

[269] J. Čejka, J. Sejkora, R. Scholz, A. López, Y. Xi, and R. L. Frost. Raman and infrared spectroscopic studies of phurcalite from Red Canyon, Utah, USA - implications for the molecular structure. *Journal of Molecular Structure*, $1068:14-19$, 2014.

[270] R. L. Frost, M. J. Dickfos, and J. Čejka. Raman spectroscopic study of the uranyl carbonate mineral zellerite. *Journal of Raman Spectroscopy*, $39:582-586$, 2008.

[271] D. L. Clark, D. E. Hobart, and M. P. Neu. Actinide complexes and their importance in actinide environmental chemistry. *Chemical Reviews*, $95:25-48$, 1995.

[272] J. Čejka and Z. Urbanec. *Transactions of the Czechoslovak Academy of Sciences, Math. Natur. History Series*, 100:1, 1990.

[273] V. Baran, F. Skvor, and V. Vosecek. Formation of the ammonium-uranyl-carbonate complexes of the type $(NH_4)_4[UO_2(CO_3)_3]$, prepared by precipitative re-extraction. *Inorganica Chimica Acta*, $81:83-89$, 1984.

[274] A. Anderson, C. Chieh, D. E. Irish, and J. P. K. Tong. An X-ray crystallographic, Raman, and infrared spectral study of crystalline potassium uranyl carbonate, $K_4UO_2(CO_3)_3$. *Canadian Journal of Chemistry*, $58:1651-1658$, 1980.

[275] J. Čejka. To chemistry of andersonite and thermal decomposition of dioxotricarbonatouranates. *Collection of Czechoslovak Chemical Communications*, 34:1635, 1969.

[276] A. Coda, A. Della Giusta, and V. Tazzoli. Structure and conformation of amino-acids containing sulfur .4. structure of N-acetyl-L-cysteine - X-ray (T=295-K) and neutron (T=16-K). *Acta Crystallographica, Part B*, $37:1496-1500$, 1981.

[277] C. K. Huang and P. F. Kerr. Infrared study of the carbonate minerals. *American Mineralogist*, $45:311-324$, 1960.

[278] K. Omori and P. F. Kerr. Infrared studies of saline sulfate minerals. *Geological Society of America Bulletin*, $74:709-734$, 1963.

[279] P. Ondrus, P. Skala, F. Veselovsky, J. Sejkora, and C. Vitti. Cejkaite, the triclinic polymorph of $Na_4(UO_2)(CO_3)_3$ - a new mineral from Jachymov, Czech Republic. *American Mineralogist*, $88:686-693$, 2003.

[280] J. Čejka, Z. Urbanec, and J. Čejka Jr. Contribution to the crystal-chemistry of andersonite. *Neues Jahrbuch fuer Mineralogie, Monatshefte*, pages $488-501$, 1987.

[281] P. C. Burns, R. C. Ewing, and F. C. Hawthorne. The crystal chemistry of hexavalent uranium: Polyhedral geometries, bond-valence parameters, and polymerization of polyhedra. *Canadian Mineralogist*, 35:1551–1570, 1997.

[282] Z. Urbanec and J. Čejka. Chemistry of uranyl carbonates .3. infrared-spectra of rutherfordine and sharpite. *Collection of Czechoslovak Chemical Communications*, 44:1–9, 1979.

[283] Z. Urbanec and J. Čejka. Chemistry of uranyl carbonates .4. infrared-spectra of liebigite, andersonite, voglite, and schroeckingerite. *Collection of Czechoslovak Chemical Communications*, 44:10–23, 1979.

[284] J. Čejka and Z. Urbanec. Thermal and infrared-spectrum analyses of natural and synthetic andersonites. *Journal of Thermal Analysis*, 33:389–394, 1988.

[285] G. C. Jones and B. Jackson. *Infrared Transmission Spectra of Carbonate Minerals*. Chapman and Hall, 1993.

[286] R. L. Frost, O. Carmody, K. L. Erickson, M. L. Weier, and J. Čejka. Molecular structure of the uranyl mineral andersonite - a Raman spectroscopic study. *Journal of Molecular Structure*, 703:47–54, 2004.

[287] R. L. Frost, K. L. Erickson, M. L. Weier, O. Carmody, and J. Čejka. Raman spectroscopic study of the uranyl tricarbonate mineral liebigite. *Journal of Molecular Structure*, 737:173–181, 2005.

[288] R. L. Frost, M. L. Weier, J. Čejka, and G. A. Ayoko. Raman spectroscopy of uranyl rare earth carbonate kamotoite-(Y). *Spectrochimica Acta, Part A*, 65:529–535, 2006.

[289] R. L. Frost, D. A. Henry, and K. L. Erickson. Raman spectroscopic detection of wyartite in the presence of rablejacite. *Journal of Raman Spectroscopy*, 35:255–260, 2004.

[290] R. Vochten, L. Van Haverbeke, K. Van Springel, N. Blaton, and O. M. Peeters. The structure and physiochemical characteristics of synthetic zippeite. *Canadian Mineralogist*, 33:1091–1101, 1995.

[291] P. Ondrus, F. Veselovsky, J. Hlousek, R. Skala, I. Vavrin, J. Frya, J. Čejka, and A. Gabasova. Secondary minerals of the Jachymov (Joachimsthal) ore district. *Journal of the Czech Geological Society*, 42:3–76, 1997.

[292] J. Sejkora, J. Čejka, P. Škácha, A. Gabašová, and M. Novotná. Minerals of the zippeite group from the Jánská vein, Brezové Hory, Príbram (Czech Republic. *Bull. Mineral.-Petrolog. Odd. Nár. Muz (Praha)*, 11:183 – 189, 2003.

[293] N. Meisser. *La minéralogie de l'uranium dans le massif des Aiguilles Rouges (Alpes occidentales)*. PhD thesis, Université de Lausanne, 2003.

[294] N. J. Elton and J. J. Hooper. Sodium zippeite from Geevor Mine, St. Just, Cornwall. *Mineralogical Magazine*, 57:352 – 354, 1993.

[295] R. L. Frost, K. L. Erickson, J. Čejka, and B. J. Reddy. A Raman spectroscopic study of the uranyl sulphate mineral johannite. *Spectrochimica Acta, Part A*, 61:2702 – 2707, 2005.

[296] J. Čejka, Z. Urbanec, J. Čejka Jr., and Z. Mrazek. Contribution to the thermal-analysis and crystal-chemistry of johannite $Cu[(UO_2)_2(SO_4)_2(OH)_2] \cdot 8H_2O$. *Neues Jahrbuch fuer Mineralogie, Abhandlungen*, 159:297, 1988.

[297] F. Sokol and J. Čejka. A thermal and mass-spectroscopic studi of synthetic johannite $[Cu(UO_2)_2(SO_4)_2(OH)_2] \cdot 8H_2O$. *Thermochimica Acta*, 206:235 – 242, 1992.

[298] C. S. Hurlbut. Studies of uranium minerals .4. johannite. *American Mineralogist*, 35:531 – 535, 1950.

[299] J. D. H. Donnay. The primitive cell of johannite. *American Mineralogist*, 40:1131 – 1132, 1955.

[300] R. L. Frost, J. Čejka, G. Ayoko, and M. L. Weier. Raman spectroscopic and SEM analysis of sodium-zippeite. *Journal of Raman Spectroscopy*, 38:1311 – 1319, 2007.

[301] C. Frondel and A. D. Weeks. Recent progress in the descriptive mineralogy of uranium. *Proceedings of the 2nd UN International Conference of Peaceful Uses Atomic Energy, Geneva*, 2:277 – 285, 1958.

[302] B. E. McCollam. PhD thesis, University of Notre Dame, Indiana, 2004.

[303] C. Frondel, J. Ito, R. M. Honea, and A. M. Weeks. Mineralogy of the zippeite group. *Canadian Mineralogist*, 14:429 – 436, 1976.

[304] A. O. Matkovskii, S. V. Gevorkyan, A. S. Povarennykh, G. A. Sidorenko, and A. N. Tarashchan. *Mineralogicheskii Sbornik (Lvov)*, 33:11, 1979.

[305] R. L. Frost, M. L. Weier, G. A. Ayoko, W. Martens, and J. Čejka. An XRD, SEM and TG study of a uranopilite from Australia. *Mineralogical Magazine*, 70:299 – 307, 2006.

[306] J. Plášil, E. Buixaderas, J. Čejka, J. Sejkora, J. Jehlicka, and M. Novak. Raman spectroscopic study of the uranyl sulphate mineral zippeite: Low wavenumber and U-O stretching regions. *Analytical and Bioanalytical Chemistry*, 397:2703, 2010.

[307] R. L. Frost, J. Čejka, M. L. Weier, and W. N. Martens. Raman spectroscopy study of selected uranophanes. *Journal of Molecular Structure*, 788:115 – 125, 2006.

[308] D. J. Wronkiewicz, J. K. Bates, T. J. Gerding, E. Veleckis, and B. S. Tani. Uranium release and secondary phase formation during unsaturated testing of UO_2 at 90°C. *Journal of Nuclear Materials*, 190:107 – 127, 1992.

[309] E. C. Pearcy, J. D. Prikryl, W. M. Murphy, and B. W. Leslie. Alteration of uraninite from the Nopal I deposit, Peña Blanca District, Chihuahua, Mexico, compared to degradation of spent nuclear fuel in the proposed U.S. high-level nuclear waste repository at Yucca Mountain, Nevada. *Applied Geochemistry*, 9:713 – 732, 1994.

[310] D. J. Wronkiewicz, J. K. Bates, S. F. Wolf, and E. C. Buck. Ten-year results from unsaturated drip tests with UO_2 at 90°C: Implications for the corrosion of spent nuclear fuel. *Journal of Nuclear Materials*, 238:78 – 95, 1996.

[311] R. J. Finch, E. C. Buck, P. A. Finn, and J. K. Bates. Oxidative corrosion of spent UO_2 fuel in vapor and dripping groundwater at 90°C. *Materials Research Society, Symposium Proceedings*, 556:431 – 438, 1999.

[312] M. Douglas, S. B. Clark, J. I. Friese, B. W. Arey, E. C. Buck, and B. D. Hanson. Neptunium(V) partitioning to uranium(VI) oxide and peroxide solids. *Environmental Science and Technology*, 39:4117 – 4124, 2005.

[313] M. Douglas, S. B. Clark, J. I. Friese, B. W. Arey, E. C. Buck, and B. D. Hanson. Microscale characterization of uranium(VI) silicate solids and associated neptunium(V). *Radiochimica Acta*, 93:265 – 272, 2005.

[314] A. J. Locock and P. C. Burns. Structures and syntheses of layered and framework amine-bearing uranyl phosphate and uranyl arsenates. *Journal of Solid State Chemistry*, 177:2675 – 2684, 2004.

[315] P. C. Burns, R. C. Ewing, and M. L. Miller. Incorporation mechanisms of actinide elements into the structures of U^{6+} phases formed during the oxidation of spent nuclear fuel. *Journal of Nuclear Materials*, 245:1 – 9, 1997.

[316] P. C. Burns. Cs boltwoodite obtained by ion exchange from single crystals: Implications for radionuclide release in a nuclear repository. *Journal of Nuclear Materials*, 265:218 – 223, 1999.

[317] P. C. Burns, K. M. Deely, and S. Skanthakumar. Neptunium incorporation into uranyl compounds that form as alteration products of spent nuclear fuel: Implications for geological repository performance. *Radiochimica Acta*, 92:151 – 160, 2004.

[318] A. V. Barinova, R. K. Rastsvetaeva, G. A. Sidorenko, and D. Y. Pushcharovskii. Crystal structure of high-symmetry alpha-uranophane. *Doklady Akademiia Nauk*, 378:122 – 124, 2001.

[319] F. Cesbron, P. Ildefonse, and M. C. Sichere. New mineralogical data on uranophane and beta-uranophane - synthesis of uranophane. *Mineralogical Magazine*, 57:301 – 308, 1993.

[320] S. V. Gevork'yan, A. S. Povarennykh, S. I. Ignatov, and E. A. Il'chenko. *Mineral. Z.*, 3:3, 1981.

[321] P. C. Burns. A new uranyl oxide hydrate sheet in vandendriesscheite: Implications for mineral paragenesis and the corrosion of spent nuclear fuel. *American Mineralogist*, 82:1176 – 1186, 1997.

[322] P. C. Burns and F. C. Hill. A new uranyl sheet in $K_5[(UO_2)_{10}O_8(OH)_9]H_2O$): New insight into sheet anion-topologies. *Canadian Mineralogist*, 38:163 – 173, 2000.

[323] J. Huang, X. Wang, and A. J. Jacobson. Hydrothermal synthesis and structures of the new open-framework uranyl silicates $Rb_4(UO_2)_2(Si_8O_{20})$ (USH2Rb), $Rb_2(UO_2)(Si_2O_6)\cdot H_2O$ (USH4Rb) and $A_2(UO_2)(Si_2O_6)\cdot 0.5H_2O$ (USH5A; A = Rb, Cs). *Journal of Materials Chemistry*, 13:191 – 196, 2003.

[324] R. Vochten, N. Blaton, and O. M. Peeters. *Neues Jahrbuch fuer Mineralogie., Monatshefte*, 100:569, 1990.

[325] B. M. Biwer, W. L. Ebert, and J. K. Bates. The Raman spectra of several uranyl-containing minerals using a microprobe. *Journal of Nuclear Materials*, 175:188, 1990.

[326] J. Protas. *Bulletin de la Societe Francaise Mineralogie et de Cristallographie*, 87:365, 1964.

[327] P. Ondrus, J. Jansa, F. Novak, and I. Vavrin. *Vestnik Ceskeho Geologickeho Ustavu*, 69:79, 1994.

[328] G. W. Brindley and M. Bastovanov. Interaction of uranyl ions with synthetic zeolites of type-A and the formation of compreignacite-like and becquerelite-like products. *Clays and Clay Minerals*, 30:135 – 142, 1982.

[329] D. J. Wronkiewicz and E. C. Buck. Uranium mineralogy and the geological deposal of spent nuclear fuel. *Reviews In Mineralogy*, 38:475 – 497, 1999.

[330] M. C. A. Sandino and B. Grambow. Solubility equilibria in the U(VI)-Ca-K-Cl-H_2O system - transformation of schoepite into becquerelite and compreignacite. *Radiochimica Acta*, 66:37 – 43, 1994.

[331] M. E. Torrero, I. Casas, J. de Pablo, M. C. A. Sandino, and B. Grambow. A comparison between unirradiated $UO_2(s)$ and schoepite solubilities in 1M NaCl medium. *Radiochimica Acta*, 66:29 – 35, 1994.

[332] M. M. Granger and J. Protas. Etude de la structure cristalline de la compreignacite. *Bulletin de la Societe Francaise Mineralogie et de Cristallographie*, 88:211, 1965.

[333] P. C. Burns. The structure of richetite, a rare lead uranyl oxide hydrate. *Canadian Mineralogist*, 36:187 – 199, 1998.

[334] P. C. Burns and K. M. Deely. A topologically novel sheet of uranyl pentagonal bipyramids in the structure of $Na[(UO_2)_4O_2(OH)_5](H_2O)_2$. *Canadian Mineralogist*, 36:1579 – 1586, 1998.

[335] R. J. Finch, M. A. Cooper, F. C. Hawthorne, and R. C. Ewing. The crystal structure of schoepite, $[(UO_2)_8O_2(OH)_{12}](H_2O)_{12}$. *Canadian Mineralogist*, 34:1071 – 1088, 1996.

[336] M. L. Miller, R. J. Finch, P. C. Burns, and R. C. Ewing. Description and classification of uranium oxide hydrate sheet anion topologies. *Journal of Materials Research*, 11:3048 – 3056, 1996.

[337] A. J. Locock and P. C. Burns. The crystal structure of triuranyl diphosphate tetrahydrate. *Journal of Solid State Chemistry*, 163:275 – 280, 2002.

[338] R. J. Finch and T. Murakami. Systematics and paragenesis of uranium minerals. *Reviews in Mineralogy*, 38:91 – 179, 1999.

[339] R. J. Finch, R. C. Burns, F. C. Hawthorne, and R. C. Ewing. Refinement of the crystal structure of billietite, $Ba[(UO_2)_6O_4(OH)_6](H_2O)_8$. *Canadian Mineralogist*, 44:1197 – 1205, 2006.

[340] J. Čejka, J. Sejkora, R. Skala, J. Čejka, M. Novotna, and J. Ederova. Contribution to the crystal chemistry of synthetic becquerelite, billietite and protasite. *Neues Jahrbuch Fur Mineralogie-Abhandlungen*, 174:159 – 180, 1998.

[341] J. Čejka, R. Skala, J. Sejkora, and A. Muck. New data on curite from Shinkolobwe, Zaire. *Neues Jahrbuch Fur Mineralogie-Monatshefte*, pages 385 – 402, 1998.

[342] Y. Li, P. C. Burns, and R. A. Gault. A new rare-earth-element uranyl carbonate sheet in the structure of bijvoetite-(Y). *Canadian Mineralogist*, 38:153 – 162, 2000.

[343] M. T. Weller, M. E. Light, and T. Gelbrich. Structure of uranium(VI) oxide dihydrate, $UO_3 \cdot 2H_2O$; synthetic meta-schoepite $(UO_2)_4O(OH)_6 \cdot 5H_2O$. *Acta Crystallographica, Part B*, B56:577 – , 2000.

[344] A. S. Povarennykh. *Konstit. Svoist. Mineral.*, 13:53, 1979.

[345] A. S. Povarennykh. *Konstit. Svoist. Mineral.*, 13:78, 1979.

[346] S. Amayri, T. Arnold, H. Foerstendorf, G. Geipel, and G. Bernhard. Spectroscopic characterization of synthetic becquerelite, $Ca[(UO_2)_6O_4(OH)_6] \cdot 8H_2O$, and swartzite, $CaMg[UO_2(CO_3)_3] \cdot 12H_2O$. *Canadian Mineralogy*, 42:953 – 962, 2004.

[347] P. G. Allen, D. K. Shuh, J. J. Bucher, N. M. Edelstein, C. E. A. Palmer, R. J. Silva, S. N. Nguyen, L. N. Marquez, and E. A. Hudson. Determinations of uranium structures by EXAFS: Schoepite and other U(VI) oxide precipitates. *Radiochimica Acta*, 75:47 – 53, 1996.

[348] H. R. Hoekstra and S. Siegel. Uranium trioxide-water system. *Journal of Inorganic and Nuclear Chemistry*, 35:761 – 761, 1973.

[349] D. G. Dothée. *Vibrational Spectroscopy of Hydrated Potassium Hexauranate for the Phase Study of the Uranium(VI)Oxide-Potassium Chloride-Water System*. PhD thesis, University of Besancon, France, 1980.

[350] D. G. Dothée, M. M. Camelot, and J. L. Bernard. Hydrothermal synthesis of new phases in the UO_3-KCl-H_2O system. *Bulletin de la Societe Chimique de France Partie I-Physicochimie des Systemes Liquides Electrochimie Catalyse Genie Chimique*, pages 221 – 227, 1980.

[351] L. Maya and G. M. Begun. A Raman-spectroscopy study of hydroxo and carbonato species of the uranyl(VI) ion. *Journal of Inorganic and Nuclear Chemistry*, 43:2827 – 2832, 1981.

[352] R. L. Frost, J. Čejka, and M. L. Weier. Raman spectroscopic study of the uranyl oxyhydroxide hydrates: Becquerelite, billietite, curite, schoepite and vandendriesscheite. *Journal of Raman Spectroscopy*, 38:460, 2007.

[353] J. R. Bartlett and R. P. Cooney. On the determination of uranium oxygen bond lengths in dioxouranium(VI) compounds by Raman-spectroscopy. *Journal of Molecular Structure*, 193:295 – 300, 1989.

[354] W. Jinhai, Y. Zhengan, L. Jinquan, Z. Chuanzuo, and R. Lihua. Determination of trace uranium in environment by laser induced fluorescence method. *Journal of Environmental Sciences*, 6:93 – 98, 1994.

[355] M. Basile, D. K. Unruh, E. Flores, A. Johns, and T. Z. Forbes. Structural characterization of environmentally relevant ternary uranyl citrate complexes present in aqueous solutions and solid state materials. *Dalton Transactions*, 44:2597 – 2605, 2015.

[356] P. Di Pietro and A. Kerridge. U-O_{yl} stretching vibrations as a quantitative measure of the equatorial bond covalency in uranyl complexes: A quantum-chemical investigation. *Inorganic Chemistry*, 55:573 – 583, 2016.

[357] M. Åberg, D. Ferri, J. Glaser, and I. Grenthe. Structure of the hydrated dioxouranium(VI) ion in aqueous-solution - an X-ray-diffraction and H-1-NMR study. *Inorganic Chemistry*, 22:3986 – 3989, 1983.

[358] R. D. Rogers, A. H. Bond, W. G. Hipple, A. N. Rollins, and R. F. Henry. Synthesis and structural elucidation of novel uranyl crown-ether compounds isolated from nitric, hydrochloric, sulfuric, and acetic-acids. *Inorganic Chemistry*, 30:2671 – 2679, 1991.

[359] P. G. Allen, J. J. Bucher, D. K. Shuh, N. M. Edelstein, and T. Reich. Investigation of aquo and chloro complexes of UO_2^{2+}, NpO_2^{+}, Np^{4+}, and Pu^{3+} by X-ray absorption fine structure spectroscopy. *Inorganic Chemistry*, 36:4676 – 4683, 1997.

[360] S. Spencer, L. Gagliardi, N. C. Handy, A. G. Ioannou, C.-K. Skylaris, A. Willetts, and A. M. Simper. Hydration of UO_2^{2+} and PuO_2^{2+}. *Journal of Physical Chemistry A*, 103:1831 – 1837, 1999.

[361] J. Neuefeind, L. Soderholm, and S. Skanthakumar. Experimental coordination environment of uranyl(VI) in aqueous solution. *Journal of Physical Chemistry A*, 108:2733–2739, 2004.

[362] P. J. Hay, R. L. Martin, and G. Schreckenbach. Theoretical studies of the properties and solution chemistry of AnO_2^{2+} and AnO_2^+ aquo complexes for An = U, Np, and Pu. *Journal of Physical Chemistry A*, 104:6259–6270, 2000.

[363] K. I. M. Ingram, L. J. L. Häller, and N. Kaltsoyannis. Density functional theory investigation of the geometric and electronic structures of $[UO_2(H_2O)_m(OH)_n]_{2-n}$ (n+m=5). *Dalton Transactions*, pages 2403–2414, 2006.

[364] J. P. Austin, M. Sundararajan, M. A. Vincent, and I. H. Hillier. The geometric structures, vibrational frequencies and redox properties of the actinyl coordination complexes $([AnO_2(L)_n]_m$; An = U, Pu, Np; L = H_2O, Cl^-, CO_3^{2-}, CH_3CO^{2-}, OH^-) in aqueous solution, studied by density functional theory methods. *Dalton Transactions*, pages 5902–5909, 2009.

[365] U. Wahlgren, H. Moll, I. Grenthe, B. Schimmelpfennig, L. Maron, V. Vallet, and O. Cropen. Structure of uranium(VI) in strong alkaline solutions. a combined theoretical and experimental investigation. *Journal of Physical Chemistry A*, 103:8257–8264, 1999.

[366] V. Vallet, U. Wahlgren, B. Schimmelpfennig, H. Moll, Z. Szabó, and I. Grenthe. Solvent effects on uranium(VI) fluoride and hydroxide complexes studied by EXAFS and quantum chemistry. *Inorganic Chemistry*, 40:3516–3525, 2001.

[367] J. L. Sonnenberg, P. J. Hay, R. L. Martin, and B. E. Bursten. Theoretical investigations of uranyl-ligand bonding: Four- and five-coordinate uranyl cyanide, isocyanide, carbonyl, and hydroxide complexes. *Inorganic Chemistry*, 44:2255–2262, 2005.

[368] M. Straka, K. G. Dyall, and P. Pyykkö. Ab initio study of bonding trends for f(0) actinide oxyfluoride species. *Theoretical Chemistry Accounts*, 106:393–403, 2001.

[369] J.-C. Berthet, P. Thuéry, and M. Ephritikhine. The first actinyl cyanide. *Chemical Communications*, pages 604–606, 2007.

[370] C. E. Rowland, M. G. Kanatzidis, and L. Soderholm. Tetraalkylammonium uranyl isothiocyanates. *Inorganic Chemistry*, 51:11798–11804, 2012.

[371] N. Iché-Tarrat, N. Barros, C. J. Marsden, and L. Maron. Linear uranium complexes X_2UL_5 with L=cyanide, isocyanate: DFT evidence for similarities between uranyl (X = O) and uranocene (X = Cp) derivatives. *Chemistry-A European Journal*, 14:2093–2099, 2008.

[372] C. Fillaux, D. Guillaumont, J.-C. Berthet, R. Copping, D. K. Shuh, T. Tyliszczak, and C. Den Auwer. Investigating the electronic structure and bonding in uranyl compounds by combining NEXAFS spectroscopy and quantum chemistry. *Physical Chemistry Chemical Physics*, 12:14253–14262, 2010.

[373] A. Abdelouas, W. Lutze, and E. Nuttall. Chemical reactions of uranium in ground water at a mill tailings site. *Journal of Contaminant Hydrology*, 34:343–361, 1998.

[374] W. A. de Jong, E. Apra, T. L. Windus, J. A. Nichols, R. J. Harrison, K. E. Gutowski, and D. A. Dixon. Complexation of the carbonate, nitrate, and acetate anions with the uranyl dication: Density functional studies with relativistic effective core potentials. *Journal of Physical Chemistry A*, 109:11568–11577, 2005.

[375] F. Schlosser, L. V. Moskaleva, A. Kremleva, S. Krüger, and N. Rösch. Comparative density functional study of the complexes $[UO_2(CO_3)_3]^{4-}$ and $[(UO_2)_3(CO_3)_6]^{6-}$ in aqueous solution. *Dalton Transactions*, 39:5705–5712, 2010.

[376] J. Vázquez, C. Bo, J. M. Poblet, J. de Pablo, and J. Bruno. DFT studies of uranyl acetate, carbonate, and malonate, complexes in solution. *Inorganic Chemistry*, 42:6136–6141, 2003.

[377] C. Nguyen-Trung, G. M. Begun, and D. A. Palmer. Aqueous uranium complexes .2. Raman-spectroscopy study of the complex-formation of the dioxouranium(VI) ion with a variety of inorganic and organic-ligands. *Inorganic Chemistry*, 31:5280–5287, 1992.

[378] S. Fortier and T. W. Hayton. Oxo ligand functionalization in the uranyl ion (UO_2^{2+}). *Coordination Chemistry Reviews*, 254:197–214, 2010.

[379] P. Castaldi, M. Silvetti, E. Mele, G. Garau, and S. Delana. Arsenic mobilization by citrate and malate from a red mud-treated contaminated soil. *Journal of Environmental Quality*, 42:774–781, 2013.

[380] S. A. Wasay, S. Barrington, and S. Tokunaga. Organic acids for the in situ remediation of soils polluted by heavy metals: Soil flushing in columns. *Water Air and Soil Pollution*, 127:301–314, 2001.

[381] H. M. Steele, K. Wright, and I. H. Hillier. Modelling the adsorption of uranyl on the surface of goethite. *Geochimica et Cosmochimica Acta*, 66:1305 – 1310, 2002.

[382] J. A. Greathouse, R. J. O'Brien, G. Bemis, and R. T. Pabalan. Molecular dynamics study of aqueous uranyl interactions with quartz (010). *Journal of Physical Chemistry B*, 106:1646 – 1655, 2002.

[383] O. F. Zaidan, J. A. Greathouse, and R. T. Pabalan. Monte Carlo and molecular dynamics simulation of uranyl adsorption on montmorillonite clay. *Clays and Clay Minerals*, 51:372 – 381, 2003.

[384] J. A. Greathouse and R. T. Cygan. Molecular dynamics simulation of uranyl(VI) adsorption equilibria onto an exernal montmorillonite surface. *Physical Chemistry Chemical Physics*, 7:3580 – 3586, 2005.

[385] J. A. Greathouse and R. T. Cygan. Water structure and aqueous uranyl(VI) adsorption equilibria onto external surface of beidellite, montmorillonite, and pyrophyllite: Results from molecular simulations. *Environmental Science and Technology*, 40:3865 – 3871, 2006.

[386] J.-F. Boily and K. M. Rosso. Crystallographic controls on uranyl binding at the quartz/water interface. *Physical Chemistry Chemical Physics*, 13:7845 – 7851, 2011.

[387] S. Doudou, K. Arumugam, D. J. Vaughan, F. R. Livens, and N. A. Burton. Investigation of ligand exchange reactions in aqueous uranyl carbonate complexes using computational approaches. *Physical Chemistry Chemical Physics*, 13:11402 – 11411, 2011.

[388] S. Doudou, D. J. Vaughan, F. R. Livens, and N. A. Burton. Atomistic simulations of calcium uranyl(VI) carbonate adsorption on calcite and stepped-calcite surfaces. *Environmental Science and Technology*, 46:7587 – 7594, 2011.

[389] S. Kerisit and C. Liu. Diffusion and adsorption of uranyl carbonate species in nanosized mineral fractures. *Environmental Science and Technology*, 46:1632, 2012.

[390] S. Kerisit and C. Liu. Molecular dynamics simulations of uranyl and uranyl carbonate adsorption at aluminosilicate surfaces. *Environmental Science and Technology*, 48:3899 – 3907, 2016.

[391] R. Drot, J. Roques, and E. Simoni. Molecular approach of the uranyl/mineral interfacial phenomena. *C.R. Chim.*, 10:1078 – 1091, 2007.

[392] A. Kremleva, S. Krüger, and N. Rösch. Density functional model studies of uranyl adsorption on (001) surfaces of kaolinite. *Langmuir*, 24:9515–9524, 2008.

[393] D. M. Sherman, C. L. Peacock, and C. G. Hubbard. Surface complexation of U(VI) on goethite (α-FeOOH). *Geochimica et Cosmochimica Acta*, 72:298–310, 2008.

[394] A. Kremleva, S. Krüger, and N. Rösch. Quantum chemical modeling of uranyl adsorption on mineral surfaces. *Radiochimica Acta*, 98:635–646, 2010.

[395] V.-A. Glezakou and W. A. de Jong. Cluster-models for uranyl(VI) adsorption on α-alumina. *Journal of Physical Chemistry A*, 115:1257–1263, 2011.

[396] F. N. Skomurski, E. S. Ilton, M. H. Engelhard, B. W. Arey, and K. M. Rosso. Heterogeneous reduction of U^{6+} by structural Fe^{2+} from theory and experiment. *Geochimica et Cosmochimica Acta*, 75:7277–7290, 2011.

[397] A. Kremleva, B. Martorell, S. Krüger, and N. Rösch. Uranyl adsorption on solvated edge surfaces of pyrophyllite: a DFT model study. *Physical Chemistry Chemical Physics*, 14:5815–5823, 2012.

[398] S. Lectez, J. Roques, M. Salanne, and E. Simoni. Car-Parrinello molecular dynamics study of the uranyl behaviour at the gibbsite/water interface. *Journal of Chemical Physics*, 137:154705, 2012.

[399] S. M. Walker and U. Becker. Uranyl (VI) and neptunyl (V) incorporation in carbonate and sulfate minerals: Insight from first-principles. *Geochimica et Cosmochimica Acta*, 161:19–35, 2015.

[400] A. Kremleva, S. Krüger, and N. Rösch. Toward a reliable energetics of adsorption at solvated mineral surfaces: A computational study of uranyl(VI) on 2:1 clay minerals. *Journal of Physical Chemistry C*, 120:324–335, 2016.

[401] M. Ross, H. T. Evans Jr., and D. E. Appleman. Studies of the torbernite minerals (II): The crystal structure of meta-torbernite. *American Mineralogist*, 49:1603–1621, 1964.

[402] A. G. Nord and P. Kierkegaard. The crystal structure of $Mg_3(PO_4)_2$. *Acta Chemica Scandinavica*, 22:1466–1474, 1968.

[403] G. L. Shoemaker, J. B. Anderson, and E. Kostiner. Copper(II) phosphate. *Acta Crystallographica B*, 33:2969–2972, 1977.

[404] S. Asbrink and L. J. Norrby. A refinement of the crystal structure of copper(II) oxide with a discussion of some exceptional E.s.d.'s. *Acta Crystallographica B*, 26:8 – 15, 1970.

[405] A. J. Locock, P. C. Burns, and T. M. Flynn. Divalent transition metals and magnesium in structures that contain the autunite-type sheet. *Canadian Mineralogist*, 42:1699 – 1718, 2004.

[406] F. Franks. *Water: A Matrix of Life*. Royal Society of Chemistry, 2nd edition, 2000.

[407] P. G. Dickens, S. D. Lawrence, and M. T. Weller. *Materials Research Bulletin*, 20:635 – 641, 1985.

[408] G. W. Watt, S. L. Achorn, and J. L. Marley. Some chemical and physical properties of uranium peroxide. *Journal of the American Chemical Society*, 72:3341, 1950.

[409] I. Sheft, S. Fried, and N. Davidson. Preparation of uranium trioxide. *Journal of the American Chemical Society*, 72:2172 – 2173, 1950.

[410] E. Wait. A cubic form of uranium trioxide. *Journal of Inorganic and Nuclear Chemistry*, 1:309, 1955.

[411] H. Hoekstra and S. Siegel. *Proceedings of the 2nd International Conference for Peaceful Uses of Atomic Energy, Geneva*, 28:231, 1958.

Chapter A
Raman Spectral Analysis

To assist in the analysis of the Raman spectra, we used a peak-fitting algorithm written by J. Skelton to identify and characterise the major spectral features [85]. The fitting routine proceeds in two stages. In the first, the spectrum is divided into 5 equal segments, each of which is fitted to a slope to approximate the average spectral intensity in that region. Bands with intensities above 1.05 times this line are temporarily removed, and the remaining complete spectrum is then smoothed with an 11-point median filter, and the smoothed spectrum fitted to a 10-order polynomial to obtain a background function.

In the second step, the background polynomial is subtracted and the peaks in customisable regions of interest (ROIs) are found. In each ROI, the baseline intensity is again fitted to a slope, with intensities 1.1 times the average within the region being excluded from the fit. A 11-point triangle filter is applied, and candidate peaks are identified from intensity maxima in the smoothed spectrum. Those within 1.5 multiples of the baseline are discarded, and the remaining are fitted to a sum of Lorentzian functions, initialised with one function positioned at the centre of each candidate peak, scaled to match the peak height and with an initial full width at half maximum (FWHM) of 5.0. The peaks are optimised against the unsmoothed spectrum with the baseline slope subtracted, using a least-squares algorithm. Finally, functions in the optimised set whose centres fall outside their ROI are discarded.

The algorithm returns the coefficients of the background polynomial and peak functions, the latter of which serve as a peak table providing the position, intensity, and FWHM of major spectral features. By testing a subset of the spectra for each mineral sample and visually comparing the original and fitted spectra, we confirmed that, with these parameters and ROIs set to 100-1200 cm^{-1} this fitting routine could successfully identify and characterise all the major peaks across a wide variety of spectra.

Chapter B

Experimental Preparation of UO$_3$ Samples

Unpublished Raman spectra for α, β, γ and δ-UO$_3$ were provided by G. C. Allen for the investigation in Chapter 5. XPS and IR spectra have been published for the same samples [80, 200]. A brief description of the synthesis and Raman collection methods is given in this section.

Finely powdered samples of the α, β and δ phases of UO$_3$ were synthesised by Dickens *et al.* [191, 407] using previously published methods [408–411]. γ-UO$_3$ was produced by heating a commercially supplied sample of γ-UO$_3$·2H$_2$O from Koch-Light Laboratories in a stream of dry air at 300°C for 24 hours [200]. All phases were identified by comparing the X-ray diffraction pattern against previously published experimental data [198, 200].

Raman spectra were recorded using an Instruments SA Ramanor U-1000 spectrometer, with a Spectra-Physics Model 164 5 W argon-ion laser source that provided a 514 nm excitation [186]. The powdered samples were mounted on microscope slides and examined using 40x long-range microscope objectives with 180° scattering. In order to reduce surface heating, the power at the sample was kept below 2 mW and defocused, illuminating a spot of 10 μm in diameter. To improve the signal-to-noise ratio, a large number of spectra were accumulated and averaged, using software provided by Instruments SA.

Vibrational Analysis of UO$_3$

Table C.1: The Raman active modes seen in simulated spectra of the five phases of UO$_3$. E1–E5 represents different uranium environments in β- and γ-UO$_3$, which may vibrate in different ways at the same frequency. The modes that only involve a single environment and vibration are highlighted in **bold**.

U-O length	Motion	α-UO$_3$	β-UO$_3$					γ-UO$_3$		δ-UO$_3$	η-UO$_3$
			E1	E2	E3	E4	E5	E1	E2		
<1.9 Å	Symm. str.	-	856 787 535	-	-	856 787	**878**	732 449	**823**	-	**780** **658**
	Asym. str.	-	-	-	-	-	-	-	-	-	**836**
	U-O str.	-	-	-	-	-	680	-	-	-	-
	Bend (U)	-	-	-	-	-	-	-	325	-	- **366** **205**
1.9 - 2.1 Å	Symm. str.	-	-	535	-	-	-	-	-	**847** **478** **171**	-
	Asym. str.	-	-	680	-	-	-	-	-	-	-
	U-O str.	-	-	787 711	787 711 680 535	-	-	-	-	-	-
2.1 - 2.3 Å	Symm. str.	**536**	-	-	-	-	-	732 449 325	-	**847** **171**	-
	Asym. str.	-	-	-	-	-	-	-	**376**	-	-
	U-O str.	-	-	-	-	-	-	-	-	-	466
	Bend (no U)	**298**	-	-	-	-	-	-	-	-	-

Table C.2: The IR active modes seen in simulated spectra of the five phases of UO$_3$. E1–E5 represents different uranium environments in β- and γ-UO$_3$, which may vibrate in different ways at the same frequency. The modes that only involve a single environment and vibration are highlighted in **bold**.

U-O length	Motion	α-UO$_3$	β-UO$_3$ E1	E2	E3	E4	E5	γ-UO$_3$ E1	E2	δ-UO$_3$	η-UO$_3$
<1.9 Å	Symm. str.	-	-	-	-	-	-	-	860 761	-	**771** **687**
	Asym. str.	-	**879**	-	-	996	996	860 761 **758**	**950**	-	**863** **854** **845**
	U-O str.	-	-	-	-	-	-	-	-	-	478
	Bend (U)	-	-	-	-	- 268	-	**290** **282**	**335** **310**	-	**310** **307** **291**
	Bend (no U)	-	-	-	-	-	-	-	-	-	**371** **332**
1.9 - 2.1 Å	Symm. str.	-	-	727 495	727 495	-	-	-	-	-	-
	Asym. str.	**464**	-	568 565 436	568 565 436	-	-	-	-	**698**	-
	Bend (U)	**241**	-	281	-	-	-	-	-	**277**	-
2.1 - 2.3 Å	Symm. str.	-	-	-	-	-	-	-	465	-	-
	Asym. str.	**360**	-	568	576 **386**	-	-	-	-	**504**	-
	U-O str.	-	-	-	-	-	-	-	-	-	478 443
	Bend (U)	**304**	-	268	281 268	-	-	-	-	**250** **158**	-
>2.3 Å	Bend (U)	-	268	-	-	-	281	**397** **368** **300**	-	-	-
U Lattice Mode		-	-	-	-	-	-	125	125	-	-

Vibrational Properties of γ-UO$_3$
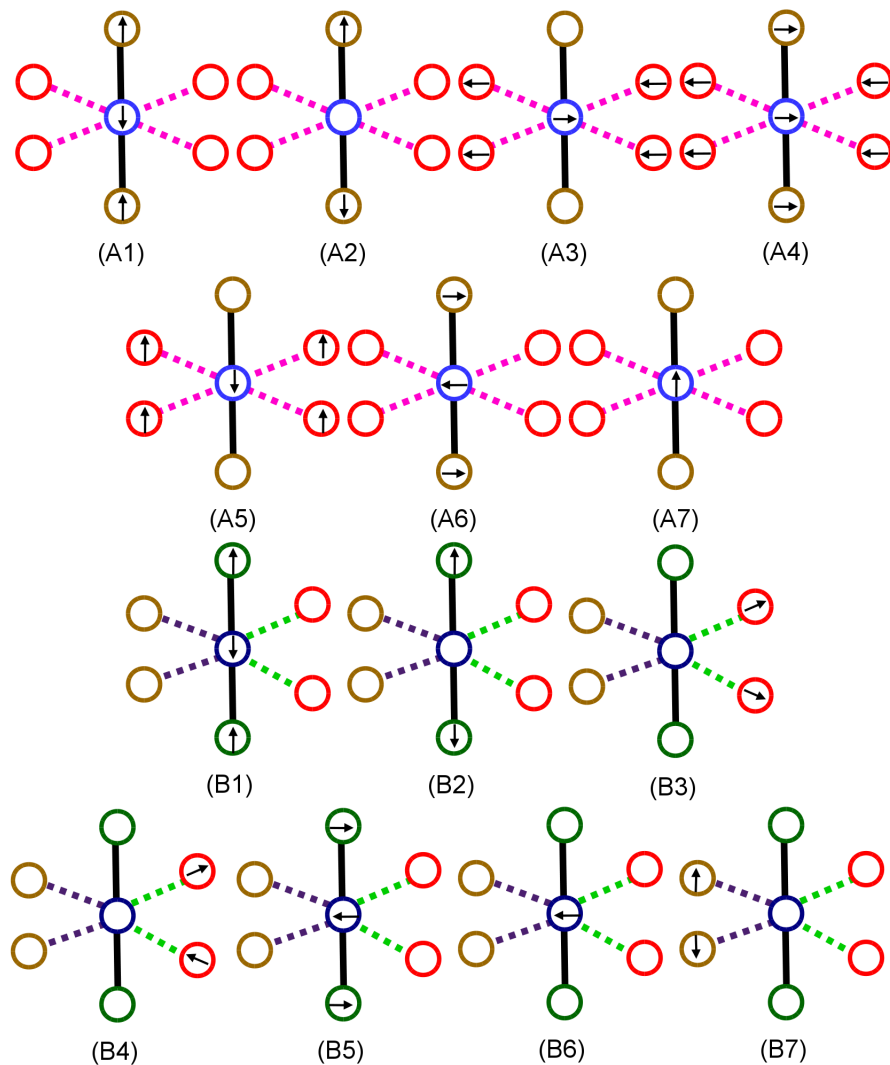
Figure C.1: Schematics showing the vibrational motions found in the simulated spectrum of γ-UO$_3$. A1–7 refer to motions involving environment 1 (Figure 5.2.c) and B1–7 refer to motions involving environment 2 (Figure 5.2.d).
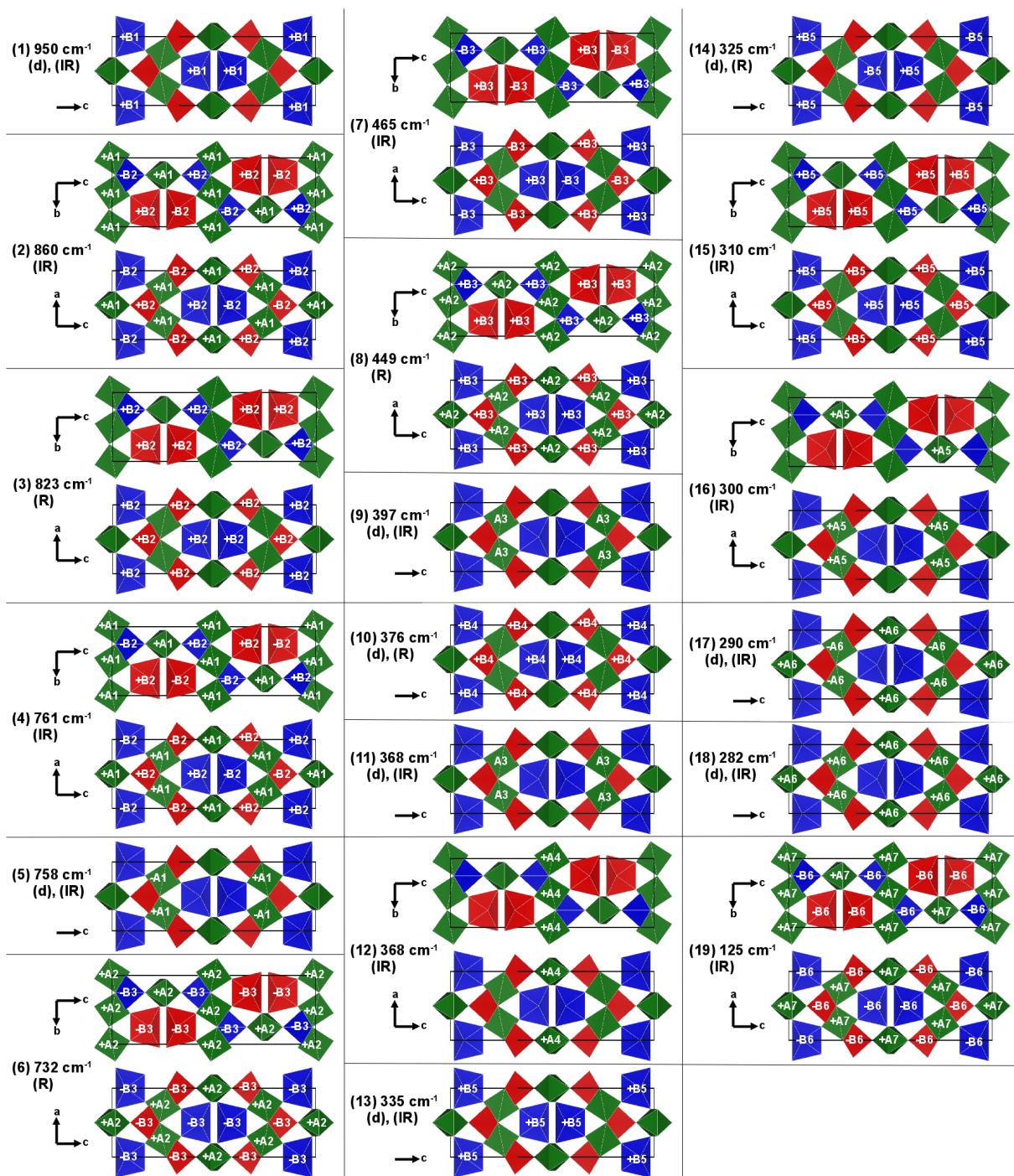
Figure C.2: Diagrams to represent the vibrational motions on each environment at each frequency for the simulated γ-UO$_3$ spectrum. The numbers refer to the motions given in Figure C.1 and the signs show whether motions are in- or out-of-phase. The vibrations are considered Raman or IR active if the calculated activity is greater than 5 % of the highest intensity peak.

Vibrational Properties of δ-UO$_3$
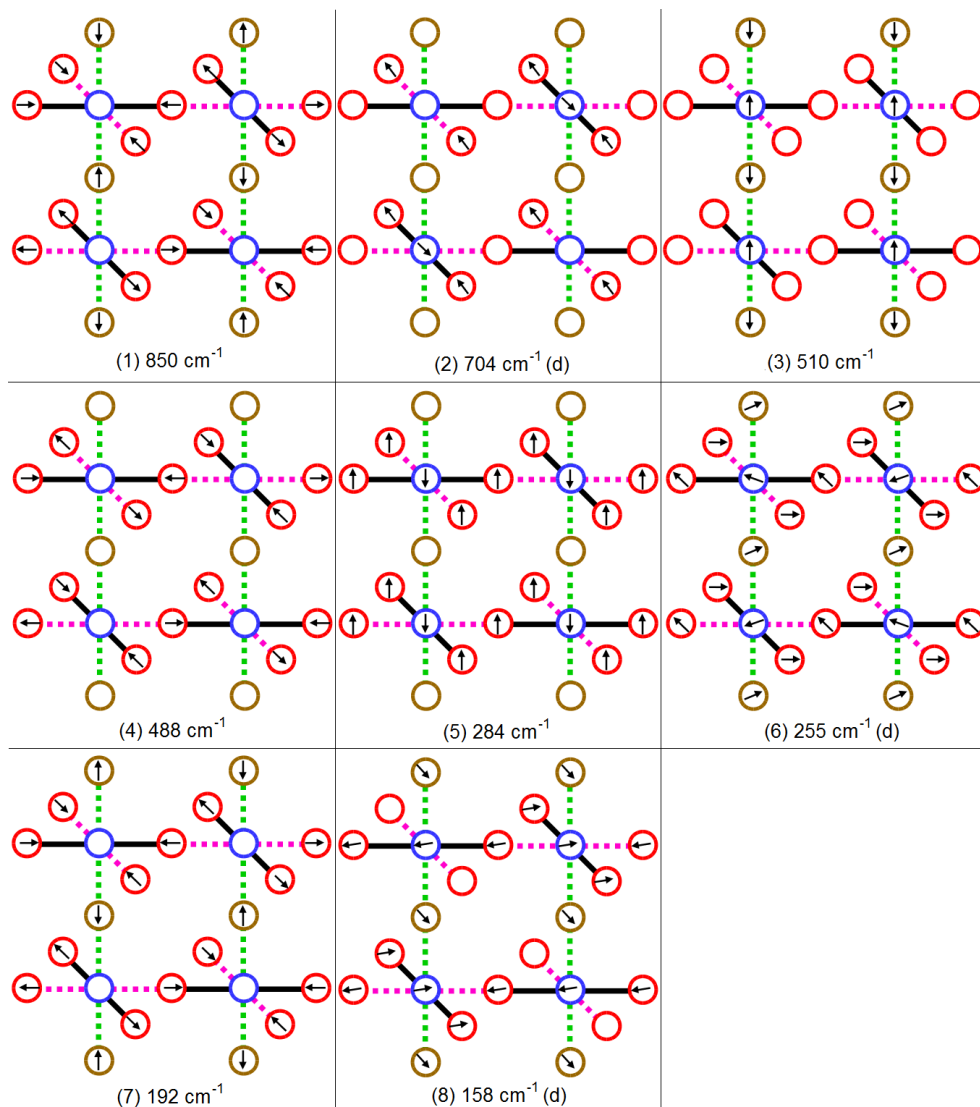
Figure C.3: Schematic diagrams showing the vibrational motions within the 16 atom unit cell of δ-UO$_3$ at each Raman or IR active vibrational frequency. Blue, red and brown circles represent uranium and two oxygen environments, respectively, the solid black lines represent uranyl bonds (1.9 Å) and the green (2.1 Å) and purple (2.3 Å) dashed lines represent longer U-O bonds. (d) represents doubly degenerate vibrations.

Table C.3: Calculated vibrational frequencies for the 16 atom unit cell of δ-UO_3. The first column links the motion to Figure C.3.

Motion	Activity	DFT (cm^{-1})	Description
(1)	R	850	Breathing
(2)	IR	704/703	Antisymm. stretch (1.9 Å)
(3)	IR	510	Antisymm. stretch (2.1 Å)
(4)	R	488	Symm. stretch (1.9 Å)
(5)	IR	284	Bending (1.9 Å and 2.3 Å)
(6)	IR	255	Bending (All U–O)
(7)	IR	253	Bending (1.9 Å)
(8)	R	192	Breathing (Out-of-phase)
(9)	IR	158	Bending (U-O-U-O chain)
(10)	IR	156	Lattice mode (U)

Vibrational Properties of α-UO_3

Table C.4: The calculated vibrational frequencies for α-UO_3 compared with experimental values from Allen and Holmes [80] and this work. The labels in the motion column indicate the illustration from Figure C.4.

This work (R) (cm^{-1})	Allen [80] (IR) (cm^{-1})	DFT (cm^{-1})	Motion	Symmetry label
-	930	-	-	-
$\sim$840	890	-	-	-
$\sim$760	775	-	-	-
-	710	464 (IR)	(C.4.5) Stretching	A_{2u}
$\sim$560	-	536 (R)	(C.4.1) Stretching	E_g
-	500	360 (IR)	(C.4.3) Stretching	E_u
-	390	304 (IR)	(C.4.6) Bending	A_{2u}
$\sim$370	-	298 (R)	(C.4.4) Bending	A_{1g}
$\sim$240	-	241 (IR)	(C.4.2) Bending	E_u
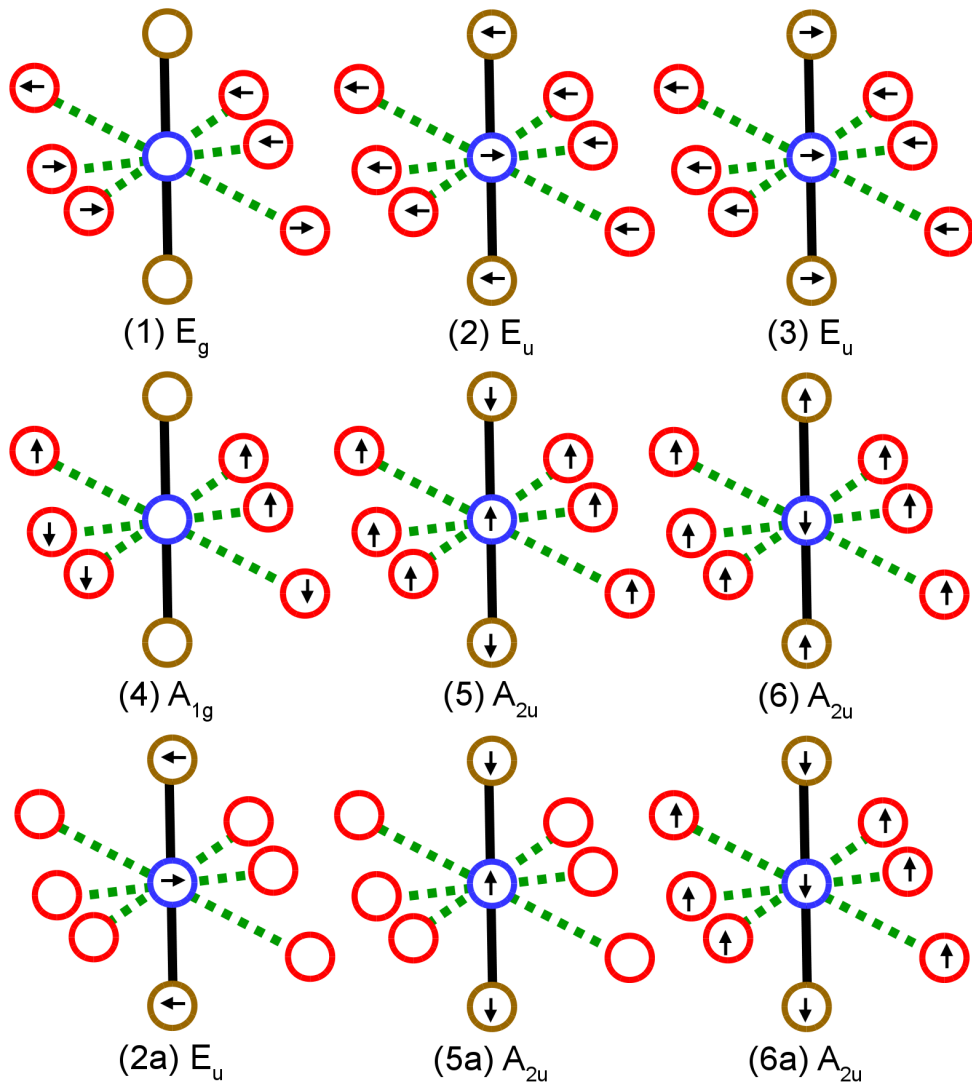
Figure C.4: (1–6) Schematic representation of the motions associated with each irreducible representation of the α-UO$_3$ coordination environment, which has D$_{3d}$ symmetry. (2a, 5a and 6a) The three motions predicted by Tsuboi *et al.* [64] that differ from those in this investigation.

Vibrational Properties of β-UO$_3$
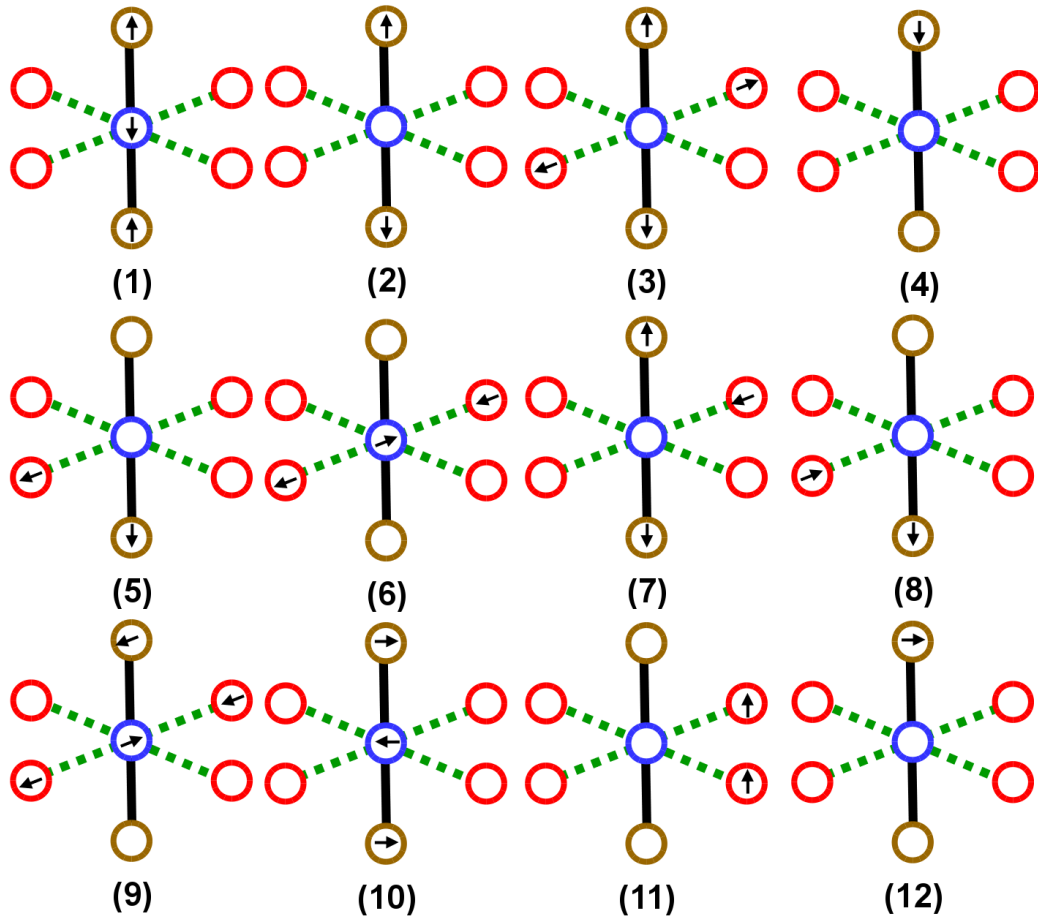
Figure C.5: Diagrams representing the vibrational motions for uranium environments in β-UO$_3$; these motions refer to the schematics presented in Figure C.6.

Figure C.6: Schematics representing the vibrational motions seen in each Raman or IR active frequency in the simulated spectrum of β-UO_3. The numbers refer to the motions described in Figure C.5, while the sign shows which motions are in and out of phase to one another. Environments 1 to 5 are coloured blue, green, red, yellow and purple, respectively. The vibrations are considered Raman (R) or IR active if the calculated activity is greater than 15 % of the highest intensity peak.

Figure C.7: (a) The experimental unit cell of β-UO$_3$, with the five environments labelled. (b–f) Uranium environments 1–5 of the β-UO$_3$ experimental structure, with bond distances given in Å. The structure after relaxation has been presented in Figure 5.5.

Vibrational Properties of η-UO$_3$
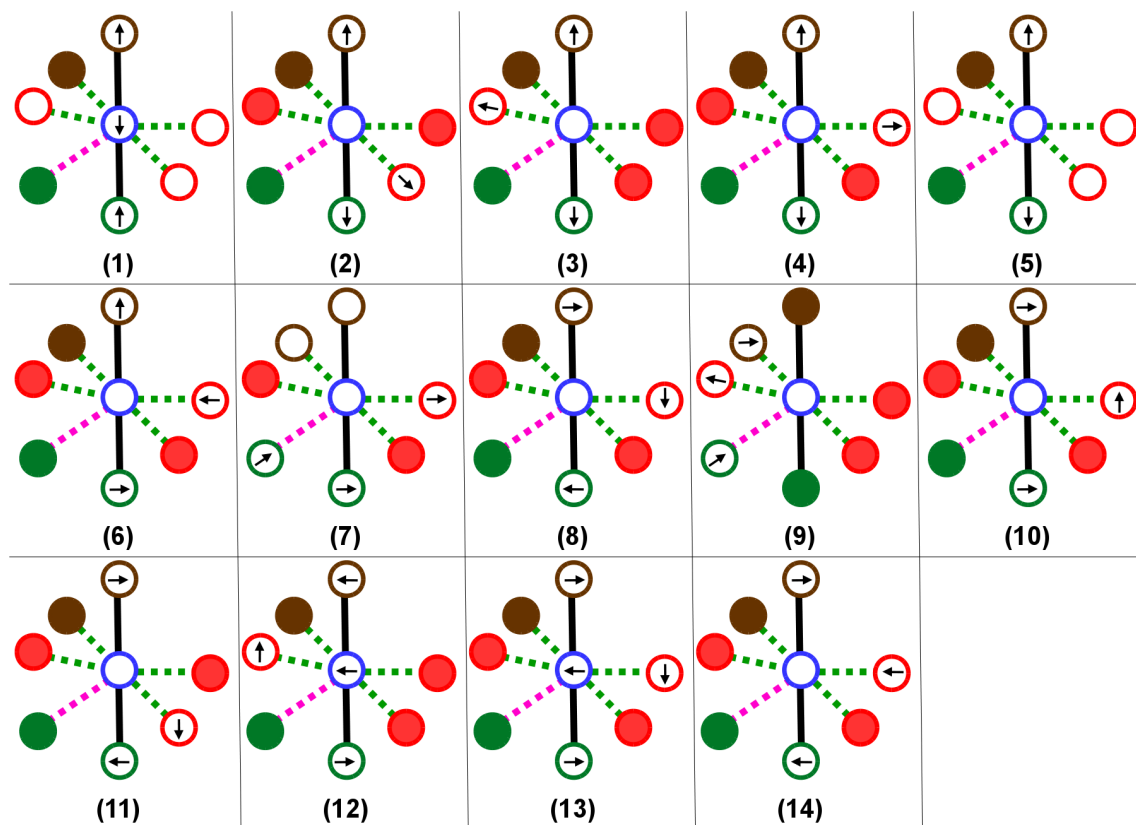
Figure C.8: The motions of uranium environments in the simulated spectrum of η-UO$_3$, associated with the vibrational frequencies shown in Figure C.9. The uranium environment is represented by a blue circle, the three oxygen environments are represented by brown, green and red circles, the collinear uranyl bonds ($\sim$1.8 Å) are represented by solid black lines, bonds between 2.0–2.5 Å are represented by dashed green lines and the longest bonds (2.7 Å) are represented by dashed pink lines. A circle with an arrow illustrates the direction of vibrational motion for that atom, an empty circle indicates that the atom is not moving and a filled circle represents an atom that is moving, but the motion is more significant for a different U-O bond.
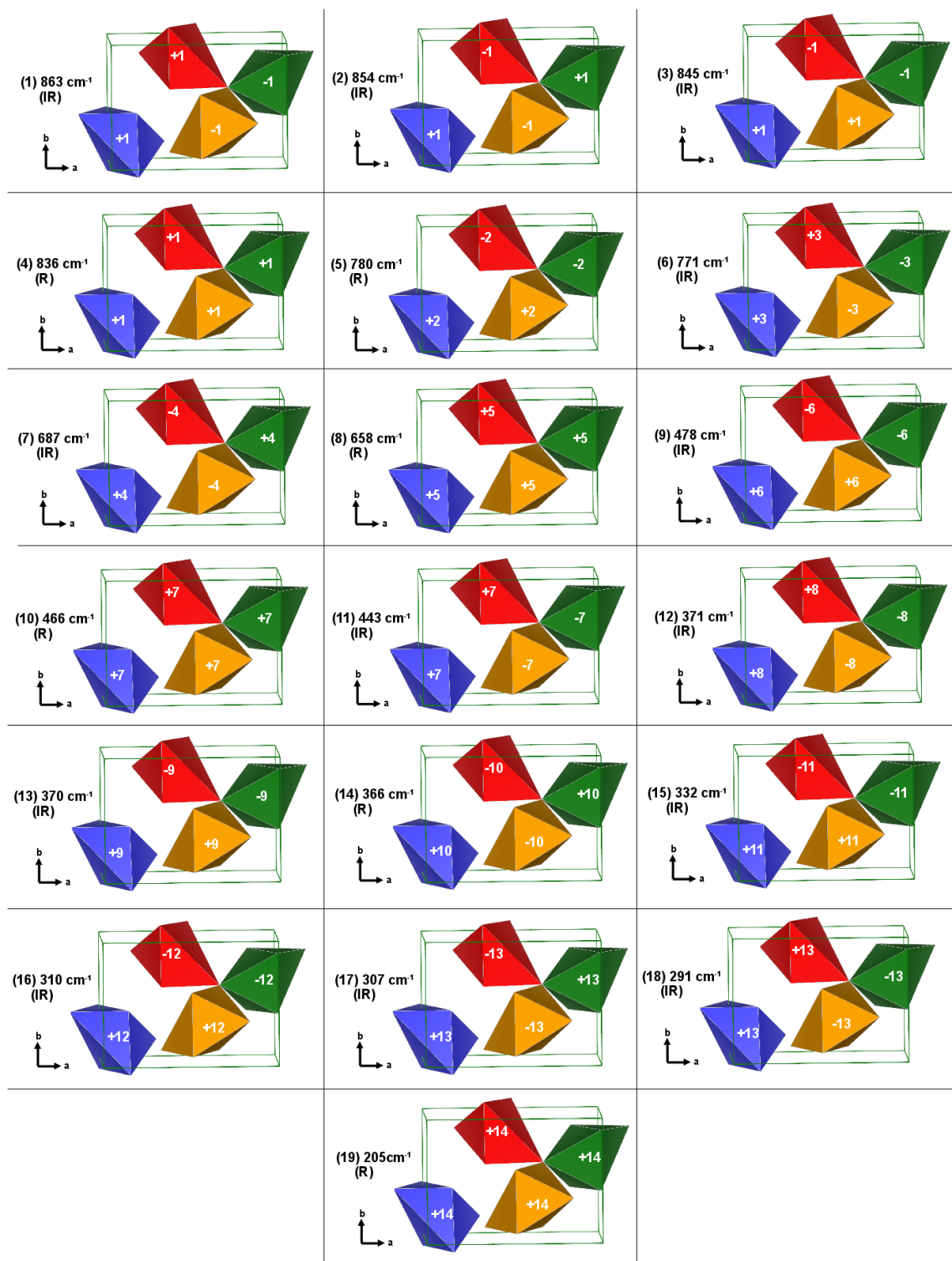
Figure C.9: Diagrams describing the vibrational modes for each Raman or IR active mode in the simulated spectrum of η-UO$_3$. The numbers correspond to the motions detailed in Figure C.8 and the signs indicate which environments are vibrating in- and out-of-phase.

Chapter D

Statistical Analysis of Experimental Raman Spectra

The tables shown in this section detail the vibrational bands seen in the Raman spectra for each mineral described in Chapter 6. The positions given are an average of the same band seen in multiple spectra of the same sample, and both the standard deviation and the number of spectra in which each peak is seen are given. Literature bands are given; these have typically been deconvoluted. The assignment is based upon that given for the published spectra. The figures shown here illustrate the Raman spectra collected using all three excitation wavelengths for each mineral.
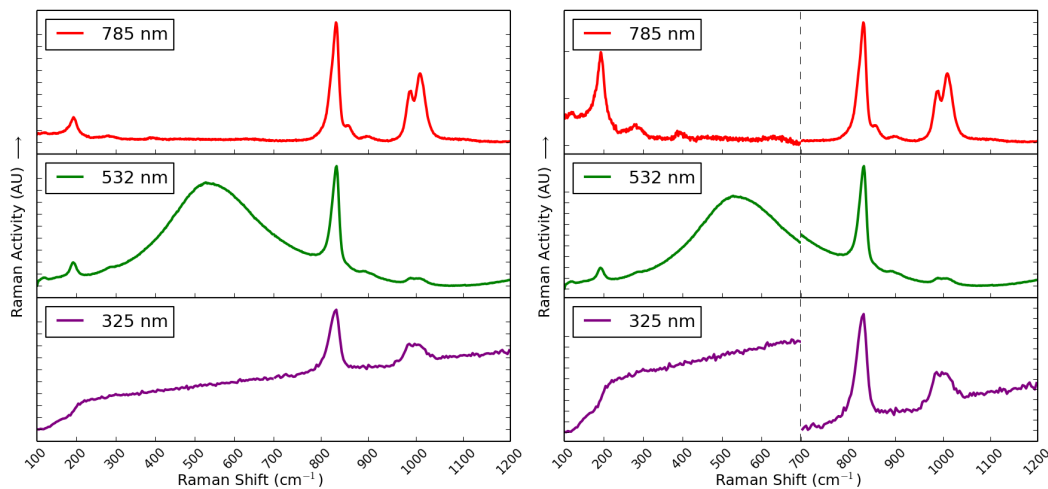
Figure D.1: A comparison of the three laser wavelengths for the uranyl phosphate mineral autunite. The left figure shows the raw spectra. Each section of the spectra shown on the right has been independently rescaled, to emphasise the bands.

Table D.1: Raman spectral bands for the uranyl phosphate mineral autunite

Position (cm^{-1})	This Study Standard Deviation	Number of spectra	Literature [69] Position (cm^{-1})	Attribution
193 †	1.7	31	190, 222	Lattice Vibrations
283 *	4.2	19	291	$v_2(UO_2)^{2+}$ bend
–	–	–	399, 406, 439, 464	$v_2(PO_4)^{3-}$ bend
–	–	–	629	$v_4(PO_4)^{3-}$ bend
830	3.6	60	816, 822, 833	$v_1(UO_2)^{2+}$ symm. stretch
899 *	4.93	9	–	$v_3(UO_2)^{2+}$ antisymm. stretch
990	2.67	21	988	
1001 §	7.53	31	1007	$v_3(PO_4)^{3-}$ symm. stretch
1008	4.16	21	1018	

Sixty individual spectra were analysed for this sample of autunite.

* Low intensity or broad bands, not always visible in spectra.

† The 193 cm^{-1} peak was most prominent within the 785 nm spectra.

§ The 1001 cm^{-1} peak was only visible when the 990 and 1008 cm^{-1} peaks were not.
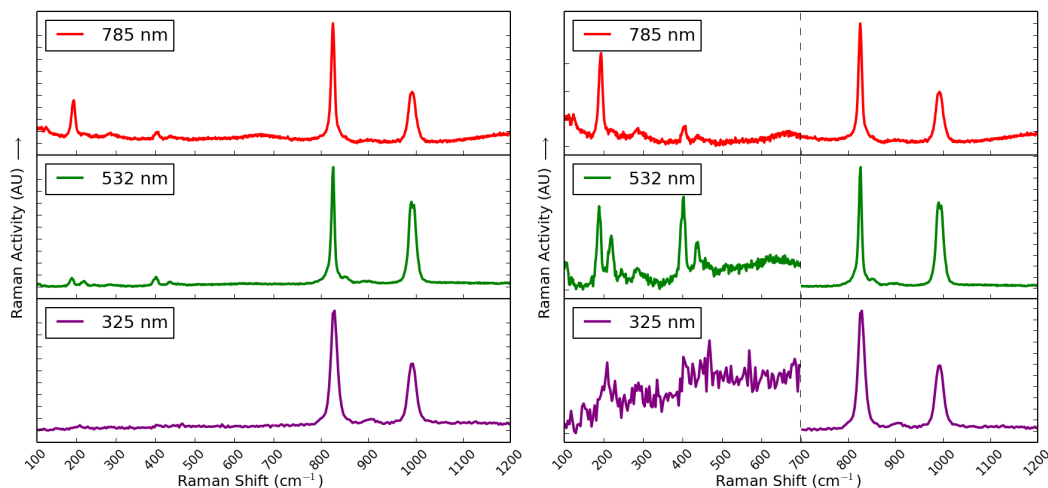
Figure D.2: A comparison of the three laser wavelengths for the uranyl phosphate mineral torbernite. The left figure shows the raw spectra. Each section of the spectra shown on the right has been independently rescaled, to emphasise the bands.

Table D.2: Raman spectral bands for the uranyl phosphate mineral torbernite

Position (cm^{-1})	This Study Standard Deviation	Number of spectra	Literature [69] Position (cm^{-1})	Attribution
191 *	2.3	26	–	Lattice Vibrations
–	–	–	222, 290	$v_2(UO_2)^{2+}$ bend
404 *	2.7	24	399, 406, 439, 464	$v_2(PO_4)^{3-}$ bend
440 *	3.9	9		
–	–	–	629	$v_4(PO_4)^{3-}$ bend
825	1.8	38	808, 826	$v_1(UO_2)^{2+}$ symm. stretch
903 *	2.1	10	900	$v_3(UO_2)^{2+}$ antisymm. stretch
992	1.75	38	957, 988, 995, 1004	$v_3(PO_4)^{3-}$ antisymm. stretch

Thirty eight individual spectra were analysed for this sample of torbernite.
* Low intensity or broad bands, not always visible in spectra.
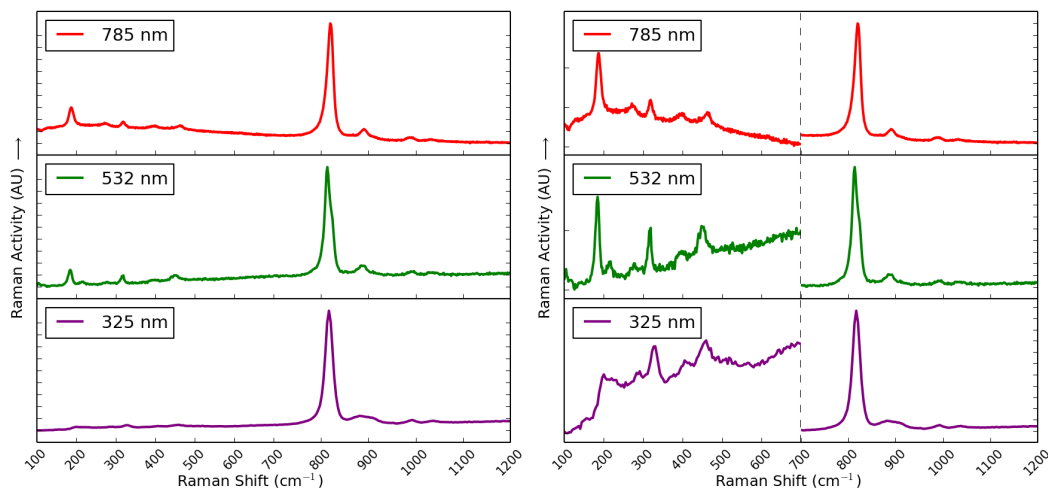
Figure D.3: A comparison of the three laser wavelengths for the uranyl arsenate mineral nováčekite. The left figure shows the raw spectra. Each section of the spectra shown on the right has been independently rescaled, to emphasise the bands.

Table D.3: Raman spectral bands for the uranyl arsenate mineral nováčekite

Position (cm^{-1})	This Study Standard Deviation	Number of spectra	Literature [70] Saléeite Peak Positions (cm^{-1})	Literature [69]	Attribution
185	2.9	28	177, 196	–	Lattice Vibrations
269 *	6.0	10	218, 234, 283	284	$v_2(UO_2)^{2+}$ bend
325 *	4.3	14			$v_2(PO_4)^{3-}$ bend
452 *	2.6	10	376, 405, 446, 471	389	or
471 *	5.5	8			$v_2(AsO_4)^{3-}$ bend
–	–	–	573, 612	643	$v_4(PO_4)^{3-}$ bend
817	2.6	55	827, 843	818, 833, 847	$v_1(UO_2)^{2+}$ symm. stretch
889	5.6	36	896	–	$v_3(UO_2)^{2+}$ antisymm. stretch
989	2.3	11	980, 994, 1007	982, 988, 1007	$v_3(PO_4)^{3-}$ antisymm. stretch
1034 *	2.6	7			

Fifty five individual spectra were analysed for this sample of nováčekite.

No literature spectra are available for a direct comparison with nováčekite, so its spectrum has been compared against saléeite, its phosphate analogue.

* Low intensity or broad bands, not always visible in spectra.
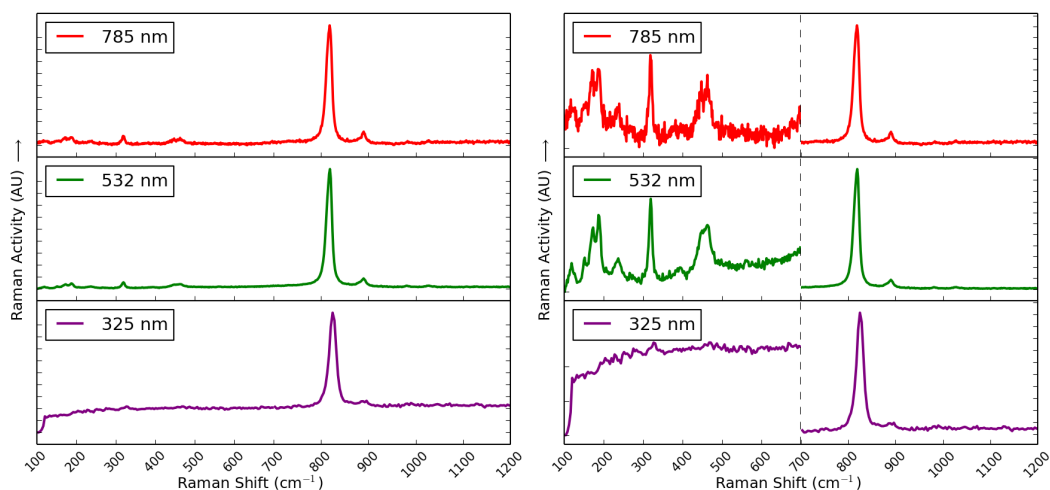
Figure D.4: A comparison of the three laser wavelengths for the uranyl arsenate mineral zeunerite. The left figure shows the raw spectra. Each section of the spectra shown on the right has been independently rescaled, to emphasise the bands.

Table D.4: Raman spectral bands for the uranyl arsenate mineral zeunerite

Position (cm^{-1})	This Study Standard Deviation	Number of spectra	Literature [87] Position (cm^{-1})	Attribution
–	–	–	182	Lattice Vibrations
–	–	–	218, 235, 275	$v_2(UO_2)^{2+}$ bend
323 *	4.9	5	320, 380	$v_2(AsO_4)^{3-}$ bend
404 *	4.6	7	396	$v_4(AsO_4)^{3-}$ bend
463	6.6	19	446, 463	
821	3.0	25	811, 818	$v_1(UO_2)^{2+}$ symm. stretch
886	4.5	16	890	$v_3(UO_2)^{2+}$ antisymm. stretch
987	1.7	9	–	unknown
1029 *	2.8	4	–	unknown

Twenty five individual spectra were analysed for this sample of zeunerite.
* Low intensity or broad bands, not always visible in spectra.

Figure D.5: A comparison of the three laser wavelengths for the uranyl phosphate mineral phosphuranylite. The left figure shows the raw spectra. Each section of the spectra shown on the right has been independently rescaled, to emphasise the bands.

Table D.5: Raman spectral bands for the uranyl phosphate mineral phosphuranylite

This Study			Literature [267]			Attribution
			Minerva Heights	Saddle Ridge	Ruggles Mine	
Position (cm^{-1})	Standard Deviation	Number of spectra		Position (cm^{-1})		
148 *	2.3	16	111, 152, 175	117, 145, 166	112, 147, 161	Lattice Vibrations
216 *	4.2	13	211	205	208	
239 *	3.7	5	220	227, 240	238	
260 *	3.9	13	263	267	267	$v_2(UO_2)^{2+}$ bend
283 *	3.4	5	295	294	287	
312 *	5.3	6				
435	6.0	25	404, 435, 452	368, 394, 417, 439	396, 398, 421, 437, 452, 476	$v_2(PO_4)^{3-}$ bend
558 *	2.7	7	564, 613, 655	500, 532, 566	511, 515, 536, 569, 616	$v_4(PO_4)^{3-}$ bend
801	4.9	29	768, 793, 805, 815	816, 837, 843, 847	812, 817, 832, 841	$v_1(UO_2)^{2+}$ symm. stretch
–	–	–	–	–	894	$v_3(UO_2)^{2+}$ antisymm. stretch
992 †	2.8	10	992	1009	1005	
1017 †	1.2	8	1016	1050	1032, 1050, 1055	$v_3(PO_4)^{3-}$ antisymm. stretch
–	–	–	1122	1125	1124	

Twenty nine individual spectra were analysed for this sample of phosphuranylite.

* Low intensity or broad bands, not always visible in spectra.

† The 992 and 1017 cm^{-1} bands appear together, in a small number of 785 nm spectra.
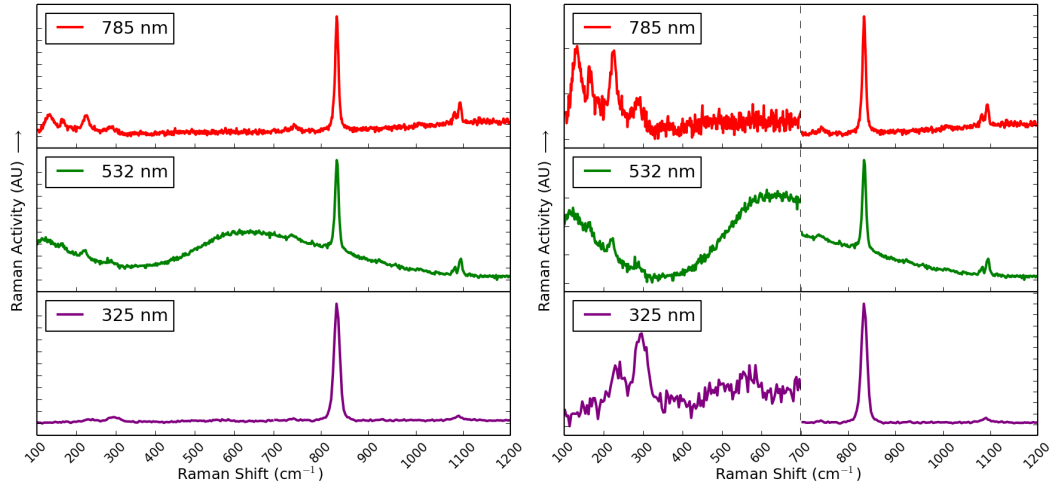
Figure D.6: A comparison of the three laser wavelengths for the uranyl carbonate mineral andersonite. The left figure shows the raw spectra. Each section of the spectra shown on the right has been independently rescaled, to emphasise the bands.

Table D.6: Raman spectral bands for the uranyl carbonate mineral andersonite

Position (cm^{-1})	This Study Standard Deviation	Number of spectra	Literature [286] Position (cm^{-1})	Attribution
130	3.1	7	164, 182	Lattice Vibrations
225 *	5.2	8	224, 242, 284, 299	$v_2(UO_2)^{2+}$ bend
291 *	3.3	6		
743 *	2.0	4	697, 732, 744	$v_4(CO_3)^{2-}$ bend
833	0.5	15	830, 833	$v_1(UO_2)^{2+}$ symm. stretch
1092	2.3	15	1080, 1092	$v_1(CO_3)^{2-}$ symm. stretch
–	–	–	1370, 1406	$v_3(CO_3)^{2-}$ antisymm. stretch

Fifteen individual spectra were analysed for this sample of andersonite.
* Low intensity or broad bands, not always visible in spectra.
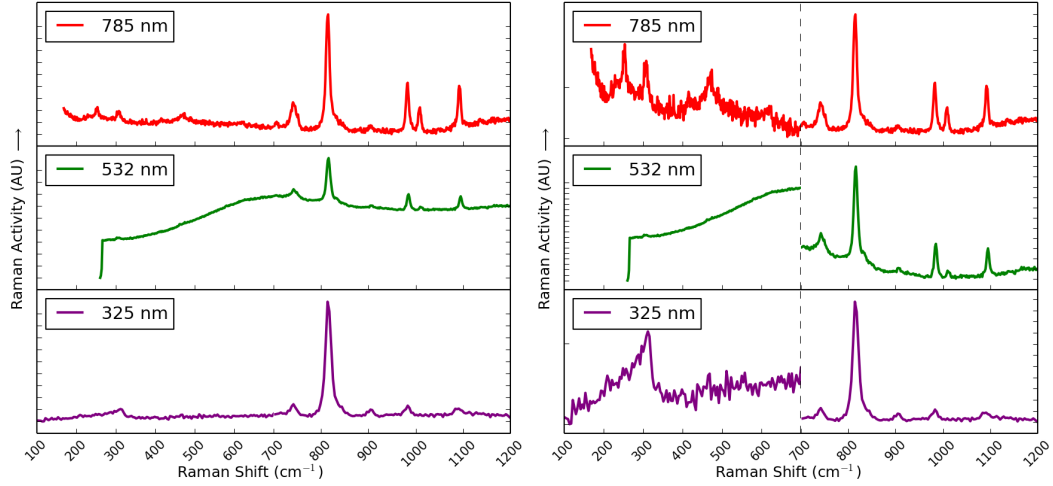
Figure D.7: A comparison of the three laser wavelengths for the uranyl carbonate mineral schröckingerite. The left figure shows the raw spectra. Each section of the spectra shown on the right has been independently rescaled, to emphasise the bands.

Table D.7: Raman spectral bands for the uranyl carbonate mineral schröckingerite

Position (cm^{-1})	This Study Standard Deviation	Number of spectra	Literature [76] Position (cm^{-1})	Attribution
–	–	–	157	Lattice Vibrations
253 *	0.5	3	308	$v_2(UO_2)^{2+}$ bend
307 *	2.9	4		
416 *	3.8	5	471	$v_2(SO_4)^{2-}$ bend
496 *	3.6	6		
743	2.1	16	707, 742	$v_4(CO_3)^{2-}$ bend
815	1.0	21	815	$v_1(UO_2)^{2+}$ symm. stretch
984	2.0	14	983	$v_1(SO_4)^{2-}$ symm. stretch
1009 *	0.8	12		
1093	1.8	12	1092	$v_1(CO_3)^{2-}$ symm. stretch
1136	3.3	9	1090, 1100, 1147	$v_3(SO_4)^{2-}$ antisymm. stretch

Twenty one individual spectra were analysed for this sample of schröckingerite.
* Low intensity or broad bands, not always visible in spectra.
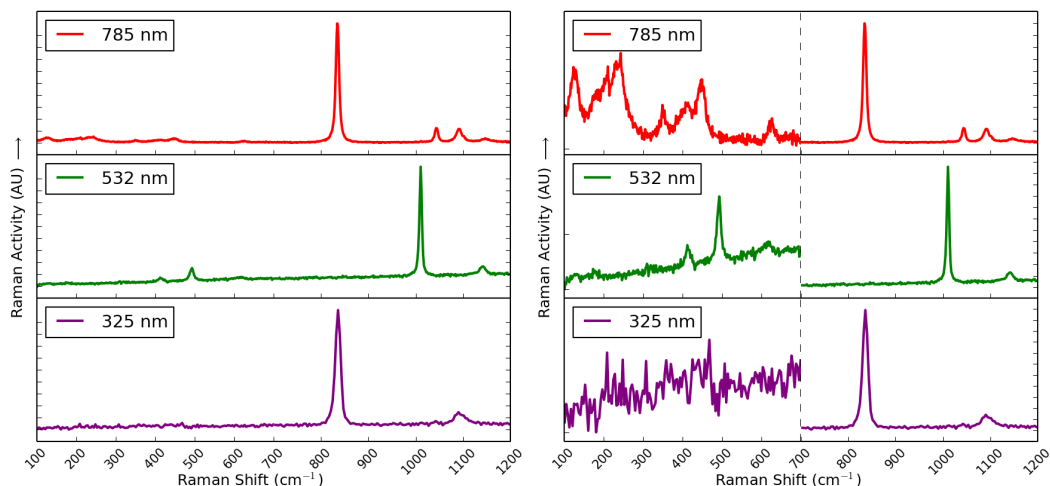
Figure D.8: A comparison of the three laser wavelengths for the uranyl sulphate mineral johannite. The left figure shows the raw spectra. Each section of the spectra shown on the right has been independently rescaled, to emphasise the bands.

Table D.8: Raman spectral bands for the uranyl sulphate mineral johannite

Position (cm^{-1})	This Study Standard Deviation	Number of spectra	Literature [295] Position (cm^{-1})	Attribution
–	–	–	184	Lattice Vibrations
203 *	3.0	13	205	$v_2(UO_2)^{2+}$ bend
244 *	2.4	10	277	
–	–	–	302	Cu-O stretch
352 *	0.8	6	384	$v_2(SO_4)^{2-}$ bend
448 *	1.7	7	481, 539	$v_4(SO_4)^{2-}$ bend
836	1.1	30	756, 788, 812	$v_1(UO_2)^{2+}$ symm. stretch
–	–	–	948, 975	$v_3(UO_2)^{2+}$ antisymm. stretch
1045	1.3	14	1042	$v_1(SO_4)^{2-}$ symm. stretch
1095	3.1	18	1009, 1100, 1147	$v_3(SO_4)^{2-}$ antisymm. stretch

Thirty individual spectra were analysed for this sample of johannite.
* Bands are only visible in a number of 532 and 785 nm spectra.
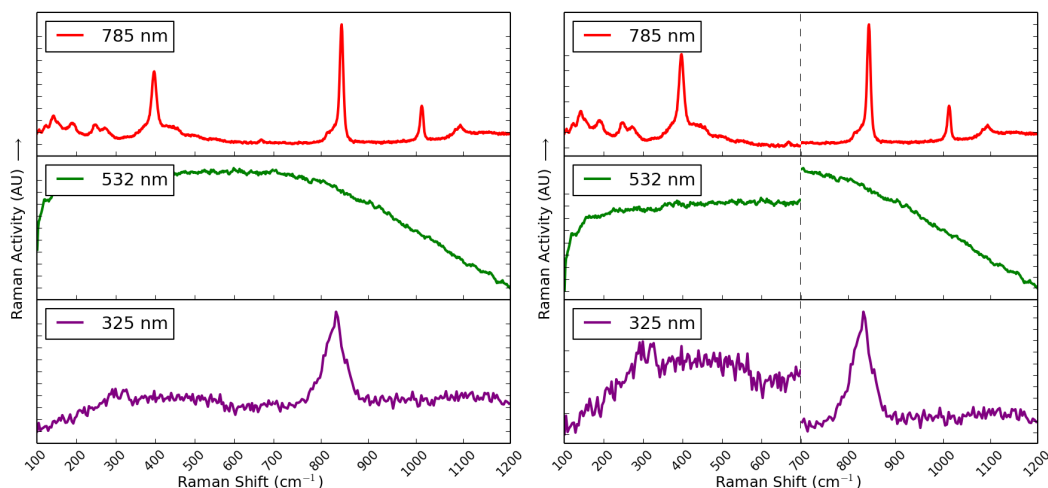
Figure D.9: A comparison of the three laser wavelengths for the uranyl sulphate mineral natrozippeite. The left figure shows the raw spectra. Each section of the spectra shown on the right has been independently rescaled, to emphasise the bands.

Table D.9: Raman spectral bands for the uranyl sulphate mineral natrozippeite

Position (cm^{-1})	This Study Standard Deviation	Number of spectra	Literature [300] Position (cm^{-1})	Attribution
191 *	1.1	16	196	Lattice Vibrations
250 *	2.1	10	250	$v_2(UO_2)^{2+}$ bend
397	1.8	28	373, 398, 431, 498	$v_2(SO_4)^{2-}$ bend
–	–	–	669	$v_4(SO_4)^{2-}$ bend
840	4.5	38	813, 823, 834, 840, 841	$v_1(UO_2)^{2+}$ symm. stretch
1013	0.7	21	980, 1007, 1010	$v_1(SO_4)^{2-}$ symm. stretch
1094 *	1.5	15	1081, 1091, 1130	$v_3(SO_4)^{2-}$ antisymm. stretch
1159 *	4.1	12		

Thirty eight individual spectra were analysed for this sample of natrozippeite.
No information was forthcoming from the 532 nm spectra, as a fluorescence band drowned the region under investigation. The wavelength that gave the best spectra was 785 nm.
* Bands are not consistently visible in all spectra.
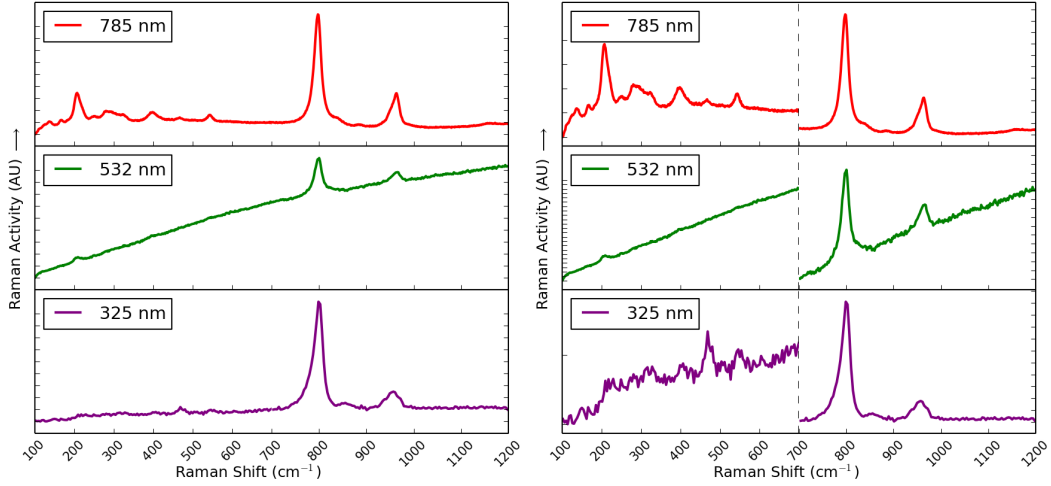
Figure D.10: A comparison of the three laser wavelengths for the uranyl silicate mineral uranophane. The left figure shows the raw spectra. Each section of the spectra shown on the right has been independently rescaled, to emphasise the bands.

Table D.10: Raman spectral bands for the uranyl silicate mineral uranophane

Position (cm^{-1})	This Study Standard Deviation	Number of spectra	Literature [78] Position (cm^{-1})	Attribution
209 *	2.8	13	213, 250, 280, 288, 324	$v_2(\text{UO}_2)^{2+}$ bend
283 *	3.4	6		
399 *	2.0	6	398, 469	$v_2(\text{SiO}_4)^{4-}$ bend
544 *	0.9	6	544	$v_4(\text{SiO}_4)^{4-}$ bend
800	1.4	21	711, 786, 792, 796	$v_1(\text{UO}_2)^{2+}$ symm. stretch
856 *	1.7	3	–	$v_3(\text{UO}_2)^{2+}$ antisymm. stretch
961	3.5	16	960, 963	$v_3(\text{SiO}_4)^{4-}$ antisymm. stretch

Twenty one individual spectra were analysed for the sample of uranophane.
* Bands are not consistently visible in all spectra.
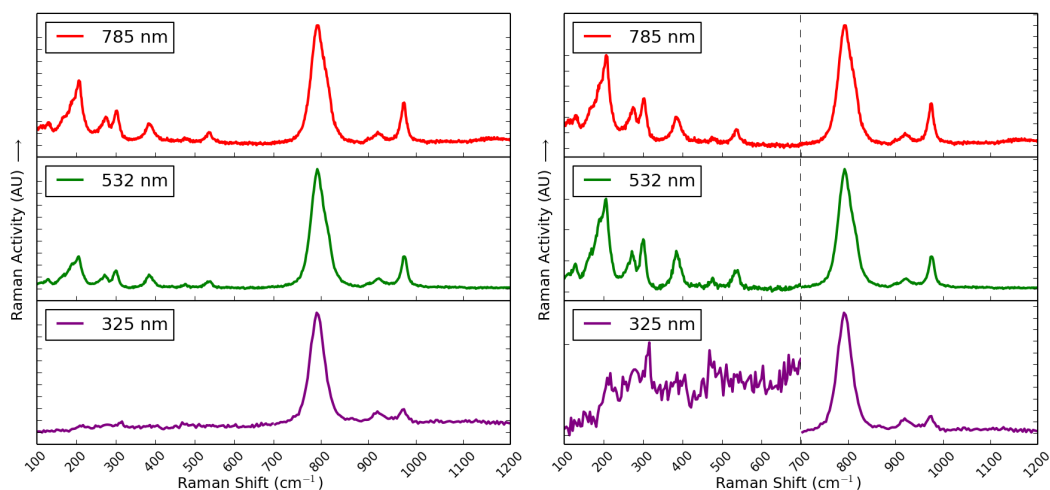
Figure D.11: A comparison of the three laser wavelengths for the uranyl silicate mineral cuprosklodowskite. The left figure shows the raw spectra. Each section of the spectra shown on the right has been independently rescaled, to emphasise the bands.

Table D.11: Raman spectral bands for the uranyl silicate mineral cuprosklodowskite

| Position (cm^{-1}) | This Study | | Literature [78] | Attribution |
	Standard Deviation	Number of spectra	Position (cm^{-1})	
203	2.4	13	205, 217	
273 *	3.1	5	267, 276	
299 *	1.0	5	301	$v_2(UO_2)^{2+}$ bend
312 *	0.9	3		
384 *	0.5	3	411, 476	$v_2(SiO_4)^{4-}$ bend
–	–	–	507, 535	$v_4(SiO_4)^{4-}$ bend
792	1.6	19	746, 758, 774, 787	$v_1(UO_2)^{2+}$ symm. stretch
919 *	2.0	6	–	$v_3(UO_2)^{2+}$ antisymm. stretch
974	2.1	13	974	$v_3(SiO_4)^{4-}$ antisymm. stretch

Nineteen individual spectra were analysed for the sample of cuprosklodowskite.
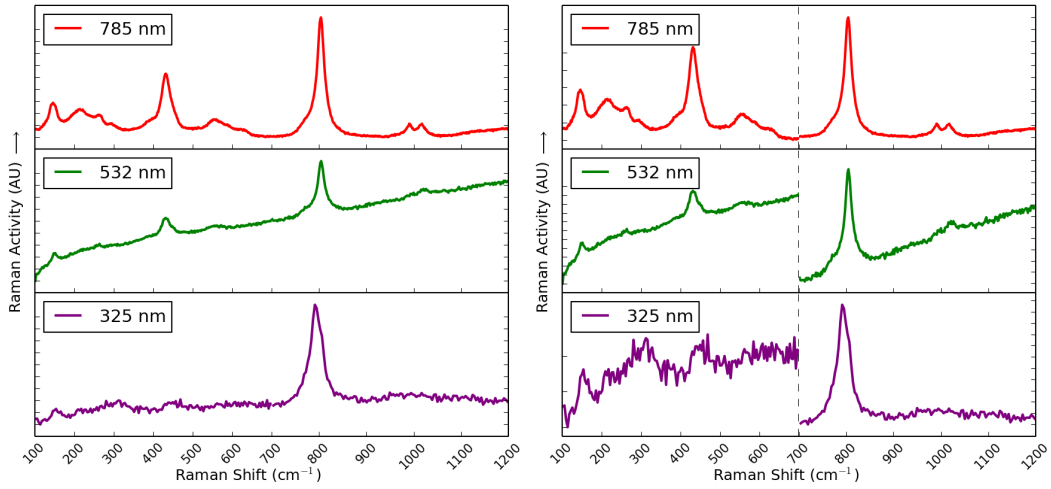* Bands are not consistently visible in all spectra.
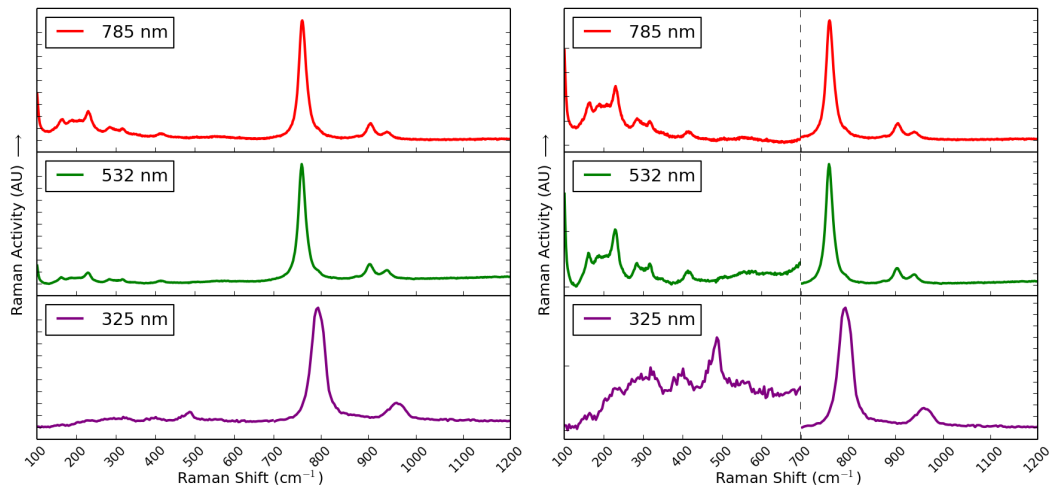
Figure D.12: A comparison of the three laser wavelengths for the uranyl silicate mineral kasolite. The left figure shows the raw spectra. Each section of the spectra shown on the right has been independently rescaled, to emphasise the bands.

Table D.12: Raman spectral bands for the uranyl silicate mineral kasolite

Position (cm^{-1})	This Study Standard Deviation	Number of spectra	Literature [78] Position (cm^{-1})	Attribution
196	8.5	8	154, 165, 185	Lattice Vibrations
230	0.5	8	217, 231, 234, 285, 302	$v_2(UO_2)^{2+}$ bend
415 *	1.0	3	415, 454	$v_2(SiO_4)^{4-}$ bend
–	–	–	501, 533, 575	$v_4(SiO_4)^{4-}$ bend
760	0.5	9	721, 750, 758, 766, 793	$v_1(UO_2)^{2+}$ symm. stretch
904	0.9	8	903	$v_3(UO_2)^{2+}$ antisymm. stretch
939	0.9	6	–	$v_3(SiO_4)^{4-}$ antisymm. stretch

Nine individual spectra were analysed for this sample of kasolite.
* Bands are not consistently visible in all spectra.
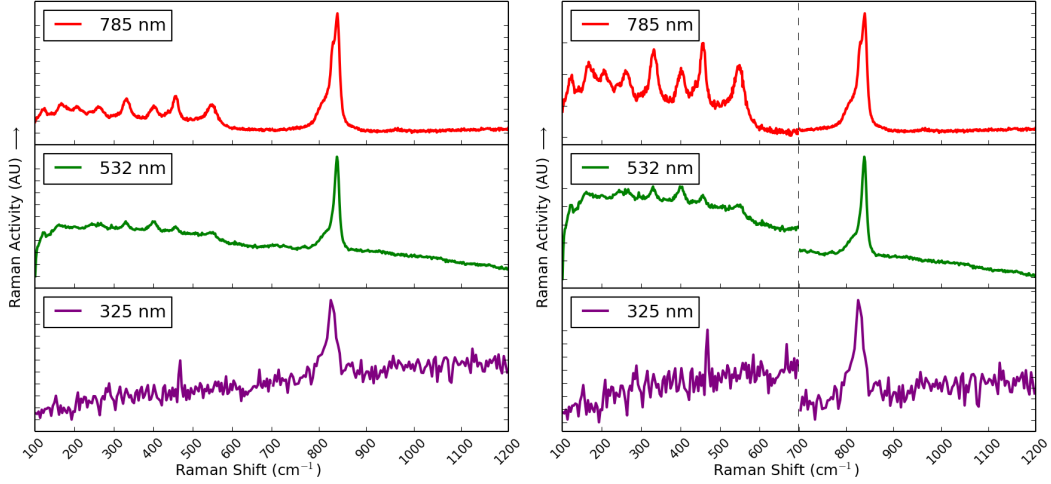
Figure D.13: A comparison of the three laser wavelengths for the uranyl hydrate mineral compreignacite. The left figure shows the raw spectra. Each section of the spectra shown on the right has been independently rescaled, to emphasise the bands.

Table D.13: Raman spectral bands for the uranyl silicate mineral compreignacite

Position (cm^{-1})	This Study Standard Deviation	Number of spectra	Literature [29] Position (cm^{-1})	Attribution
164 *	3.0	6	153	Lattice Vibrations
204 *	1.9	7	197, 253	$v_2(UO_2)^{2+}$ bend
329 *	5.3	10	–	unknown
402 *	3.7	8	439	$v(U_3O)$ stretch)
460 *	5.0	12	–	unknown
549	1.1	7	602, 687	U-O-H bend and water liberation
834 †	4.24	38	824, 848	$v_1(UO_2)^{2+}$ symm. stretch
–	–	–	1010, 1050, 1080, 1110, 1160, 1190, 1330, 1454	U-O-H bending

Thirty eight individual spectra were analysed for this sample of compreignacite.

* Bands are not consistently visible in all spectra.

† A smaller peak or shoulder is sometimes present about 804 cm^{-1} in 785 nm spectra, or about 858 cm^{-1} in 325 nm spectra.

Chapter E

Vibrational Analysis of Autunite Minerals

This appendix presents the vibrational analysis for the simulated autunite minerals in Chapter 7. First, schematics illustrating the vibrational motions are given, followed by tables and spectra for each individual phase.

Table E.1: The calculated energies and k-point meshes used in the simulations of the $M_3(XO_4)_2$ and MO structures. These systems were used to calculate E_m for the simulated saléeite, nováčekite, torbernite, zeunerite and mixed structures in Section 7.4. The calculated energies of γ-UO_3 and H_2O are also given.

System	k-point mesh (no. k-points)	Calculated Energy per 1formula unit (eV)
$Mg_3(PO_4)_2$	$2 \times 2 \times 4$ (12)	-79.93
$Mg_3(AsO_4)_2$	$2 \times 2 \times 4$ (12)	-89.26
$Cu_3(PO_4)_2$	$2 \times 2 \times 4$ (12)	-80.33
$Cu_3(AsO_4)_2$	$2 \times 2 \times 4$ (12)	-71.44
MgO	$4 \times 4 \times 4$ (36)	-11.87
CuO	$4 \times 4 \times 4$ (36)	-9.84
γ-UO_3	—	-34.94
H_2O	—	-14.75

Vibrational Motions
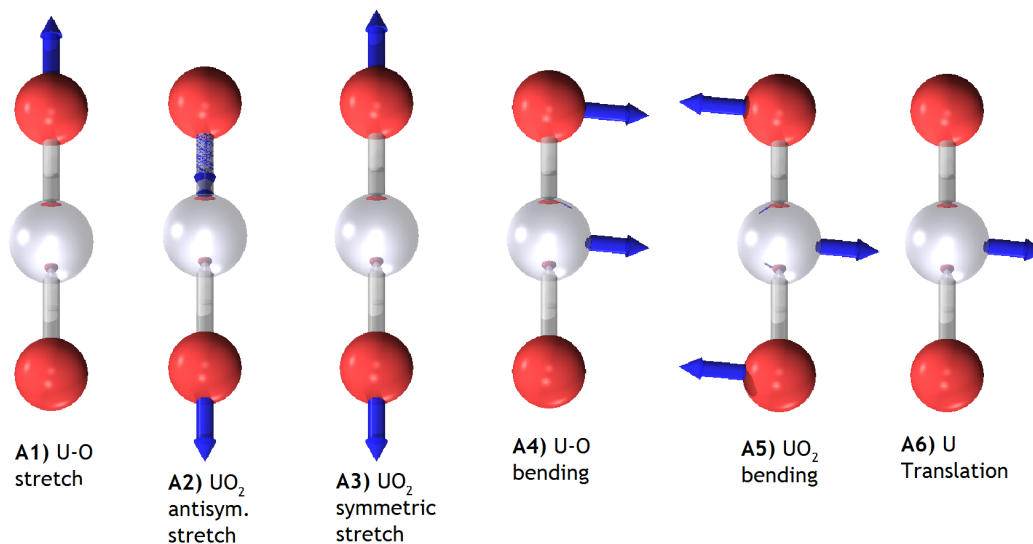
Figure E.1: The vibrational motions that involve the uranyl cations (str. = stretch; sym. = symmetric; antisym. = antisymmetric). The labels refer to those given in Tables E.2–E.15.
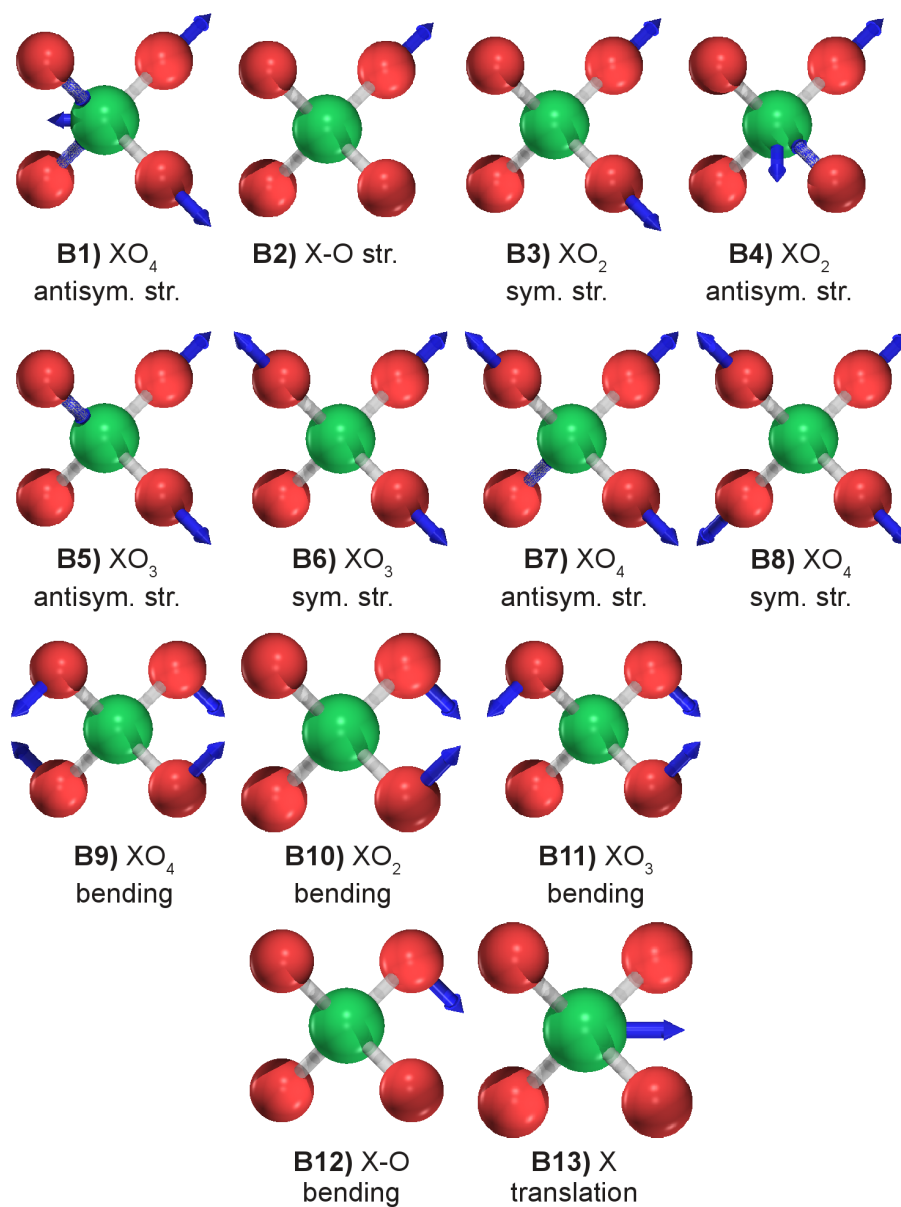
Figure E.2: The vibrational motions that involve the phosphate and arsenate anions (X = P/As; str. = stretch; sym. = symmetric; antisym. = antisymmetric). The labels refer to those given in Tables E.2–E.15.

Saléeite
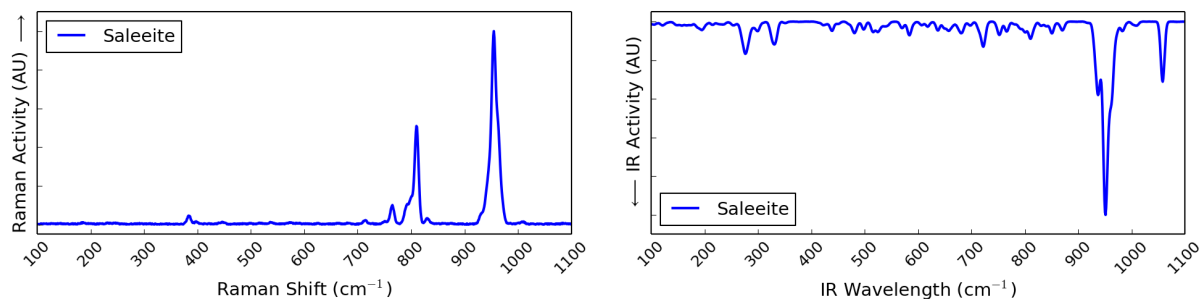
Figure E.3: The simulated Raman and IR spectra of saléeite $(Mg(UO_2)_2(PO_4)_2 \cdot 10H_2O)$ from 100–1100 cm^{-1}.

Table E.2: Analysis of the Raman and IR active modes seen in the simulated spectra of saléeite. The frequencies are given in cm^{-1}. The Raman (R) and infrared (IR) activities are noted.

Freq. (cm^{-1})	Act. (R/IR)	U1	U2	U3	U4	Motion P1	P2	P3	P4	
1058	IR	A1	A1	A1	A1	B1	B1	B1	B1	U-O str.; PO$_4$ antisym. str.
963	R/IR	-	A1	-	A1	B4	B4	B4	B2	U-O str.; PO$_2$ antisym. str.; P-O str.
958	IR	-	A2	-	-	B5	B2	B3	B1	UO$_2$ antisym. str.; P-O str.; PO$_2$ sym. str.; PO$_4$ antisym. str.
957	IR	-	A2	A1	A2	B4	B3	B3	B3	UO$_2$ antisym. str.; U-O str.; PO$_2$ antisym. str.; PO$_2$ sym. str.
955	R	-	-	-	-	B1	-	-	B1	PO$_4$ antisym. str.
954	R/IR	-	A2	A1	A2	-	B3	B5	-	UO$_2$ antisym. str.; U-O str.; PO$_2$ sym. str.; PO$_3$ antisym. str.
951	IR	A1	-	-	A2	B5	-	-	B1	U-O str.; UO$_2$ antisym. str.; PO$_4$ antisym. str.
950	IR	A1	-	-	A2	B5	-	-	B5	U-O str.; UO$_2$ antisym. str.; PO$_3$ antisym. str.
947	R	-	A2	-	-	-	B4	B5	-	UO$_2$ antisym. str.; PO$_2$ antisym. str.; PO$_3$ antisym. str.
937	IR	A1	A1	-	-	B8	B2	B2	B2	U-O str.; PO$_4$ sym. str.; P-O str.
935	IR	-	A2	-	-	B3	B8	B8	B8	UO$_2$ antisym. str.; PO$_2$ sym. str.; PO$_4$ sym. str.
811	R	A3	A1	-	A3	-	-	-	-	UO$_2$ sym. str.; U-O str.
810	R	A3	A3	-	A3	-	-	-	-	UO$_2$ sym. str.
800	R	-	A1	A3	-	-	B2	-	-	U-O str.; UO$_2$ sym. str.; P-O str.
792	R	A3	A3	-	A3	-	-	-	B13	UO$_2$ sym. str.; P translation
764	R	-	A3	A3	-	-	B13	-	-	UO$_2$ sym. str.; P translation
722	IR	-	A1	-	A1	-	-	-	B13	U-O str.; P translation
583	IR	-	-	-	-	B11	B10	B9	B9	PO$_3$ bending; PO$_2$ bending; PO$_4$ bending
384	R	-	-	-	-	B9	B9	B9	B9	PO$_4$ bending
333	IR	A5	A5	A5	-	-	-	-	-	UO$_2$ bending
278	IR	-	-	A4	A4	B10	B9	B11	B9	U-O bending; PO$_2$ bending; PO$_4$ bending; PO$_3$ bending
275	IR	A4	-	A4	A4	B9	-	B10	-	U-O bending; PO$_4$ bending; PO$_2$ bending
269	IR	A4	-	A4	-	-	B9	-	B9	U-O bending; PO$_4$ bending

Saléeite-Nováčekite P_3As_1
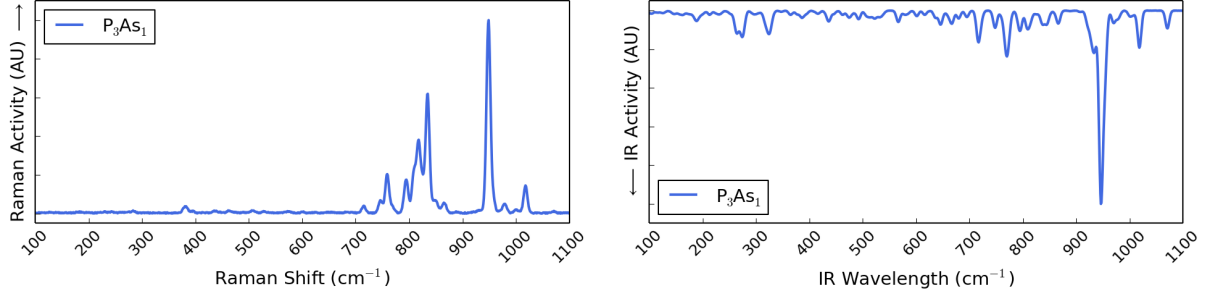
Figure E.4: The simulated Raman and IR spectra of the P_3As_1 mixed phase of saléeite-nováčekite $(Mg(UO_2)_2(PO_4)_{1.5}(AsO_4)_{0.5} \cdot 10H_2O)$ from 100–1100 cm^{-1}.

Table E.3: Analysis of the Raman and IR active modes seen in the simulated spectra of the P_3As_1 mixed phase of saléeite-nováčekite. The frequencies are given in cm^{-1}. The Raman (R) and infrared (IR) activities are noted.

Freq. (cm^{-1})	Act. (R/IR)	U1	U2	U3	U4	Motion P1	P2	P3	As4	
1071	IR	A1	A1	A1	A1	B1	B13	B1	-	U-O str.; PO_4 antisym. str.
1018	R/IR	-	A1	A2	-	B2	B1	B13	B1	UO_2 antisym. str.; PO_4 antisym. str.; AsO_4 antisym. str.
953	IR	-	A1	-	-	-	B5	-	-	U-O str.; PO_3 antisym. str.
949	R	-	-	-	-	B1	-	B1	-	PO_4 antisym. str.
947	IR	-	-	-	-	B1	-	B5	-	PO_4 antisym. str.; PO_3 antisym. str.
945	IR	A2	A2	A1	A1	B5	B2	B3	-	UO_2 antisym. str.; PO_3 antisym. str.; PO_2 sym. str.
945	IR	-	A2	A1	A2	B3	B2	B3	-	UO_2 antisym. str.; U-O str.; PO_2 sym. str.; P-O str.
936	IR	A1	-	-	A1	B8	B2	B6	-	U-O str.; PO_4 sym. str.; P-O str.; PO_3 sym. str.
933	IR	-	A1	-	-	B6	B7	B3	-	U-O str.; PO_4 antisym. str.; PO_3 sym. str.; PO_2 sym. str.
835	R	-	A1	A3	-	-	B5	-	B1	U-O str.; UO_2 sym. str.; PO_3 antisym. str.; AsO_4 antisym. str.
818	R	A3	-	-	A3	B2	-	-	-	UO_2 sym. str.; P-O str.
809	R	-	A3	-	A3	-	-	-	B2	UO_2 sym. str.; As-O str.
796	R	A3	A3	A3	A3	-	-	-	B2	UO_2 sym. str.; As-O str.
772	IR	-	-	-	-	-	-	-	B1	AsO_4 antisym. str.
768	IR	-	A3	-	-	-	-	-	B1	UO_2 sym. str.; AsO_4 antisym. str.
759	R	-	A3	A3	-	-	-	-	B5	UO_2 sym. str.; AsO_3 antisym. str.
717	IR	-	A1	-	-	-	-	-	B2	U-O str.; As-O str.
383	R	-	-	-	-	B9	-	B9	-	PO_4 bending
326	IR	A5	A4	A5	A5	-	-	-	B10	UO_2 bending; U-O bending; AsO_2 bending
322	IR	A5	-	-	A5	-	-	-	-	UO_2 bending
317	IR	-	A5	A4	-	-	-	-	B9	UO_2 bending; U-O bending; AsO_4 bending
277	IR	A4	A4	-	A4	B10	B11	B9	B9	U-O bending; PO_2 bending; PO_4 bending; AsO_4 bending
262	IR	-	A4	A4	-	-	B9	B10	-	U-O bending; PO_4 bending; PO_2 bending

Saléeite-Nováčekite P_2As_2a
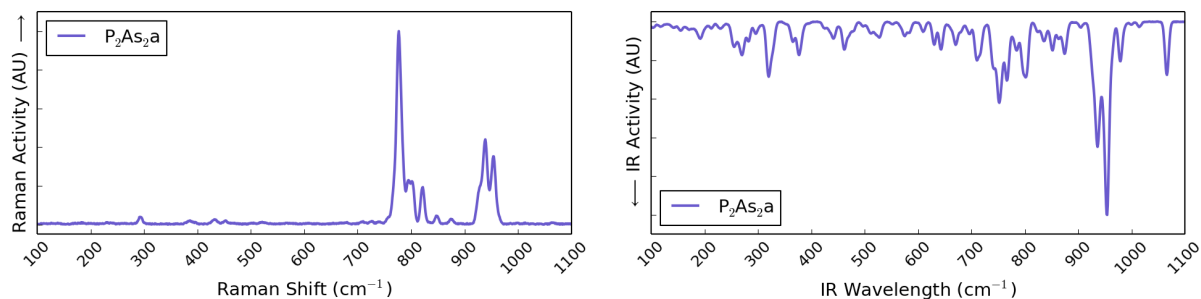
Figure E.5: The simulated Raman and IR spectra of the P_2As_2a mixed phase of saléeite-nováčekite $(Mg(UO_2)_2(PO_4)(AsO_4)\cdot10H_2O)$ from 100–1100 cm^{-1}, in which phosphate and arsenate ions are found in alternating layers.

Table E.4: Analysis of the Raman and IR active modes seen in the simulated spectra of the P_2As_2a mixed phase of saléeite-nováčekite. The frequencies are given in cm^{-1}. The Raman (R) and infrared (IR) activities are noted.

Freq. (cm^{-1})	Act. (R/IR)	U1	U2	U3	U4	P1	P2	As3	As4	Motion
1066	IR	-	A1	A1	-	B1	B1	-	-	U-O str.; PO_4 antisym. str.
979	IR	A2	A2	A2	A2	B2	-	-	-	UO_2 antisym. str.; P-O str.
955	R/IR	-	A2	-	A1	B4	B5	-	-	UO_2 antisym. str.; U-O str.; PO_3 antisym. str.; PO_2 antisym. str.
953	IR	-	A2	A1	A2	B2	B6	-	-	UO_2 antisym. str.; U-O str.; PO_3 antisym. str.; P-O str.
948	IR	-	A2	-	A1	B6	B1	-	-	UO_2 antisym. str.; U-O str.; PO_3 sym. str.; PO_4 antisym. str.
940	R/IR	-	A1	-	-	B7	B5	-	-	U-O str.; PO_4 antisym. str.; PO_3 antisym. str.
935	IR	-	A2	-	-	B6	B1	-	-	UO_2 antisym. str.; PO_3 sym. str.; PO_4 antisym. str.
929	R/IR	-	A2	A1	-	B8	B8	-	-	UO_2 antisym. str.; U-O str.; PO_4 sym. str.
852	IR	-	-	-	A1	-	-	-	-	U-O str.
821	R	-	-	A3	-	-	-	-	-	UO_2 sym. str.
804	IR	-	-	A3	-	-	-	-	-	UO_2 sym. str.
803	R	-	A3	A3	-	-	-	-	B2	UO_2 sym. str.; As-O str.
797	IR	A1	A1	A3	-	-	-	-	B2	U-O str.; UO_2 sym. str.; As-O str.
782	R	-	A3	-	-	B2	B7	-	-	UO_2 sym. str.; P-O str.; PO_4 antisym. str.
776	R	-	-	-	A3	-	-	B5	B1	UO_2 sym. str.; AsO_3 antisym. str.; AsO_4 antisym. str.
756	IR	-	-	-	-	-	-	B1	B5	AsO_4 antisym. str.; AsO_3 antisym. str.
751	IR	-	-	-	-	-	-	B4	B1	AsO_2 antisym. str.; AsO_4 antisym. str.
743	IR	A1	-	-	-	-	-	B2	B5	U-O str.; As-O str.; AsO_3 antisym. str.
738	IR	-	-	-	-	-	-	B4	B1	AsO_2 antisym. str.; AsO_4 antisym. str.
717	IR	A1	-	-	A1	-	-	B2	B2	U-O str.; As-O str.
375	IR	A4	-	-	A4	-	-	B11	B9	U-O bending; AsO_4 bending; AsO_2 bending
318	IR	A5	A5	-	A5	-	-	B10	B10	UO_2 bending; AsO_2 bending
293	R	-	-	-	-	-	-	B9	B9	AsO_4 bending

Saléeite-Nováčekite P_2As_2b
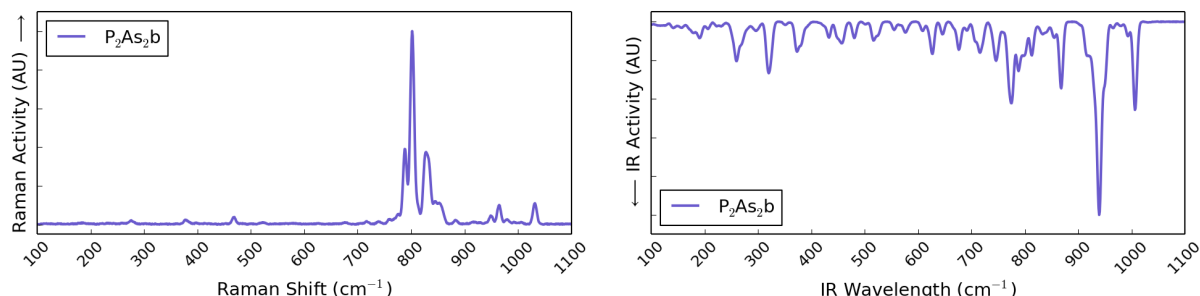
Figure E.6: The simulated Raman and IR spectra of the P_2As_2b mixed phase of saléeite-nováčekite ($Mg(UO_2)_2(PO_4)(AsO_4)\cdot 10H_2O$) from 100–1100 cm^{-1}, in which phosphate and arsenate ions alternate within the layers.

Table E.5: Analysis of the Raman and IR active modes seen in the simulated spectra of the P_2As_2b mixed phase of saléeite-nováčekite. The frequencies are given in cm^{-1}. The Raman (R) and infrared (IR) activities are noted.

| Freq. (cm^{-1})	Act. (R/IR)	U1	U2	U3	U4	P1	P2	As3	As4	Motion
1032	R	A2	A1	A2	A2	B1	B1	-	-	UO$_2$ antisym. str.; U-O str.; PO$_4$ antisym. str.
1007	IR	A1	A1	A2	A2	B1	B1	-	-	U-O str.; UO$_2$ antisym. str.; PO$_4$ antisym. str.
1005	IR	-	-	-	-	B13	B2	-	-	P translation; P-O str.
965	R	A2	A2	-	A2	B2	B1	-	-	UO$_2$ antisym. str.; P-O str.; PO$_4$ antisym. str.
950	IR	-	A2	A1	A2	B4	-	-	-	UO$_2$ antisym. str.; U-O str.; PO$_2$ antisym. str.
942	IR	-	A1	A1	-	B7	-	-	-	U-O str.; PO$_4$ antisym. str.
940	IR	-	-	-	-	-	B5	-	-	PO$_3$ antisym. str.
937	IR	-	-	-	A1	-	B5	-	-	U-O str.; PO$_3$ antisym. str.
930	IR	-	A2	-	-	B5	-	-	-	UO$_2$ antisym. str.; PO$_3$ antisym. str.
922	IR	-	-	-	-	B2	B8	-	-	P-O str.; PO$_4$ sym. str.
915	IR	-	A1	A1	-	B8	B2	-	-	U-O str.; PO$_4$ sym. str.; P-O str.
868	IR	-	-	-	-	-	-	B2	B2	As-O str.
835	R	A3	-	-	A3	-	B3	-	B3	UO$_2$ sym. str.; PO$_2$ sym. str.; AsO$_2$ sym. str.
832	R	A3	-	-	A1	-	B1	-	B1	UO$_2$ sym. str.; U-O str.; PO$_4$ antisym. str.; AsO$_4$ antisym. str.
826	R	-	A1	A1	-	B3	-	B5	-	U-O str.; PO$_2$ sym. str.; AsO$_3$ antisym. str.
813	IR	-	A1	-	-	B13	-	B5	-	U-O str.; AsO$_3$ antisym. str.; P translation
803	R	A3	-	-	A3	-	-	-	B8	UO$_2$ sym. str.; AsO$_4$ sym. str.
801	R	-	A3	A3	-	-	-	B7	-	UO$_2$ sym. str.; AsO$_4$ antisym. str.
789	R	A1	A3	A3	A3	-	-	B7	B4	U-O str.; UO$_2$ sym. str.; AsO$_4$ antisym. str.; AsO$_2$ antisym. str.
787	IR	A3	A3	A1	A3	-	-	B2	B7	UO$_2$ sym. str.; U-O str.; AsO$_4$ antisym. str.
777	IR	-	A1	-	-	-	-	B1	B3	U-O str.; AsO$_4$ antisym. str.; AsO$_2$ sym. str.
776	IR	A3	-	-	A3	-	-	B4	B5	UO$_2$ sym. str.; AsO$_2$ antisym. str.; AsO$_3$ antisym. str.
770	IR	-	A3	-	-	-	-	B5	B4	UO$_2$ sym. str.; AsO$_3$ antisym. str.; AsO$_2$ antisym. str.
750	IR	-	A3	-	-	-	-	B4	B2	UO$_2$ sym. str.; AsO$_2$ antisym. str.; As-O str.
745	IR	-	-	-	-	-	-	B1	B4	AsO$_4$ antisym. str.; AsO$_2$ antisym. str.
715	IR	-	-	-	A1	-	-	-	B2	U-O str.; As-O str.
706	IR	-	-	-	-	-	-	-	B2	As-O str.
627/676	IR	-	-	-	-	-	-	-	-	Water only
516	IR	-	-	-	-	B9	B9	-	-	PO$_4$ bending
468	R	-	-	-	-	-	-	B9	B9	PO$_4$ bending
381	IR	A5	-	-	A5	-	-	B11	B9	UO$_2$ bending; AsO$_4$ bending; AsO$_3$ bending
378	R	-	-	-	-	B9	-	B10	-	PO$_4$ bending; AsO$_2$ bending
372	IR	A5	A6	A4	A6	-	-	B9	B9	UO$_2$ bending; U translation; U-O bending; AsO$_4$ bending
324	IR	A5	A5	A5	A5	-	-	-	-	UO$_2$ bending
318	IR	A5	A5	A5	-	-	-	B9	-	UO$_2$ bending; AsO$_4$ bending
259	IR	A4	A6	A4	A4	-	-	B9	B9	U-O bending; U translation; AsO$_4$ bending

Saléeite-Nováčekite P_2As_2c
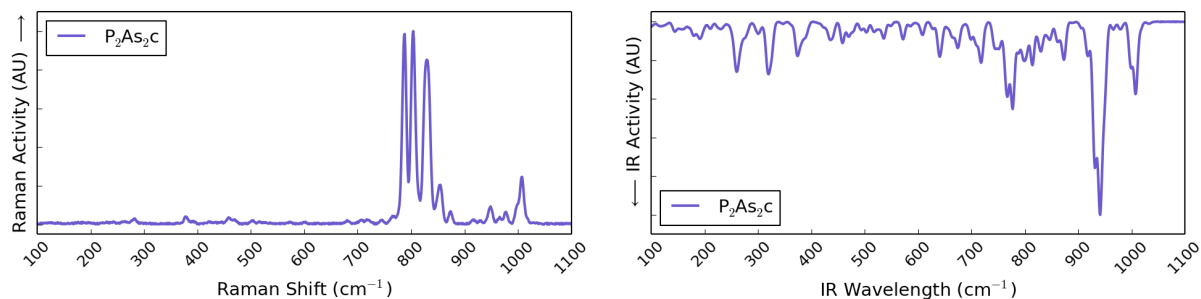
Figure E.7: The simulated Raman and IR spectra of the P_2As_2c mixed phase of saléeite-nováčekite ($Mg(UO_2)_2(PO_4)(AsO_4)\cdot10H_2O$) from 100–1100 cm^{-1}, in which the mixed layers of phosphate and arsenate ions are offset from one another.

Table E.6: Analysis of the Raman and IR active modes seen in the simulated spectra of the P_2As_2c mixed phase of saléeite-nováčekite. The frequencies are given in cm^{-1}. The Raman (R) and infrared (IR) activities are noted.

| Freq. (cm^{-1})	Act. (R/IR)	U1	U2	U3	U4	P1	P2	As3	As4	Motion
1008	R/IR	A1	A1	A2	A1	B1	B1	-	-	U-O str.; PO$_4$ antisym. str.
998	IR	A2	-	-	A1	B4	B5	-	-	UO$_2$ antisym. str.; U-O str.; PO$_2$ antisym. str.; PO$_3$ antisym. str.
950	IR	-	A2	A1	A2	B4	-	-	-	UO$_2$ antisym. str.; U-O str.; PO$_2$ antisym. str.
947	IR	A2	A2	-	-	B2	B4	-	-	UO$_2$ antisym. str.; P-O str.; PO$_2$ antisym. str.
942	IR	-	-	A1	-	B7	-	-	-	U-O str.; PO$_3$ antisym. str.
940	IR	-	-	-	-	-	B5	-	-	PO$_3$ antisym. str.
933	IR	-	-	-	-	-	B7	-	-	PO$_4$ antisym. str.
930	IR	-	A2	-	-	B5	-	-	-	UO$_2$ antisym. str.; PO$_3$ antisym. str.
917	R/IR	-	A1	-	-	B8	-	-	-	U-O str.; PO$_4$ sym. str.
856	R	-	-	A3	-	-	-	-	B8	UO$_2$ sym. str.; AsO$_4$ sym. str.
850	R	A1	-	A3	A3	B2	-	B8	B3	U-O str.; UO$_2$ sym. str.; P-O str.; AsO$_4$ sym. str.; AsO$_2$ sym. str.
833	R	A3	-	-	A3	-	B1	B1	-	UO$_2$ sym. str.; PO$_4$ antisym. str.; AsO$_4$ antisym. str.
826	R	-	A1	-	-	B3	-	-	B5	U-O str.; PO$_2$ sym. str.; AsO$_3$ antisym. str.
814	IR	-	-	-	-	B13	-	-	B7	P translation; AsO$_4$ antisym. str.
806	R	A3	-	-	A3	-	B2	B8	-	UO$_2$ sym. str.; AsO$_4$ sym. str.; P-O str.
802	R	-	A3	A3	-	-	-	-	B6	UO$_2$ sym. str.; AsO$_3$ sym. str.
796	IR	-	A3	A3	-	-	-	-	B5	UO$_2$ sym. str.; AsO$_3$ antisym. str.
788	R	-	A3	A3	A3	-	-	B2	B7	UO$_2$ sym. str.; As-O str.; AsO$_4$ antisym. str.
784	R	A3	-	A3	A3	-	-	B5	B5	UO$_2$ sym. str.; AsO$_3$ antisym. str.
778	R	A3	-	-	A3	-	-	B5	B1	UO$_2$ sym. str.; AsO$_4$ antisym. str.; AsO$_3$ antisym. str.
777	IR	-	-	-	A3	-	-	B5	B5	UO$_2$ sym. str.; AsO$_3$ antisym. str.
776	IR	-	-	-	-	-	-	B1	B1	AsO$_4$ antisym. str.
768	IR	-	A3	-	-	-	-	B1	B4	UO$_2$ sym. str.; AsO$_4$ antisym. str.; AsO$_2$ antisym. str.
763	IR	-	A3	A3	-	-	-	B4	B2	UO$_2$ sym. str.; AsO$_2$ antisym. str.; As-O str.
718	IR	-	-	-	A1	-	-	B4	-	U-O str.; AsO$_2$ antisym. str.
674	IR	-	-	-	-	-	-	-	-	Water only
640	IR	-	-	-	-	-	-	-	-	Water only
373	IR	A6	A5	A4	A4	-	-	B9	B9	U translation; UO$_2$ bending; U-O bending; AsO$_4$ bending
318	IR	-	A5	A5	A5	-	-	-	B9	UO$_2$ bending; AsO$_4$ bending
318	IR	A5	A5	-	A5	-	-	B9	-	UO$_2$ bending; AsO$_4$ bending
258	IR	A4	A4	A4	A4	-	B9	B10	B9	U-O bending; PO$_4$ bending; AsO$_2$ bending; AsO$_4$ bending

Saléeite-Nováčekite P_1As_3
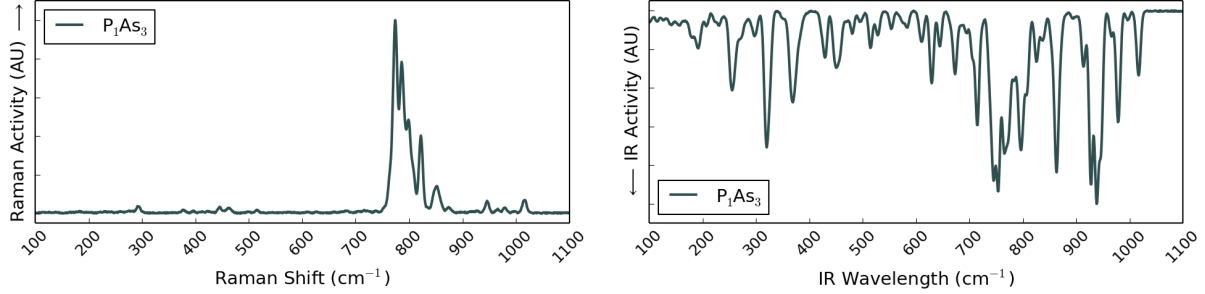
Figure E.8: The simulated Raman and IR spectra of the P_1As_3 mixed phase of saléeite-nováčekite $(Mg(UO_2)_2(PO_4)_{0.5}(AsO_4)_{1.5} \cdot 10H_2O)$ from 100–1100 cm^{-1}.

Table E.7: Analysis of the Raman and IR active modes seen in the simulated spectra of the P_1As_3 mixed phase of saléeite-nováčekite. The frequencies are given in cm^{-1}. The Raman (R) and infrared (IR) activities are noted. Doubly degenerate modes are labelled by 'd'.

Freq. (cm^{-1})	Act. (R/IR)	U1	U2	U3	U4	P1	As2	As3	As4	Motion
1017	R/IR	A2	A1	A2	A2	B1	-	B1	-	UO$_2$ antisym. str.; PO$_4$ antisym. str.; AsO$_4$ antisym. str.
980	IR	A2	A1	A2	A1	B1	-	-	-	UO$_2$ antisym. str.; U-O str.; PO$_4$ antisym. str.
946	R/IR	-	A2	A1	A2	B4	-	-	-	UO$_2$ antisym. str.; U-O str.; PO$_2$ antisym. str.
938	IR	-	-	A1	-	B7	-	-	-	U-O str.; PO$_4$ antisym. str.
927	IR	-	A2	-	-	B1	-	-	-	UO$_2$ antisym. str.; PO$_4$ antisym. str.
863	IR	-	-	-	A1	-	-	B2	B3	U-O str.; As-O str.; AsO$_2$ sym. str.
852	R	-	-	A3	A1	B2	B3	B6	-	UO$_2$ sym. str.; U-O str.; P-O str.; AsO$_2$ sym. str.
846	R	A3	-	A3	A3	B2	B8	B3	B3	UO$_2$ sym. str.; P-O str.; AsO$_4$ sym. str.; AsO$_2$ sym. str.
822	R	-	A1	A3	-	B1	-	B5	-	U-O str.; UO$_2$ sym. str.; PO$_4$ antisym. str.; AsO$_3$ antisym. str.
808	R/IR	-	A1	-	-	B13	-	B5	-	U-O str.; P translation; AsO$_3$ antisym. str.
800	R/IR	A1	A3	A3	-	-	B2	B6	B2	U-O str.; UO$_2$ sym. str.; As-O str.; AsO$_3$ sym. str.
795	IR	A3	-	A3	A3	-	B3	B5	B8	UO$_2$ sym. str.; AsO$_3$ antisym. str.; AsO$_4$ sym. str.
792	R/IR	A3	A1	A3	-	-	B2	B5	B3	UO$_2$ sym. str.; U-O str.; AsO$_3$ antisym. str.; AsO$_2$ sym. str.
786	R	-	A3	A3	-	-	-	B7	-	UO$_2$ sym. str.; AsO$_4$ antisym. str.
777	R	A3	-	-	A1	-	B2	B3	B5	UO$_2$ sym. str.; U-O str.; AsO$_2$ sym. str.; AsO$_3$ antisym. str.
775 (d)	R/IR	-	-	-	A3	-	B5	B4	B4	UO$_2$ sym. str.; AsO$_3$ antisym. str.; AsO$_2$ antisym. str.
769	IR	A3	A3	-	A3	-	B4	B1	B5	UO$_2$ sym. str.; AsO$_2$ antisym. str.; AsO$_4$ antisym. str.
764	R	A3	A3	-	A3	-	B2	B4	B4	UO$_2$ sym. str.; As-O str.; AsO$_2$ antisym. str.
764	IR	A3	-	-	-	-	B5	-	B5	UO$_2$ sym. str.; AsO$_3$ antisym. str.
754	IR	-	A1	-	-	-	B1	B4	B4	U-O str.; AsO$_2$ antisym. str.
746	IR	-	A1	-	-	-	B4	B5	B4	U-O str.; AsO$_4$ antisym. str.; AsO$_2$ antisym. str.
714	IR	A3	-	-	A3	-	B4	-	B4	UO$_2$ sym. str.; AsO$_2$ antisym. str.
630	IR	-	-	-	-	-	-	-	-	Water only
463	R	-	-	-	-	-	B12	B9	B12	As-O bending; AsO$_4$ bending
444	R	-	-	-	-	-	B9	-	B9	AsO$_4$ bending
372	IR	A4	-	-	A4	-	B11	B10	B11	U-O bending; AsO$_3$ bending; AsO$_2$ bending
366	IR	A4	A6	A5	-	-	B11	B9	B11	U-O bending; U translation; UO$_2$ bending; AsO$_4$ bending
320	IR	-	A5	A5	A5	-	-	B10	B12	UO$_2$ bending; AsO$_2$ bending; As-O bending
317	IR	A5	-	-	A5	-	B11	-	B10	UO$_2$ bending; AsO$_3$ bending; AsO$_2$ bending
293	R	-	-	-	-	-	B9	-	B9	AsO$_4$ bending
253	IR	A5	-	-	A5	B10	B9	-	B9	UO$_2$ bending; PO$_2$ bending; AsO$_4$ bending

Nováčekite
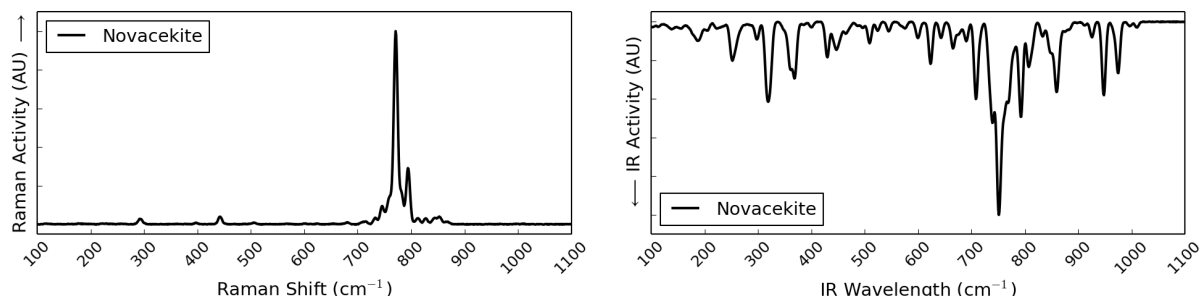
Figure E.9: The simulated Raman and IR spectra of nováčekite $(Mg(UO_2)_2(AsO_4)_2 \cdot 10H_2O)$ from 100–1100 cm^{-1}.

Table E.8: Analysis of the Raman and IR active modes seen in the simulated spectra of nováčekite. The frequencies are given in cm^{-1}. The Raman (R) and infrared (IR) activities are noted.

Freq. (cm^{-1})	Act. (R/IR)	U1	U2	U3	U4	As1	As2	As3	As4	Motion
975	IR	A2	-	A2	-	-	-	-	-	UO$_2$ antisym. str.
948	IR	A1	A2	-	A2	-	-	-	-	U-O str.; UO$_2$ antisym. str.
859	IR	-	A1	A1	A1	-	-	-	B2	U-O str.; As-O str.
806	IR	-	A1	-	A3	B2	-	B2	B5	U-O str.; UO$_2$ sym. str.; As-O str.; AsO$_3$ antisym. str.
795	R	-	-	A3	A1	B2	B8	B8	-	UO$_2$ sym. str.; U-O str.; As-O str.; AsO$_4$ sym. str.
793	IR	-	-	A3	-	-	B8	-	-	UO$_2$ sym. str.; AsO$_4$ sym. str.
790	IR	A3	A3	-	-	B2	B4	-	B3	UO$_2$ sym. str.; As-O str.; AsO$_2$ sym. str.; AsO$_2$ antisym. str.
782	R/IR	A3	-	A3	A3	B3	B2	-	B8	UO$_2$ sym. str.; As-O str.; AsO$_4$ sym. str.; AsO$_2$ sym. str.
771	R	A1	A3	A3	-	B2	B6	B5	-	U-O str.; UO$_2$ sym. str.; AsO$_3$ sym. str.; AsO$_3$ antisym. str.
769	IR	A3	A1	A1	A3	B3	B5	-	B5	UO$_2$ sym. str.; U-O str.; AsO$_2$ sym. str.; AsO$_3$ antisym. str.
761	IR	-	A1	-	-	-	B2	-	-	U-O str.; As-O str.
760	R	-	-	-	A3	B5	B1	B4	B5	UO$_2$ sym. str.; AsO$_4$ antisym. str.; AsO$_2$ antisym. str.
754	IR	A3	-	-	-	B5	B4	-	B4	UO$_2$ sym. str.; AsO$_2$ antisym. str.; AsO$_3$ antisym. str.
752	IR	-	A3	-	A3	B2	B4	B2	B5	UO$_2$ sym. str.; As-O str.; AsO$_2$ antisym. str.; AsO$_3$ antisym. str.
749	IR	-	A3	-	-	B4	B4	B5	B4	UO$_2$ sym. str.; AsO$_2$ antisym. str.; AsO$_3$ antisym. str.
746	R	-	A3	-	-	B2	B4	B5	B5	UO$_2$ sym. str.; As-O str.; AsO$_2$ antisym. str.; AsO$_3$ antisym. str.
740	IR	-	A3	A1	-	B1	B4	B5	B1	UO$_2$ sym. str.; U-O str.; AsO$_4$ antisym. str.; AsO$_2$ antisym. str.
623	IR	-	-	-	-	B9	B9	B9	B9	AsO$_4$ bending
430	IR	A4	-	-	A4	B9	B9	B11	B9	U-O bending; AsO$_4$ bending; AsO$_3$ bending
369	IR	-	A3	A1	-	B4	B4	B5	B5	UO$_2$ sym. str.; U-O str.; AsO$_2$ antisym. str.; AsO$_3$ antisym. str.
360	IR	A4	-	A4	A5	B9	B10	B11	B9	U-O bending; UO$_2$ bending; AsO$_4$ bending; AsO$_2$ bending
292	R	-	-	-	-	B9	B9	B9	B9	AsO$_4$ bending

Torbernite
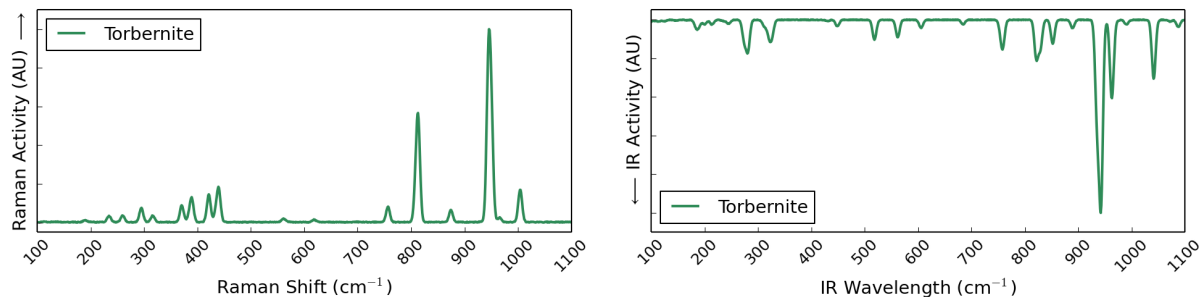
Figure E.10: The simulated Raman and IR spectrum of torbernite $(Cu(UO_2)_2(PO_4)_2 \cdot 8H_2O)$ from 100–1100 cm^{-1}.

Table E.9: Analysis of the Raman and IR active modes seen in the simulated spectra of torbernite. The frequencies are given in cm^{-1}. The Raman (R) and infrared (IR) activities are noted. Doubly degenerate modes are labelled by 'd'.

Freq. (cm^{-1})	Act. (R/IR)	U1	U2	U3	U4	P1	P2	P3	P4	Motion
1041	IR	A1	A1	A1	A1	B1	B1	B1	B1	U-O str.; PO$_4$ antisym. str.
1004	R	-	-	-	-	-	-	-	-	Water only
963 (d)	IR	-	-	-	-	B4	B4	-	-	PO$_2$ antisym. str.
962	IR	A2	A2	A2	A2	-	-	-	-	UO$_2$ antisym. str.
950	R	-	-	-	-	-	-	B1	B1	PO$_4$ antisym. str.
945	R	-	-	-	-	B1	B1	-	-	PO$_4$ antisym. str.
943	IR	-	-	-	-	-	-	B5	B5	PO$_3$ antisym. str.
943	IR	-	-	-	-	-	-	B1	B1	PO$_4$ antisym. str.
935 (d)	IR	-	-	-	-	B4	B4	-	-	PO$_2$ antisym. str.
852 (d)	IR	-	-	-	-	-	-	-	-	Water only
829 (d)	IR	-	-	-	-	-	-	-	-	Water only
821	IR	A1	A1	A1	A1	-	-	-	-	U-O str.
813	R	A3	A3	A3	A3	-	-	-	-	UO$_2$ sym. str.
809	R	A3	A3	A3	A3	-	-	-	-	UO$_2$ sym. str.
759	IR	A3	A3	A3	A3	-	-	-	-	UO$_2$ sym. str.
757	R	A3	A3	-	-	-	-	-	-	UO$_2$ sym. str.
755 (d)	IR	-	-	-	-	-	-	-	-	Water only
562	IR	-	-	-	-	B9	B9	-	-	PO$_4$ bending
518 (d)	IR	-	-	-	-	B9	B9	B9	B9	PO$_4$ bending
440	R	-	-	-	-	B9	B9	B9	B9	PO$_4$ bending
421	R	-	-	-	-	B9	B9	-	-	PO$_4$ bending
389	R	-	-	-	-	B9	B9	-	-	PO$_4$ bending
370	R	-	-	-	-	B9	B9	-	-	PO$_4$ bending
326 (d)	IR	-	-	A5	A5	-	-	-	-	UO$_2$ bending
322 (d)	IR	A5	A5	-	-	-	-	-	-	UO$_2$ bending
281 (d)	IR	-	-	A4	A4	B10	B10	B9	B9	U-O bending; PO$_2$ bending; PO$_4$ bending
274 (d)	IR	A4	A4	-	-	B9	B9	B9	B9	U-O bending; PO$_4$ bending

Torbernite-Zeunerite P$_3$As$_1$
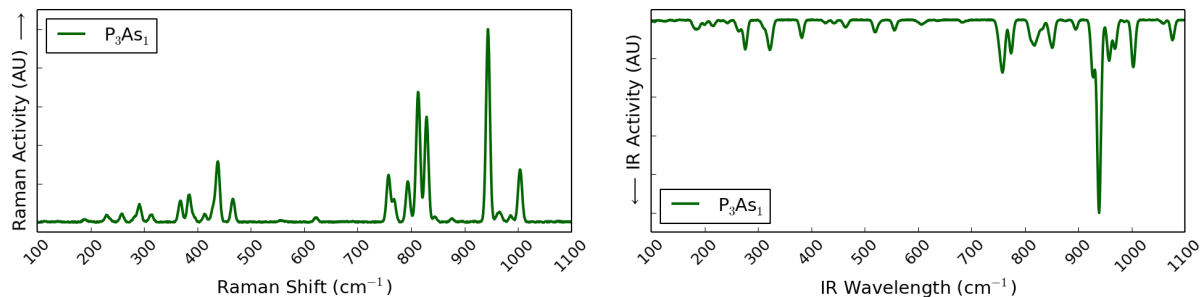
Figure E.11: The simulated Raman and IR spectrum of the P$_3$As$_1$ mixed phase of torbernite-zeunerite (Cu(UO$_2$)$_2$(PO$_4$)$_{1.5}$(AsO$_4$)$_{0.5}$·8H$_2$O) from 100–1100 cm^{-1}.

Table E.10: Analysis of the Raman and IR active modes seen in the simulated spectra of the P$_3$As$_1$ mixed phase of torbernite-zeunerite. The frequencies are given in cm^{-1}. The Raman (R) and infrared (IR) activities are noted. Doubly degenerate modes are labelled by 'd'.

| Freq. (cm^{-1})	Act. (R/IR)	U1	U2	U3	U4	P1	P2	P3	As4	Motion
1077	IR	-	-	A1	A1	-	B1	B1	-	U-O str.; PO$_4$ antisym. str.
1005	R	-	-	-	-	-	-	-	-	Water only
1003	IR	A2	A2	A1	A1	B1	B1	B1	B1	UO$_2$ antisym. str.; U-O str.; PO$_4$ antisym. str.; AsO$_4$ antisym. str.
969	IR	A1	A1	A2	A2	B1	B13	B13	-	U-O str.; UO$_2$ antisym. str.; PO$_4$ antisym. str.; P translation
957	IR	-	-	-	-	B4	-	-	-	PO$_2$ antisym. str.
944	R	-	-	-	-	-	B1	B1	-	PO$_4$ antisym. str.
939 (d)	IR	-	-	-	-	-	B1	B1	-	PO$_4$ antisym. str.
927 (d)	IR	-	-	-	-	B4	-	-	-	PO$_2$ antisym. str.
895	IR	A1	A1	A1	A1	-	-	-	-	U-O str.
853 (d)	IR	-	-	-	-	-	-	-	-	Water only
829	R	A3	A3	A1	-	B1	-	-	B1	UO$_2$ sym. str.; U-O str.; PO$_4$ antisym. str.; AsO$_4$ antisym. str.
818	IR	A1	A1	A1	A3	-	-	-	-	U-O str.; UO$_2$ sym. str.
814	R	A3	A3	A3	A3	-	-	-	-	UO$_2$ sym. str.
810	IR	-	-	A1	A1	-	-	-	-	U-O str.
793	R	A3	A3	-	-	-	-	-	B8	UO$_2$ sym. str.; AsO$_4$ sym. str.
774 (d)	IR	-	-	-	-	-	-	-	B4	AsO$_2$ antisym. str.
760	IR	A3	A3	A1	A1	-	-	-	B1	UO$_2$ sym. str.; U-O str.; AsO$_4$ antisym. str.
758	R	A3	A3	-	-	-	-	-	B3	UO$_2$ sym. str.; AsO$_2$ sym. str.
466	R	-	-	-	-	-	-	-	B9	AsO$_4$ bending
438	R	-	-	-	-	B9	B9	B9	B9	PO$_4$ bending; AsO$_4$ bending
384	R	-	-	-	-	B9	B9	B9	-	PO$_4$ bending
382 (d)	IR	A5	A6	-	-	-	-	-	B9	UO$_2$ bending; U translation; AsO$_4$ bending
368	R	-	-	-	-	B9	B9	-	-	PO$_4$ bending
321 (d)	IR	A5	A5	-	A5	-	-	-	B10	UO$_2$ bending; AsO$_2$ bending
314	R	-	-	-	-	-	-	-	-	Water only
291	R	-	-	-	-	-	-	-	-	Water only
276 (d)	IR	-	-	A4	A4	-	B9	B9	-	U-O bending; PO$_4$ bending

Torbernite-Zeunerite P_2As_2a
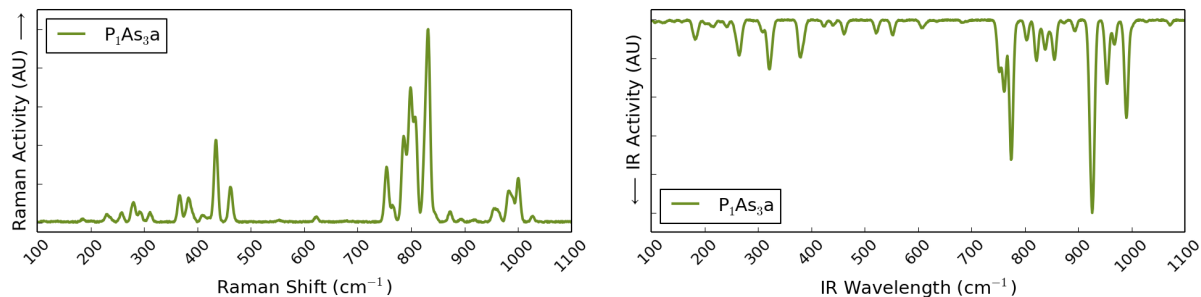
Figure E.12: The simulated Raman and IR spectra of the P_2As_2a mixed phase of torbernite-zeunerite $(Cu(UO_2)_2(PO_4)(AsO_4)\cdot 8H_2O)$ from 100–1100 cm^{-1}, in which phosphate and arsenate ions are found in alternating layers.

Table E.11: Analysis of the Raman and IR active modes seen in the simulated spectra of the P_2As_2a mixed phase of torbernite-zeunerite. The frequencies are given in cm^{-1}. The Raman (R) and infrared (IR) activities are noted. Doubly degenerate modes are labelled by 'd'.

| Freq. (cm^{-1})	Act. (R/IR)	U1	U2	U3	U4	P1	P2	As3	As4	Motion
1001	R	A2	A2	-	-	B13	-	-	-	UO$_2$ antisym. str.; P translation
990	IR	A2	A2	A1	A1	B1	B1	-	-	UO$_2$ antisym. str.; U-O str.; PO$_4$ antisym. str.
955	IR	A2	A2	A2	A2	B4	B1	-	-	UO$_2$ antisym. str.; PO$_2$ antisym. str.; PO$_4$ antisym. str.
954	IR	-	-	A1	-	B4	-	-	-	U-O str.; PO$_2$ antisym. str.
953	IR	A1	A1	-	A2	B4	-	-	-	U-O str.; UO$_2$ antisym. str.; PO$_2$ antisym. str.
928 (d)	IR	-	-	-	-	-	B1	-	-	PO$_4$ antisym. str.
923 (d)	IR	-	-	-	-	B1	-	-	-	PO$_4$ antisym. str.
855 (d)	IR	-	-	-	-	-	-	-	-	Water only
838 (d)	IR	-	-	-	-	-	-	-	-	Water only
832	R	-	-	A3	A3	-	B1	-	B1	UO$_2$ sym. str.; PO$_4$ antisym. str.; AsO$_4$ antisym. str.
826	R	A3	A3	-	-	B1	-	B1	B1	UO$_2$ sym. str.; PO$_4$ antisym. str.; AsO$_4$ antisym. str.
822	IR	A1	A1	-	-	-	-	-	-	U-O str.
821	IR	A1	A1	-	-	-	-	-	-	U-O str.
809	R	A3	A3	A3	A3	-	-	-	-	UO$_2$ sym. str.
803	R/IR	-	-	A1	A1	-	-	-	-	U-O str.
799	R	-	-	A3	A3	-	-	-	B8	UO$_2$ sym. str.; AsO$_4$ sym. str.
791	R	A3	A3	-	-	-	-	B8	-	UO$_2$ sym. str.; AsO$_4$ sym. str.
785	R	-	-	A3	A3	-	-	B1	B1	UO$_2$ sym. str.; AsO$_4$ antisym. str.
774 (d)	IR	-	-	-	-	-	-	B1	B4	AsO$_4$ antisym. str.; AsO$_2$ antisym. str.
761 (d)	IR	-	-	-	-	-	-	B4	-	AsO$_2$ antisym. str.
755	R	A3	A3	-	-	-	-	B8	-	UO$_2$ sym. str.; AsO$_4$ sym. str.
752	IR	A3	-	A3	A3	-	-	-	B1	UO$_2$ sym. str.; AsO$_4$ antisym. str.
462	R	-	-	-	-	-	-	B9	B9	AsO$_4$ bending
434	R	-	-	-	-	B9	-	B9	-	PO$_4$ bending; AsO$_4$ bending
383	R	-	-	-	-	B9	-	-	-	PO$_4$ bending
378 (d)	IR	A5	A4	-	-	-	-	B9	B10	UO$_2$ bending; U-O bending; AsO$_4$ bending; AsO$_2$ bending
366	R	-	-	-	-	B9	-	-	-	PO$_4$ bending
320 (d)	IR	A5	A5	A5	A4	-	-	B9	-	UO$_2$ bending; U-O bending; AsO$_4$ bending
265 (d)	IR	A4	A4	A5	A5	-	B9	B9	B9	U-O bending; UO$_2$ bending; PO$_4$ bending; AsO$_4$ bending

Torbernite-Zeunerite P_2As_2b
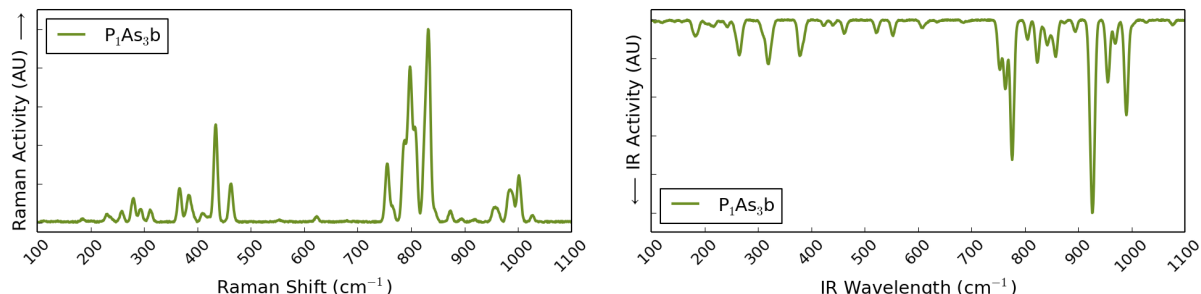
Figure E.13: The simulated Raman and IR spectra of the P_2As_2b mixed phase of torbernite-zeunerite $(Cu(UO_2)_2(PO_4)(AsO_4)\cdot 8H_2O)$ from 100–1100 cm^{-1}, in which phosphate and arsenate ions alternate within the layers.

Table E.12: Analysis of the Raman and IR active modes seen in the simulated spectra of the P_2As_2 mixed phase of torbernite-zeunerite. The frequencies are given in cm^{-1}. The Raman (R) and infrared (IR) activities are noted. Doubly degenerate modes are labelled by 'd'.

Freq. (cm^{-1})	Act. (R/IR)	U1	U2	U3	U4	P1	P2	As3	As4	Motion
1002	R	A2	-	-	-	B13	-	-	-	UO$_2$ antisym. str.; P translation
990	R/IR	A2	A2	A1	A1	B1	B1	-	-	UO$_2$ antisym. str.; U-O str.; PO$_4$ antisym. str.
983	R	A2	A2	-	-	B1	B3	-	-	UO$_2$ antisym. str.; PO$_4$ antisym. str.; PO$_2$ sym. str.
970 (d)	IR	-	-	-	-	-	-	-	-	Water only
956	IR	A1	A1	A2	A2	B4	B13	-	-	U-O str.; UO$_2$ antisym. str.; PO$_2$ antisym. str.; P translation
956	IR	-	-	A1	-	B4	-	-	-	U-O str.; PO$_2$ antisym. str.
954	IR	A2	A2	A2	A2	B4	B1	-	-	UO$_2$ antisym. str.; PO$_2$ antisym. str.; PO$_4$ antisym. str.
928 (d)	IR	-	-	-	-	-	B4	-	-	PO$_2$ antisym. str.
923 (d)	IR	-	-	-	-	B4	-	-	-	PO$_2$ antisym. str.
858 (d)	IR	-	-	-	-	-	-	-	-	Water only
842 (d)	IR	-	-	-	-	-	-	-	-	Water only
833	R	-	-	A3	A3	-	B1	-	B1	UO$_2$ sym. str.; PO$_4$ antisym. str.; AsO$_4$ antisym. str.
823	IR	A1	A1	-	-	-	-	B13	-	U-O str.; As translation
809	R	A3	A3	A3	A3	-	-	-	-	UO$_2$ sym. str.
805	IR	-	-	A1	A1	-	-	-	-	U-O str.
798	R	-	-	A3	A3	-	-	-	B8	UO$_2$ sym. str.; AsO$_4$ sym. str.
792	R	A3	A3	-	-	-	-	B8	-	UO$_2$ sym. str.; AsO$_4$ sym. str.
786	R	-	-	A3	A3	-	-	B1	B1	UO$_2$ sym. str.; AsO$_4$ antisym. str.
776 (d)	IR	-	-	-	-	-	-	B4	B1	AsO$_2$ antisym. str.; AsO$_4$ antisym. str.
763	IR	-	-	-	-	-	-	B5	-	AsO$_3$ antisym. str.
763	IR	-	-	-	-	-	-	B1	-	AsO$_4$ antisym. str.
756	R	A3	A3	-	-	-	-	B8	-	UO$_2$ sym. str.; AsO$_4$ sym. str.
753	IR	-	-	A3	A3	-	-	-	B1	UO$_2$ sym. str.; AsO$_4$ antisym. str.
462	R	-	-	-	-	-	-	B9	B9	AsO$_4$ bending
434	R	-	-	-	-	B9	-	B9	-	PO$_4$ bending; AsO$_4$ bending
384	R	-	-	-	-	B9	-	-	-	PO$_4$ bending
378 (d)	IR	A5	A6	-	-	-	-	B9	B9	UO$_2$ bending; U translation; AsO$_4$ bending
366	R	-	-	-	-	B9	-	-	-	PO$_4$ bending
318	IR	A5	A5	A4	-	-	-	B9	-	UO$_2$ bending; U-O bending; AsO$_4$ bending
318	IR	A5	A5	-	A5	-	-	B9	-	UO$_2$ bending; AsO$_4$ bending
265 (d)	IR	A4	A4	A5	A5	-	B9	B10	B9	U-O bending; UO$_2$ bending; PO$_4$ bending; AsO$_4$ bending

Torbernite-Zeunerite P$_2$As$_2$c

Figure E.14: The simulated Raman and IR spectra of the P$_2$As$_2$c mixed phase of torbernite-zeunerite (Cu(UO$_2$)$_2$(PO$_4$)(AsO$_4$)·8H$_2$O) from 100–1100 cm^{-1}, in which the mixed layers of phosphate and arsenate ions are offset from one another.

Table E.13: Analysis of the Raman and IR active modes seen in the simulated spectra of the P$_2$As$_2$c mixed phase of torbernite-zeunerite. The frequencies are given in cm^{-1}. The Raman (R) and infrared (IR) activities are noted. Doubly degenerate modes are labelled by 'd'.

Freq. (cm^{-1})	Act. (R/IR)	U1	U2	U3	U4	P1	P2	As3	As4	Motion
1029	R	A2	A2	A2	A2	B1	B1	-	B1	UO$_2$ antisym. str.; AsO$_4$ antisym. str.
999	R	-	-	-	-	-	-	-	-	Water only
993	IR	A2	A2	A1	A1	B1	B1	-	-	UO$_2$ antisym. str.; U-O str.; PO$_4$ antisym. str.
962	R	A1	A1	A2	A2	B1	B1	-	-	U-O str.; UO$_2$ antisym. str.; PO$_4$ antisym. str.
955 (d)	IR	-	-	-	-	B4	-	-	-	PO$_2$ antisym. str.
929 (d)	IR	-	-	-	-	-	B4	-	-	PO$_2$ antisym. str.
924 (d)	IR	-	-	-	-	B1	-	-	-	PO$_4$ antisym. str.
889	IR	A1	A1	A1	A1	-	-	-	-	U-O str.
851 (d)	IR	-	-	-	-	-	-	-	-	Water only
847 (d)	IR	-	-	-	-	-	-	-	B8	AsO$_4$ sym. str.
834	R	-	-	A3	A3	-	B1	-	B1	UO$_2$ sym. str.; PO$_4$ antisym. str.; AsO$_4$ antisym. str.
830 (d)	IR	-	-	-	-	-	-	-	-	Water only
828	R	A3	A3	-	-	B1	-	B1	-	UO$_2$ sym. str.; PO$_4$ antisym. str.; PO$_4$ antisym. str.
814	IR	A1	A1	-	-	-	-	-	B13	U-O str.; As translation
810	R	A3	A3	A1	-	-	-	-	-	UO$_2$ sym. str.; U-O str.
807	R	-	A1	-	-	-	-	-	-	U-O str.
801	R	-	-	A3	A3	-	-	-	B8	UO$_2$ sym. str.; AsO$_4$ sym. str.
792	R	A3	A3	-	-	-	-	B8	-	UO$_2$ sym. str.; AsO$_4$ sym. str.
775 (d)	IR	-	-	-	-	-	-	B4	B4	AsO$_2$ antisym. str.
770 (d)	IR	-	-	-	-	-	-	B4	B4	AsO$_2$ antisym. str.
768	R	A3	A3	A3	A3	-	-	B1	-	UO$_2$ sym. str.; AsO$_4$ antisym. str.
754	R	A3	A3	-	-	-	-	B8	-	UO$_2$ sym. str.; AsO$_4$ sym. str.
752	IR	A3	-	A3	A3	-	-	B2	B1	UO$_2$ sym. str.; AsO$_4$ antisym. str.; As-O str.
434	R	-	-	-	-	B9	-	B9	-	PO$_4$ bending; AsO$_4$ bending
384	R	-	-	-	-	B9	-	-	-	PO$_4$ bending
383 (d)	IR	-	-	A5	A4	-	-	-	B9	UO$_2$ bending; U-O bending; AsO$_4$ bending
366	R	-	-	-	-	B9	-	-	-	PO$_4$ bending
318 (d)	IR	A5	A5	-	A5	-	-	B9	-	UO$_2$ bending; AsO$_4$ bending
265 (d)	IR	A5	A4	A4	A4	B9	B9	B9	B9	UO$_2$ bending; U-O bending; PO$_4$ bending; AsO$_4$ bending

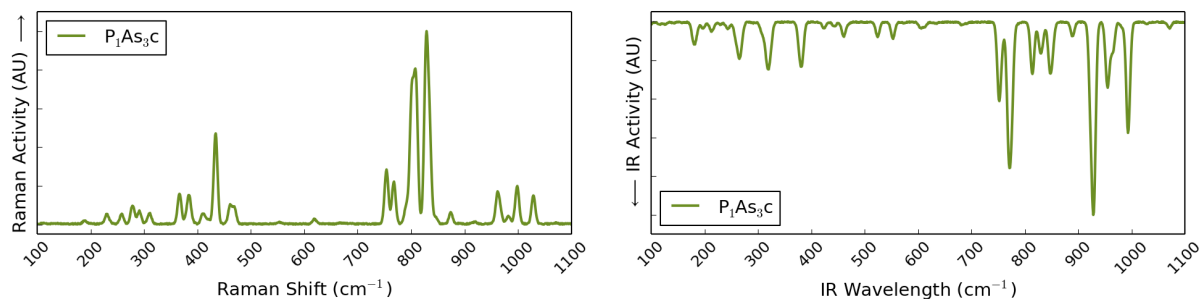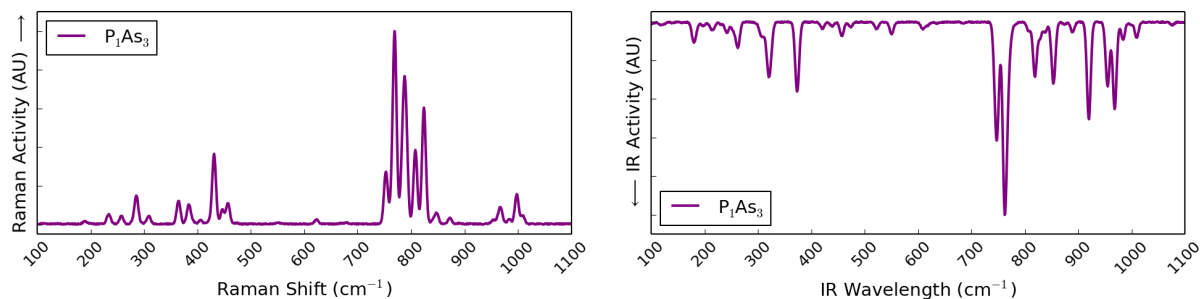# Torbernite-Zeunerite P_1As_3

Figure E.15: The simulated Raman and IR spectra of the P_1As_3 mixed phase of torbernite-zeunerite $(Cu(UO_2)_2(PO_4)_{0.5}(AsO_4)_{1.5} \cdot 8H_2O)$ from 100–1100 cm^{-1}.

Table E.14: Analysis of the Raman and IR active modes seen in the simulated spectra of the P_1As_3 mixed phase of torbernite-zeunerite. The frequencies are given in cm^{-1}. The Raman (R) and infrared (IR) activities are noted. Doubly degenerate modes are labelled by 'd'.

Freq. (cm^{-1})	Act. (R/IR)	U1	U2	U3	U4	P1	As2	As3	As4	Motion
1009	IR	A2	A2	A2	A2	B1	-	-	B1	UO$_2$ antisym. str.; PO$_4$ antisym. str.; AsO$_4$ antisym. str.
998	R	A1	-	-	-	-	-	-	-	U-O str.
984	IR	A2	A2	A2	A2	-	-	-	-	UO$_2$ antisym. str.
968	IR	A1	A1	A2	A2	-	-	-	B1	U-O str.; UO$_2$ antisym. str.; AsO$_4$ antisym. str.
968 (d)	IR	-	-	-	-	-	-	-	-	Water only
956	IR	-	-	-	-	-	-	-	B4	AsO$_2$ antisym. str.
955	IR	A1	A1	A1	-	-	-	-	B4	U-O str.; AsO$_2$ antisym. str.
953	IR	A2	A2	A1	A2	-	-	-	B5	U-O str.; UO$_2$ antisym. str.; AsO$_3$ antisym. str.
920 (d)	IR	-	-	-	-	-	-	-	B1	AsO$_4$ antisym. str.
854 (d)	IR	-	-	-	-	-	-	-	-	Water only
848	R	-	-	A3	A3	-	B8	B8	-	UO$_2$ sym. str.; AsO$_4$ sym. str.
824	R	A3	A3	-	-	B1	-	-	B1	UO$_2$ sym. str.; PO$_4$ antisym. str.; AsO$_4$ antisym. str.
819	IR	A1	A1	-	-	-	-	-	-	U-O str.
808	R	A3	A3	-	-	-	-	-	-	UO$_2$ sym. str.
791	R	A3	A3	A3	A3	B8	-	-	-	UO$_2$ sym. str.; PO$_4$ sym. str.
786	R	A1	A1	A3	A3	-	B8	B8	-	U-O str.; UO$_2$ sym. str.; AsO$_4$ sym. str.
769	R	-	-	-	-	-	B1	B1	-	AsO$_4$ antisym. str.
767 (d)	IR	-	-	-	-	B4	B4	B4	-	PO$_2$ antisym. str.; AsO$_4$ antisym. str.
762 (d)	IR	-	-	-	-	B4	B4	B4	-	PO$_2$ antisym. str.; AsO$_4$ antisym. str.
753	R	A3	A3	-	-	B8	-	-	-	UO$_2$ sym. str.; PO$_4$ sym. str.
748 (d)	IR	-	-	-	-	-	B1	B1	-	AsO$_4$ antisym. str.
745	IR	-	-	A3	A3	-	B1	B1	-	UO$_2$ sym. str.; AsO$_4$ antisym. str.
431	R	-	-	-	-	B9	-	-	B9	PO$_4$ bending; AsO$_4$ bending
383	R	-	-	-	-	-	-	-	B9	AsO$_4$ bending
373 (d)	IR	-	A4	A4	A4	B9	B9	B9	-	U-O bending; PO$_4$ bending; AsO$_4$ bending
364	R	-	-	-	-	-	-	-	B9	AsO$_4$ bending
319 (d)	IR	-	A5	A4	A5	B9	-	-	-	UO$_2$ bending; U-O bending; PO$_4$ bending
286	R	-	-	-	-	-	B9	B9	-	AsO$_4$ bending
263 (d)	IR	A5	A4	A4	A5	B9	B9	B10	B9	UO$_2$ bending; U-O bending; PO$_4$ bending; AsO$_4$ bending

Zeunerite
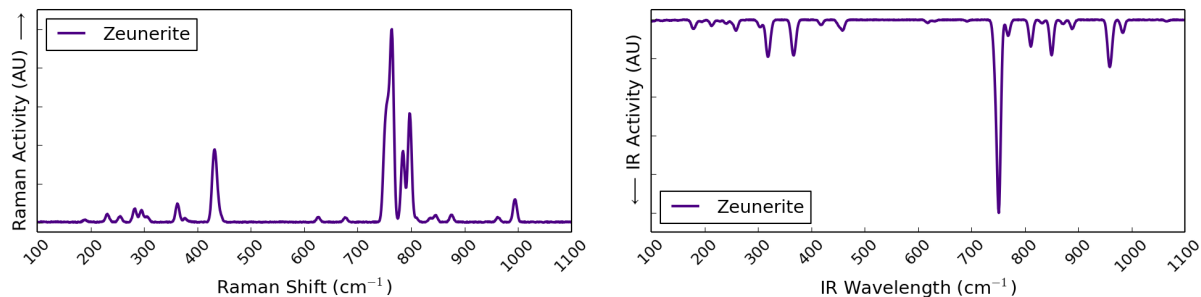
Figure E.16: The simulated Raman and IR spectrum of zeunerite $(Cu(UO_2)_2(AsO_4)_2 \cdot 8H_2O)$ from 100–1100 cm^{-1}.

Table E.15: Analysis of the Raman and IR active modes seen in the simulated spectra of zeunerite. The frequencies are given in cm^{-1}. The Raman (R) and infrared (IR) activities are noted. Doubly degenerate modes are labelled by 'd'.

Freq. (cm^{-1})	Act. (R/IR)	U1	U2	U3	U4	As1	As2	As3	As4	Motion
995	R	-	-	-	-	-	-	-	-	Water only
983	IR	A2	A2	A2	A2	-	-	-	-	UO$_2$ antisym. str.
957	IR	A2	A2	A2	A2	-	-	-	-	UO$_2$ antisym. str.
850 (d)	IR	-	-	-	-	-	-	-	-	Water only
811	IR	A1	A1	-	-	-	-	-	-	U-O str.
798	R	A3	A3	A3	A3	B8	B8	-	-	UO$_2$ sym. str.; AsO$_4$ sym. str.
785	R	A1	A1	A3	A3	-	-	B8	B8	U-O str.; UO$_2$ sym. str.; AsO$_4$ sym. str.
764	R	-	-	-	-	-	-	B1	B1	AsO$_4$ antisym. str.
757	R	-	-	-	-	B1	B1	-	-	AsO$_4$ antisym. str.
751 (d)	IR	-	-	-	-	B1	B1	B1	B1	AsO$_4$ antisym. str.
751	R	A3	A3	-	-	B8	B8	-	-	UO$_2$ sym. str.; AsO$_4$ sym. str.
746	IR	-	-	A3	A3	-	-	B1	B1	UO$_2$ sym. str.; AsO$_4$ antisym. str.
459	IR	-	-	-	-	B9	B9	B9	B9	AsO$_4$ bending
435	R	-	-	-	-	B9	B9	-	-	AsO$_4$ bending
430	R	-	-	-	-	-	-	-	-	Water only
369 (d)	IR	-	-	A4	A4	B10	B10	B9	B9	U-O bending; AsO$_2$ bending; AsO$_4$ bending
365 (d)	IR	A5	A5	-	-	B10	B10	B10	B10	UO$_2$ bending; AsO$_2$ bending
362	R	-	-	-	-	B13	B13	-	-	As translation
318 (d)	IR	A5	A5	-	A5	B9	B10	-	-	UO$_2$ bending; AsO$_4$ bending; AsO$_2$ bending
282	R	-	-	-	-	-	-	B9	B9	AsO$_4$ bending
259	R/IR	-	-	A5	A5	B13	B10	B9	B9	UO$_2$ bending; As translation; AsO$_2$ bending; AsO$_4$ bending
259	R/IR	-	-	A5	A5	B10	-	B9	B9	UO$_2$ bending; AsO$_2$ bending; AsO$_4$ bending